

1-1-2011

Finite element reconstruction of real world aortic injury in near-side lateral automotive crashes with conceptual countermeasures

Aditya Neelakanta Belwadi
Wayne State University,

Follow this and additional works at: http://digitalcommons.wayne.edu/oa_dissertations

Recommended Citation

Belwadi, Aditya Neelakanta, "Finite element reconstruction of real world aortic injury in near-side lateral automotive crashes with conceptual countermeasures" (2011). *Wayne State University Dissertations*. Paper 303.

This Open Access Dissertation is brought to you for free and open access by DigitalCommons@WayneState. It has been accepted for inclusion in Wayne State University Dissertations by an authorized administrator of DigitalCommons@WayneState.

**FINITE ELEMENT RECONSTRUCTION OF REAL WORLD AORTIC INJURY IN
NEAR-SIDE LATERAL AUTOMOTIVE CRASHES WITH CONCEPTUAL
COUNTERMEASURES**

by

ADITYA NEELAKANTA BELWADI

DISSERTATION

Submitted to the Graduate School

of Wayne State University,

Detroit, Michigan

in partial fulfillment of the requirements

for the degree of

DOCTOR OF PHILOSOPHY

2011

MAJOR: BIOMEDICAL ENGINEERING

Approved by:

Advisor Date

Date

Date

Date

External Date

© COPYRIGHT BY
ADITYA NEELAKANTA BELWADI
2011
All Rights Reserved

DEDICATION

To all those who willed their body for scientific research

I also dedicate this work to my late grandfather, Belavadi Srikantia and my late grandmother, Belavadi Kaveri, both of whom believed in diligence and pursuit of academic excellence.

ACKNOWLEDGEMENTS

It is a pleasure to thank the many people who made this dissertation possible. It is difficult to overstate my gratitude to my advisor, Dr. King Yang. With his enthusiasm, his inspiration, and his great efforts to explain things clearly and simply, he helped to make Biomechanics fun for me. Throughout my research, he provided encouragement, sound advice, great teaching, and many great ideas. I am also grateful to Dr. Albert King for providing timely encouragement and thought provoking questions. I would also like to thank my committee members Drs. Cavanaugh, Melvin, and Schneider for their timely feedback on my research.

I'm extremely grateful to the Southern Consortium of Injury Biomechanics (SCIB) for funding the project. I'm also grateful to Dr. John Siegel from University of Dentistry, New Jersey Medical School for his support in providing the much needed real-world crash data. As a recipient of the 2009 Drs. Anthony and Kales scholarship, I'm indebted to them for funding part of my research.

I owe a further debt of gratitude to the members of the Bioengineering Center who have labored tirelessly to help with everything from data collection, simulation to publication. I'm obliged to Dr. Paul Begeman for all his help in keeping the much needed computing facilities going. Special thanks to Drs. Chirag Shah and Haojie Mao for all their help, encouragement, and support provided during my research.

Most importantly, I would like to thank my family and friends for their everlasting support and encouragement. Specifically, my mother Dr. Sandhya Belwadi and father Mr. Neelakanta Belwadi, from whom I have always had undying love and support. My

lovely wife, Dr. Divya Moodalbail has been a pillar of support and strength during these testing times. I'm also grateful to my friend, philosopher and guide Dr. Krish Aekbote for constantly helping me give direction to my life.

Lastly, I would like to thank all my family and friends, here in the States and back in India, whose support has been invaluable throughout the toughest times of my life so far.

TABLE OF CONTENTS

Dedication	ii
Acknowledgements.....	iii
List Of Figures	xi
List of Tables	xviii
CHAPTER 1	1
INTRODUCTION	1
1.1 EPIDEMIOLOGY	2
1.2 AIMS OF THE STUDY.....	4
CHAPTER 2	7
REVIEW OF THE ANATOMY	7
2.1 CLINICAL ANATOMY OF THE HUMAN AORTA.....	7
2.2 MICRO-ANATOMY OF THE AORTA	10
2.3 PECULIARITIES AND AORTIC VARIATIONS	12
2.4 ATHEROSCLEROSIS.....	14
CHAPTER 3	16
LITERATURE REVIEW.....	16
3.1 INJURY MECHANISMS FOR TRA	16
3.1.1 INERTIA BASED HYPOTHESES	18
3.1.2 PRESSURE BASED HYPOTHESES.....	19

3.1.3 OTHER FACTORS	21
3.1.4 STRAIN BASED HYPOTHESES.....	23
3.2 WHOLE BODY CADAVERIC STUDIES	25
3.3 MATERIAL PROPERTIES OF AORTIC TISSUE.....	27
3.5 FINITE ELEMENT (FE) HUMAN BODY MODELS	28
CHAPTER 4	33
REAL-WORLD CIREN CRASH DATA	33
4.1 INTRODUCTION	33
4.2 MATERIALS AND METHODS	33
4.3 LEFT LATERAL CIREN DATA.....	34
4.3.1 CASE #4 DESCRIPTIONS	35
4.3.2 CASE #5 DESCRIPTIONS	37
4.3.3 CASE #6 DESCRIPTIONS	40
4.3.4 CASE #7 DESCRIPTIONS	43
4.3.5 CASE #8 DESCRIPTIONS	46
4.3.6 CASE #15 DESCRIPTIONS	49
4.3.7 CASE #16 DESCRIPTIONS.....	53
4.3.8 CASE #17 DESCRIPTIONS.....	56
4.3.9 CASE #T1 DESCRIPTIONS	59
4.3.10 CASE #T2 DESCRIPTIONS	61
4.3.11 CASE #T3 DESCRIPTIONS	63
CHAPTER 5	66

FINITE ELEMENT ACCIDENT RECONSTRUCTION METHODOLOGY	66
5.1 FE RECONSTRUCTION INTRODUCTION.....	66
5.2 STAGE I METHODOLOGY	66
5.3 STAGE II RECONSTRUCTION	69
CHAPTER 6	70
AIM A: FINITE ELEMENT ACCIDENT RECONSTRUCTION OF LEFT- LATERAL CIREN ACCIDENT DATA.....	70
6.1 INTRODUCTION	70
6.2 NASS-CDS DATABASE REVIEW.....	71
6.3 RECONSTRUCTION OF LATERAL CIREN CASES.....	72
6.4 RESULTS	78
6.5 DISCUSSION	83
6.5.1 LIMITATIONS OF THE CURRENT STUDY.....	89
6.6 AIM A: CONCLUSIONS	91
CHAPTER 7	93
AIM B: IDENTIFICATION OF KEY PARAMETERS RESPONSIBLE FOR INJURY MECHANISM IN LATERAL IMPACTS – DESIGN OF COMPUTER EXPERIMENTS STUDY (DOCE).....	93
7.1 INTRODUCTION	93
7.2 METHODS AND MATERIALS	94
7.3 RESULTS AND DISCUSSION.....	96
7.4 AIM B: CONCLUSIONS	104

8.1 INTRODUCTION	106
8.2 INJURY MECHANISMS FOR TRA	106
8.3 MATERIALS AND METHODS	111
8.3.1 CIREN CASE DETAILS.....	111
8.3.2 SENSITIVITY STUDY DETAILS	114
8.4 RESULTS	115
8.5 DISCUSSION.....	118
8.5.1 COMPARISON OF KINEMATICS DATA	123
8.6: AIM C: CONCLUSIONS	143
CHAPTER 9	145
AIM D: KINEMATICS OF THE AORTA IN HIGH-SPEED RACING CRASHES	145
9.1 INTRODUCTION	145
9.2 MATERIALS AND METHODS	147
9.3 RESULTS AND DISCUSSION.....	154
9.4 AIM D CONCLUSIONS	165
CHAPTER 10	167
AIM E: CONCEPTUAL COUNTERMEASURES IN NEARSIDE LEFT LATERAL IMPACTS TO REDUCE AORTIC STRAIN	167
10.1 INTRODUCTION	167
10.2 AIM E1 - METHODS AND MATERIALS.....	168
10.2.2 DOCE SIMULATIONS	172

10.3 RESULTS AND DISCUSSION	176
10.4 AIM E1 - CONCLUSIONS.....	185
10.5 AIM E2 - MATERIALS AND METHODS	186
10.6 RESULTS	190
10.7 AIM E2 - CONCLUSIONS.....	196
CHAPTER 11	197
CONCLUSIONS, LIMITATIONS, AND SCOPE FOR FUTURE WORK.....	197
11.1 CONCLUSIONS.....	197
11.11 CIREN RECONSTRUCTIONS	199
11.12 DOCE SIMULATIONS	200
11.13 HIGH-SPEED RACINGS SIMULATIONS	201
11.14 CONCEPTUAL COUNTERMEASURES.....	202
11.2 LIMITATIONS AND COMMENDATIONS FOR FUTURE WORK	203
11.2.1 ATHEROSCLEROSIS.....	205
Appendix A.....	208
Appendix B.....	211
Appendix C.....	219
Appendix D.....	221
Appendix E.....	225
References	226
Abstract.....	235

Autobiographical Statement..... 238

LIST OF FIGURES

FIGURE 2.1: ANATOMICAL COMPONENTS AND THEIR RESPECTIVE POSITIONS OF THE HUMAN MEDIASTINUM CONTENTS EXCEPT THE LEFT LUNG [GRAY, H. (1918) ANATOMY OF THE HUMAN BODY].....	8
FIGURE 2.2: THE NORMAL AORTIC ARCH AND ITS REGIONS (MODIFIED WITH PERMISSION FROM SHAH ET AL. 2007)	9
FIGURE 2.3: THE THREE LAYERS OF THE AORTA (FENEIS, 1994).....	11
FIGURE 2.4: COARCTATION OF THE AORTA (CAHILL, 1997)	13
FIGURE 2.5: FIFTEEN DIFFERENT POSSIBLE VARIATIONS OF THE <i>NORMAL</i> HUMAN AORTA (LIECHTY ET AL. 1957)	14
FIGURE 2.6: SCHEDULE OF PLAQUE BUILD-UP IN AN ARTERY (AMERICAN HEART ASSOCIATION, 1998)	15
FIGURE 3.1: (A) THE WAYNE STATE HUMAN BODY MODEL – II (WSHBM) SHAH ET AL. (2007) (B) WSHBM UPPER TORSO (C) SAGITTAL SECTION OF THE THORAX WITH THE SHOULDER, RIBCAGE AND THE LEFT LUNG REMOVED TO VIEW THE MEDIASTINUM CONTENTS.....	32
FIGURE 4.1: ACCIDENT SCENE FOR CASE #4.....	35
FIGURE 4.2: DEFORMATION PATTERN OF THE STRUCK VEHICLE, CASE #4	36
FIGURE 4.3: CASE #4, PARTIAL AORTIC TRANSECTION AT THE LEVEL OF THE ISTHMUS	37
FIGURE 4.4: ACCIDENT SCENE FOR CASE #5.....	38
FIGURE 4.5: DEFORMATION PATTERN OF THE CASE VEHICLE, CASE #5	39
FIGURE 4.6: CASE #5, AORTIC TRANSECTION AT THE LEVEL OF THE ISTHMUS	40
FIGURE 4.7: ACCIDENT SCENE FOR CASE #6.....	41
FIGURE 4.8: DEFORMATION PATTERN OF THE STRUCK VEHICLE, CASE#6	42
FIGURE 4.9: CASE 6, AORTIC TRANSECTION AT THE LEVEL OF THE ISTHMUS	43

FIGURE 4.10: ACCIDENT SCENE FOR CASE #7	44
FIGURE 4.11: DEFORMATION PATTERN OF THE STRUCK VEHICLE, CASE#7	45
FIGURE 4.12: CASE #7, AORTIC TRANSECTION AT THE LEVEL OF THE ISTHMUS	46
FIGURE 4.14: DEFORMATION PATTERN OF THE STRUCK VEHICLE, CASE#8	48
FIGURE 4.15: CASE #8, AORTIC TRANSECTION AT THE LEVEL OF THE ISTHMUS	49
FIGURE 4.16: ACCIDENT SCENE FOR CASE #15	50
FIGURE 4.17: DEFORMATION PATTERN OF THE STRUCK VEHICLE, CASE#15	51
FIGURE 4.18: CASE #15, AORTIC TRANSECTION AT THE LEVEL OF THE ISTHMUS	52
FIGURE 4.19: ACCIDENT SCENE FOR CASE #16	54
FIGURE 4.20: DEFORMATION PATTERN OF THE STRUCK VEHICLE, CASE#16	55
FIGURE 4.21: CASE #16, AORTIC TRANSECTION AT THE LEVEL OF THE ISTHMUS.....	56
FIGURE 4.22: ACCIDENT SCENE FOR CASE #17	57
FIGURE 4.23: DEFORMATION PATTERN OF THE STRUCK VEHICLE, CASE#17	58
FIGURE 4.24: CASE #17, AORTIC DISRUPTION AT THE LEVEL OF THE ISTHMUS.....	59
FIGURE 4.25: ACCIDENT SCENE FOR CASE #T1	60
FIGURE 4.26: DEFORMATION PATTERN OF THE STRUCK VEHICLE, CASE# T1	61
FIGURE 4.27: ACCIDENT SCENE FOR CASE #T2.....	62
FIGURE 4.28: DEFORMATION PATTERN OF THE STRUCK VEHICLE, CASE# T2	63
FIGURE 4.29: ACCIDENT SCENE FOR CASE #T3.....	64
FIGURE 4.30: DEFORMATION PATTERN OF THE STRUCK VEHICLE, CASE# T3	65
FIGURE 5.1: LATERAL CRUSH PROFILE MEASUREMENT (SAE J2433)	68
FIGURE 6.1: LEFT LATERAL THORACIC AORTIC INJURIES BY SOURCE (1993-2008)	72
FIGURE 6.2: C1-C6 DEFORMATION-TIME HISTORIES	78

FIGURE 6.3: AVERAGE MAXIMUM PRINCIPAL STRAIN-TIME HISTORIES FOR THE RIGHT CIREN CASES RECONSTRUCTED	81
FIGURE 6.4: (A) AVERAGE MAXIMUM PRINCIPAL STRAIN LOCATION – ISTHMUS OF THE AORTA, (B) LEFT SIDE DOOR INTRUSION PATTERN (RED MESH INDICATES HIGHER AMPS)....	87
FIGURE 6.5: MAXIMUM PRINCIPAL STRAIN PROFILE OF THE SPLEEN, LIVER, AND LEFT RIBS.....	88
FIGURE 7.1: (A) POSITION OF THE IMPACT ON THE VEHICLE, HEIGHT OF IMPACT AND OCCUPANT SEATING POSITION (B) RANGE OF PDOF IN THE SIMULATIONS.....	95
FIGURE 7.2: MAIN EFFECTS CHART FOR AMPS IN THE ISTHMUS OF AORTA	98
FIGURE 7.3: MAIN EFFECTS CHART FOR MAXIMUM PRESSURE (kPa) IN THE AORTA	99
FIGURE 7.4: PARETO CHART OF EFFECTS FOR ISTHMUS AMPS	101
FIGURE 7.5: PARETO CHART OF EFFECTS FOR MAXIMUM PRESSURE (kPa) IN THE AORTA	102
FIGURE 8.1: LOGISTIC REGRESSION PLOT WITH 50 TH AND 90 TH PERCENT PROBABILITY OF FAILURE FOR AMPS.....	120
FIGURE 8.2: LOGISTIC REGRESSION PLOT WITH 50 TH AND 90 TH PERCENT PROBABILITY OF FAILURE FOR MAXIMUM PRESSURE	121
FIGURE 8.3: I) RUN #A: PDOF=260 DEGREES II) RUN #B: PDOF=270 DEGREES	124
FIGURE. 8.4: (I) RUN #C: PDOF=250 DEGREES (II) RUN #D: PDOF=270 DEGREES	124
FIGURE 8.5: (I) RUN #F: PDOF=270 DEGREES (II) RUN #E: PDOF=310 DEGREES.....	125
FIGURE 8.6: (I) RUN #H: PDOF=260 DEGREES (II) RUN #G: PDOF=310 DEGREES	125
FIGURE 8.7: SAGITTAL VIEW (A) WSHBM WITH THE DOOR STRUCTURES (B) ISOLATED AORTA HIGHLIGHTED WITH THE NODES BEING TRACKED (RED).....	128
FIGURE 8.8: MOTION OF THE AORTA TRACKED, SAGITTAL VIEW – ARROW INDICATES DIRECTION OF IMPACT	129
FIGURE 8.9: HARDY ET AL. (2008) MOTION OF THE AORTA TRACKED, SAGITTAL VIEW – ARROW INDICATES DIRECTION OF IMPACT.....	130
FIGURE 8.10: CORONAL VIEW OF (A) WSHBM CONTACTS WITH THE DOOR STRUCTURES (B) ISOLATED AORTA HIGHLIGHTED WITH THE NODES BEING TRACKED (RED)	132

FIGURE 8.11: MOTION OF THE AORTA TRACKED, CORONAL VIEW – ARROW INDICATES DIRECTION OF IMPACT	133
FIGURE 8.12: HARDY ET AL. (2008) MOTION OF THE AORTA TRACKED, CORONAL VIEW – ARROW INDICATES DIRECTION OF IMPACT.....	134
FIGURE 8.13: RUN #10: (A) PDOF = 250 DEGREES :	135
CONTOURS OF RESULTANT DISPLACEMENT (MM) – (B) 35 MS (C) 38 MS.....	135
FIGURE 8.14: RUN #5: (A) PDOF = 270 DEGREES :	136
CONTOURS OF RESULTANT DISPLACEMENT (MM) – (B) 30 MS (C) 34 MS.....	136
FIGURE 8.15: RUN #11: (A) PDOF = 290 DEGREES :.....	137
CONTOURS OF RESULTANT DISPLACEMENT (MM) – (B) 52 MS (C) 58 MS.....	137
FIGURE 8.16: RUN #7: (A) PDOF = 310 DEGREES :	138
CONTOURS OF RESULTANT DISPLACEMENT (MM) – (B) 70 MS (C) 78 MS.....	138
FIGURE 8.17: AVERAGE Y-DISPLACEMENT (MM) OF THE STERNUM AND SPINE FOR A PDOF OF 260 DEGREES.....	139
FIGURE 8.18: AVERAGE Y-DISPLACEMENT (MM) OF THE STERNUM AND SPINE FOR A PDOF OF 300 DEGREES.....	140
FIGURE 8.19: AVERAGE RELATIVE Y-DISPLACEMENT (MM) OF THE STERNUM AND SPINE	141
FIGURE 8.20: AVERAGE RELATIVE Y-DISPLACEMENT (MM) - 260 DEGREES.....	142
FIGURE 8.21: AVERAGE RELATIVE Y-DISPLACEMENT (MM) - 300 DEGREES.....	143
FIGURE 9.1: TYPICAL INDY CAR CONFIGURATION [ADAPTED FROM MELVIN ET AL. 1998]	146
FIGURE 9.2: ACCELERATION-TIME HISTORY FOR CASE #LAS12 (BEGEMAN AND MELVIN (2002)).....	149
FIGURE 9.3: ACCELERATION-TIME HISTORY FOR CASE #99TX (BEGEMAN AND MELVIN (2002))	150
FIGURE 9.4: ACCELERATION-TIME HISTORY FOR CASE #IND14 (BEGEMAN AND MELVIN (2002))	151
FIGURE 9.5: SEAT, SIX-POINT HARNESS SYSTEM, SHOULDER SUPPORT PADS, AND HEAD SUPPORT.....	152

FIGURE 9.6: INITIAL POSITION OF WSHBM IN THE RACING BUCK.....	153
FIGURE 9.7: MAXIMUM PRINCIPAL STRAIN - SEVERE SHOULDER DEFORMATION IN THE ABSENCE OF SHOULDER SUPPORT PADS – DOTS SHOW THE OTHERWISE LOCATION OF SHOULDER SUPPORT PADS.....	156
FIGURE 9.8: CASE #99TX: (A) WSHBM KINEMATICS WITH THE RACING BUCK (B) CONTOURS OF LOWER SURFACE MAXIMUM PRINCIPAL STRAIN IN THE AORTA.....	157
FIGURE 9.9: COMPARISON OF AVERAGE AMPS WITH PUBLISHED DATA	159
FIGURE 9.10: COMPARISON OF AVERAGE MAXIMUM PRESSURE WITH PUBLISHED DATA	160
FIGURE 9.11: MAIN EFFECTS PLOT FOR AMPS	161
FIGURE 9.12: PARETO CHART OF EFFECTS FOR AMPS.....	162
FIGURE 9.13: MAIN EFFECTS PLOT FOR MAXIMUM PRESSURE	163
FIGURE 9.14: PARETO CHART OF EFFECTS FOR MAXIMUM PRESSURE	164
FIGURE 9.15: INITIAL (0 MS) AND DEFORMED (30 MS AND 60 MS) THORACIC CAVITY - CORONAL SECTION.....	165
FIGURE 10.1: CASE 7 CIREN DATA WITH A) RIB FRACTURE B) AORTIC RUPTURE C) SKULL FRACTURE AND D) HINGE FRACTURE.....	169
FIGURE 10.2: (A) VEHICLE DEFORMATION PATTERNS OF THE ACTUAL CASE VEHICLE (B) FE SIMULATION USING THE SCALED FE VEHICLE MODEL.....	171
FIGURE 10.3: EXPLODED VIEW OF STRUCTURES INVOLVED IN THE DOCE (A) EXTERIOR VIEW AND (B) INTERIOR VIEW	174
FIGURE 10.4: LEFT SIDE DOOR STRUCTURES, WSHBM ALONG WITH A CONCEPTUAL UNFOLDED BLANKET AIRBAG	175
FIGURE 10.5: (A) OCCUPANT KINEMATICS AND (B) MAXIMUM PRINCIPAL STRAIN PATTERN AT THE TIME OF MAXIMUM VEHICLE DEFORMATION FOR RUN VI	179
FIGURE 10.6: MAIN EFFECTS ANALYSIS PLOT – AMPS.....	180
FIGURE 10.7: MAIN EFFECTS ANALYSIS PLOT - MAXIMUM AORTIC PRESSURE (KPA)	181
FIGURE 10.8: MAIN EFFECTS ANALYSIS PLOT – MAXIMUM B-PILLAR INTRUSION (MM)	182
FIGURE 10.9: PARETO CHART OF EFFECTS FOR AMPS.....	183

FIGURE 10.10: PARETO CHART OF EFFECTS FOR MAXIMUM PRESSURE	184
FIGURE 10.11: PARETO CHART OF EFFECTS FOR MAXIMUM B-PILLAR INTRUSION.....	185
FIGURE 10.9: SHOWS THE WSHBM WITH THE NEW REDESIGNED CONTOURED SEAT, SHOULDER SUPPORT PADS AND HEAD PADDING – ADVANCED BILATERAL PROTECTION SEAT [®] (ABPS [®]).....	187
FIGURE 10.10: AMPS - WITH AND WITHOUT ABPS [®]	192
FIGURE 10.11: MAXIMUM PRESSURE (kPA) IN THE AORTA - WITH AND WITHOUT ABPS [®]	193
FIGURE 10.12: BOX-PLOT OF AMPS FOR CASES WITH AND WITHOUT ABPS [®]	194
FIGURE 10.13: BOX-PLOT OF MAXIMUM PRESSURE FOR CASES WITH AND WITHOUT ABPS [®] .	195
FIGURE 11.1: AIMS AND CONCLUSIONS - SUMMARY	198
FIGURE 11.2: ATTACHMENT OF THE SUPERIOR VASCULATURE IN THE WSHBM.....	203
FIGURE B1: VEHICLE DEFORMATION COMPARISON OF SIMULATED FE VEHICLE AGAINST ACTUAL VEHICLE - CASE 4.....	211
FIGURE B2: VEHICLE DEFORMATION COMPARISON OF SIMULATED FE VEHICLE AGAINST ACTUAL VEHICLE – CASE 5	211
FIGURE B3: VEHICLE DEFORMATION COMPARISON OF SIMULATED FE VEHICLE AGAINST ACTUAL VEHICLE – CASE 6	212
FIGURE B4: VEHICLE DEFORMATION COMPARISON OF SIMULATED FE VEHICLE AGAINST ACTUAL VEHICLE – CASE 7	212
FIGURE B5: VEHICLE DEFORMATION COMPARISON OF SIMULATED FE VEHICLE AGAINST ACTUAL VEHICLE – CASE 8	213
FIGURE B6: VEHICLE DEFORMATION COMPARISON OF SIMULATED FE VEHICLE AGAINST ACTUAL VEHICLE – CASE 15	213
FIGURE B7: VEHICLE DEFORMATION COMPARISON OF SIMULATED FE VEHICLE AGAINST ACTUAL VEHICLE – CASE 16	214
FIGURE B8: VEHICLE DEFORMATION COMPARISON OF SIMULATED FE VEHICLE AGAINST ACTUAL VEHICLE – CASE 17	214
FIGURE B9: (A) OCCUPANT KINEMATICS AND (B) MAXIMUM PRINCIPAL STRAIN PATTERN AT THE TIME OF MAXIMUM VEHICLE DEFORMATION – CASE 4.....	215

FIGURE B10: (A) OCCUPANT KINEMATIC AND (B) MAXIMUM PRINCIPAL STRAIN PATTERN AT THE TIME OF MAXIMUM VEHICLE DEFORMATION – CASE 5.....	215
FIGURE B11: (A) OCCUPANT KINEMATICS AND (B) MAXIMUM PRINCIPAL STRAIN PATTERN AT THE TIME OF MAXIMUM VEHICLE DEFORMATION – CASE 6.....	216
FIGURE B12: (A) OCCUPANT KINEMATICS AND (B) MAXIMUM PRINCIPAL STRAIN PATTERN AT THE TIME OF MAXIMUM VEHICLE DEFORMATION – CASE 7.....	216
FIGURE B13: (A) MAXIMUM PRINCIPAL STRAIN PATTERN AND (B) OCCUPANT KINEMATICS AT THE TIME OF MAXIMUM VEHICLE DEFORMATION – CASE 8.....	217
FIGURE B14: (A) MAXIMUM PRINCIPAL STRAIN PATTERN (B) OCCUPANT KINEMATICS AT THE TIME OF MAXIMUM VEHICLE DEFORMATION – CASE 15	217
FIGURE B15: (A) OCCUPANT KINEMATICS AND (B) MAXIMUM PRINCIPAL STRAIN PATTERN AT THE TIME OF MAXIMUM VEHICLE DEFORMATION – CASE 16.....	218
FIGURE B16: (A) MAXIMUM PRINCIPAL STRAIN PATTERN (B) OCCUPANT KINEMATICS AT THE TIME OF MAXIMUM VEHICLE DEFORMATION – CASE 17	218
FIGURE C1: AVERAGE MAXIMUM PRINCIPAL STRAIN IN THE ISTHMUS AND MAXIMUM PRESSURE IN THE AORTA: RUNS #01 THROUGH #08.....	219
FIGURE C2: AVERAGE MAXIMUM PRINCIPAL STRAIN IN THE ISTHMUS AND MAXIMUM PRESSURE IN THE AORTA: RUNS #09 THROUGH #16.....	220
FIGURE D1: MID-STERNUM VS. T4-SPINE KINEMATICS FOR RUN #A	221
FIGURE D2: MID-STERNUM VS. T4-SPINE KINEMATICS FOR RUN #B	221
FIGURE D4: MID-STERNUM VS. T4-SPINE KINEMATICS FOR RUN #D	222

LIST OF TABLES

TABLE 3.1: LIST OF THE VARIOUS INJURY MECHANISMS HYPOTHESIZED FOR TRA PUBLISHED IN THE LITERATURE.....	16
TABLE 5.1: CRUSH PROFILES FOR THE EIGHT LEFT LATERAL CIREN CASES.....	68
TABLE 6.1: SUMMARY OF LEFT LATERAL CASES USED IN THE CRASH RECONSTRUCTION PROCESS.....	74
TABLE 6.2: SUMMARY OF VEHICLE MODELS AND THEIR INITIAL SETUP (AFTER SCALING) USED IN THE LEFT LATERAL CRASH RECONSTRUCTION PROCESS	77
TABLE 6.3: DETAILS OF THE VEHICLE FE MODELS USED IN THE RECONSTRUCTION.....	77
TABLE 6.4: COMPARISON OF ACTUAL DEFORMATIONS OBTAINED FROM CIREN VERSUS	79
TABLE 6.5: OUTPUT DETAILS FOR THE FE RECONSTRUCTIONS – STAGE II.....	80
TABLE 6.6: COMPARISON OF AORTIC INJURY LOCATIONS BETWEEN REAL WORLD CIREN DATA AND WSHBM PREDICTED REGIONS OF STRAIN	82
TABLE 7.1: RANGE OF VALUES FOR THE FIVE DESIGN FACTORS CHOSEN FOR THE DOCE STUDY	95
TABLE 7.2: LATIN SQUARE SAMPLING FOR DOCE AND OUTPUT RESPONSE VARIABLES: AMPS AND MAXIMUM PRESSURE IN THE AORTA	97
TABLE 7.3: SIGNIFICANCE OF EACH DESIGN FACTOR FOR AN $P=0.05$: AMPS AND MAXIMUM PRESSURE IN THE AORTA.....	100
TABLE 8.1: LIST OF THE VARIOUS INJURY MECHANISMS HYPOTHESIZED FOR TRA PUBLISHED IN THE LITERATURE.....	107
TABLE 8.1: SUMMARY OF LEFT LATERAL CASES USED IN THE CRASH RECONSTRUCTION PROCESS.....	112
TABLE 8.2: SUMMARY OF VEHICLE MODELS AND THEIR INITIAL SETUP (AFTER SCALING) USED IN THE LEFT LATERAL CRASH RECONSTRUCTION PROCESS	113
TABLE 8.3: DETAILS OF THE VEHICLE FE MODELS USED IN THE RECONSTRUCTION.....	113
TABLE 8.4: PAIRED SENSITIVITY TABLE TO ACCESS THE MECHANISM OF INJURY BASED ON PDOF	115

TABLE 8.5: COMPARISON OF ACTUAL DEFORMATIONS OBTAINED FROM CIREN VERSUS THE DEFORMATIONS PREDICTED BY THE FE RECONSTRUCTION – STAGE I.....	116
TABLE 8.6: OUTPUT DETAILS FOR THE FE RECONSTRUCTIONS – STAGE II.....	117
TABLE 8.7: PAIRED SENSITIVITY TABLE TO ACCESS THE MECHANISM OF INJURY BASED ON PDOF	118
TABLE 8.8: X, Y, AND Z DISPLACEMENTS OF THE STERNUM AND SPINE	126
TABLE 9.1: CASES SELECTED FROM BEGEMAN AND MELVIN (2002).....	148
TABLE 9.2: SIMULATION MATRIX GENERATED USING A LATIN SQUARE ALGORITHM IN MODEFRONTIER 4.1	154
TABLE 9.3: AMPS AND MAXIMUM PRESSURE IN THE AORTA RECORDED FOR THE CASES WITH THE WSHBM IN A RACING BUCK.....	155
TABLE 10.1: DEFORMATION COMPARISON OF THE SIMULATION WITH THE ACTUAL VEHICLE ...	171
TABLE 10.1: DOCE MATRIX GENERATED USING MODEFRONTIER 4.1 FOR THE SIMULATION RUNS.....	176
TABLE 10.2: AMPS (%), MAXIMUM PRESSURE (kPa) IN THE AORTA AND B-PILLAR INTRUSION (MM).....	177
TABLE 10.3: MATERIAL PROPERTIES AND LS-DYNA MATERIAL MODELS USED FOR THE NEW REDESIGNED SEAT.....	188
TABLE 10.4: INPUT DESIGN FACTORS FOR THE SEAT BASED COUNTERMEASURE	189
TABLE 10.5: AMPS AND MAXIMUM PRESSURE FOR THE CASES WITH AND WITHOUT ABPS® .	191
TABLE A1: MATERIAL PROPERTIES OF THE WAYNE STATE HUMAN BODY MODEL – II: THORACIC CAVITY (SHAH ET AL. 2007)	208
TABLE A2: MATERIAL PROPERTIES OF THE LEFT SIDE DOOR STRUCTURE OF A 2001 FORD TAURUS FE MODEL	208
TABLE A3: MATERIAL PROPERTIES OF THE FRONT BUMPER AND HOOD STRUCTURES OF THE STRIKING VEHICLES USED IN PHASE A OF THE RECONSTRUCTION.....	209
TABLE E1: THICKNESS OF SIDE DOOR STRUCTURES.....	225

CHAPTER 1

INTRODUCTION

Since the first recorded motor vehicle fatality in 1869 (World Health Organization), motor vehicle fatalities and injuries have proven to be a lasting concern. In 2006, motor vehicle traffic crashes in the United States were the leading cause of death for individuals aged 3-34 years, while heart disease was the leading cause of death for ages 64 and above (Traffic Safety Facts: NHTSA, 2008). Motor vehicle traffic crashes ranked third overall in terms of the years of life lost, behind only cancers and heart diseases (Traffic Safety Facts: NHTSA, 2008). The societal cost associated with vehicle crash-related injuries in the United States was estimated at over 260 billion dollars (NHTSA, 2008). In 2009, 33,808 people lost their lives in motor vehicle crashes and another two and one half million were injured (Fatality and Injury Rates per population and Vehicle Miles Traveled, 1994-2009). In 2009, the fatality rate per 100 million vehicle miles of travel (VMT) fell to a historic low of 1.13 as compared to 1.73 in 1994. Accordingly, it has become increasingly important to reduce the number and severity of these injuries instead of focusing only on the number of fatality. In recent years, the trend towards accident mitigation and prevention has augmented.

Traumatic rupture of the aorta (TRA) remains the second most common cause of death associated with motor vehicle crashes after brain injury (Smith and Chang, 1986; Sauaia et al. 1995). On an average, nearly 8,000 people die annually in the United States due to blunt injury to the aorta (Mattox, 1989). It is observed that more than 80% of occupants who suffer an aortic injury die at the scene due to exsanguination into the chest cavity. The probability of an occupant surviving the injury depends on the nature

of emergency care taken within the first one hour of injury causation (Primm et al. 1979; Wilson and Hutchins, 1982). Data published by the National Automotive Sampling System (NASS) show that more than 58% of crashes are frontal crashes and nearly 28% are lateral impacts (left and right inclusive).

According to Sailer (1942), Vesalius made the first reference to traumatic rupture of the thoracic aorta in 1557. However, aortic injury was rare until the advent of high-speed motor vehicle crashes in the mid 1900's. TRA and blunt aortic injury (BAI) are leading causes of death in high-speed blunt impact trauma. More specific injuries that fall under these classifications include myocardial contusion (MC), traumatic aortic disruption (TAD), sternal fracture (SF), flail chest (FC) and tracheobronchial disruption (TBD) (Swan et al. 2001).

1.1 Epidemiology

Reference to aortic injury and aortic disease has existed from as early as 1500 B.C. Archaeologists have found evidence that the ancient Egyptians suffered from aortic injury and aortic disease; signs of atherosclerosis have been found in Egyptian mummies (Willerson and Teaff, 1996). Over the last four decades, closed chest trauma concerning ruptures of the thoracic organs and blood vessels have caused 25-40% of all automotive fatalities in which 10-20% of those fatalities were due to aortic trauma (Viano, 2011). In side impacts (left and right inclusive), the incidence was higher at 2.4% than those in frontal impacts at 1.1% (Siegel et al. 2004; 2006).

Bertrand et al. (2008) reviewed in-depth crash data for TRA from 1998 to 2006 from the Co-operative Crash Injury Study (CCIS) database and concluded that although

TRA victims accounted for only 1.2% of all injured occupants, these victims accounted for 21.4% of all fatalities. The injury risk increased with impact velocity, occupant compartment intrusion, and age. It was also noted that almost 79.1% of the injured had multiple rib fractures, mostly from the second to the seventh ribs. Bertrand et al. (2008) concluded that the mechanism of aortic injury was primarily due to a direct chest impact or compression.

In a similar study, Franklyn et al. (2003) reviewed NASS database cases from 1993 to 2000 and the CCIS database from 1983 to 2001 and concluded that, in near side crashes, the risk of aortic injury was greater on the left side of the body than that on the right regardless of seating position. Further, the average change in collision speed, delta-v of crashes with aortic injury was higher than crashes where occupants did not sustain aortic injuries. Burkhart et al. (2001) reviewed 242 autopsy cases with fatal BAI and concluded that in most cases aortic injury was accompanied by head injury, rib fractures, and/or hepatic trauma.

Augenstein et al. (1997) reported that AIS 3+ injuries inflicted to the heart were due to seatbelts in frontal crashes. Approximately 90% of those injuries were to the aortic isthmus, 5-10% to the ascending aorta, and 1-3% to the descending aorta at the level of the diaphragmatic hiatus and 98% of them died at the scene. A number of researchers have reported transverse or circumferential tears to the longitudinal axis of the aorta, distal to the subclavian artery known as the peri-isthmic region or isthmus, as the primary site of aortic laceration (Greendyke, 1966; Symbas, 1973; Sevitt, 1977; Viano, 1983; Katyal et al. 1997). The location presents an evolution from a relatively mobile arch to a tethered descending portion (at the level of the third and fourth thoracic

vertebral body) with posterior intercostal arteries that lead off. Cahill (1997) revealed that the aorta has a natural coarctation at the side of attachment of the ligamentum arteriosum (remnants of the ductus arteriosus).

Aortic tears can range from partial tears of the inner wall, typically the intima and medial layers to complete transection involving the adventitia (Strassmann, 1947; Cammack et al., 1959; Symbas, 1977; Sevitt, 1977; Viano, 1983; Hardy et al. 2006). The tears usually occur on the intervascular surface of the isthmus that has the shortest curvature and is vulnerable to longitudinal stretch (Sevitt, 1977; Hardy et al. 2006). Tears have also been seen to occur at the aortic root, attachment to the heart and the aortic hiatus at the diaphragm (Sevitt, 1977).

1.2 Aims of the study

To augment the knowledge of aortic injury biomechanics, following objectives are achieved in this dissertation:

(A) Accident Injury Reconstruction (AIR)

Finite element accident reconstruction of eight near side left lateral real world Crash Injury Research Engineering Network (CIREN) cases with FE vehicle models and the second version of the Wayne State Human Body FE model to accurately predict aortic injury.

(B) Sensitivity study of factors

Sensitivity study utilizing the Wayne State Human Body Model – II (WSHBM) with respect to the impact velocity, impact position, impact height, and PDOF of the striking vehicle along with occupant position in the struck vehicle was conducted to assess causation factors and their effect on aortic strain, aortic pressure, and compartmental intrusion in left lateral cases.

(C) Mechanisms for TRA

Qualitative validation of data from WSHBM with existing experimental data and compare existing mechanisms of TRA with CIREN reconstruction simulations

(D) Aorta mechanics in high-speed racing crashes

Drivers in high-speed crashes (Indycar, NASCAR, Formula One) are typically involved in severe crashes but survive through with minimal injuries. An Indycar buck with WSHBM is simulated to study the effect of the seat, six-point harness and shoulder support pads.

(E) Conceptual Countermeasures to reduce aortic strain in nearside left lateral impacts

Simulations using design of computer experiments (DOCE) method of the left side door structure with the introduction of a B-pillar beam, increased dimensions of the beam, elevated yield strength of the beam, introduction of a cross-beam, increased thickness of the side sheet metal structures and introduction of an “overall” side

airbag to study their effect on aortic strain, pressure in the aorta and compartmental intrusion.

Chapter 2 reviews the relevant anatomy of aorta associated with the current study while Chapter 3 consolidates the Literature Review. Real world crash data used in the study are described in Chapter 4 with the methodology of accident reconstruction in Chapter 5. Methods used to reconstruct cases with aortic injuries (**Aim A**) are provided in Chapter 6 while Chapter 7 describes the sensitivity study (**Aim B**) to analyze factors affecting the maximum principal strain and maximum pressure in the aorta. Chapter 8 summarizes the numerous injury mechanism hypothesized in the literature (**AIM C**) and compares the data from the left lateral reconstructions performed with existing literature. Chapter 9 compares the strains in three Indycar simulations with the WSHBM (**AIM D**) and establishes the usefulness of protecting the shoulder and thoracic cavity in side impacts. Chapter 10 describes the DOCE study to reduce compartmental intrusion thus reducing thoracic deformation, which is deemed as a precursor to aortic strain (**AIM E**) along with other measures to reduce aortic strain. Chapter 11 provides the scope of the current study and looks at future directions for TRA mitigation.

CHAPTER 2

REVIEW OF THE ANATOMY

The cardio-vascular (CV) system consists primarily of the heart (cardio pump) and blood vessels (vascular system). The primary function of the CV system is to circulate blood via the artery-capillary-vein network and back. The aorta is the most proximal artery of the heart and serves as a conduit and an elastic chamber (Kassab, 2006). The aorta's elasticity serves to convert the heart's pulsatile flow to near steady flow in the peripheral vessels. Basile and Ventura in 2006 reported that in 1733, the English Reverend Stephen Hales concluded from his experiments on horses that the aorta expands to accommodate a large fraction of the stroke volume.

2.1 Clinical Anatomy of the Human Aorta

Figure 2.1 illustrates the various anatomical components and their respective positions of the human mediastinum contents except the left lung. The aorta is the primary artery among the great vessels, which carries oxygenated blood purified in the lungs to the rest of the body.

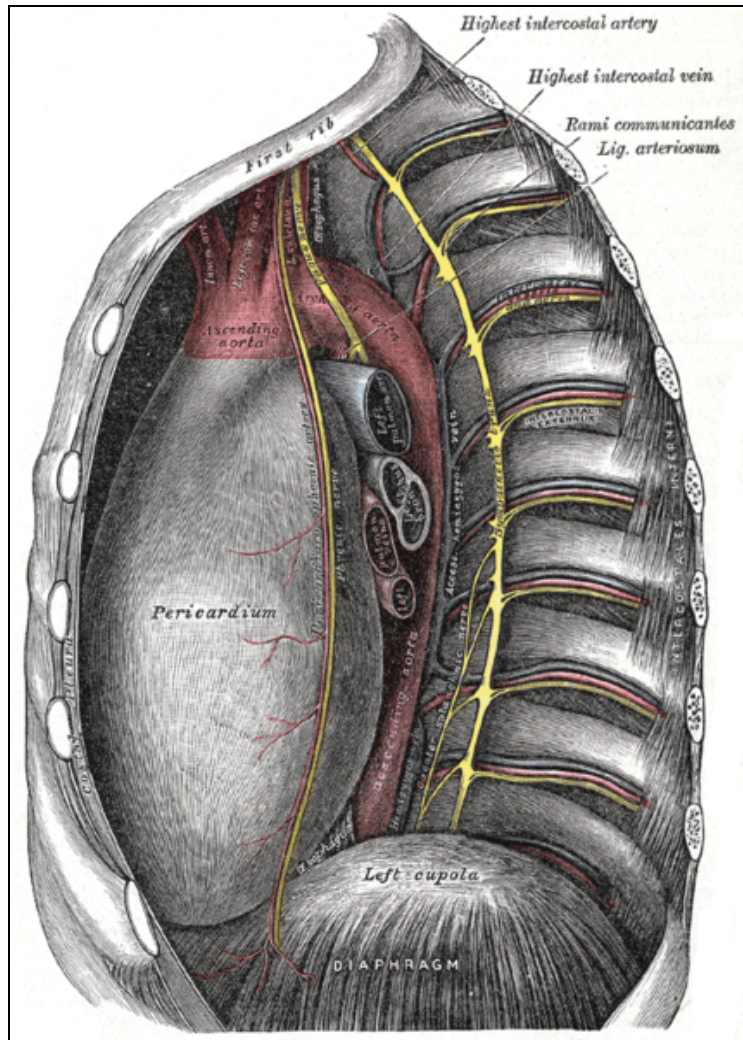


Figure 2.1: Anatomical components and their respective positions of the human mediastinum contents except the left lung [Gray, H. (1918) Anatomy of the Human Body]

According to Sundt and Clingman (2008), the normal human aorta is defined anatomically by the origins of the brachiocephalic vessels. The three main branches: the innominate or the brachiocephalic trunk, left common carotid artery, and the left subclavian artery collectively called the superior vasculature arise in that order from the arch of the aorta. The remnants of the fetal arterial circulation (ductus arteriosus), ligamentum arteriosum (Botallo's ligament), arises from the pulmonary trunk and

connects to the aorta, distal to the left subclavian artery. The aortic arch begins proximal to the origin of the innominate artery and ends distal to the left subclavian artery. The normal aorta is greatest in diameter at its origin, where it averages to about 30 mm and narrows to about 20 mm at the isthmus. However, it is recorded that the diameter and the stiffness of the aorta increases with normal aging (Sundt and Clingman, 2008).

The Oxford English dictionary refers to an isthmus as “A constriction or narrow passage connecting two larger parts of an organ or other anatomical structure.” According to Sundt and Clingman (2008), the isthmus is defined as *“the region of the distal arch lying just between the origin of the subclavian artery and the ductus arteriosus (or ligamentum arteriosum in the adult) may have a mild narrowing which is a normal variant.”*

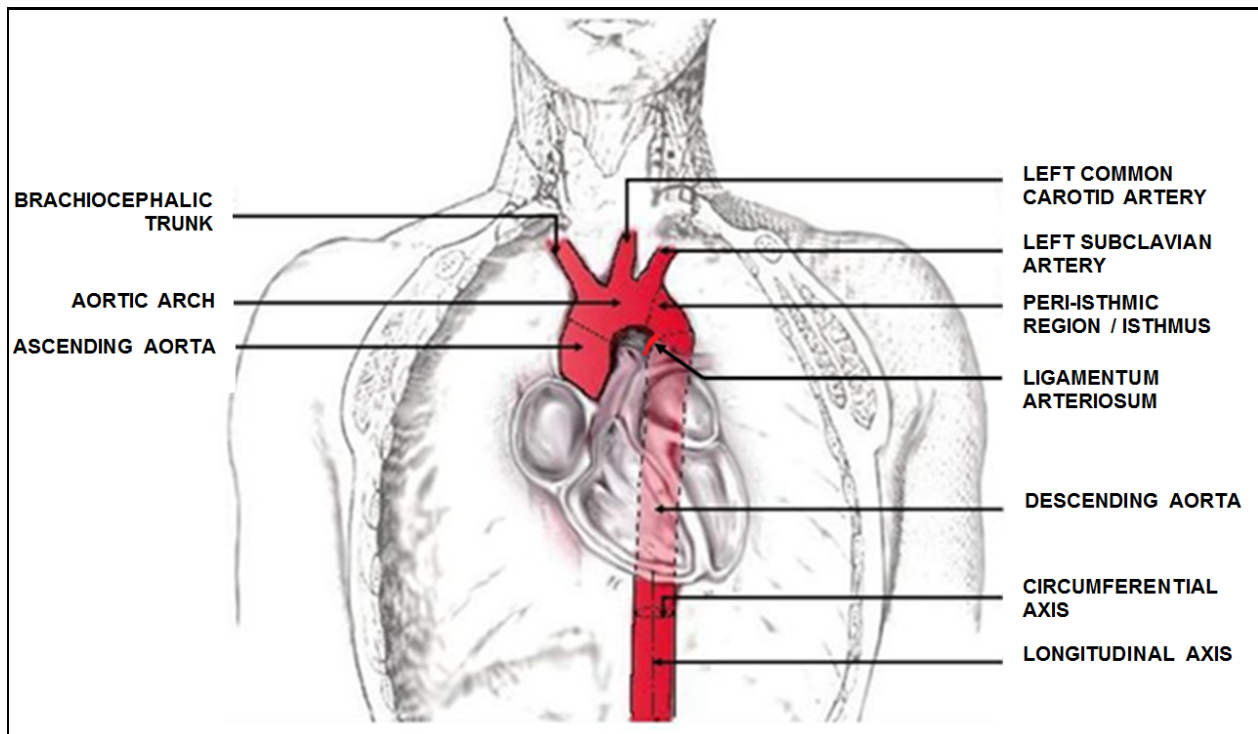


Figure 2.2: The normal aortic arch and its regions (Modified with permission from Shah et al. 2007)

From Figure 2.2, the ascending aorta begins at the aortic valve at the base of the left ventricle and ascends to about the second right sternocostal joint. The aortic arch begins at the second right sternocostal joint and further arches superiorly to the left, anterior to the right pulmonary artery and bifurcation of the trachea, passes over the root of the right lung and then begins its descend at the body of the fourth thoracic vertebra. The descending aorta descends on the left side of the bodies of T5 to T12 vertebrae, posterior to the root of the left lung and the pericardium, enters the abdomen through the aortic hiatus at the level of the twelfth thoracic vertebral body (Netter, 2006).

Another important aspect is the attachment of the descending aorta to the spine. This attachment is through the parietal pleura, paravertebral fascia, and intercostal arteries. These structures hold the descending aorta fixed to the spine rendering it less vulnerable to injuries. The fixation increases the risk of injury to the peri-isthmic region, which is attached to the relatively mobile arch at its proximal margin.

2.2 Micro-Anatomy of the Aorta

The aortic wall is divided into three layers, from the innermost, the tunica intima, tunica media, and the tunica adventitia (Soloman and Phillips 1987). The intima is comprised primarily of endothelial cells, while the media and adventitia are comprised of elastic tissue and interconnecting muscle fibers. These fibers allow the aorta to stretch to prevent over-expansion due to the pressure that is exerted on the walls by blood flow (Feneis, 1994). Figure 2.3 shows the three layers of the aortic wall obtained using staining techniques.

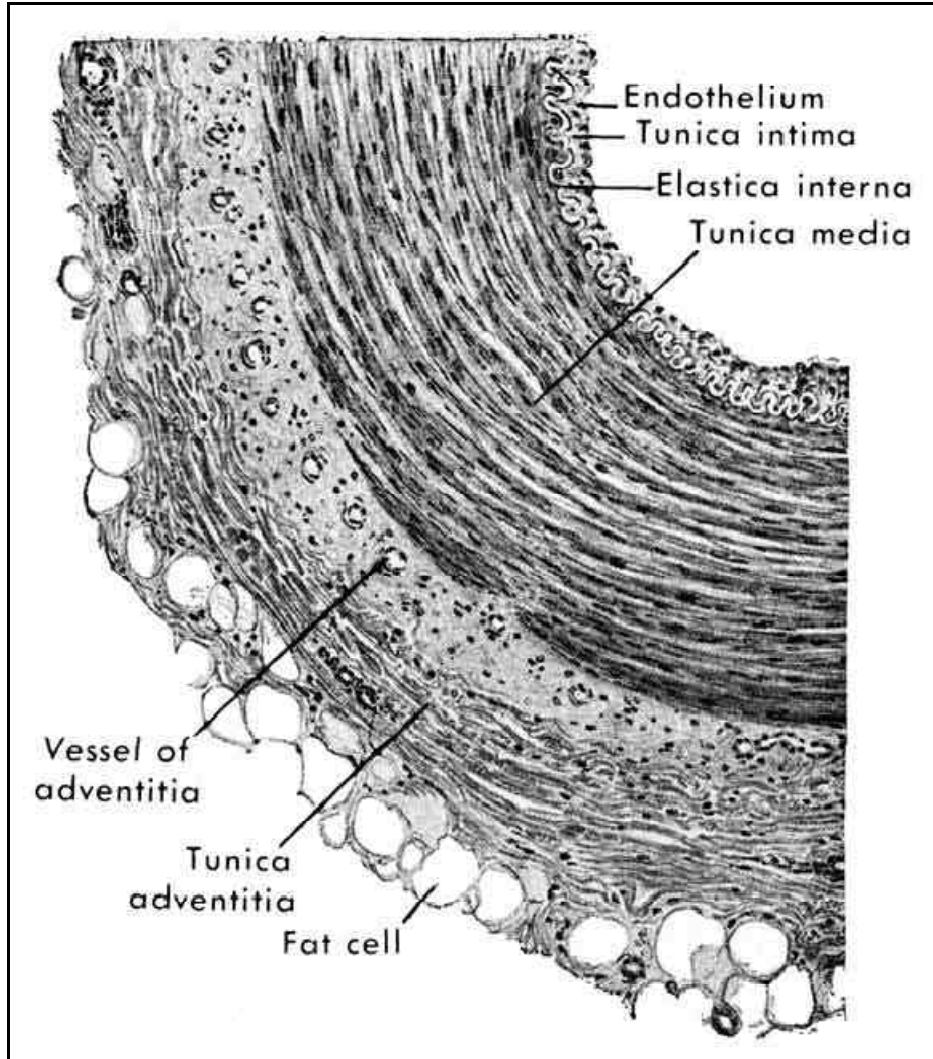


Figure 2.3: The three layers of the aorta (Feneis, 1994)

Studies have been performed to investigate injuries to specific regions of the aorta in order to determine if there is some region-related correlation to injury risk. As mentioned in Chapter 1, Augenstein et al. (1997) reported that, for AIS 3+ injuries inflicted to the aorta, 90% were to the aortic isthmus, 5-10% to the ascending aorta, and 1-3% to the descending aorta at the level of the diaphragmatic hiatus. Additionally, the group reported that 98% of injured with aortic AIS 3+ injuries died at the scene. According to Katyal et al. (1997), 94% of all TRA's involved the isthmic region of the

aorta, distal to the attachment of the left subclavian artery. They also suggested from crash data that nearly all complete transections of the aorta were transverse about the longitudinal axis, and 94% of those occurred near the isthmic region. In a pathological stand, the lesion to the aortic wall is a “Tear” and not a “Dissection.” Typically, the tear is through the intima and media, with the thin but tough adventitia containing the blood volume as a pseudo aneurysm.

2.3 Peculiarities and Aortic Variations

Between the origin of the left subclavian artery and the attachment of the ligamentum arteriosum, the lumen of the aorta is considerably narrowed, forming what is termed the **aortic isthmus**. Immediately beyond the ductus arteriosus, the vessel presents a fusiform dilation called the **aortic spindle**, the point of junction of the two parts being marked in the concavity of the arch by an indentation or angle (Moore and Persaud, 1998). Distinct from this diffuse and moderate stenosis at the isthmus is the condition known as *coarctation of the aorta, or marked stenosis* occurring a little below the insertion of the ligamentum arteriosum into the aorta (Figure 2.4).

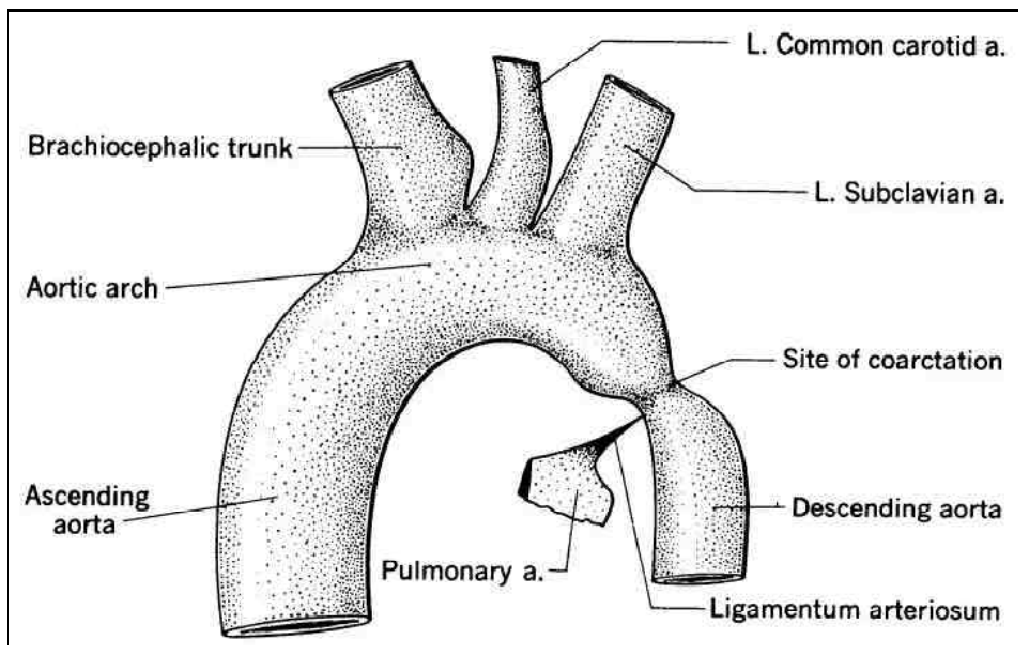


Figure 2.4: Coarctation of the aorta (Cahill, 1997)

According to Bonnet et al. (1996), this coarctation is never found in the fetus or at birth, and is due to an abnormal extension of the peculiar tissue of the ductus into the aortic wall, which gives rise to a simultaneous stenosis of both vessels as it contracts after birth. While this may not be relevant to the current study, it is worthy a note here, that the nature of injury gets further complicated with the fact there could be as many as 15 different possible variations of the aortic arch and its branches. Based on a study on 1000 cadavers, Liechty et al. (1957) concluded that only 64.9% of the general population had a normal aortic anatomy (Figure 2.5).

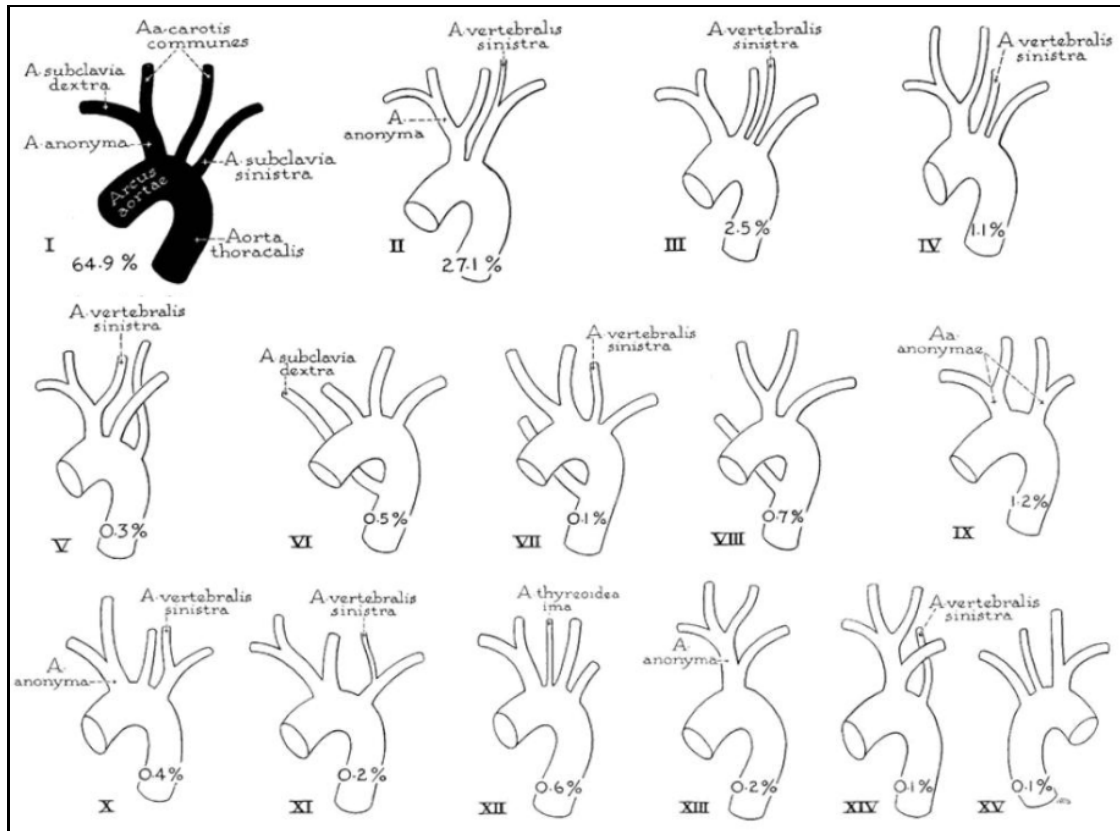


Figure 2.5: Fifteen different possible variations of the normal human aorta (Liechty et al. 1957)

2.4 Atherosclerosis

Atherosclerosis (also known as **Arteriosclerotic Vascular Disease** or **ASVD**) is the condition in which an artery wall thickens as the result of a build-up of fatty materials such as cholesterol. It is a syndrome affecting arterial blood vessels, a chronic inflammatory response in the walls of arteries, in large part due to the accumulation of macrophage white blood cells and promoted by low-density lipoproteins (LDL) without adequate removal of fats and cholesterol from the macrophages by functional high-density lipoproteins (HDL). Figure 2.6 shows the progression of plaque

build-up in an artery. The atheromatous plaque is divided into three distinct components:

1. The atheroma, which is the nodular accumulation of a soft, flaky, yellowish material at the center of large plaques, composed of macrophages
2. Underlying areas of cholesterol crystals
3. Calcification at the outer base of older/more advanced lesions

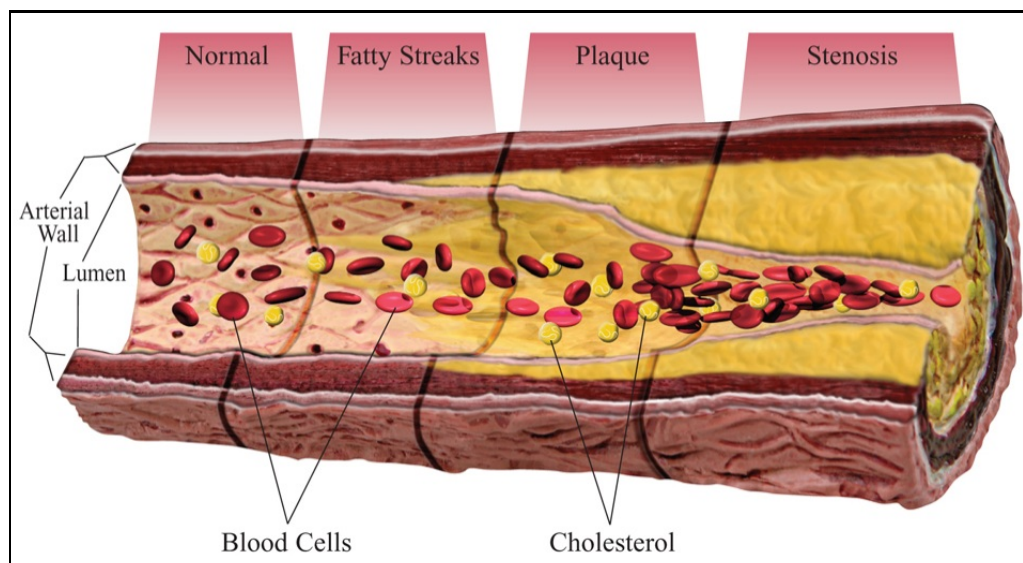


Figure 2.6: Schedule of plaque build-up in an artery (American Heart Association, 1998)

CHAPTER 3

LITERATURE REVIEW

3.1 Injury Mechanisms for TRA

There are numerous mechanisms hypothesized for aortic injury in the literature. Table 3.1 briefly summarizes 30 different publications, which speculated such mechanisms. More descriptions of these studies are provided in the sections followed.

Table 3.1: List of the various injury mechanisms hypothesized for TRA published in the literature

No.	Author and Year	Mechanism
Inertia based		
1	Letterer, 1924	Downward traction of the heart as a result of falling is responsible for aortic root avulsion
2	Hass, 1944	Differential acceleration (jerk) of the structures within the mediastinum
3	Roberts et al., 1966	Inertia component not primarily required for rupture
4	Creasy et al., 1997	High rate of deceleration along with chest compression might cause aortic injuries
5	Forman et al., 2008	Acceleration alone cannot cause TRA. Thoracic deformation is essential for TRA
Pressure based		
6	Oppenheim, 1918	Overpressure – 400 kPa
7	Klotz and Simpson, 1932	Overpressure due to hemodynamic effect of acceleration – explosive

8	Taylor, 1962	Shock waves could initiate a retrograde aortic bulge causing a localized weakness
9	Lundevall, 1964	Water hammer effect due to over pressure
10	Roberts et al., 1966	Transverse tear from pressure to occur if ratio of ultimate transverse stress to ultimate long. Stress > 2
11	Carson and Roach, 1990	Intimal tears at 79 kPa
12	Siegel et al., 2004	Archimedes Lever Hypothesis
Others		
No.	Author and Year	Mechanism
13	Marshall, 1958	Squeezing of the aorta by the parietal pleura
14	Cammack et al., 1959	Torsion of the aorta due to deceleration
15	Zehnder, 1960	Hyper flexion displacement of the aortic arch with the hilum of the lungs acting as a fulcrum
16	Hossack, 1980	Non-circumferential tears as a result of laceration from the ribcage
17	Crass et al., 1990	Osseous pinch mechanism
18	Sevitt, 1977	Discussed multiple mechanisms of injury - ligamentum arteriosum
19	Voigt and Wilfert, 1969	Traction of the superior vasculature - aorta is subjected to tension via the carotid arteries as a result of rapid rearward pitch of the head – involves a dorso-cranial motion of the heart in response to frontal impact to the abdomen and thorax – Shoveling mechanism: where compression of the sternum forces the heart upward causing tension in the aorta at the isthmus.
20	Cavanaugh et al. (1990,1993)	Inertial forces exerted by laterally accelerating heart and vessels may pulled on the descending thoracic aorta, which is firmly anchored to the posterior chest wall, causing aortic tears between the aortic arch and the descending thoracic aorta

21	Melvin et al., (1998)	Anterior motion of the sternum away from the spine is limited substantially – Passenger car occupants, the sternum is driven away from the spine anteriorly due to medial motion of the shoulder complex and the deforming ribcage – Sternal popping
22	Cavanaugh et al. (2005)	Suggested the importance of anterior motion of the sternum in side impacts
23	Shah et al., 2007	Sternal popping may not be a mechanism of injury. Hilum of the lung may play a role in TRA
Stretch based		
No.	Author and Year	Mechanism
24	Rindfleisch, 1893	Stretch deformation was a significant component of TRA
25	Mohan and Melvin, 1982	Ratio of ultimate transverse stress to ultimate longitudinal axis Stress = 1.2~2.12
26	Hardy et al., 2006	No pulmonary artery injury – motion of aortic arch and heart relative to the fixed descending aorta which straightens the inferior aortic arch
27	Shah et al. 2007	Longitudinal stretch of the aorta
28	Hardy et al., 2008	Tethering of the aorta to the parietal pleura
29	Belwadi et al. 2011	Longitudinal stretch of the thoracic aorta from FE CIREN reconstructions
30	King et al. 2011	Summarized the tests from Hardy et al. (2008) - Longitudinal stretch of the thoracic aorta and tethering of the aorta to the parietal pleura

3.1.1 Inertia based hypotheses

In 1966, Roberts et al. contradicted earlier studies published by Letterer (1924) and Hass (1944) on inertia based theories, and hypothesized that both inertia and pressure were not primarily responsible for aortic rupture. Colonel John Stapp (1957)

withstood more than 45 g's without significant injury in a frontal sled system. It is also evident that drivers in racecars experience far more accelerations in both frontal and side crashes (Melvin et al. 1998). Further, Forman et al. in 2008 tested nine cadaveric thoraces in an impact-sled configuration, placed in drums filled with beads to limit chest compression. In most cases, the sled tests resulted in spinal accelerations of up to 80 g for 20 ms. A maximum chest compression of $7.0 \pm 3.1\%$ of the total chest depth, and maximum-recorded increases in intra-aortic, tracheal, and esophageal pressure of 177, 112, and 156 kPa, respectively were reported. No macroscopic injuries to the thoracic aorta resulted from these tests, though other limited visceral injury was observed. They concluded that posteriorly directed acceleration alone was not sufficient to cause gross aortic injury. Hardy et al. (2006) carried out four quasi-static tests and one dynamic test on cadavers to failure and concluded that *intraluminal pressure and whole-body acceleration was not required for TRA to occur.*

3.1.2 Pressure based hypotheses

There have been numerous hypotheses published arguing about pressure being the primary mechanism of TRA. As early as 1918, Oppenheim concluded that overpressure in the aorta (400 kPa) was the primary reason for aortic tears. Klotz and Simpson (1932) and Taylor (1962) conjectured that pressure changes due to acceleration could cause shock waves to propagate within the aorta leading to failure due to burst or explosion, while Lundevall (1964) called this a "Water hammer" effect. In 1966, Roberts et al. negated earlier inertia and pressure based theories, hypothesized that both inertia and pressure were not primarily responsible for aortic

rupture, and concluded that if the aorta has to fail due to pressure alone then the ratio of ultimate stress in the transverse direction to ultimate stress in the longitudinal direction must be more than two. Mohan and Melvin (1982) found the ratio of ultimate transverse stress to ultimate longitudinal stress to be in the range of 1.2 to 2.12 in quasi-static uniaxial tests of human aorta. Bass et al. in 2001 pressurized human cadaveric aortas at an average rate of 730 kPa/s during *in vivo* and *in situ* experiments. More than half of these tests had longitudinal tears and reported a 50% risk of tear to the aorta at 101 kPa and raised it to 120 kPa for occupants 68 years of age. Siegel et al. (2004) reviewed 876 motor vehicle crashes (MVC) involving adult drivers or front-seat passengers whose injuries were evaluated by one of ten Level 1 Crash Injury Research Engineering Network (CIREN) centers for Injury trauma. It was concluded that pressure, along with torsional strain, was responsible for isthmus failure. In 2006, Siegel et al. proposed the “Archimedes Lever Hypothesis,” where the thoracic aorta, *super-pressurized* by the thoracic impact force, functions as a rigid lever system. The long arm of the lever is the proximal aorta (i.e., the aortic arch), and the short arm would be the aortic isthmus fixed distally at the descending aorta. The fulcrum of the system is at the left subclavian artery junction with the aorta. In contrast, Viano (1983) argued that pressure alone was not sufficient to cause injury. Shah et al. (2006) and Hardy et al. (2006) argued that clinical data had shown that the primary failure pattern was a transverse tear and not a longitudinal tear, indicating that it may be more likely that aortic tears are due to longitudinal stretch than burst failure. Although at this point, the direction of failure may not be the best predictor for failure, since studies such as Bass et al. (2001) have obtained both longitudinal and transverse tears. In the current FE

CIREN reconstructions (Belwadi et al. 2011), data has shown that elements fail in both longitudinal and circumferential axes. It is also to be noted that due to the inherent curvature of the aorta, it can be quite a challenge to accurately identify the direction of failure. Hence, it is highly *unlikely that hemodynamic pressure alone can produce aortic tears, although it is a contributing factor to rupture, and particularly to tears of the intima.*

3.1.3 Other factors

In one of the earlier studies, Marshall (1958) proposed an alternative method of failure mechanism for TRA; hypothesized that during an impact the parietal pleura may squeeze the aorta leading to rupture. Cammack et al. (1959) theorized torsional forces on the aorta while Zehnder (1960) said that hyperflexion of the aortic arch with the fulcrum at the hilum of the lung acted as a lever leading to failure of the aorta. Hossack (1980) hypothesized that lacerations to the aorta were due to the penetrating ribcage, while Crass et al. (1990) proposed the “The Osseous Pinch.” The authors hypothesized that pinching of the aorta between the posterior thoracic spine and the anterior bony (osseous) thorax (manubrium, clavicle, and first ribs) during chest compression because of sudden deceleration was responsible for aortic isthmus tears. Sevitt (1977) reviewed multiple injury mechanisms published at that time and concluded from literature that the ligamentum arteriosum (remnants of ductus arteriosum from the fetal circulation system) might play a crucial role in the mechanism of TRA. Shah et al. (2006) and Hardy et al. (2006) argued that since there were no injuries to the pulmonary artery in a typical crash, the ligamentum arteriosum may not be as significant as previous thought to cause injury. However, it is important to note that the aorta can have a natural

coarctation at the site of ligamentum arteriosum attachment (Cahill, 1997). Voigt and Wilfert (1969) proposed the “Shoveling” mechanism for TRA. Compression of the sternum resulted in the heart moving upward causing a tensile force acting on the aorta in the region of the isthmus of the aorta causing a tear. Cavanaugh et al. (1990, 1993) concluded from 17 cadaveric tests in a Heidelberg-type seat fixture at speeds of 6.7 to 10.5 m/s (five aortic tears) that the inertial forces exerted by laterally accelerating heart and vessels may have pulled on the descending thoracic aorta, which is firmly anchored to the posterior chest wall, causing aortic tears between the aortic arch and the descending thoracic aorta. Melvin et al. (1998) in their study showed that Indycar drivers can sustain very high accelerations (50.7 g in 13 frontal crashes and 53.3 g in 143 side impacts) with no aortic laceration. Further, there were no serious thoracic injuries reported. It is to be noted that in most cases, peak accelerations sustained were usually within a time window of 3 to 10 ms. It was hypothesized that the six-point restraint system worn by the drivers limited chest deformation. They proposed the “Sternal Popping” as a mechanism of failure. In passenger car occupants, the sternum moved away from the spine anteriorly due to medial motion of the shoulder complex and the deforming ribcage. Cavanaugh et al. (2005) reanalyzed their earlier findings and suggested the importance of anterior motion of the sternum in side impacts. Shah et al. (2007) concluded from a combination of cadaveric tests and FE simulations that the sternum moved about 20 mm anteriorly and might not be responsible for aortic tears. They instead hypothesized that the hilum of the lung might play a role in the injury. It is to be noted that they measured only anterior displacement of the sternum

and not the deformation of the thoracic cavity, which may be a better predictor for sternal motion.

Calcified aortic plaques changes the elastic properties of the aorta making it inextensible in the region of calcification (Sherebrin et al. 1994). Viano (1983) suggested that the presence of atherosclerotic plaque is the weakest link in any traumatic aortic rupture. More recently in their cadaveric test setups, Hardy et al. (2006, 2008) found that in cases with atherosclerotic plaques the aorta failed in regions with plaque.

3.1.4 Strain based hypotheses

At the end of the 19th century, Rindfleisch (1893) utilizing data of riders falling from horses concluded that stretch deformation was a significant component for aortic injury. No major study has been published since then on stretch mechanism for TRA due to lack of sophisticated cadaveric testing and high speed imaging techniques. In 1983, Mohan and Melvin were able to produce rupture stresses in the human aortic tissues at an average inflation pressure (not the aortic pressure) of 800 kPa in biaxial loading experiments producing spherical tissue deformation. In 2006, Hardy et al. investigated TRA mechanisms using *in situ* human cadavers loaded in four quasi-static and one dynamic configurations. The tests were carried out by perturbing the mediastinal structures of the cadavers. All injuries occurred in the isthmic region. The authors concluded that intraluminal pressure and whole-body acceleration were not required to induce a TRA. Tethering of the descending aorta to the parietal pleura was deemed the principal aspect of injury. Shah et al. (2007) tested six whole aortas (from

root to thoracic) in a tensile loading configuration at 1 and 5 m/s until failure. They concluded that longitudinal tensile stretch caused rupture of the aorta, more so in the transverse direction, similar to tears found from autopsy data. Further, Hardy et al. (2008) tested eight unembalmed human cadavers in various dynamic blunt loading modes using a high-speed biplane x-ray to visualize aortic motion within the mediastinum. The cadavers were inverted during testing to ensure accurate placement of the aorta and the mediastinal contents during testing. Clinically relevant TRA was observed in seven of those eight tests. However, the authors did not validate if inverting the cadavers indeed resulted in a realistically positioned aorta, analogous to *in vivo* conditions. Tensile stretch along the longitudinal axis of the aorta, caused by thoracic deformation was found to be the principal component of injury causation. More recently, Viano (2011) reanalyzed their pendulum impact studies carried out in 1986 on 11 unembalmed cadavers. They concluded that the absence of TRA (except in one cadaver), in spite of using higher impact energies, was attributed to the fact that the cadavers were not inverted as in Hardy et al. (2008), causing inaccurate placement of the cadaveric aorta and the mediastinal contents. Unfortunately, no further test data or clarification was provided to support the theory. It might be possible that the inversion of the cadaver can cause artificial loading via the superior vasculature, which can load the aorta prior to testing. King et al. (2011) summarized cadaveric test data from Hardy et al. (2008) and deemed longitudinal stretch of the aorta to be the main source of TRA. They also hypothesized that attachment of the parietal pleura to the thoracic aorta may play a role in the injury mechanics.

3.2 Whole Body Cadaveric Studies

Numerous whole body cadaveric impact testing have been conducted to reproduce TRA in a laboratory setting. Kroell et al. (1974) impacted 23 unembalmed cadavers midsternal with a saline pressurized aorta using an impactor with a mass of 19.5 kg or 23.1 kg at speeds ranging from 4.0 to 10.0 m/s. Although the pressure generated was 210 kPa, only two aortic tears were generated. Shatsky et al. (1974) observed TRA after impacting primate chests with a pendulum at a speed of 5 m/s. Using flash X-ray cinematography, they observed high compression of the intra-thoracic organs. Entrapment of the aorta between the heart and spine was deemed as the probable cause of aortic tears. Nusholtz et al. (1985) carried out experiments on live anesthetized canine using a 10 kg hydraulic ram at speeds of up to 14 m/s. Aortic injuries at the aorta-heart junction and at the junctions between the aorta and its superior branches were generated. It was concluded that aortic trauma was only possible if subjects were frontally impacted above the sternum, causing compression of the chest followed by downward motion of the heart.

Viano (1989) reported on 14 unembalmed human cadavers subjected to a total of 44 blunt lateral impacts to the chest and abdomen. The impacts were delivered using a 150 mm diameter and 23.4 kg mass pendulum launched at nominal a speed of 4.5, 6.7, or 9.4 m/s. The objective of this study was to develop response corridors for the chest and abdomen subjected to blunt side impact. No aortic ruptures occurred during those tests. Cavanaugh et al. (1990, 1993) were able to produce five aortic tears among 17 tests performed using a horizontally accelerated sled and a Heidelberg-type seat fixture at speeds of 6.7 to 10.5 m/s. The arterial system was pressurized to 100

mmHg before the crash. It was hypothesized that the inertial forces exerted by laterally accelerating heart and vessels might have pulled on the descending thoracic aorta, which was firmly anchored to the posterior chest wall, causing aortic tears between the aortic arch and the descending thoracic aorta. Cavanaugh et al. in 2005 re-analyzed their earlier sled test data to examine potential injury parameters and their relative predictive abilities. From multivariate analysis, it was concluded that combining the upper sternum postero-anterior acceleration with Average Spine Acceleration (ASA) (Cavanaugh et al. 1993) and T12 vertical acceleration with $V \cdot C_{\max}$ (Lau and Viano 1986), resulted in the best predictors for TRA.

Hardy et al. further validated this thinking in 2006 and in 2008 with their cadaveric studies. Hardy et al. in (2006) investigated TRA mechanisms using *in situ* human cadavers loaded in four quasi-static and one dynamic configurations. The tests were carried out by perturbing the mediastinal structures of the cadavers. All injuries occurred in the isthmic region. The authors concluded that intraluminal pressure and whole-body acceleration were not required to induce a TRA. Tethering of the descending aorta to the parietal pleura was deemed the principal aspect of injury. Forman et al. (2008) conducted nine sled tests using partial cadavers placed in drums filled with beads to limit chest compression. The tests examined the inertial mechanism for aortic rupture. Peak accelerations averaging 169 g's did not result in aortic rupture with 7% chest compression and 177 kPa aortic pressure. The authors concluded that chest compression was required for injury. Further, Hardy et al. (2008) tested eight unembalmed human cadavers in various dynamic blunt loading modes using a high-speed biplane x-ray to visualize aortic motion within the mediastinum. The cadavers

were inverted during testing to ensure accurate placement of the aorta and the mediastinal contents during testing. Clinically relevant TRA was observed in seven of those eight tests despite that the authors did not validate if indeed this inverted posture more realistically positioned the aorta in *in vivo* conditions. Tensile stretch along the longitudinal axis of the aorta, caused by thoracic deformation was found to be the principal component of injury causation. It is to be noted here that very few authors distinguished the injury mechanism based on impact direction, a vast majority focused on a mechanism based on frontal loading to the body. More recently, Viano (2011) reanalyzed their pendulum impact studies carried out in 1986 on 11 unembalmed cadavers and concluded that the absence of TRA (except in one cadaver), in spite of higher impact energies were used, was due to the fact that the cadavers were not inverted as in Hardy et al. (2008) leading to inaccurate placement of the cadaveric aorta and the mediastinal contents. Unfortunately, no further test data or explanation was provided to validate the theory. It might be possible that the inversion of the cadaver can cause artificial loading via the superior vasculature, which can load the aorta prior to testing leading to TRA.

3.3 Material Properties of Aortic Tissue

Material properties of the aorta are crucial for the development of accurate finite element models. Lundevall (1964) concluded that the strength of the isthmus and the descending aorta were 63% and 80% of baseline strength (ascending aorta), respectively. He concluded that the aortic tissue was non-linear, anisotropic, and rate sensitive. Viano (1983) reported that the Young's modulus of the human aorta ranged

from 360 to 400 kPa in the circumferential direction and 220 to 300 kPa in the longitudinal direction. Mohan and Melvin (1982; 1983) studied the failure stress of the human aorta under uniaxial and biaxial tensile loads and found that the average stress at failure was 3.53 and 5.07 MPa for specimens loaded in the longitudinal and transverse directions, respectively.

Bass et al. (2001) tested 11 whole cadaveric aortas and established a 50% risk of failure to be 852 kPa in the circumferential direction and 426 kPa in the longitudinal direction. They concluded from three *in-situ* tests that the internal thoracic boundary conditions might not be important in the stress/strain levels for aortic failure. Shah et al. (2007) performed biaxial tissue tests on cruciate-shaped samples and longitudinal stretch tests on whole aortas at a strain rate of 85 s^{-1} , which was proportionate with loading rates seen in an automotive crash environment. Three regions of the aorta: ascending, descending, and peri-isthmus were tested to investigate regional differences of the aorta. Structural response of the aorta was obtained by longitudinal stretch test at a rate of 1 m/s. The circumferential direction (Young's modulus $11.37 \pm 7.50 \text{ MPa}$) of the aortic tissue was stiffer than the longitudinal direction (Young's modulus $7.79 \pm 3.63 \text{ MPa}$). Further, they found that most of the tears to occur in the peri-isthmic region of the aorta at an axial strain of 22.1%.

3.5 Finite Element (FE) Human Body Models

With the advent of more accurate and established human body FE models, FE crash reconstruction methods have become a valuable tool when assessing crash scenarios and occupant injury mechanisms (Shah et al. 2005; Guan et al. 2010). In a

typical vehicular crash reconstruction, software packages based on rigid body dynamics methods fed data from physical evidence, such as tire marks, measurements of the deformed vehicles, and photographs of the accident scene determine the crash energy, impact velocity, and principal direction of force (PDOF), as per SAE J224. However, accurate determination of these parameters requires more sophisticated numerical methods, such as finite element analysis since rigid body dynamics methods cannot be used to account for parameters such as the extent of deformation and the location of the impact. Hence, it becomes imperative to reconstruct real world crash data utilizing FE models and then use vehicle kinematics with human body FE models to further understand the mechanism of aortic injury.

Roberts and Chen (1970) developed one of the first FE human thoracic skeleton models for investigating biomechanical responses of the human chest. Later, utilizing a beam element approach, Sudaram and Feng (1977) developed another three-dimensional model. The bony ribcage, sternum and musculature were represented by beam, plate and membrane elements, respectively. Plank and Eppinger (1991) developed a more realistic model of the human thorax, while Huang et al. (1994) developed a simplified human torso model to predict side impact injury parameters. Wang (1995) developed a side impact finite element human thoracic model using geometry data from Schneider et al. (1983) for a mid-sized seated male in a driving position. The model consisted of 4,333 solid elements and 11,075 shell elements. Lizee et al. (1998) developed a whole-body human model with a limited number of elements to study a wide variety of impact conditions. More recently Toyota Central R&D Lab., Inc. developed the Total Human Model for Safety (THUMS) representing a

50th percentile adult male (Iwamoto et al. 2002). None of the reviewed whole body models has enough anatomical details in the thoracic cavity or a sufficiently accurate aortic model to predict TRA.

In 2001, Shah et al. modified the thorax model developed by Wang (1995) to create a detailed FE model of the thorax appropriate for the study of aortic injuries. The new model was comprised of a detailed skeletal structure and internal organs in the thoracic cavity representing the thorax of a 50th percentile male. In 2004, Shah et al. integrated three detailed, validated models, the thorax model by Shah et al. (2001), the abdomen model by Lee and Yang (2001), and the shoulder model by Iwamoto et al. (2000), to create the Wayne State Human Body Model (WSHBM-I). During integration, the model was further improved to include blood in the aorta. This was achieved by using the *AIRBAG_LINEAR_FLUID airbag option available in the LS-DYNA (LSTC, Livermore, CA) airbag library. Additionally, the aortic mesh was refined in order to predict stress distribution more accurately. In this model, the major internal organs, the heart and lungs, were modeled using nonlinear solid elements while the blood vessels within the mediastinum, including the aorta, pulmonary trunk, pulmonary veins, and superior and inferior vena cava, were modeled using linear elastic shell elements. The esophagus, trachea, diaphragm and intercostal muscles were modeled with linear elastic shell elements as well. All twelve pairs of rib, the sternum, costal cartilage, and the spinal column from C1 to S1 (with intervertebral discs) were modeled using solid elements to represent trabecular bone. The completed thoracic model was validated against chest deformation data reported by Kroell et al. (1974) and Viano et al. (1989). Additional thoracic modeling and validation information can be found in Wang (1995)

and Shah et al. (2001). In 2005, Shah et al. combined this improved thorax model with the first version of the WSHBM to develop the WSHBM-II (Figures 3.1a, 3.1b and 3.1c). For several connections in the model, tied interfaces were used. The pericardial sac surrounding the heart, the reflections of which attach to the aorta and pulmonary artery, was modeled and connected to the central tendon of the diaphragm by direct nodal connections. Three airbags representing the hollow abdominal organs in the abdomen subcomponent model developed by Lee and Yang (2001) were replaced by one airbag to represent the peritoneum. This airbag was reflected on the liver, spleen, and kidneys to represent visceral part of the peritoneum. Additional WSHBM-II modeling and validation information can be found in Shah et al. (2007). The WSHBM-II has a total of 79,471 nodes and 94,484 elements with a mass of 75.6 kilograms. Throughout the remainder of this thesis, WSHBM will refer to the second version of the model. Table A1 in Appendix A lists the material properties of the second version of the Wayne State Human Body Model.

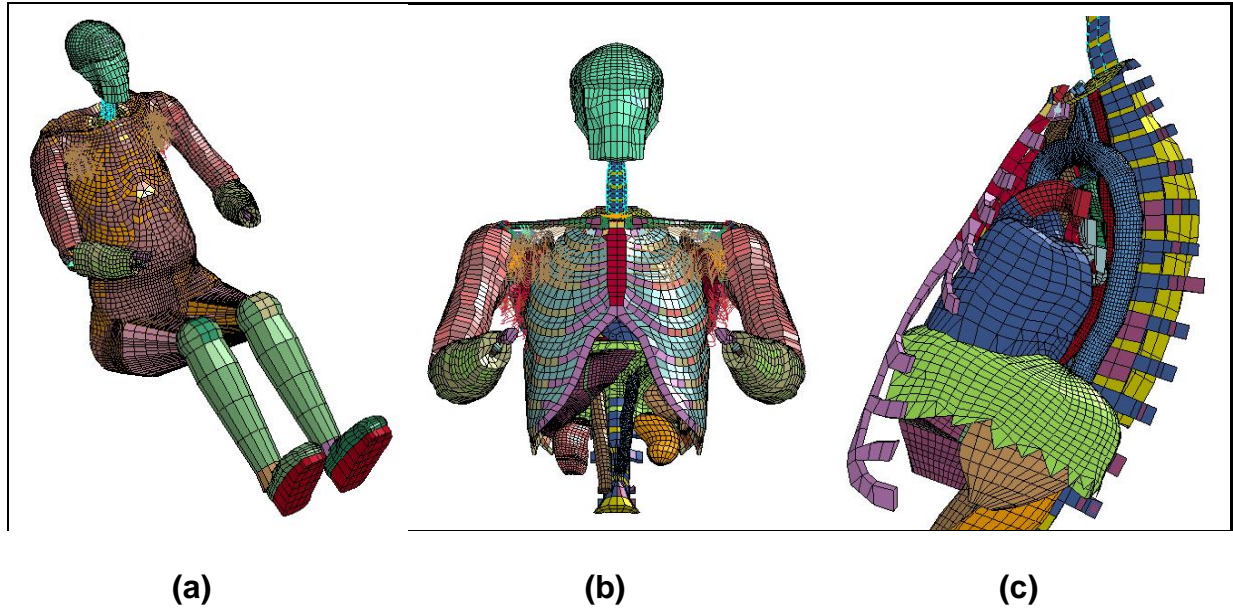


Figure 3.1: (a) The Wayne State Human Body Model – II (WSHBM) Shah et al. (2007) (b) WSHBM upper torso (c) Sagittal section of the Thorax with the shoulder, ribcage and the left lung removed to view the mediastinum contents

CHAPTER 4

REAL-WORLD CIREN CRASH DATA

4.1 Introduction

With the advent of sophisticated finite element (FE) vehicle models and human body models that are highly representative of human anthropometry and anatomy, it is imperative that these models can be used to assist the understanding of the mechanism of aorta injury. As described in Chapter 3, real world incidence data provide a unique platform to investigate aortic injury in live person instead of cadavers more realistically than laboratory created aortic ruptures. On the other hand, conditions in real world accidents are not well controlled and the accuracy of reconstruction could greatly be affected for lack of engineering measurements for model validation.

4.2 Materials and Methods

The case materials for this study consisted of detailed analyses of 15 real life cases of crash-induced aortic rupture taken from a previous study in which 80 Motor Vehicle Crashes (MVCs) induced Aortic Injuries (AIs) were reported (Siegel et al. 2004). Victims of all these cases were either admitted alive to a Level I Trauma Center, or if fatalities, were immediately subjected to a complete post mortem examination with detailed photographs of the injuries documented by the Regional Medical Examiner associated with the institution associated with CIREN. In each case, transported alive or scene fatal, a team of NHTSA approved crash investigators examined the scene and the vehicle to make quantitative estimates of the nature of the crash, and recorded the type and weight of the case vehicle, if the crash involved a fixed object, or both the

bullet and target cars. On the case vehicles, the investigators calculated the principal direction of force (PDOF), the delta-v, the impact energy (IE) dissipation on the struck vehicle, and evidences of specific sites to which the crash victim might have come to contact. They also determined whether the subject was wearing a seatbelt and/or whether a frontal or side airbag had deployed. After all the data and photographs of the vehicle and the patient medical records had been acquired, a confirmation conference was held on each case to resolve any disparities and to validate all of the case data (Siegel et al. 2004). Of the 80 cases of MVC-induced AI studied, there were 34 occupants who were injured or killed in a lateral impact MVC (LMVC). From these 34 LMVC cases, eight left lateral MVC-induced AI cases and two right lateral cases were chosen for FE simulations. These cases all had their aortic rupture in the most frequent location, the aortic Isthmus that represented the site of AI in 91% of the 34 LMVCs in this series. Five frontal AI cases were chosen from 46 cases of frontal MVC for FE simulations.

To protect the privacy of the patient and their families wherever necessary, any pictures with identifiable features have been hidden.

4.3 Left Lateral CIREN data

11 near-side left lateral CIREN cases used in the FE reconstruction processes are presented. They are identified as Case numbers 4, 5, 6, 7, 8, 15, 16, 17, T1, T2, and T3 discussed in some degrees of detail along with injuries sustained by these victims in the next section.

4.3.1 Case #4 descriptions

The patient was a **29 years old Hispanic male driver** (Height = 1.83 m; weight = 100 kg) of a 1992 Volkswagen Jetta sedan (V1) (Vehicle weight = 1,046 kg) impacted in a left lateral MVC by a nearly identical 1992 Volkswagen Jetta sedan (V2) (Vehicle weight = 1,046 kg) which entered the intersection. V2 struck V1 on the left side (Scene Diagram, Figure 4.1) just at the junction of the driver's side door with the body. The WinSMASH software program estimated speed for V1 at 62 km/hr, with an Impact Energy of 313,502 joules. The Collision Deformation Classification (CDC) was 10YEW5, with a Principal Direction of Force (PDOF) of 310 degrees (Figure 4.2).

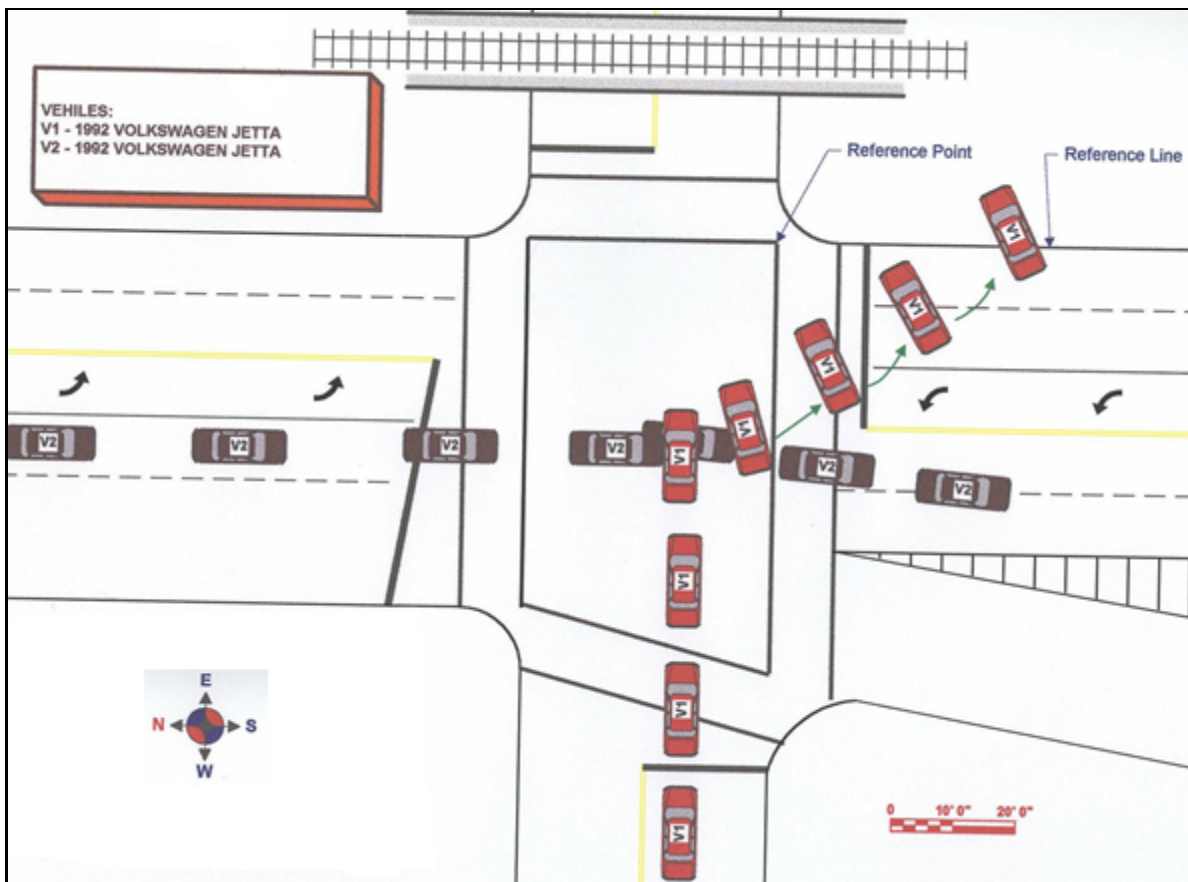


Figure 4.1: Accident scene for case #4



Figure 4.2: Deformation pattern of the struck vehicle, case #4

The patient had a brief loss of consciousness, but showed no neurologic injury on recovery (GCS 15). He was normotensive, [Blood Pressure (BP) = 160/80 mmHg; Pulse (P) = 94; Respiratory Rate (RR) = 15], but complained of mild shortness of breath, left anterior chest pain and left scapular pain. Admission chest radiograph showed a widened mediastinum; Computed Tomography (CT) of thorax demonstrated a probable aortic injury at the level of the aortic isthmus (Figure 4.3) which was confirmed by an angiography, a 50% aortic transection of the inner surface of the aorta at the level of the aortic isthmus that was contained within the tissues of the posterior mediastinum. There was also a small splenic contusion and mildly widened pubic symphysis. The patient was hemodynamically stable and was taken to the Operating Room (OR) where under left heart bypass, the transection was completed and a #16 Hemashield Dacron

woven graft was sewn in place. The patients' post-operative course was uneventful and he was discharged from the hospital alive.

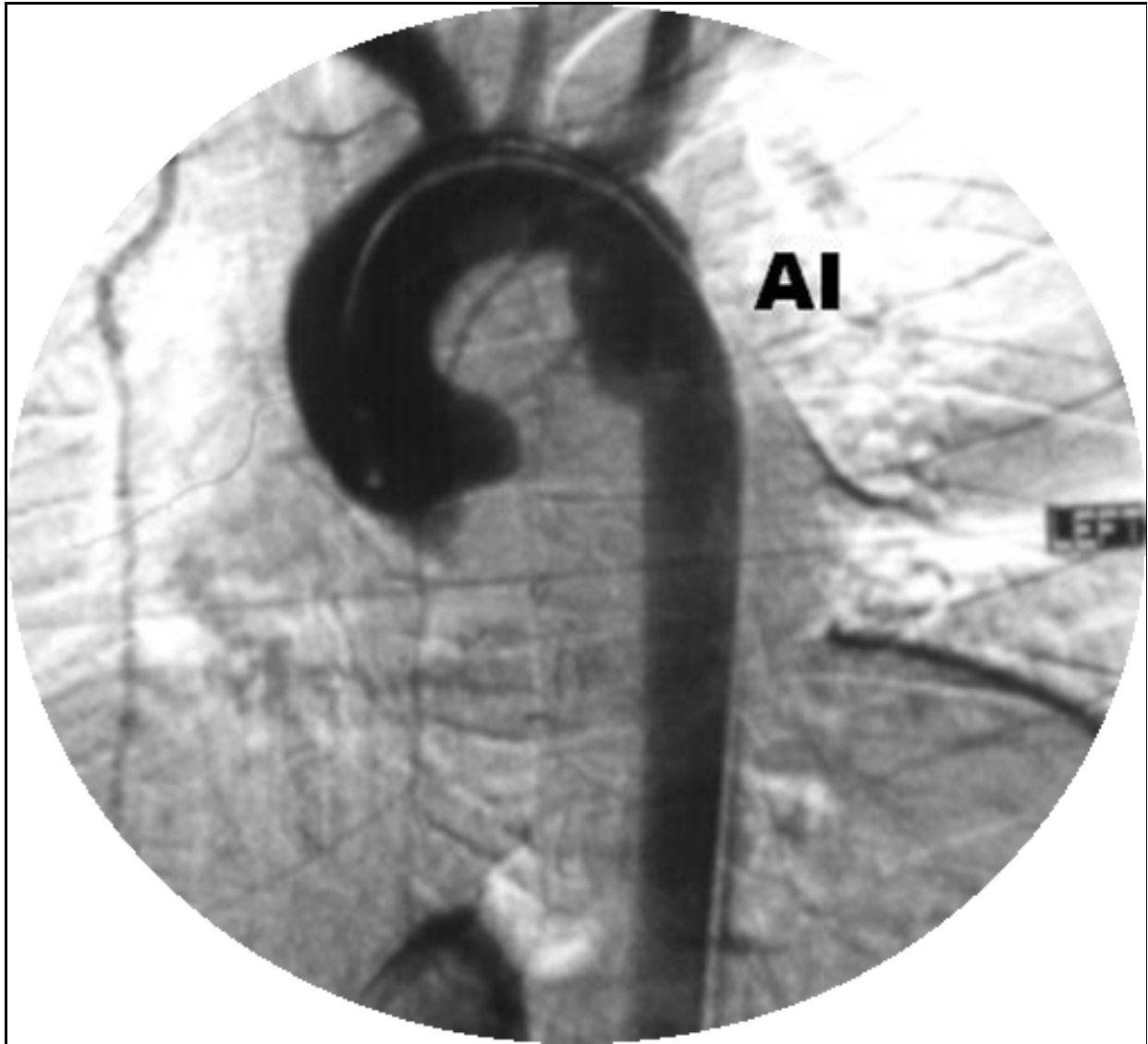


Figure 4.3: Case #4, partial aortic transection at the level of the isthmus

4.3.2 Case #5 descriptions

The patient was a **24 years old Caucasian male driver** (Height = 1.71 m; weight = 91.6 kg) of a 2001 Honda Prelude coupe (V1) (Vehicle weight = 1,340 kg) which lost control and struck a tree (Figure 4.4) on the left front side at the driver's side door.

There was some secondary deformation of the left front end at the level of the left headlight and the frontal airbag was deployed (Figure 4.5).

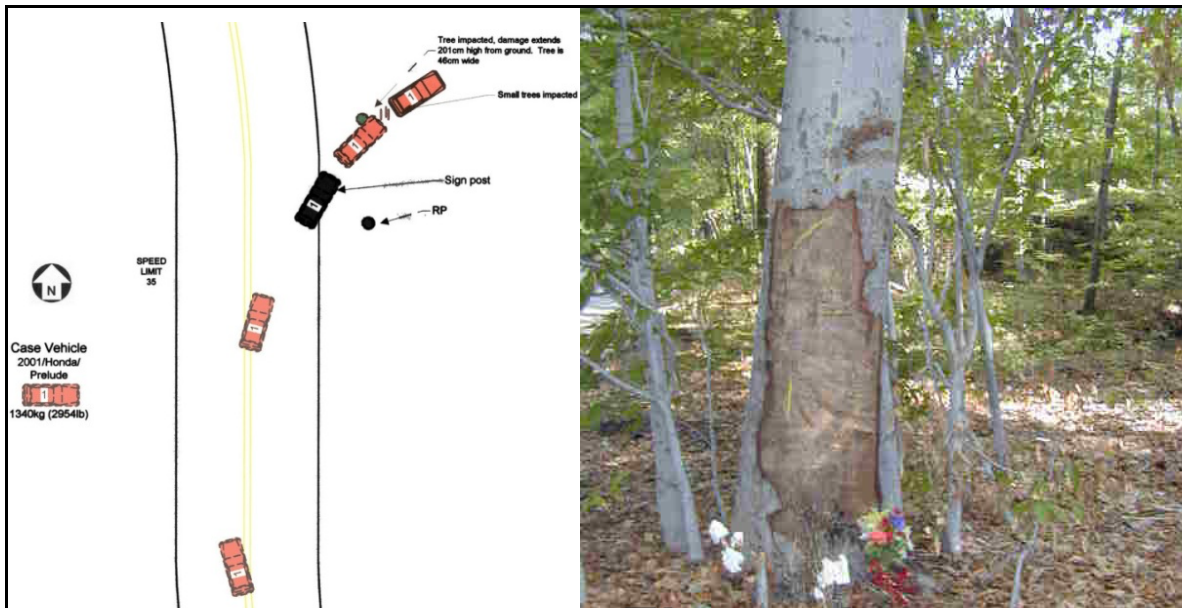


Figure 4.4: Accident scene for case #5

WinSMASH calculated delta-v was 27.5 km/hr with an Impact Energy of 46,051 Joules with a CDC of 1OLYAW3. The PDOF was 310 degrees.



Figure 4.5: Deformation pattern of the case vehicle, case #5

The autopsy showed a complete transection of the thoracic aorta four centimeters distal to the left subclavian artery in the area of the aortic isthmus, which was fatal (Figure 4.6). The thoracic mediastinum was also ruptured in the region of the aortic tear, permitting a massive left hemothorax to occur.



Figure 4.6: Case #5, Aortic transection at the level of the isthmus

4.3.3 Case #6 descriptions

The case involved a **28 years old African-American male driver** (Height = 1.85 m; weight = 84 kg) of a 2000 Mazda 626 (V1) (Weight = 1299 kg) struck broadside by a 2000 Honda CRV (V2) (Weight = 1,452 kg) (Figure 4.7). The subject vehicle was equipped with a three-point restraint system that was not in use while the supplemental frontal airbag restraint system deployed on impact. The major impact occurred at the left front door, centered at the B-pillar (Figure 4.8).

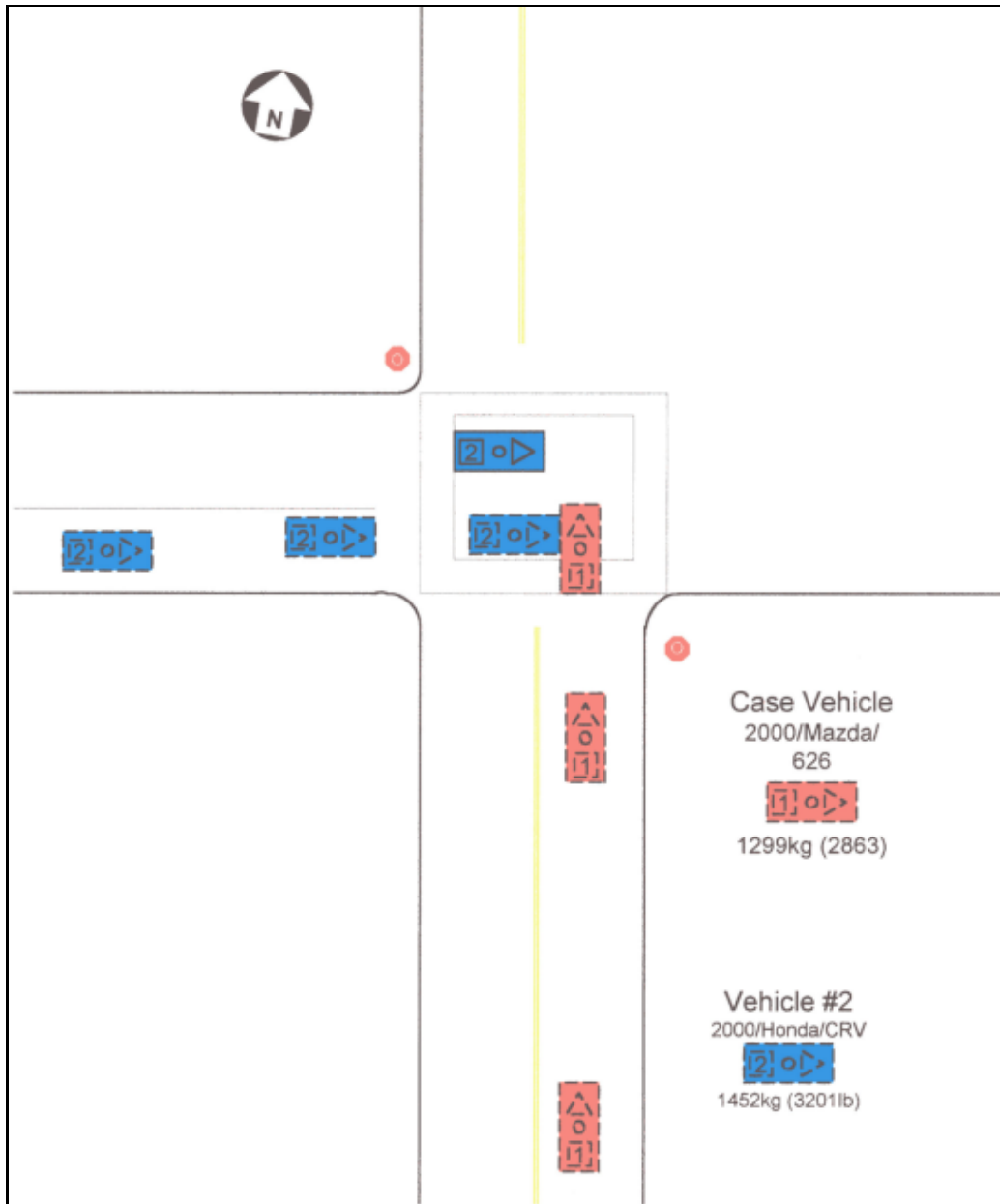


Figure 4.7: Accident scene for case #6

The delta-v on impact calculated by WinSMASH for the subject vehicle was 55 km/hr, with an energy dissipation of 163,692 Joules, at a PDOF of 280 degrees and the CDC was 09LYAW5.



Figure 4.8: Deformation pattern of the struck vehicle, case#6

The patient sustained fatal injuries including an aortic rupture and was found dead at the scene (Figure 4.9). The patient also sustained a bilateral subdural hemorrhage and multiple rib fractures.



Figure 4.9: Case 6, Aortic transection at the level of the isthmus

4.3.4 Case #7 descriptions

The case involved a **34 years old African-American male driver** (Height = 1.63 m; weight = 83 kg) of a 1993 Toyota Corolla (V1) (Weight = 1,085 kg) struck broadside by a 1996 Dodge Caravan (V2) (Weight = 1,612 kg) (Figure 4.10). The subject was utilizing a three-point belt system and the frontal air bag deployed at the time of impact.

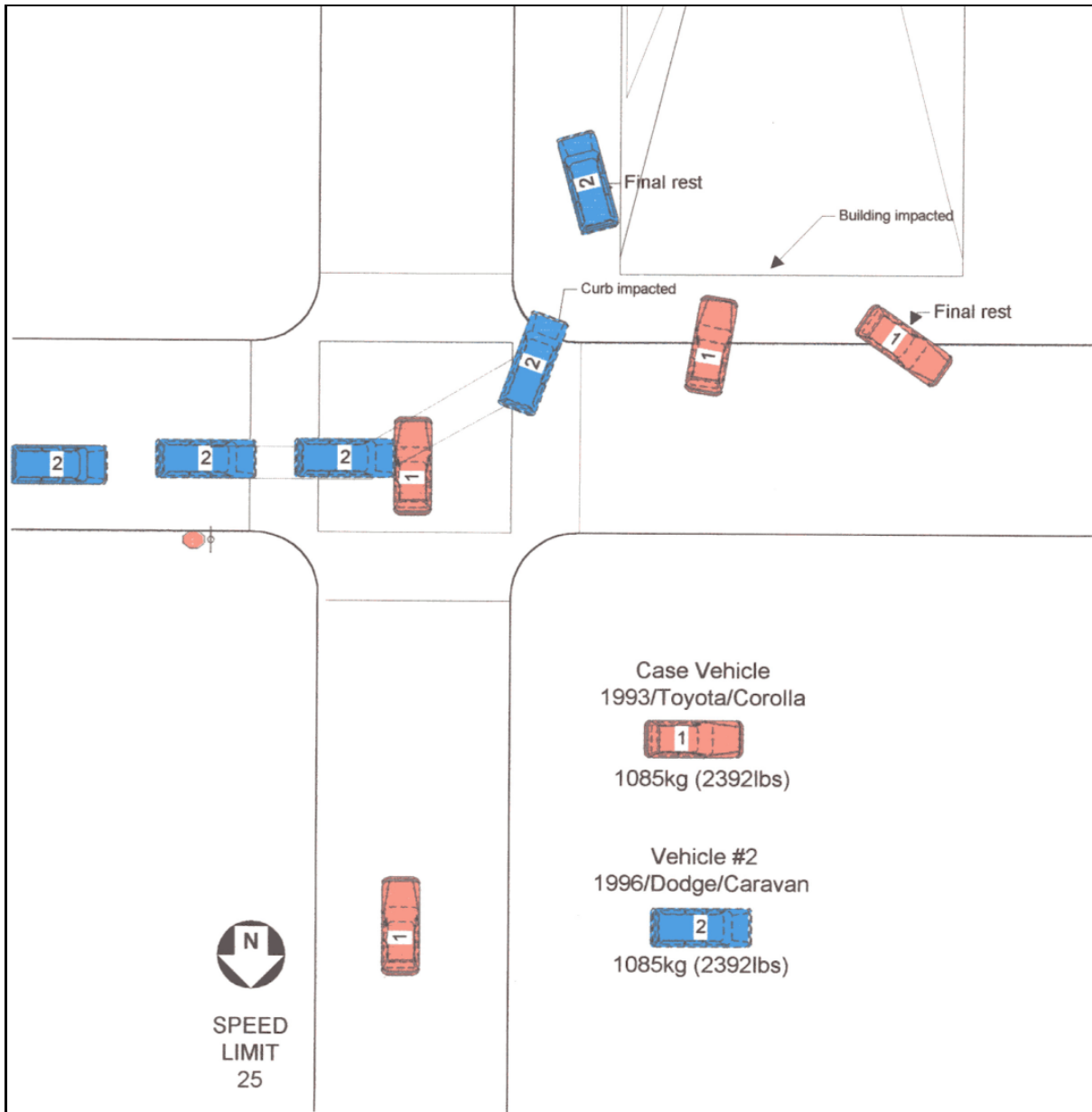


Figure 4.10: Accident scene for case #7

The delta-v on impact for the V1 vehicle calculated by WinSMASH was 59 km/hr with an impact energy dissipation of 229,599 Joules, delivered at a PDOF of 280 degrees at a CDC of 09LYAW5 (Figure 4.11).



Figure 4.11: Deformation pattern of the struck vehicle, case#7

The patient sustained fatal injuries including a three-centimeter transverse laceration of the aortic isthmus on the posterior right side of the isthmus, located three and one half centimeters distal to the left subclavian artery orifice (Figure 4.12). There was an associated aortic dissection and mediastinal hemorrhage. There was a second fatal injury involving a basilar skull fracture of the “hinge” type with atlanto-occipital dislocation. The driver was dead at the scene.

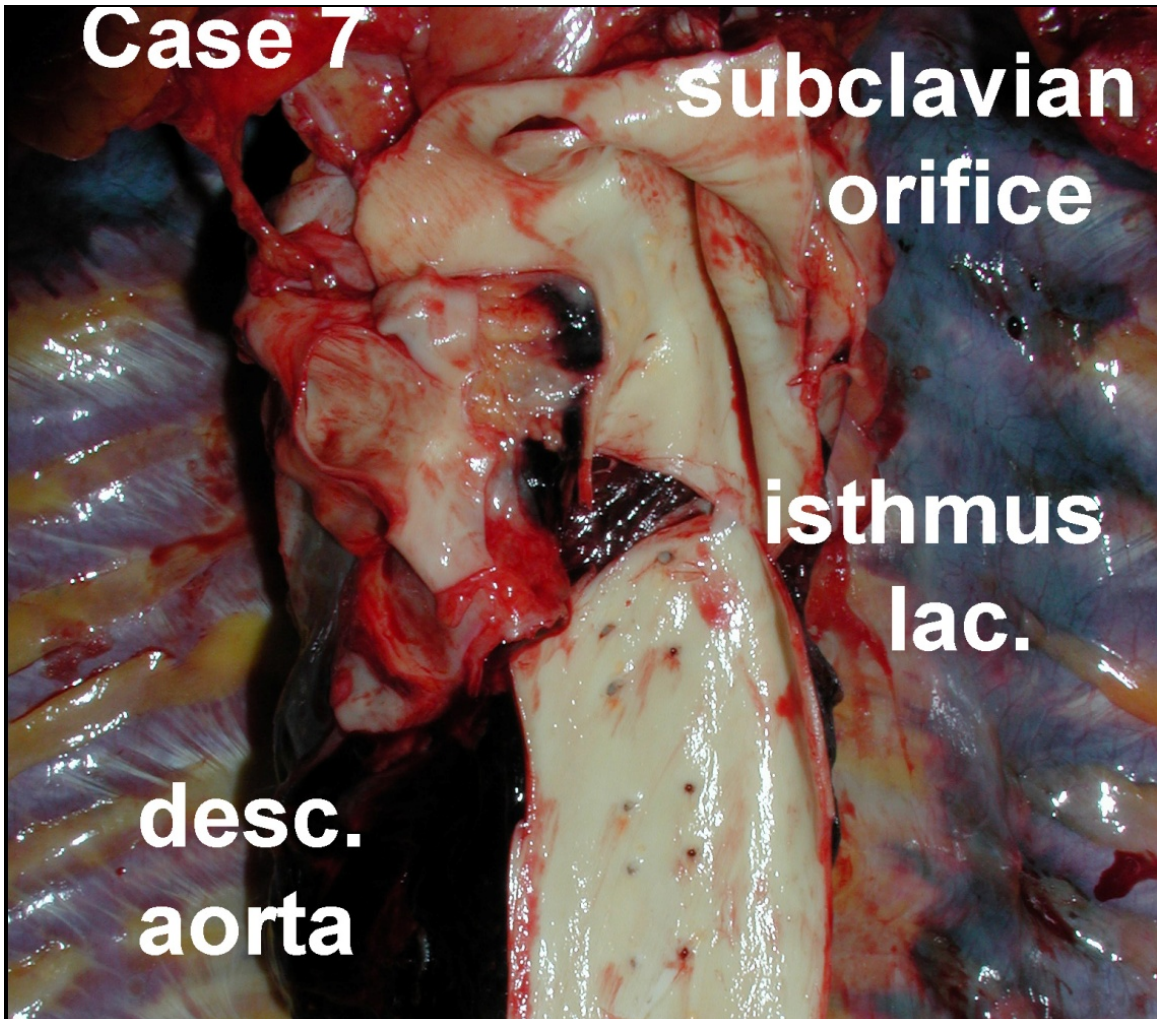


Figure 4.12: Case #7, Aortic transection at the level of the isthmus

4.3.5 Case #8 descriptions

The case involved a **65 years old Caucasian male driver** (Height = 1.81 m; weight = 101 kg). He was the driver of a 1994 Honda Accord EX (Weight = 1,469 kg) which lost control in a snowstorm and struck a utility pole with the maximum impact at the left lateral driver's side front door. The seat belt was in use by the driver and the driver's side frontal air bag deployed on impact (Figure 4.13).

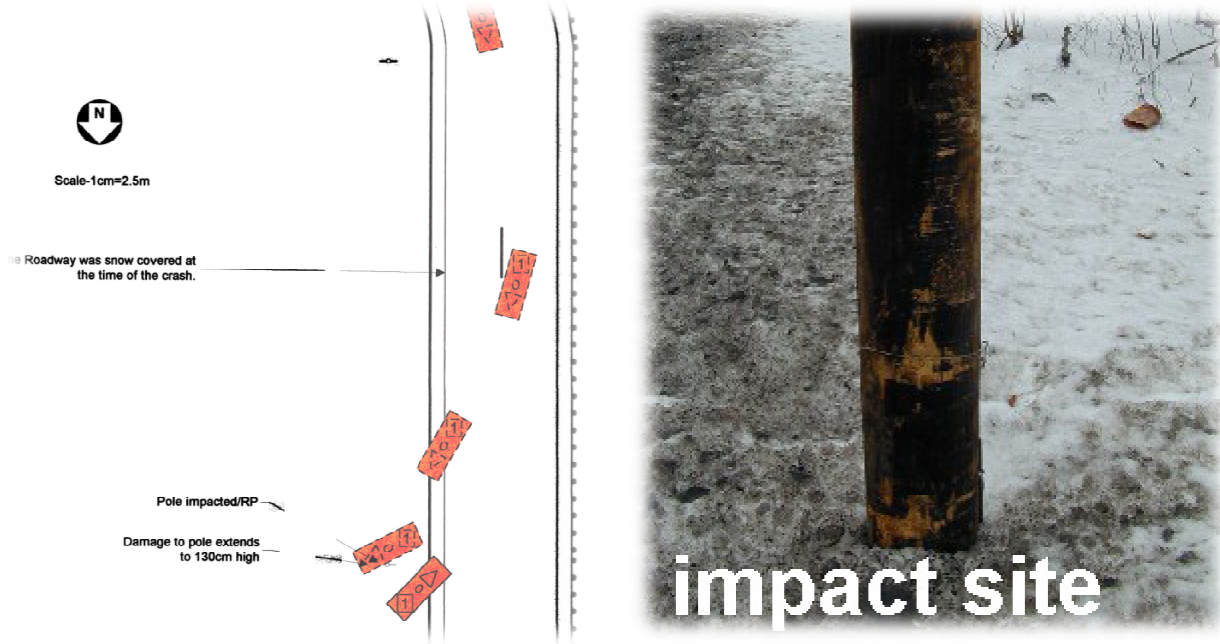


Figure 4.13: Accident scene for case #8

The delta-v on impact calculated by WinSMASH was 27.6 km/hr with an Impact Energy Dissipation of 52,024 Joules; delivered at a PDOF of 320 Degrees. The CDC was 11LPAW3 (Figure 4.14).



Figure 4.14: Deformation pattern of the struck vehicle, case#8

The subject sustained two fatal injuries: a transverse 45 mm transecting laceration of the aortic isthmus distal to the left subclavian artery orifice (Figure 4.15) and an atlanto-occipital disarticulation with proximal cord transection. The occupant also suffered a left diaphragmatic laceration with the stomach and a splenic herniation into left chest.

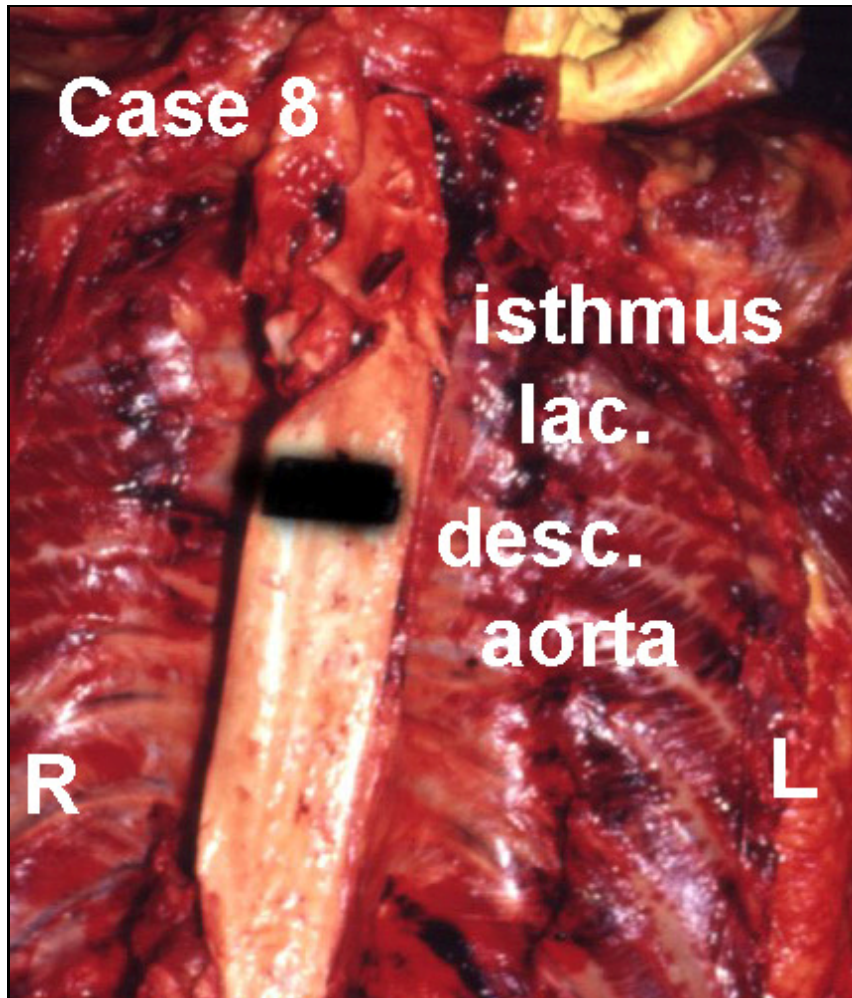


Figure 4.15: Case #8, Aortic transection at the level of the isthmus

4.3.6 Case #15 descriptions

The case involves a **35 years old African-American female driver** (Height = 1.75 m; weight = 99 kg). She was the unrestrained driver of 1985 Oldsmobile Cutlass Ciera four-door sedan (V1) (Weight = 1,257 kg), which was struck by a 1994 Nissan Pathfinder SUV (V2) (Weight = 1,812 kg). The Pathfinder driver went through a red light and struck the Oldsmobile at 47 km/hr with its full frontal plane, impacting the driver-side door and B-Pillar. Post-crash the subject vehicle rotated 90 degrees in the counterclockwise direction and came to rest facing in a direction 180 degrees from

which the vehicle entered the intersection (Figure 4.16). The subject driver was found dead at the scene.

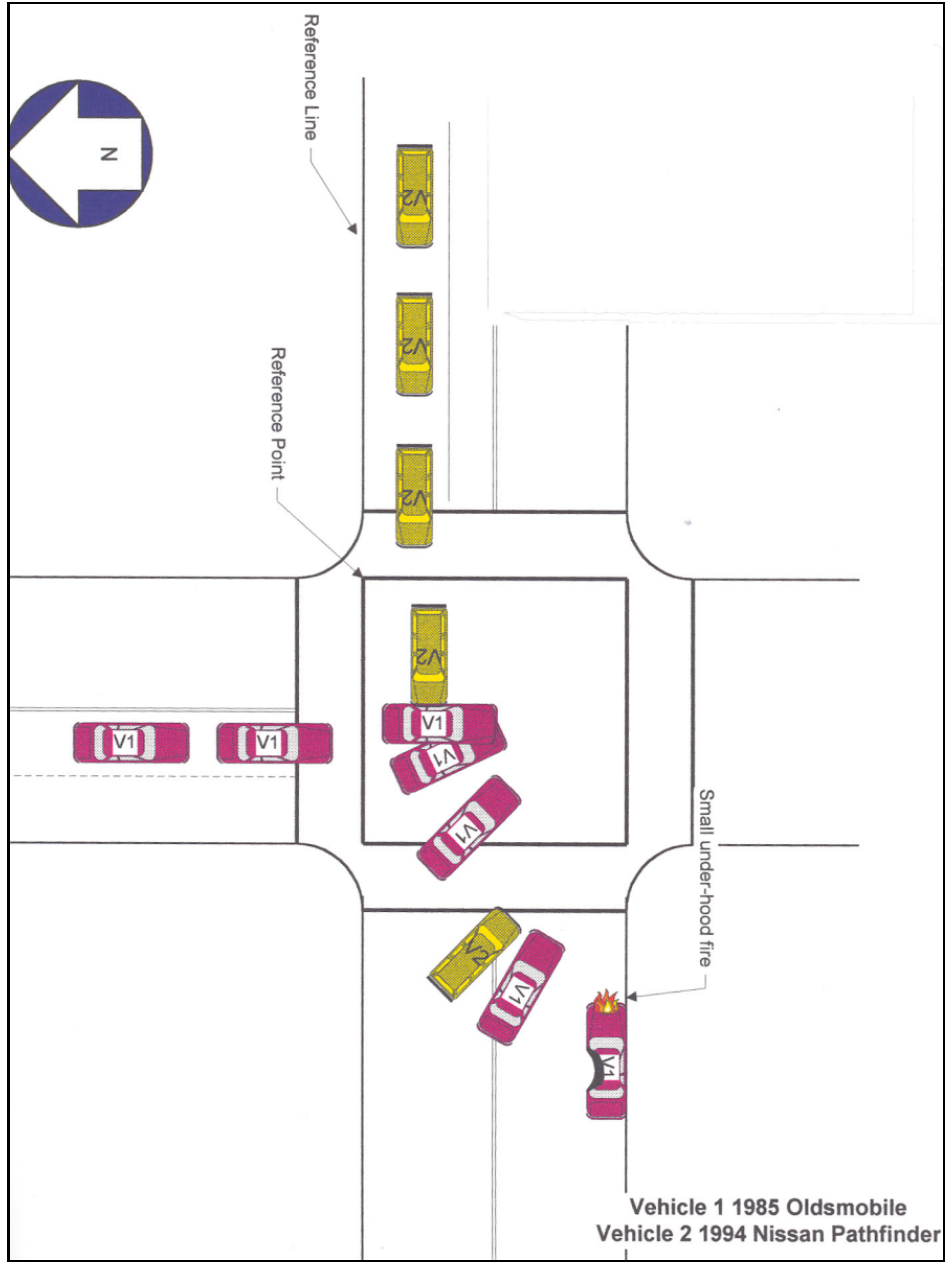


Figure 4.16: Accident scene for case #15

The PDOF was 270 degrees at a delta-v of 47 km/hr (WinSMASH) with an Energy Dissipation of 158,221 Joules at a CDC of 09LYAWS (Figure 4.17).



Figure 4.17: Deformation pattern of the struck vehicle, case#15

At impact, the driver of the Oldsmobile was thrown against the intruding B-Pillar and left front door panel. Her neck appears to have impacted the roof rail. She sustained a complete aortic transection at the aortic isthmus 20 mm distal to the left subclavian artery take-off (Figure 4.18). In addition, there was a soft tissue hemorrhage at the atlanto-axial ligament, but no consequent spinal cord injury and no brain injury, but some small patchy subarachnoid hemorrhages over the surface of the brain and a

small epidural hemorrhage at the level of the cervical spinal cord. There was a splenic laceration and a laceration of the left shoulder.

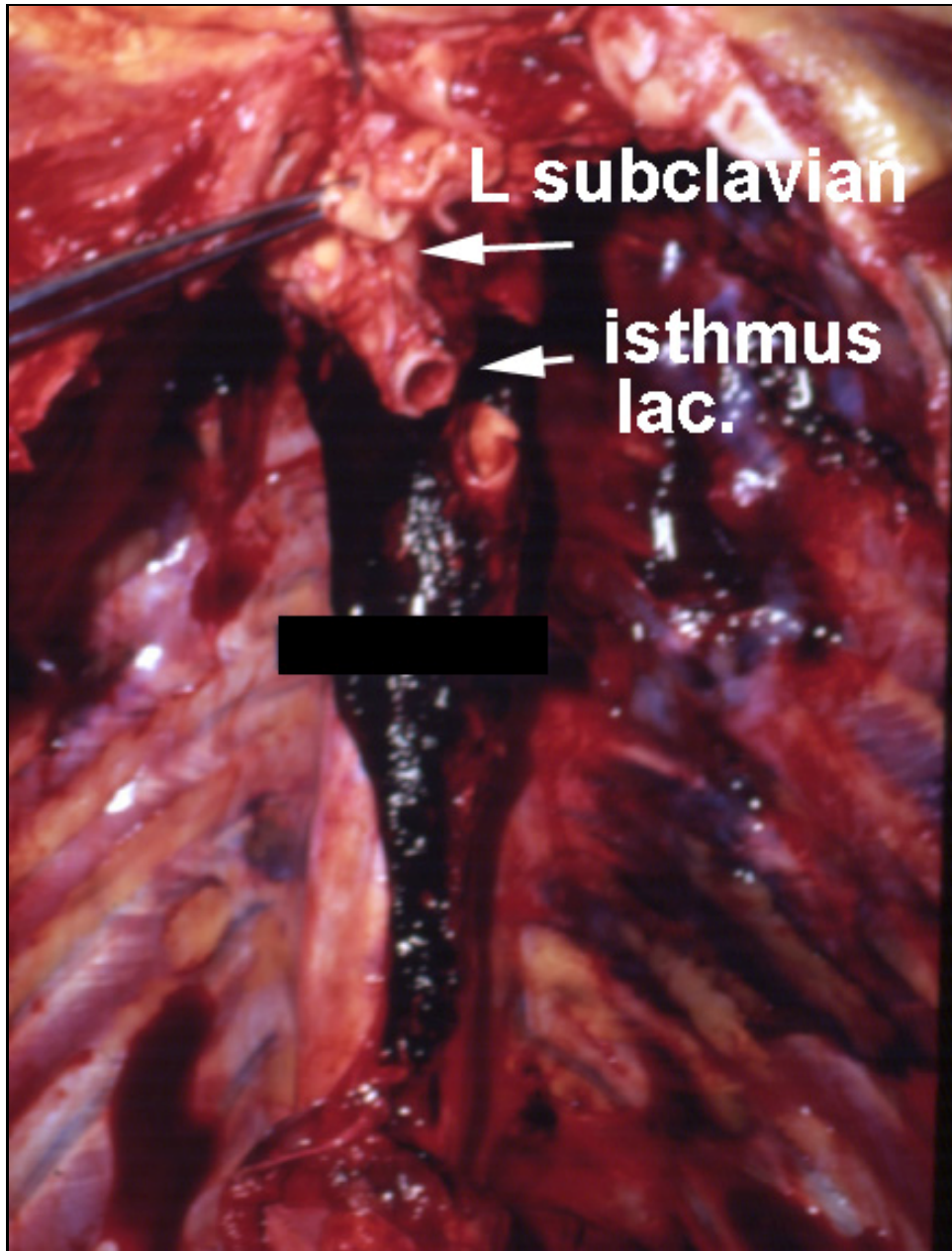


Figure 4.18: Case #15, Aortic transection at the level of the isthmus

4.3.7 Case #16 Descriptions

The case involved a **27 years old African-American male driver** (Height = 1.72 m; weight = 87 kg) of a 1997 Mazda 626 four door sedan (V1) (Weight = 1,320 kg) who lost control of the vehicle on a narrow two-lane bridge and rotated, so that the driver's side of the vehicle was approximately at a 90-degree obstruction to the driver of a 1998 Toyota RAV 4 SUV (V3) (Weight = 1,356 kg) which was traveling in the opposite direction lane (Figure 4.19). The Toyota struck the Mazda on the driver's side with a PDOF of 270 degrees, impacting the driver's side front door, the B-Pillar and the anterior portion of the rear door. The frontal airbag did not deploy on this side impact crash. The B-Pillar appears to have been a major component of the intrusion into the driver's side compartment. The driver of the Mazda was dead at the scene.

From Figure 4.19, it is evident that a 1990 Lincoln Towncar (V2) initially impacts the 1997 Mazda 626 (V1) on the right front side. This might not have caused any major structural damage, as it has not been reported in the CIREN case data. However, it might have aided in positioning the Mazda for impact with the 1998 Toyota Rav 4 (V3).

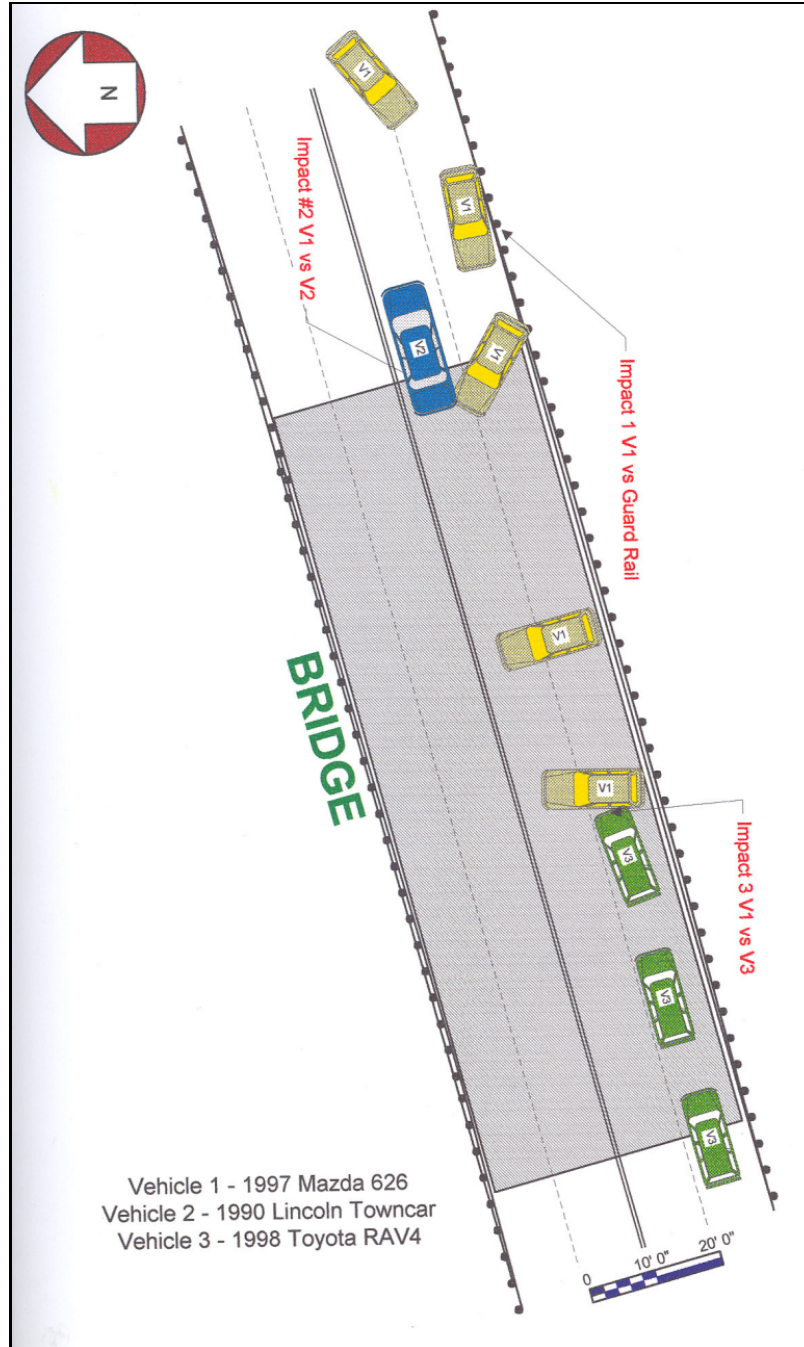


Figure 4.19: Accident scene for case #16

The PDOF was 270 degrees, at a delta-v of 54.4 km/hr (WinSMASH) with an Energy Dissipation of 273,856 Joules at a CDC of 09LZEW5 (Figure 4.20).



Figure 4.20: Deformation pattern of the struck vehicle, case#16

On impact, the driver of the Mazda was struck by the B-Pillar and upper doorframe. There was a complete transection of the upper portion of the descending aorta just below the isthmus 40 mm distal to the orifice of the left subclavian artery (Figure 4.21). A second laceration of the isthmus area occurred 20 mm below the subclavian take-off. There was a traumatic rupture of the left diaphragm with herniation of the left lobe of the liver, the cardia and fundus of the stomach and the spleen into the left pleural space.

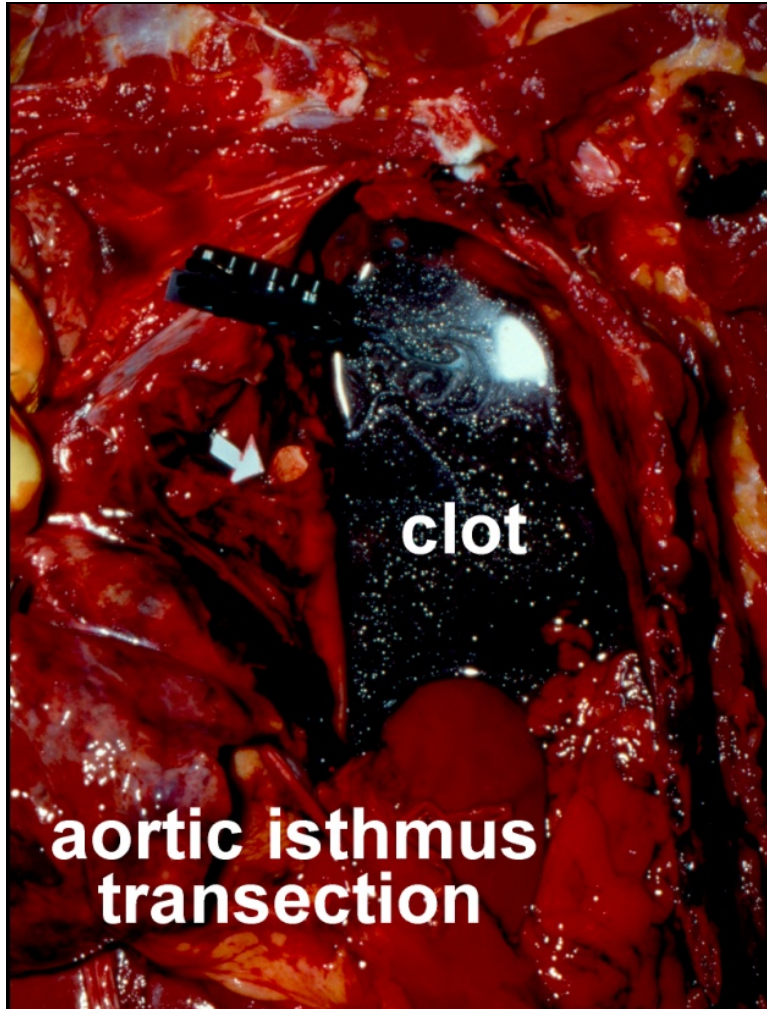


Figure 4.21: Case #16, aortic transection at the level of the isthmus

4.3.8 Case #17 Descriptions

This case involves a **55 years old Caucasian male driver** (Height = 1.63 m; weight = 100 kg) of a 2002 Dodge Stratus Sedan (V1) (Weight = 1,432 kg) who was struck by a Ford Econoline 350 van (V2) (Weight = 2,547 kg) while making a turn from a service road across a major divided highway (Figure 4.22). The driver's side door and the B-Pillar appear to have been the main sources of body impact at the time of the crash.

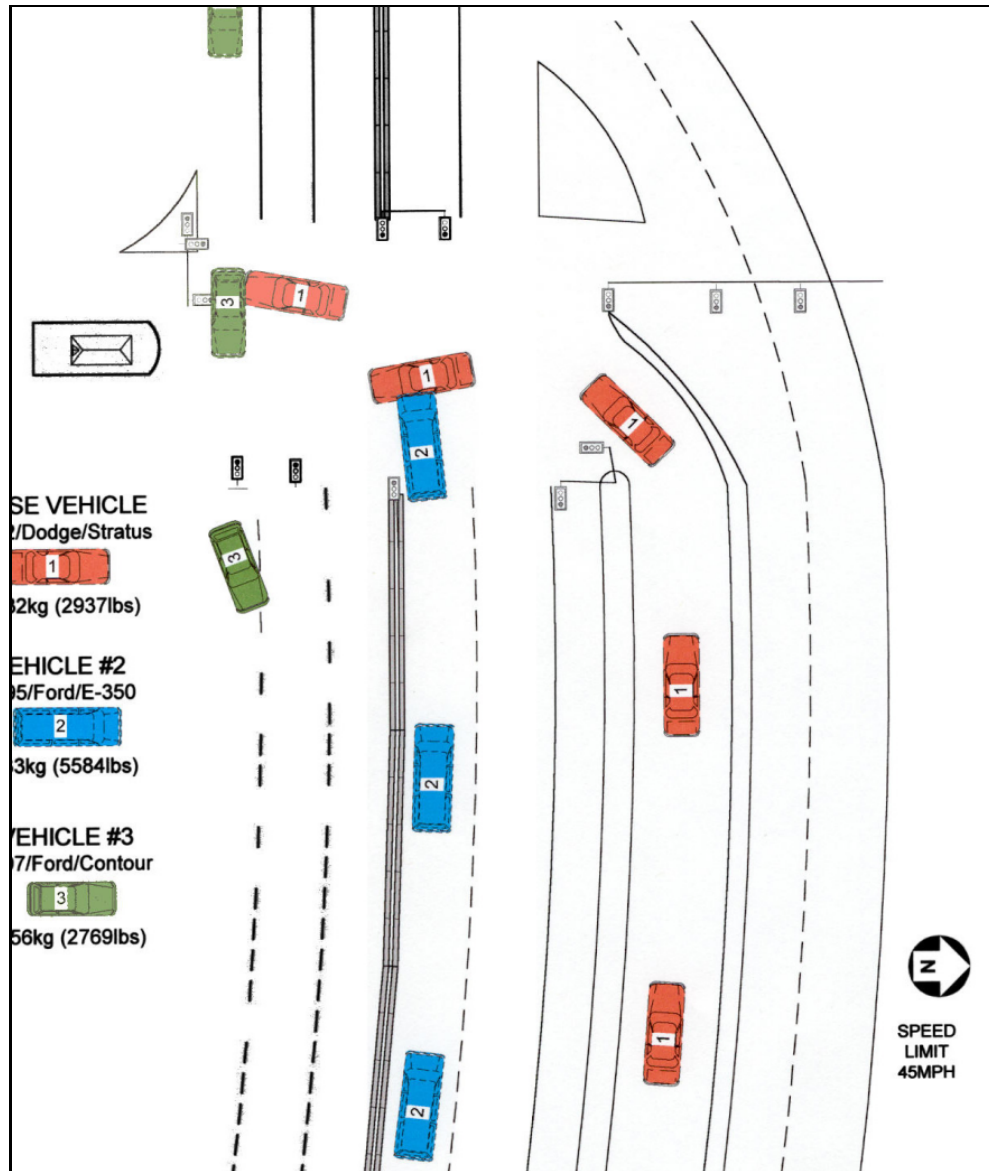


Figure 4.22: Accident scene for case #17

The PDOF was 260 degrees, at a delta-v 41 km/hr (WinSMASH) with an Energy Dissipation of 110,087 Joules at a CDC of 09LYAW3 (Figure 4.23).



Figure 4.23: Deformation pattern of the struck vehicle, case#17

Because the aortic isthmus laceration and its resulting large pulsatile hematoma were contained in the posterior mediastinal tissues, the patient was taken to the OR where the isthmus disruption was repaired using a #24 Hemashield tube graft. The patient tolerated the procedure well and survived his aortic disruption injury (Figure 4.24).

At the time of the crash, the patient sustained a left maxilla fracture and a left clavicle fracture as well as left rib fractures 3-12 postero-laterally, all appeared to be secondary to the impact with the B-Pillar. This contact also produced a left pulmonary contusion. B-Pillar contact was also implicated in the small aortic isthmus disruption. The patient also sustained a splenic laceration secondary to the lateral impact with the intruded left frontal door structures.

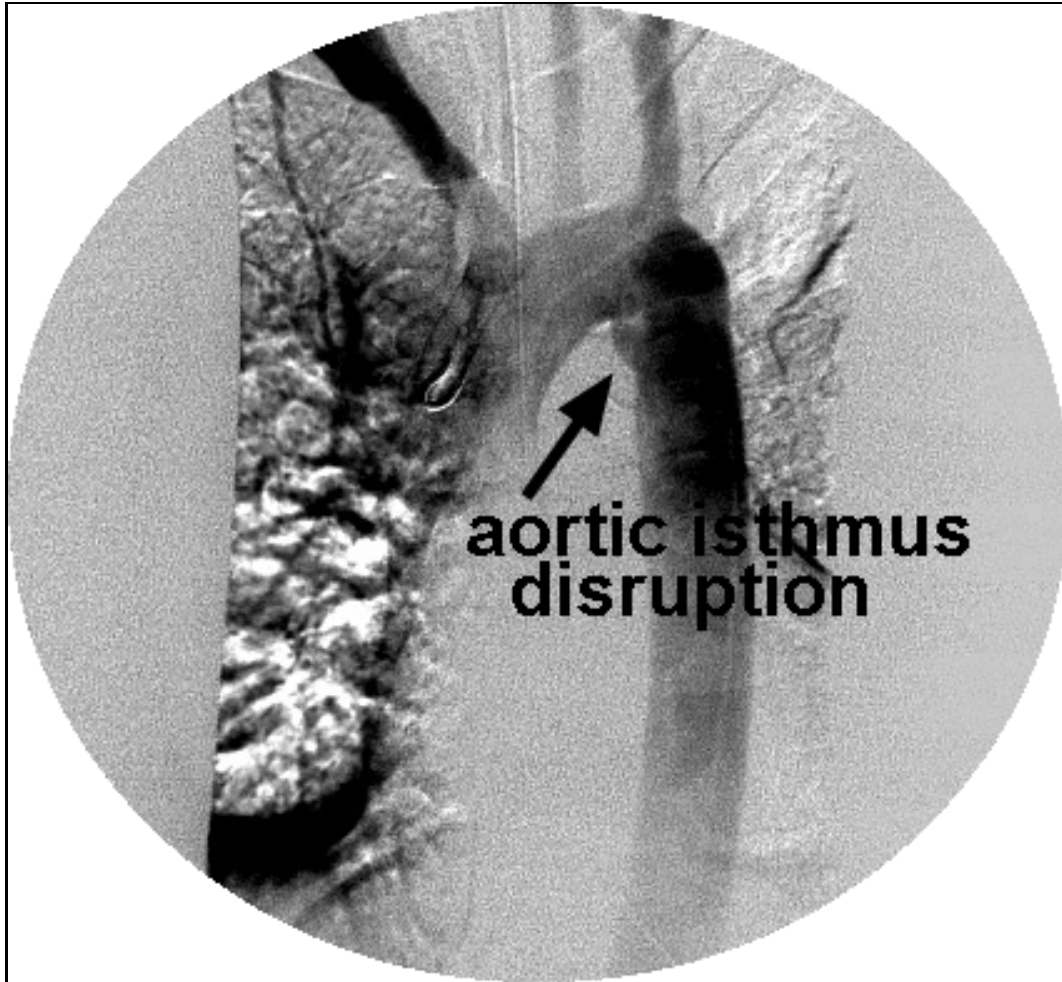


Figure 4.24: Case #17, aortic disruption at the level of the isthmus

4.3.9 Case #T1 Descriptions

This case involves a **42 years old African-American female driver** (Height = 1.60 m; weight = 86 kg) of a 1993 Mercedes Benz 190E (V1) (Weight = 1,318 kg) who was struck by a 1993 Mazda Navajo SUV (V2) (Weight = 1,760 kg) while making a U-turn from the middle lane of a three lane highway (Figure 4.25). The drivers' seat deformed severely and appears to have been the main source of body contact at the time of the crash.

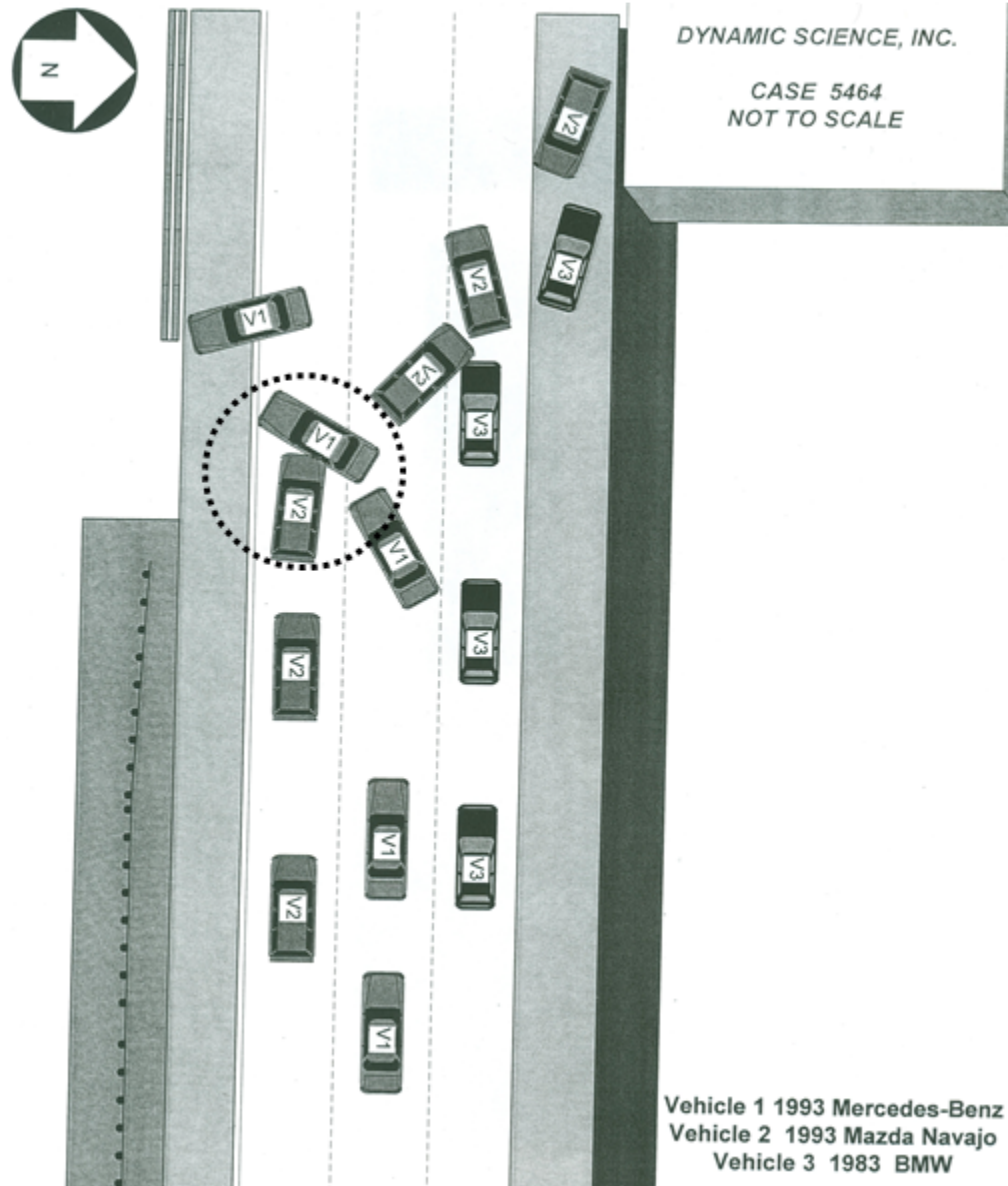


Figure 4.25: Accident scene for case #T1

The PDOF was 255 degrees, at a delta-v 33.6 km/hr (WinSMASH) with an Energy Dissipation of 37,835 Joules at a CDC of 08LYAW4 (Figure 4.26).

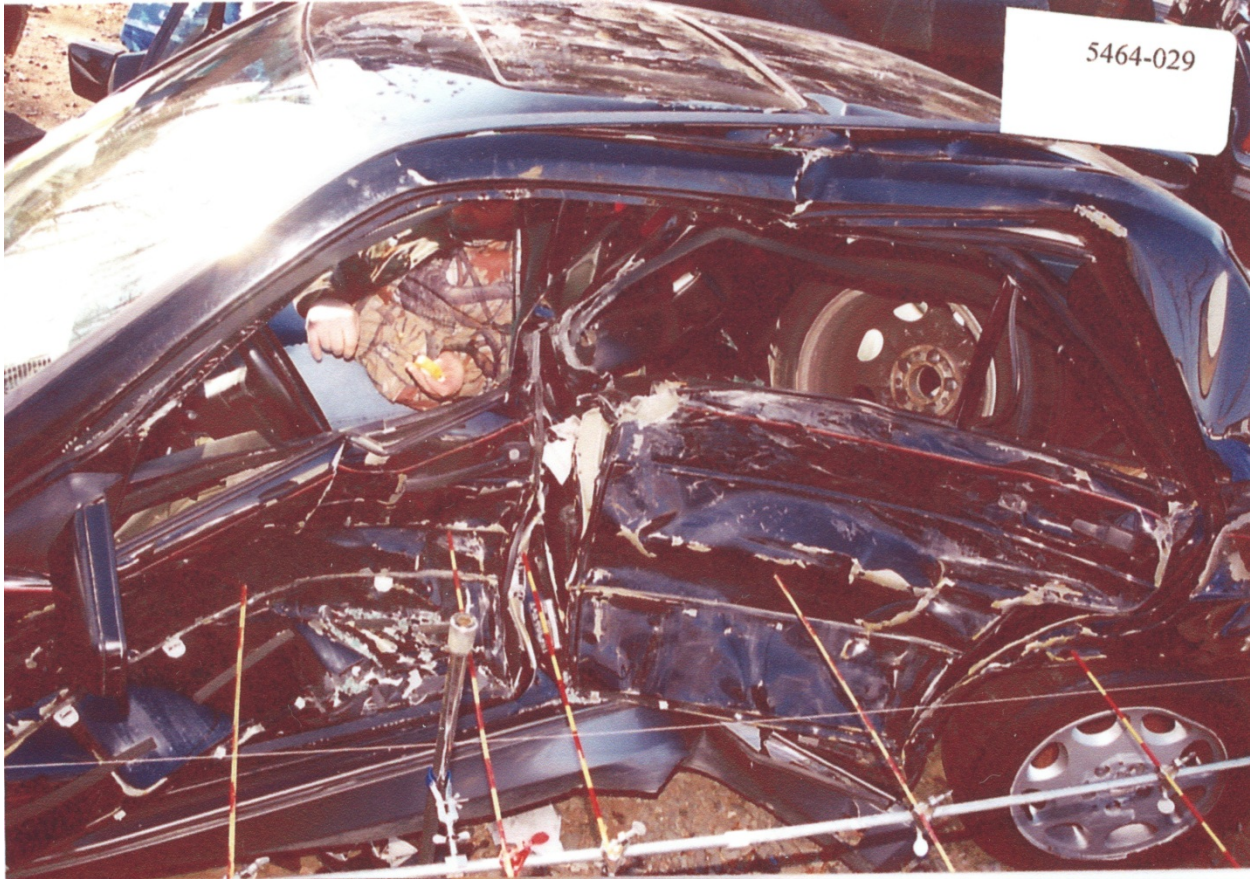


Figure 4.26: Deformation pattern of the struck vehicle, case# T1

There was no aortic injury observed. The driver sustained a brief loss of consciousness. Impact to the center console caused a grade 1 liver contusion while the rapidly deforming seat caused a splenic contusion.

4.3.10 Case #T2 Descriptions

This case involves a **26 years old Caucasian female driver** (Height = 1.65 m; weight = 61 kg) of a 1997 Honda Civic four door (V1) (Weight = 1,098 kg) who was struck by a 1991 Ford E-250 Van (V2) (Weight = 2,165 kg) while making a left turn at an intersection (Figure 4.27).

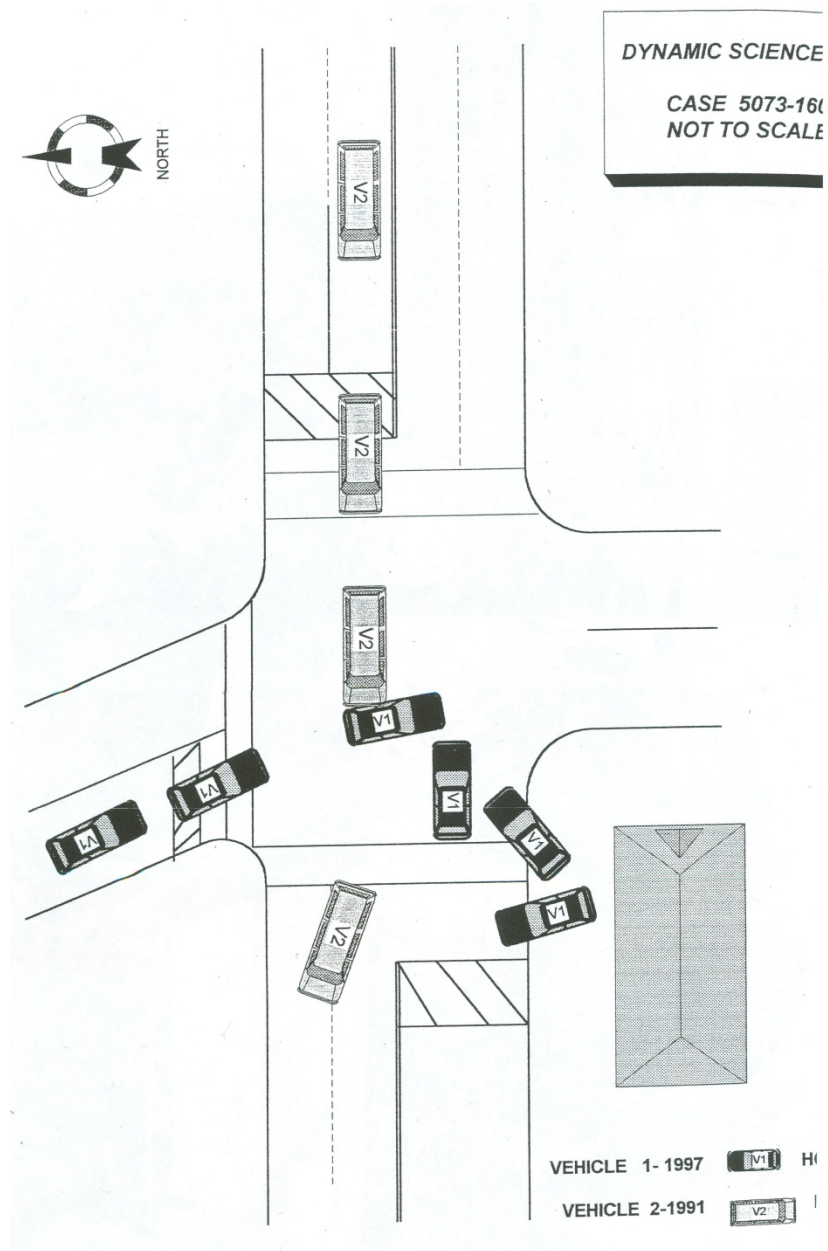


Figure 4.27: Accident scene for case #T2

The PDOF was 285 degrees, at a delta-v 29.1 km/hr (WinSMASH) with an Energy Dissipation of 24,799 Joules at a CDC of 10LYEW2 (Figure 4.28).



Figure 4.28: Deformation pattern of the struck vehicle, case# T2

There was no aortic injury observed. The driver sustained left rib fractures from the intruding side door structures. Further, she suffered a liver laceration due to contact with the center console and a splenic laceration from the B-pillar.

4.3.11 Case #T3 Descriptions

This case involves an **82 years old Caucasian female driver** (Height = 1.55 m; weight = 50 kg) of a 1996 Chevrolet Cavalier four door (V1) (Weight = 1,162 kg) who was struck by a 1994 Ford Ranger SUV (V2) (Weight = 1,350 kg) when she passed a stop sign and was struck broadside (Figure 4.29).

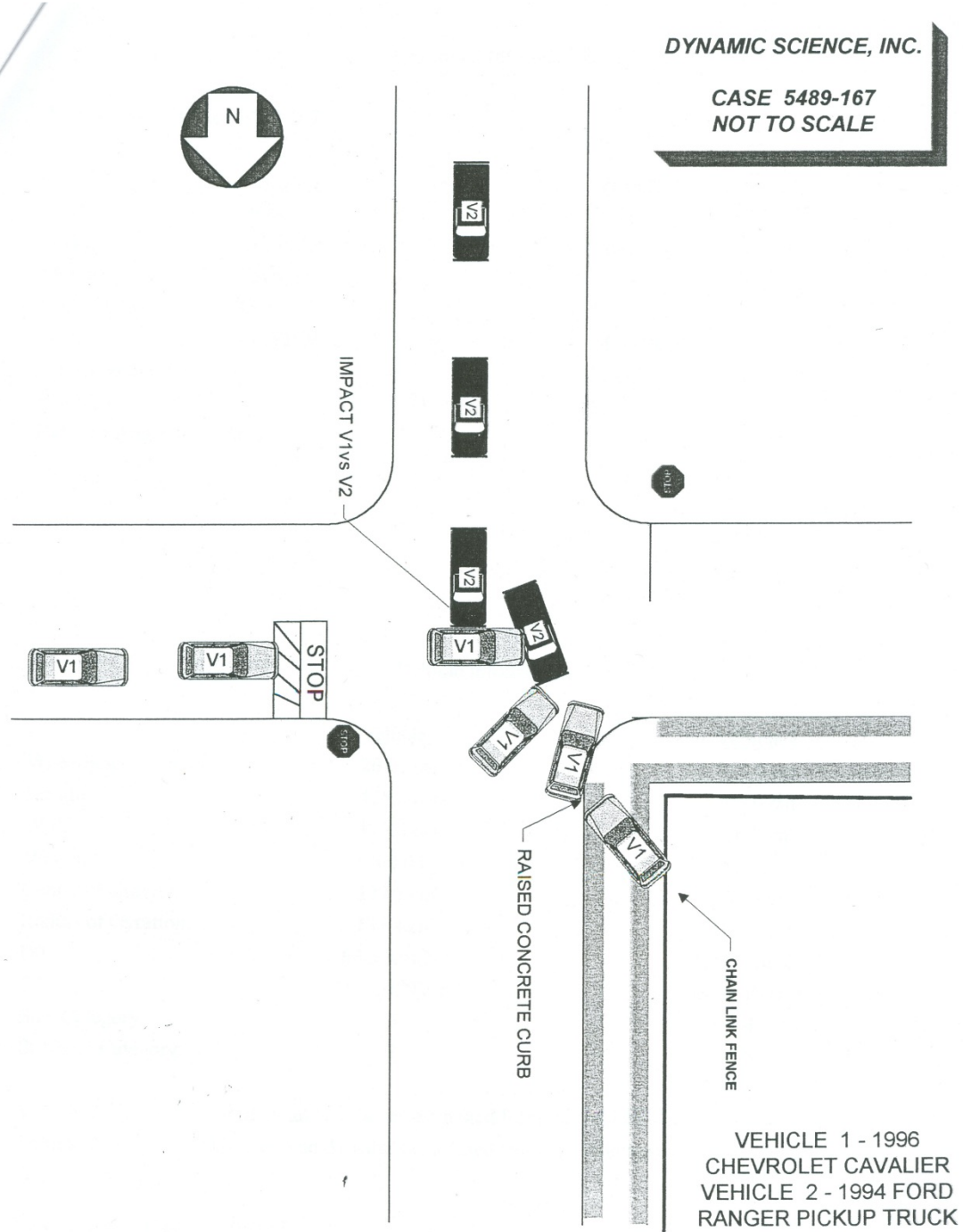


Figure 4.29: Accident scene for case #T3

The PDOF was 300 degrees, at a delta-v 22.0 km/hr (WinSMASH) with an Energy Dissipation of 24,799 Joules at a CDC of 10LYEW2 (Figure 4.30).



Figure 4.30: Deformation pattern of the struck vehicle, case# T3

There was no aortic injury observed. The driver sustained left anterior rib fractures with pneumothorax, left forearm contusion along with bilateral interior and left superior pubic rami fractures from the intruding side door structures.

CHAPTER 5

FINITE ELEMENT ACCIDENT RECONSTRUCTION METHODOLOGY

5.1 FE Reconstruction Introduction

Cases selected from the Crash Investigation Research Engineering Network (CIREN) were reconstructed in two stages as described in Sections 5.2 and 5.3. In Stage I reconstruction, validated FE models were scaled to match the case vehicles and actual deformation pattern matched simulation results while in Stage II, the WSHBM along with vehicle structures, which intruded into the occupant compartmental space, were used to predict the maximum principal strain and pressure in the aorta.

5.2 Stage I Methodology

In Stage I, vehicle models obtained from NCAC FE model archives were selected to best match the vehicle type as those of the actual case, since not all vehicle models were available. The Federal Highway Administration (FHWA) and the National Highway Traffic Safety Administration (NHTSA), through the NCAC, have put in a great deal of resources to build and validate these FE vehicle models. Further details on the validation of these models are reported on the NCAC website (<http://www.ncac.gwu.edu/vml/models.html>). The same vehicle type models were scaled to match with the overall dimensions, such as the wheelbase, width, and height, of the case vehicle(s). The vehicle mass was adjusted by either adding a lumped mass at the center of gravity of the vehicle or by removing a few unnecessary components, such as the rear bumper, which would typically not be involved in a left-lateral crash.

The driver's weight was compensated for by adding a known weight (from the case data) to the center of gravity of the driver's seat. Care was taken to ensure that the overall center of gravity and total mass were not altered. Similarly, the striking vehicle (or the fixed object) was scaled and the two vehicles (or the vehicle and fixed object) positioned and given an initial velocity (as a vector based on the PDOF) as documented by the crash investigation data.

The simulations were set to run for 120 milliseconds. All simulations were carried out using Hypermesh 10.0 (Altair Corporation, Troy, MI) as the pre-processor, a Massively Parallel Platform (MPP) version of LS-DYNA 970 on a four-node cluster (two processors/node) as the solver, and LS-PREPOST 3.1 (LSTC Corporation, Livermore, CA) as the post-processor. Structural deformation patterns of the struck vehicle obtained in the simulations were compared with the CIREN data at six different points, C1 to C6, measured as per SAE J2433 (Equidistant Crush Measurement Techniques). SAE J2433 was referenced to compare the deformations from the simulation to the actual case (Figures 5.1). Table 5.1 lists the left lateral crush profiles.

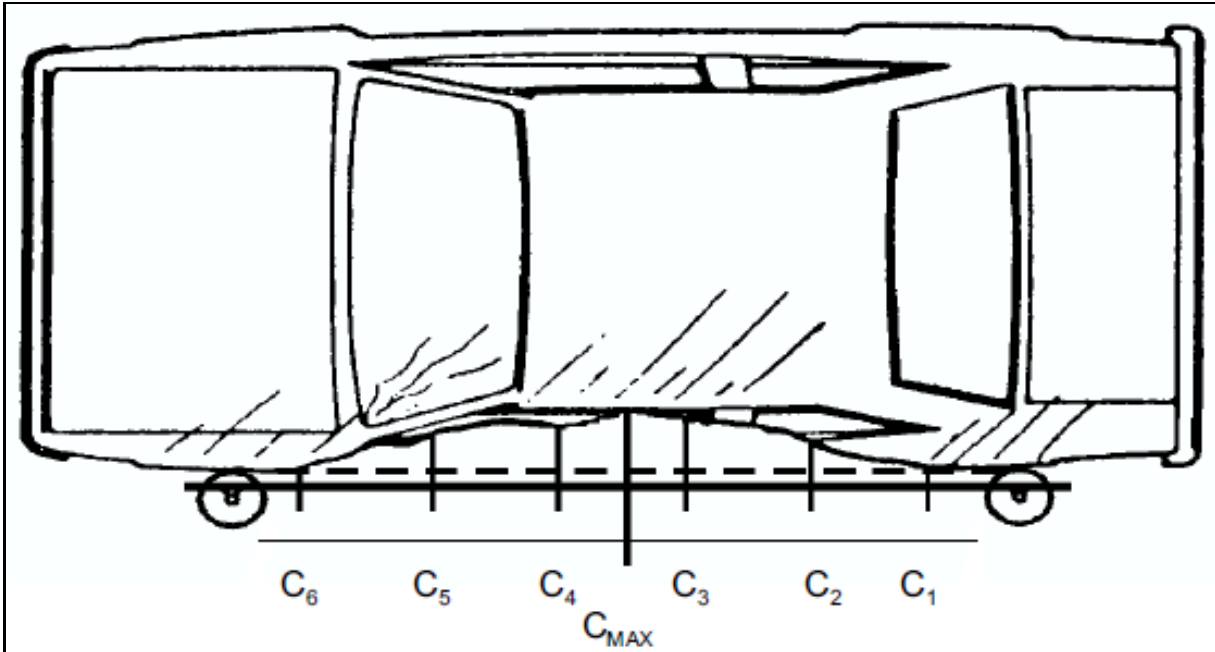


Figure 5.1: Lateral crush profile measurement (SAE J2433)

Table 5.1: Crush profiles for the eight left lateral CIREN cases

Deformation in mm	Case 4	Case 5	Case 6	Case 7	Case 8	Case 15	Case 16	Case 17
C1	0	60	0	0	0	0	0	30
C2	120	180	470	500	230	540	290	270
C3	640	250	700	730	380	890	920	450
C4	620	350	510	620	310	730	520	340
C5	500	310	320	370	150	240	590	240
C6	120	220	0	0	20	0	0	80

A local coordinate system was established on a rigid plate with its origin on the right side B-pillar of the case vehicle (for left lateral cases), where deflection was seen to be negligible, to obtain the deformation in local coordinates. The Stage I FE simulations were repeated while tuning the impact position of the striking vehicle model

until a reasonable match was obtained for the struck vehicle data. For fixed object crash cases with either a tree or a pole, the object was created as per dimensions specified in the CIREN case report using solid elements and assigned a rigid material property.

For the struck vehicles, the structures that came into contact with the occupant were grouped and their motions recorded in separate binary interface files. These interface files were used as inputs for the Stage II simulations.

5.3 Stage II Reconstruction

In Stage II, the interface file and the sub-model (structures of interest) of the struck vehicle, which consisted of the nodal kinematic histories of the structures that might interact with the occupant, were used as inputs to load the occupant model WSHBM. The occupant model was positioned in a seated posture estimated from post-crash photographs of the interior structures and seat position. A contact interface was created between the interior structures of the sub-model and the occupant model. A mean arterial pressure of 13.33 kPa or 100 mmHg was initialized to simulate average resting blood pressure in the aorta (Presola et al. 2001). The overall occupant kinematics at the time of peak vehicle deformation was observed, the average maximum principal strain (AMPS) and maximum pressures in several regions of the aorta were recorded, and the region with highest AMPS and pressure were tabulated.

CHAPTER 6

AIM A: FINITE ELEMENT ACCIDENT RECONSTRUCTION OF LEFT-LATERAL CIREN ACCIDENT DATA

6.1 Introduction

Examination of the epidemiology of traumatic rupture of aorta (TRA) began near the time of World War II, but speculation regarding the etiology of TRA began much earlier, near the end of the nineteenth century (Sailer, 1942). Because experimental efforts to reproduce clinically relevant TRA in the laboratory have had little success (Hardy et al. 2006, Hardy et al. 2008), little is known about the true mechanisms of TRA. Lumped parameter and FE models of the human thorax and its contents have been developed in an effort to gain insight into potential injury mechanisms. However, findings from these models must be considered conjectural. Some preliminary work by Shah et al. (2007) using accident reconstruction data has proven to be an effective method to investigate the mechanism of aortic injury. Study of the injury mechanisms by reconstructing the accident plays a vital role in aortic injury mitigation.

Scene inspections and data recovery involves visiting the scene of the accident and investigating all of the vehicles involved in the collision. Investigations involve collecting evidences such as scene photographs, video of the collision, measurements of the scene, eyewitness testimony, and legal depositions. Additional factors include steering angles, braking, use of restraint systems, lights, turn signals, speed, acceleration, engine rpm, cruise control, and anti-lock brakes. Witnesses are interviewed prior or during accident reconstruction and physical evidence such as tire marks are examined. Vehicle speed is frequently under-estimated or under-reported by

the case driver, so an independent estimate of speed is often essential in accident reconstruction. Inspection of the road surface is also vital, especially when traction has been lost due to black ice, diesel fuel contamination, or obstacles such as road debris. Data from an event data recorder also provide valuable information such as the speed of the vehicle a few seconds before a collision.

Vehicular accident reconstruction analysis includes processing data collected, evaluating possible hypotheses, creating numerical models, recreating accidents, testing, and utilizing software simulations. Accident reconstruction has been revolutionized by the use of powerful, inexpensive computers, and specialty software. Various types of accident reconstruction software are used to recreate crash and crime scenes and to perform other useful tasks involved in reconstructing collisions.

6.2 NASS-CDS Database Review

An analysis of the National Automotive Sampling System Crashworthiness Data System (NASS–CDS) database was performed from survey years 1993 through 2008 to get an estimate of the number of thoracic aortic injuries and the primary structures in the automobile coded to be responsible for injury. All data was taken post 1993 because it was the first year that the then newly established AIS 90 coding system, which was useful to pinpoint the exact location of injury within the occupant's body, were required by NASS. The NASS–CDS database survey performed is only a measure to understand possible patterns of thoracic aortic injury. The non-weighted data cannot be used directly to ascertain a specific injury source but is helpful in confirming a proposed trend.

From Figures 6.1, for left lateral impacts, it is observed that the interior hardware followed by armrest and B-pillar intrusion are top notable coded injury sources to the aorta.

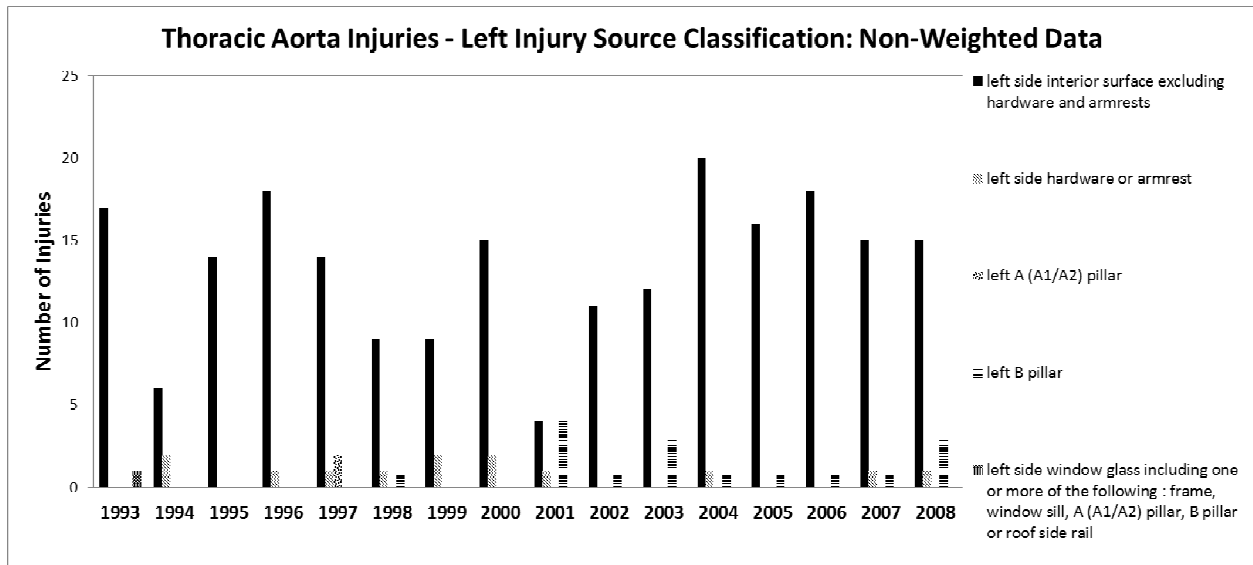


Figure 6.1: Left lateral thoracic aortic injuries by source (1993-2008)

6.3 Reconstruction of Lateral CIREN Cases

Eight left lateral reported in the CIREN database were obtained from The University of Medicine and Dentistry of New Jersey (UMDNJ) and reconstructed using the finite element vehicle models obtained from the National Crash Analysis Center (NCAC) at the George Washington University vehicle model archives as previously described in Chapter 5. For the struck vehicles, the driver or passenger side structures (based off data from NASS-CDS survey), including the front and rear doorframe, door armrest, and left/right B-pillar nodes respectively, were grouped and their kinematics

were recorded in separate binary interface files which were used as inputs for the second stage.

In Stage II, the interface file and the sub-model (left door structures) of the struck vehicle were used as inputs to calculate the occupant impact responses from the occupant model WSHBM. Tables 6.1 summarizes the eight case histories and occupant injury details while Table 6.2 details the struck and striking vehicle models involved along with their respective FE models used for each in reconstruction.

For Cases 5 and 8 where the impact was with a tree and pole respectively, fixed objects were modeled as rigid, and the velocity calculated from the accident reconstruction program (WinSMASH) were applied to the case vehicle.

Table 6.3 lists the details of these car models in their unaltered states. Tables A2 and A3 in Appendix A list the material properties of the left side door structures of the 2001 Ford Taurus FE model used as the case vehicle in all simulations and the material properties for the front bumpers and hoods of all striking vehicles. As described in Chapter 5, the WSHBM was used to calculate the parameters associated with aortic injury in Stage II based on kinematics data of the case vehicle obtained from Stage I.

The occupant model provided the overall occupant kinematics and predicted the average maximum principal strain (AMPS) and maximum pressures in the aorta.

Table 6.1: Summary of left lateral cases used in the crash reconstruction process

Parameter	Case 4	Case 5	Case 6	Case 7	Case 8	Case 15	Case 16	Case 17
Crash details								
Impact Object	Car-Car	Car-Tree	Car-SUV	Car-Car	Car-Pole	Car-SUV	Car-SUV	Car-Van
Delta V (km/hr)	62	27.5	55	59	27.6	47	54.4	41
Energy (Joule)	313,502	46,051	163,692	229,599	52,024	158,221	273,856	110,087
PDOF (Degree)	310	310	280	280	320	270	270	260
Collision Deformation Classification (CDC)	10YEW5	10LYAW3	09LYAW5	09LYAW5	11LPAW3	09LYAWS	09LZEW5	09LYAW3
Seat Belt Usage	Two-point shoulder belt, no lap belt	Three-point belt	Three-point belt, not in use	Three-point belt	Three-point belt	No belt	No belt	Three-point belt
Airbag Usage	No airbag	Driver side frontal airbags deployed	Driver side frontal airbags deployed	Driver side frontal airbags deployed	Driver side frontal airbags deployed	No airbag	No airbag	No airbag deployed
Parameter	Case 4	Case 5	Case 6	Case 7	Case 8	Case 15	Case 16	Case 17
Occupant and injury details								
Status	Survived	Fatal	Fatal	Fatal	Fatal	Fatal	Fatal	Survived
Age (Years) (37±15)	29	24	28	34	65	35	27	55
Race	Hispanic	Caucasian	African-American	African-American	Caucasian	Caucasian	African-American	Caucasian
Gender	Male	Male	Male	Male	Male	Female	Male	Male
Height (cm) (174.1±8.5)	183	171	185	163	181	175	172	163
Weight (kg) (93.1±7.7)	100	91	84	83	101	99	87	100
Aortic injury details	50% aortic transection of the intimal surface at the level of the aortic isthmus which was contained within	Complete transection of the thoracic aorta, 4 centimeters distal to the left subclavian artery at the	Aortic transection 4 centimeters in length, 1.5 centimeters distal to left subclavian artery	Transverse laceration of the aortic isthmus, 3 centimeters in length on the posterior right side of	Transverse laceration of the aortic isthmus, 4.5 centimeters in length just distal to	Complete aortic transection at the level of the isthmus, 2 centimeters distal to the	A second laceration of the isthmus occurred, 2 centimeter below the left subclavian	Aortic isthmus disruption which was contained within the posterior mediastinal

	the tissues of the posterior mediastinum	level of the isthmus		the isthmus, located 3.5 centimeters distal to the left subclavian artery	the left subclavian artery orifice	left subclavian artery orifice	orifice	tissues
Other Injuries by Body Region Head			<ul style="list-style-type: none"> • Bilateral subdural hemorrhages • Right mandible fracture 	<ul style="list-style-type: none"> • Bilateral skull Fractures with intraventricular hemorrhage and cerebellar brain laceration • Atlanto-occipital dislocation secondary to "hinge" fracture 	<ul style="list-style-type: none"> • Atlanto-occipital disarticulation with proximal cord transection • Left fronto-temporal scalp laceration • Left frontal basilar skull fracture • Atlanto-occipital cervical vertebrae dislocation 		<ul style="list-style-type: none"> • Basilar skull fracture, extending from the left middle cranial fossa through the petrous portion of the left temporal bone, across the basal portion of the occipital bone to the right middle cranial fossa 	
Parameter	Case 4	Case 5	Case 6	Case 7	Case 8	Case 15	Case 16	Case 17
Thorax and Upper Extremities		<ul style="list-style-type: none"> • Left Rib fractures (6th and 7th rib) • Rupture of the thoracic mediastinum leading to a massive left hemothorax • Left humerus fracture 	<ul style="list-style-type: none"> • Left superior pulmonary vein rupture and left hemothorax • Multiple rib fractures 	<ul style="list-style-type: none"> • Bilateral rib fractures • Left lung contusion • Laceration of left diaphragm with protrusion of stomach into left pleural cavity 	<ul style="list-style-type: none"> • Bilateral rib fractures 	<ul style="list-style-type: none"> • Left 1st through 12th ribs fractures • Bilateral hemothoraces 	<ul style="list-style-type: none"> • Anterior fractures of the left 1st through 5th ribs and posterior fractures of the left 5th, 8th & 10th ribs • Multiple lacerations on the left lung 	<ul style="list-style-type: none"> • Left maxilla and left clavicle fracture
Abdomen	<ul style="list-style-type: none"> • Splenic 		<ul style="list-style-type: none"> • Left 	<ul style="list-style-type: none"> • Laceration 	<ul style="list-style-type: none"> • Left 	<ul style="list-style-type: none"> • Splenic 		<ul style="list-style-type: none"> • Splenic

	contusion and mildly widened pubis symphysis		diaphragm tear <ul style="list-style-type: none"> • Left pleural rupture • Posterior mediastinal hemorrhage • Splenic tears 	of left diaphragm with protrusion of spleen into left pleural cavity	diaphragm laceration with stomach and splenic herniation into left chest	laceration		laceration
Pelvis and Lower Extremities			<ul style="list-style-type: none"> • Symphysis and left pubic ramus fracture • Left femoral fracture 	<ul style="list-style-type: none"> • Left pelvic fracture • Left tibia/fibula fracture 				<ul style="list-style-type: none"> • Acetabular fracture and the left superior and inferior pubic rami fractures

Table 6.2: Summary of vehicle models and their initial setup (after scaling) used in the left lateral crash reconstruction process

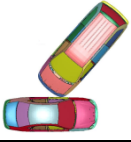



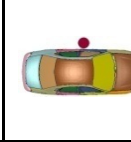

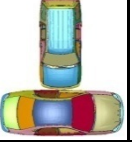

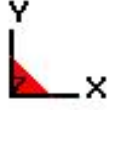
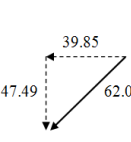
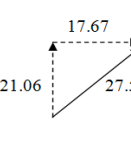
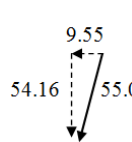
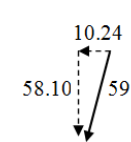
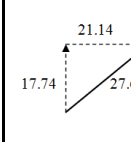
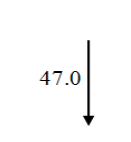
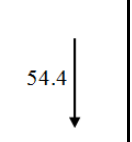
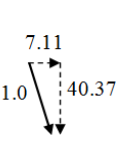
Parameter	Case 4	Case 5	Case 6	Case 7	Case 8	Case 15	Case 16	Case 17
Case Vehicle (Year, Make and Model)	1992 Volkswagen Jetta sedan	2001 Honda Prelude coupe	2000 Mazda 626 sedan	1993 Toyota Corolla sedan	1994 Honda Accord sedan	1985 Oldsmobile Cutlass Ciera sedan	1997 Mazda 626 sedan	2002 Dodge Stratus sedan
Case Vehicle Weight (kg)	1,046	1,467	1,299	1,085	1,469	1,257	1,320	1,432
FE Vehicle Model Used (Year, Make and Model)	2001 Ford Taurus sedan	2001 Ford Taurus Sedan	2001 Ford Taurus sedan	2001 Ford Taurus sedan	2001 Ford Taurus sedan	2001 Ford Taurus sedan	2001 Ford Taurus sedan	2001 Ford Taurus sedan
Striking Vehicle (Year, Make and Model)	1992 Volkswagen Jetta sedan	Tree	2000 Honda CRV SUV	1996 Dodge Caravan mini-van	Pole	1994 Nissan Pathfinder SUV	1998 Toyota RAV 4 SUV	1998 Ford Econoline 350 van
Striking Vehicle Weight or Fixed Object Diameter	1,046 kg	46 cm	1,452 kg	1,612 kg	46 cm	1,812 kg	1,356 kg	2,547 kg
FE Vehicle Model Used (Year, Make and Model)	2001 Ford Taurus sedan	Solid Elements	1998 Ford Explorer SUV	2002 Dodge Caravan mini-van	Solid Elements	1998 Ford Explorer SUV	1998 Ford Explorer SUV	1998 Ford Econoline 350 van
Initial Model Setup in the Simulation (km/hr)								
								

Table 6.3: Details of the vehicle FE models used in the reconstruction

FE Car Make and Model	Total number of parts	Total number of Elements	Width (mm)	Height (mm)	Wheel Base (mm)	Weight (kg)
2001 Ford Taurus	790	1,057,113	1,856	1,471	2,755	1,665
1998 Ford Explorer	755	619,161	1,841	1,765	2,855	2,240
2002 Dodge Caravan	510	333,455	1,897	1,760	3,030	2,043
1998 Ford Econoline 350	400	300,066	2,045	2,189	3,523	2,131

The response variables were the AMPS and instantaneous peak pressure in the aorta. For maximum principal strain, four adjacent elements in the region with the highest inner surface maximum principal strain were selected and averaged; while for pressure, the maximum value obtained during the entire simulation was tabulated.

6.4 Results

Table 6.4 compares the measured vehicle deformation values at C1 to C6 to the FE model predicted vehicular deformations at the same locations as defined in the CIREN case. As shown in Figure 6.2, the maximum resting deformation was compared with the CIREN data in order to account for elastic-plastic rebound.

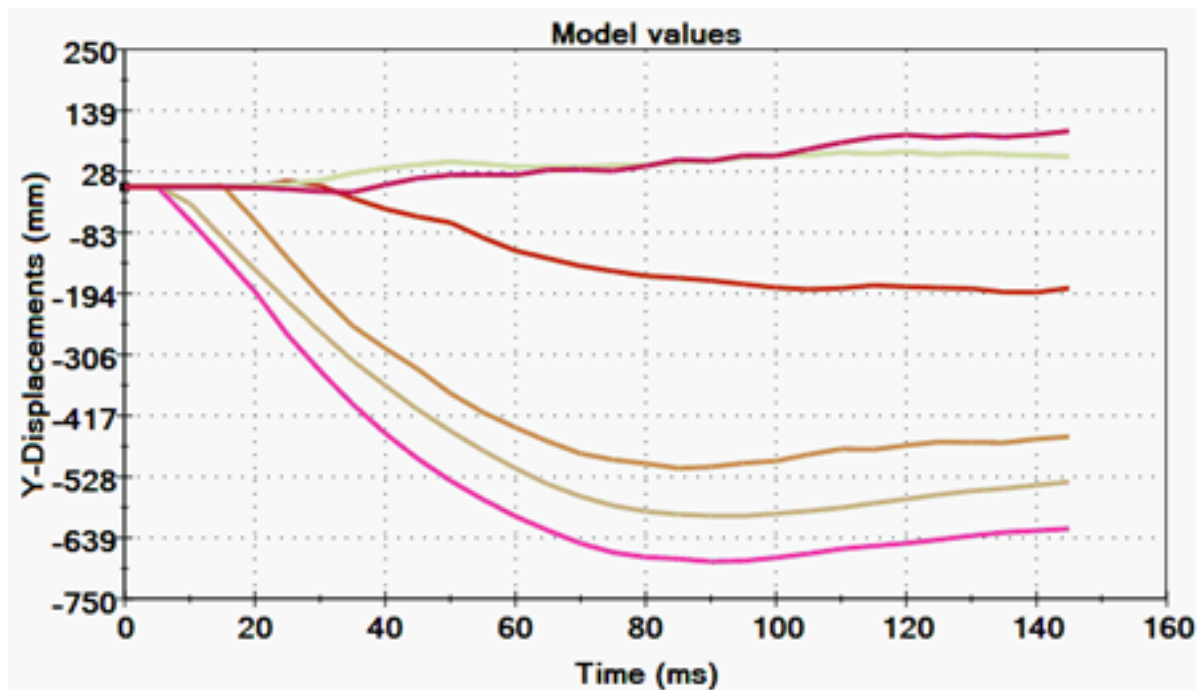


Figure 6.2: C1-C6 deformation-time histories

Table 6.4: Comparison of actual deformations obtained from CIREN versus the deformations predicted by the FE reconstruction – Stage I

Deformation in Centimeters*	Case 4		Case 5		Case 6		Case 7		Case 8		Case 15		Case 16		Case 17	
	Actual	FE	Actual	FE	Actual	FE	Actual	FE	Actual	FE	Actual	FE	Actual	FE	Actual	FE
C1	0	2	6	5	0	2	0	2	0	2	0	3	0	5	3	2
C2	12	11	18	16	47	45	50	45	23	25	54	50	29	35	27	30
C3	64	57	25	27	70	74	73	66	38	41	89	81	92	85	45	42
C4	62	54	35	39	51	55	62	59	31	34	73	78	52	56	34	33
C5	50	32	31	29	32	26	37	45	15	17	24	28	59	55	24	20
C6	12	8	22	20	0	4	0	5	2	1	0	4	0	8	8	6
Average Difference (%)	16.91		10.45		6.09		7.67		14.93		6.65		7.12		15.96	

*Note: Deformation numbers are the final resting values

It was found from the simulations that, in all cases, the maximum aortic strain was located in the region distal to the left subclavian artery, i.e. in the peri-isthmic region. Table 6.5 lists the maximum principal strain averaged from four elements in the isthmus region and the maximum pressure in the aorta for the eight CIREN cases simulated. Figures B1 through B8 in Appendix C compares the actual versus model predicted deformation pattern for the scaled vehicles used in Stage I of the reconstruction, while Figures B9 through B16 compares the deformation of WSHBM and AMPS fringes of the aorta for the eight cases reconstructed in Stage II.

Table 6.5: Output details for the FE reconstructions – Stage II

CIREN Case No.	PDOF (Deg)	Delta 'V' (km/hr)	Occupant Status	Left Side Door Structure Impact Time with Occupant (ms)	Average Maximum Principal Strain at the Isthmus (AMPS)*	Time at AMPS (ms)	Maximum Pressure (kPa)	Time at Maximum Pressure (ms)
4	310	62	Survived	14	0.1452	38	114.8	48
5	310	27.5	Fatal	34	0.1658	54	108.7	60
6	280	55	Fatal	16	0.2767	33	134.0	30
7	280	59	Fatal	22	0.2823	42	132.2	36
8	320	27.6	Fatal	30	0.1851	50	104.6	50
15	270	47	Fatal	26	0.1921	42	102.0	47
16	270	54.4	Fatal	22	0.2955	36	136.0	35
17	260	41	Survived	33	0.1941	38	103.8	52
Average					0.217±0.059		117.013±14.676	

*AMPS: Average maximum principal strain at the level of the isthmus calculated from four elements in the isthmus region

* The highlighted boxes (dotted) list the minimum and maximum AMPS recorded in the simulations and the highlighted boxed (solid) list the minimum and maximum pressure recorded in the simulation

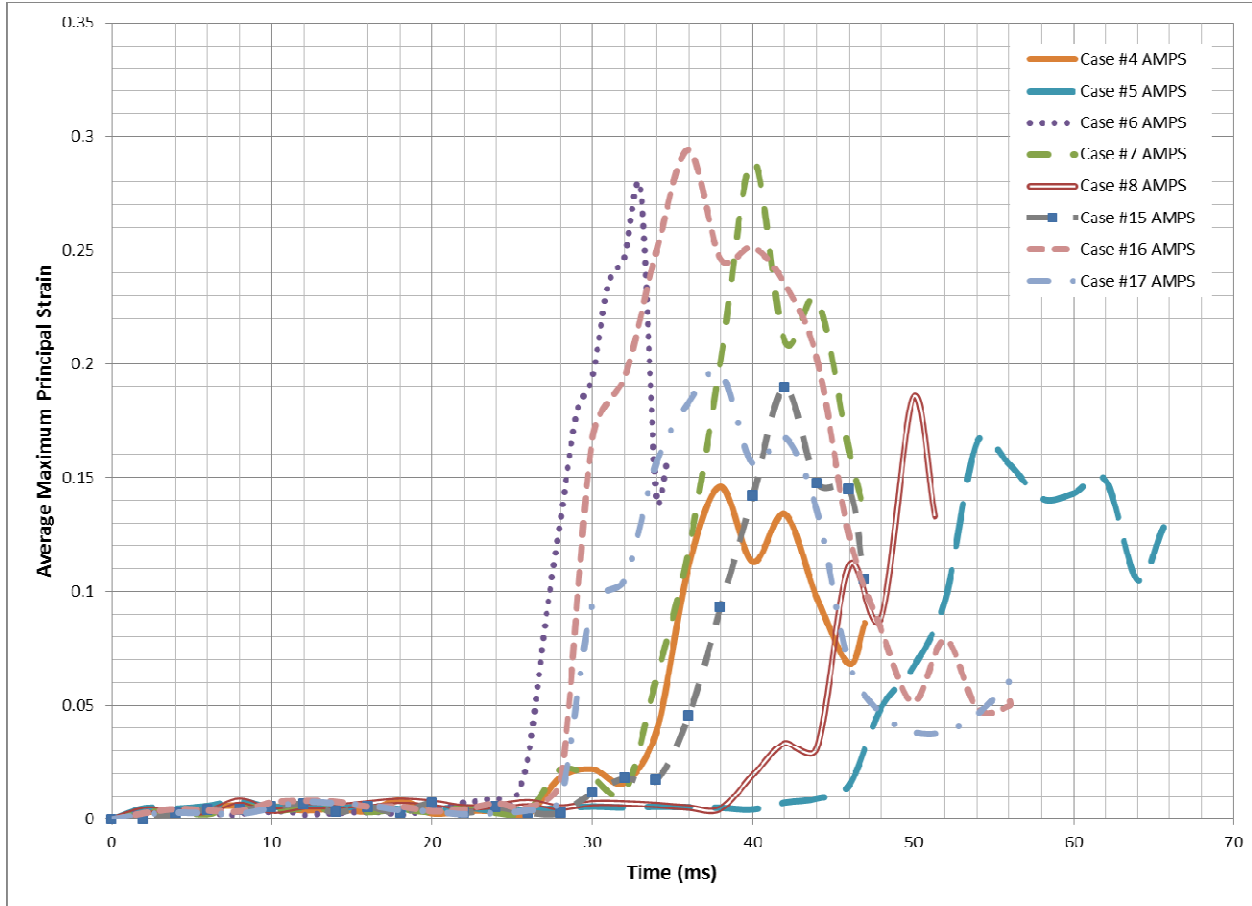
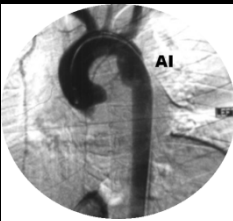
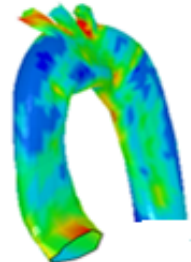

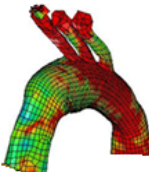

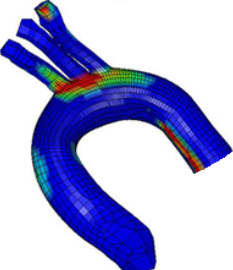
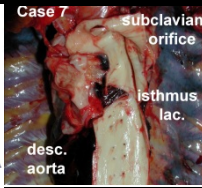
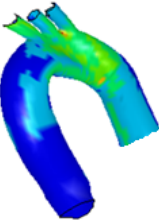
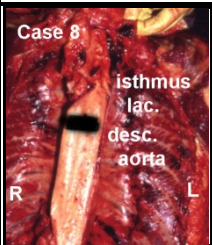
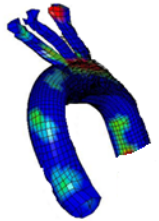

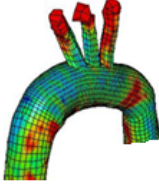
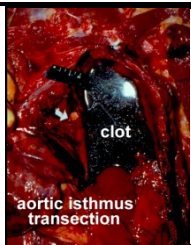
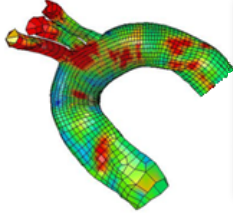
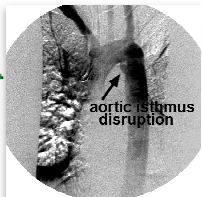
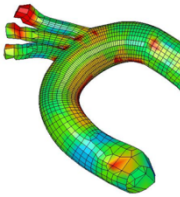


Figure 6.3: Average maximum principal strain-time histories for the right CIREN cases reconstructed

Table 6.6 compares the aortic injury location detailed from the CIREN case reports with the WSHBM predicted regions of strain while Figure 6.3 plots the AMPS-time histories for the eight CIREN cases reconstructed.

Table 6.6: Comparison of aortic injury locations between real world CIREN data and WSHBM predicted regions of strain

Case #4		Case #5		Case #6		Case #7	
CIREN data	WSHBM Predicted	CIREN data	WSHBM Predicted	CIREN data	WSHBM Predicted	CIREN data	WSHBM Predicted
							
Case #8		Case #15		Case #16		Case #17	
CIREN data	WSHBM Predicted	CIREN data	WSHBM Predicted	CIREN data	WSHBM Predicted	CIREN data	WSHBM Predicted
							

6.5 Discussion

Traumatic rupture of the aorta has been identified as the second most common cause of early death following MVC, only surpassed by brain injury (Sauaia et al. 1995). Because of the high mortality rate of aortic injury, 59% deaths at the scene of crash and in some studies up to half of the scene survivors dying in transport or in the ER of the receiving hospital according to Demetriades et al. (2008). Considerable experimental efforts have been expended to define the causative factors that produce this injury.

The maximum principal strains ranged from 14.5% to 29.6% and the pressures ranged from 102 kPa to 136 kPa for the eight near side left lateral CIREN cases reconstructed. For the two victims who sustained aortic injury but survived the crashes (Cases 4 and 17), the average AMPS was 17% and the average maximum pressure was 109 kPa. On the other hand, for the six cases with a fatal crash, the average AMPS was 23.3% and the average maximum pressure was 120 kPa. As shown in Table 6.1, the average crash energy for the two survival cases was 212 kJ compared to that of 154 kJ for the six fatal cases of aortic injury. Thus, crash energy may not be a good predictor of survivability.

A one-way ANOVA was performed using Minitab 16.1 (Minitab Inc., PA), on the average maximum principal strain obtained between the cases where the occupant survived the crash versus a fatal crash in left lateral crashes. In these cases the sample size was insufficient to reach statistical significance ($p=0.243$). Although in Case #4 the average maximum principal strain was low at 14.5% with a maximum pressure of 115 kPa in the aorta, no conclusion can be drawn (due to insufficient number of cases) as to

why the occupant survived the crash when in Case #5 the occupant suffered a fatality at 16.6% strain and 109 kPa of pressure in the aorta.

Lundevall (1964) reported that the isthmus of the aorta was only 63% as strong as that of the ascending aorta. Numerous other studies by Viano (1983), Mohan and Melvin (1982; 1983), and Fung (1993) have characterized the failure stress of the aorta under uniaxial and biaxial loading conditions. Shah et al. (2006) concluded from biaxial tensile tests on cruciate shaped specimens that the average longitudinal failure strain to be 27.7% in the ascending region, 24.4% in the descending region and 21.7% in the peri-isthmic region, with an overall average failure strain of 24.4%. In a second series of tests, high-speed longitudinal stretch tests were conducted by Shah et al. (2007b) on whole aortas until failure (1 m/s), and an average failure strain of 22.1% was reported. It should be noted that the strain data published in both series of tests were based on isolated aortic specimens and few specimens failed around the region of atherosclerotic plaque deposition. From FE reconstructions, an average maximum principal strain of 0.22 ± 0.06 and 0.16 ± 0.09 report in % to be consistent respectively in the isthmus of the aorta is recorded. Cases #6, #7 and #16 reported strains higher than those reported by Shah et al. (2007b) where each case ended in a fatal aortic isthmus tear. It is interesting to note that, Cases #5, #8, and #15 reported strains lower than those from Shah et al. (2007b) are and still ended in fatal aortic tears.

Overall, the peak maximum pressure predicted by the FE model was lower than 400 kPa, the threshold for aortic rupture as reported by Oppenheim et al. (1918) and 800 kPa obtained by Mohan and Melvin in 1983 in biaxial loading experiments producing spherical tissue deformation. Bass et al. (2001) reported that there was a

50% risk of aortic tears at nearly 101 kPa, increasing to 120 kPa for subjects below 68 years of age. In the CIREN cases, the average age for the occupants was 37 ± 15 years, and the average maximum pressure was 117 ± 15 kPa. Although the average maximum pressures predicted by the simulations were less than those reported by Bass et al. (2001), three of the eight simulations were fatal and predicted pressures greater than 120 kPa (Cases #6, #7 and #16). Further, except for Case #16 the maximum pressure and maximum AMPS did not correlate with each other. Forman et al. (2008) conducted nine sled tests using partial cadavers placed in drums filled with beads to limit chest compression. The tests examined the inertial mechanism for aortic rupture. Peak accelerations averaging 169 g's did not result in aortic rupture with 7% chest compression and 177 kPa of peak intra-aortic pressure. The authors concluded that thoracic deformation was required for aortic trauma. Although, they reported no aortic injuries three out of the nine cadavers reported higher aortic pressures than those reported by Bass et al. in 2001. It is also interesting to note that all the nine cadavers had moderate to severe atherosclerosis.

A review of published data reported in the literature concluded that a transverse tear of the thoracic aorta at the isthmus, distal to the takeoff point of the left subclavian artery, is the principal site of aortic laceration (Greendyke, 1966; Sevitt, 1977; Viano, 1983; Shah et al. 2007; Hardy et al. 2008). The isthmus/peri-isthmic region is situated near the distal aspect of the aortic arch and represents a transition from a relatively mobile arch to a tethered descending portion, beginning at the third and fourth thoracic vertebrae. Katyal et al. (1997) showed that 94% of aortic ruptures involved the isthmus.

Aortic tears are primarily circumferential or transverse to the long axis of the vessel (Viano, 1983). In some cases, the aortic injury involves a partial tear of the vessel wall, typically the intimal and medial layer so that an intact adventitia and surrounding pleura may limit blood loss (Strassmann, 1947; Cammack et al., 1959; Symbas, 1977). From the NASS-CDS database survey described above and the CIREN data listed in Table 6.1, it can be seen that the most common injury source is typically the side interior structure and/or B-pillar intrusion into the occupant compartment. From Stage I and Stage II simulation runs performed in this study, a trend in the location with the highest AMPS in the aorta was evident. All the reconstructions had high strains in the isthmus region, distal to the left subclavian artery (Figure 6.4a), the source being the side door structures including the arm rest, door interior structures, and the B-pillar (Figure 6.4b).

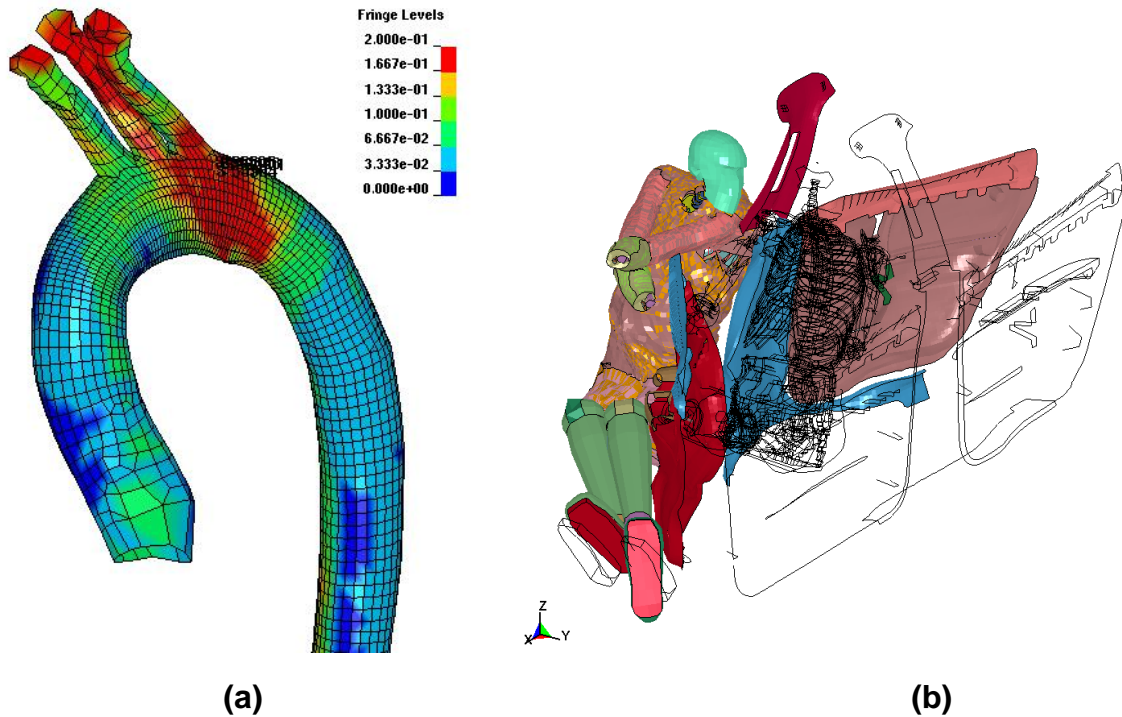


Figure 6.4: (a) Average maximum principal strain location – Isthmus of the aorta, (b) Left side door intrusion pattern (Red mesh indicates higher AMPS)

Zehnder et al. (1960) and Katyal et al. (1997) reported from field data that aortic tears were predominantly in the transverse direction perpendicular to the longitudinal axis of the aorta. Bass et al. (2001) reported longitudinal tears from their over-pressurization of *in vitro* and *in situ* human aorta specimens. Shah et al. (2007b) argued that this was expected only if the aorta was viewed as a thin-walled cylindrical vessel, but did not reflect injuries seen in the field. Shah et al. (2007b) in their tests on longitudinal stretch of the cadaveric aorta reported failure tears in the traverse direction. In their inverted cadaveric tests, Hardy et al. (2008) reported transverse tears in six of the eight cadavers tested with pressurized aortas. In the current FE reconstructions carried out, all the eight cases reconstructed had high AMPS in the transverse direction (elements that lined up with maximum principal strain). It is important to note that at the

region of the isthmus, there is an inherent concave curvature of the artery and a coarctation due to the presence of the ligamentum arteriosum (Bonnet et al., 1996).

It is to be noted that in all cases except Case #4, aorta injuries were accompanied with multiple left rib fractures (from CIREN data), which corresponded with regions of high strain and deformation in the WSHBM's ribs. Similarly, in except Case #5 and Case #16, all cases were accompanied with splenic contusions that correlated to regions of severe compression and strain in the WSHBM.

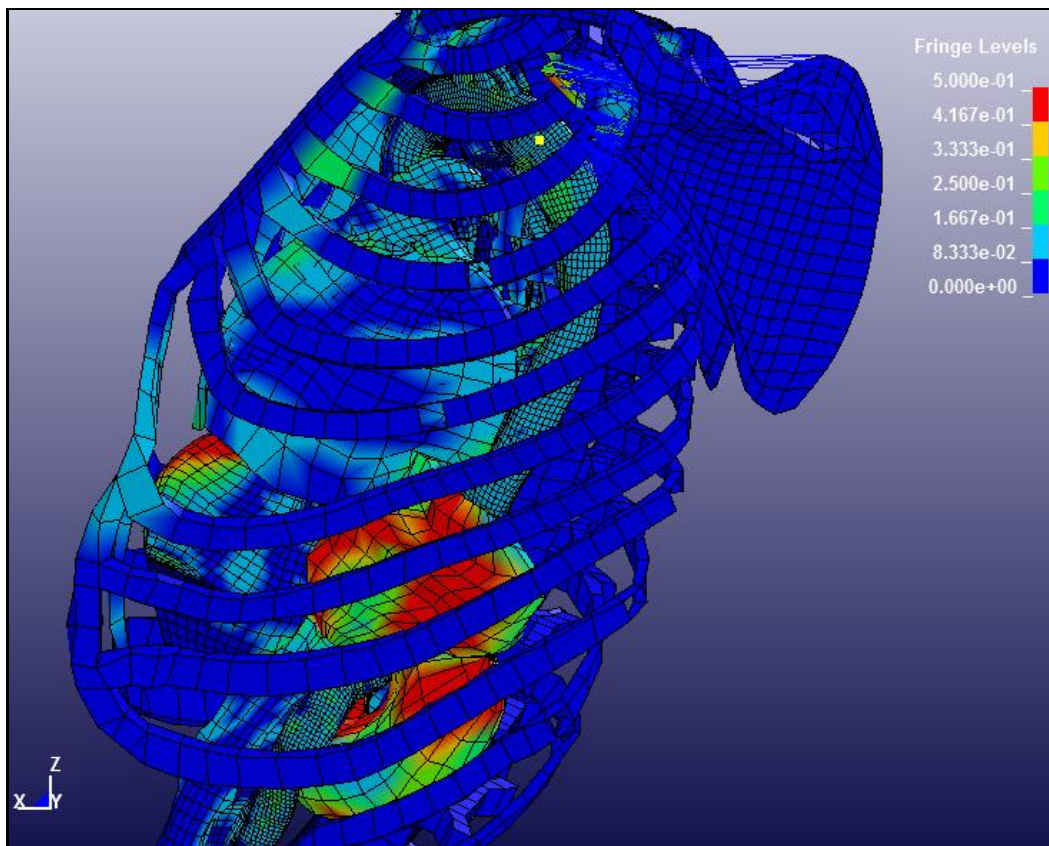


Figure 6.5: Maximum principal strain profile of the spleen, liver, and left ribs

From Figure 6.5, it is evident that the intruding left side B-pillar primarily caused strains in the left rib and spleen, which is a successor to severe thoracic deformation.

Since no failure threshold has been defined for either the spleen or the ribs in the WSHBM, the comparison is purely to augment the CIREN data.

6.5.1 Limitations of the current study

Several FE models of the human thorax have been reported in the literature. Roberts and Chen (1970) developed one of the first FE human thoracic skeleton models for investigating biomechanical responses of the human chest. Later, utilizing a beam element approach, Sudaram and Feng (1977) developed another three-dimensional chest model. The bony ribcage, sternum, and musculature were represented by beam, plate, and membrane elements, respectively. Plank and Eppinger (1991) developed a more realistic model of the human thorax, while Huang et al. (1994) developed a simplified human torso model to predict side impact injury parameters. Wang (1995) developed a side impact FE human thoracic model using geometry data from Schneider et al. (1983) for a mid-sized seated male in a driving position. The model consisted of 4,333 solid elements and 11,075 shell elements. Lizee et al. (1998) developed a whole-body human model with a limited number of elements to study a wide variety of impact conditions. More recently Toyota Central R&D Labs., Inc. developed the Total Human Model for Safety (THUMS) representing a 50th percentile adult male (Iwamoto et al. 2002). None of the reviewed whole body models has enough anatomical details in the thoracic cavity or a sufficiently accurate aortic model to predict TRA.

The current version of the WSHBM represents a 50th percentile model with a detailed thoracic cavity and has an anatomically accurate aorta model (Shah et al. 2001). However, it should be noted that in the current study, the WSHBM has been simulated without any scaling or personalized aorta model based on the CIREN data.

Even though the vehicle models were accurately scaled to match the size and weight of the struck and striking vehicles, the stiffness and interior compartment details did not simulate the actual vehicles involved. The bumper profiles of each striking vehicle and the status of pre-crash braking were different, thus generating varying crush patterns, which may explain the discrepancies in matching the measured physical deformations reported in Table 6.4.

Further, Niehoff et al. (2006) evaluated 121 NASS-CDS 2000-2003 cases and concluded that the WinSmash program underestimated the delta-v of the striking vehicle by an average of 23%. Further, if the striking vehicle is a front wheel drive, the underestimation of delta-v is up to 31%. In this study, only the 2002 Dodge Caravan FE model was a front wheel drive. It is also important to observe that measured external deformations may not correspond to similar occupant compartment intrusions and contact forces due to differences in elastic and plastic moduli of various interior components. This problem is exacerbated by the fact that deformation profiles were measured at only individual points on the external surface leading to localized variations in the actual and simulated profiles.

It is extremely challenging to truly recreate the intricacies of real world crashes due to inaccuracies in field measurement and the accident reconstruction software, which is typically based on rigid body dynamics. More importantly, variations in general anatomy and health status of the aorta in the human population are largely unknown. Heart disease, typically atherosclerotic cardiovascular disease remains the primary cause of death and disability in the United States (American Heart Association, 2008). Calcified aortic plaques change the elastic properties of the aorta, making it inextensible

in the region of calcification (Holzapfel et al. 2004). Viano (1983) suggested that the presence of atherosclerotic plaque is the weakest link in any traumatic aortic rupture. More recently, Hardy et al. (2008) agreed with Viano's conclusion in their cadaver tests and suggested that diseased aortas may have reduced failure strengths given that most failures occur in the region surrounding the diseased tissue. This could play a vital role in determining the failure threshold as well as a possible reason for occupant-specific aortic failure, which was not considered in the WSHBM model.

6.6 AIM A: Conclusions

The aortic injury reconstructions provide a unique insight using a combination of real world CIREN data and FE models in the realm of TRA. From the NASS-CDS review, the CIREN cases, and the FE aortic reconstructions, it was seen that in near side left lateral crashes the B-pillar followed by the interior door structures were primarily responsible for thoracic deformation leading to high aortic strains. Eight near side left lateral CIREN cases were reconstructed using a combination of FE vehicle models and the second version of the WSUBM.

1. The average AMPS were recorded to be 0.22 ± 0.06 use % and the average maximum pressure in the aorta was recorded to be 117 ± 15 kPa.
2. Although there was an increase in aortic pressure in the simulations, it may not be solely responsible for aortic failure.
3. The peak maximum principal strains primarily occurred in the isthmus of the aorta, distal to the left subclavian artery.
4. A large percentage of the cases (87.5%) reconstructed had multiple left rib fractures, predominantly from the fourth to the ninth rib.

5. A great number of the cases (75%) reconstructed showed high strains in the spleen due to rapid caudo-medial motion of the rib cage induced from the intruding B-pillar.

CHAPTER 7

AIM B: IDENTIFICATION OF KEY PARAMETERS RESPONSIBLE FOR INJURY MECHANISM IN LATERAL IMPACTS – DESIGN OF COMPUTER EXPERIMENTS STUDY (DOCE)

7.1 Introduction

Traumatic rupture of the aorta is one of the leading causes of death in high-speed impact trauma. Smith and Chang (1986) reported on 387 cases of blunt traumatic death in vehicular crashes and found that aortic injury was second only to head injury as the leading cause of death. They also reported that nearly 85% of the victims who sustained an aortic tear died at the scene. Further, most cases of aortic injury are accompanied by head injury, rib fractures and/or hepatic trauma (Burkhart et al. 2001).

The mechanism of injury and the threshold for injury in these cases may be related to the particular anatomy and physiology of the aorta and the surrounding tissues. Aortic strain, which has been considered a primary factor for aortic tears, is primarily regionalized in the peri-isthmic region, distal to the origin of the left subclavian artery as reported in the literature (Greendyke, 1966; Sevitt, 1977; Viano, 1983; Katyal et al. 1997; Hardy et al. 2006; Shah et al. 2007; Siegel et al. 2010). Further, data from literature has shown that, in lateral impacts, B-pillar intrusion combined with lateral sliding of the occupant into the intruding B-pillar and associated structures are mainly responsible for aortic injury (Shah et al. 2007; Siegel et al. 2010). From Chapter 6, it is imperative that the intruding B-pillar and associated structures is mainly responsible for

TRA. Further, higher aortic strain is primarily regionalized in the isthmus area, distal to the origin of the left subclavian artery.

7.2 Methods and Materials

To further understand the factors affecting aortic strain, a design of computer experiments (DOCE) study was performed on 16 different combinations of five design factors generated using a Latin Square method in modeFRONTIER 4.0 (ESTECO North America). The FE reconstructions were carried out in two stages as outlined in Chapter 5. In Stage I, the vehicle-to-vehicle crash kinematics and deformation patterns were reconstructed from accident reports obtained from the Crash Injury Research and Engineering Network (CIREN) database using scaled FE vehicle models downloaded from the National Crash Analysis Center (NCAC) model database. In Stage II, occupant impacts (WSHBM) with isolated vehicle structures were considered for 16 cases.

Five design factors were chosen, each with two to four levels of variation: impact height, impact position/bumper profile, PDOF, and initial velocity of the bullet vehicle along with varying occupant-seating positions in the case vehicle. Table 7.1 lists the design factors and ranges simulated, while Figures 7.1(a) and 7.1(b) graphically demonstrate these locations. The range for each design factor was chosen to include the eight near side left lateral cases reconstructed in Chapter 6.

Table 7.1: Range of values for the five design factors chosen for the DOCE study

No.	Design Factor		Range			
1	Striking Vehicle	Impact Height / Bumper Profile	Low	High	-	-
2		Impact Position (mm)*	- 300	0	+ 300	-
3		PDOF (degrees)	250	270	290	310
4		Initial velocity (km/hr)	30	38.3	46.6	54.9
5	Struck Vehicle	Occupant Position (mm)*	-125	0	+ 125	-

*Note: Impact Position and Occupant Position are determined from the center of the case vehicles' B-pillar

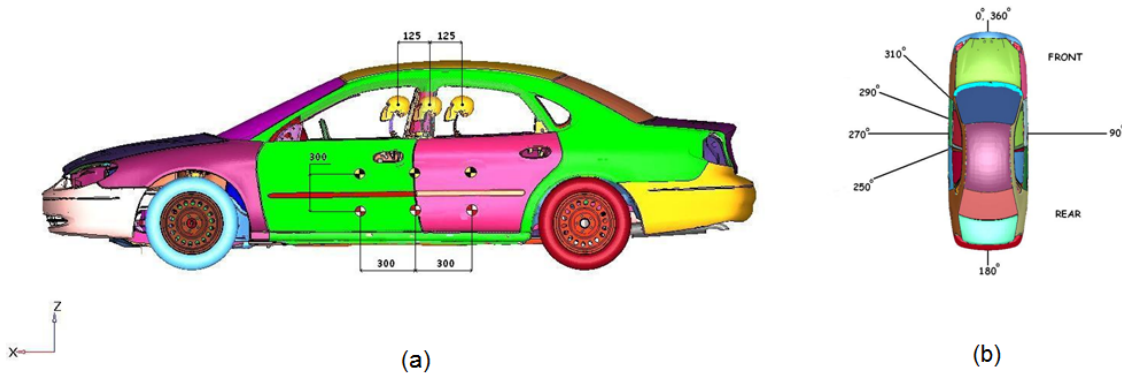


Figure 7.1: (a) Position of the impact on the vehicle, height of impact and occupant seating position (b) Range of PDOF in the simulations

The baseline case vehicle, a 2001 FE Ford Taurus model similar to the struck vehicle in the selected cases described in Chapter 6, was used as the target vehicle for the DOCE study. For the striking vehicle, FE models of a 2002 Dodge Caravan, which has a low bumper profile similar to a sedan, and a 2002 Ford Explorer, which has a higher bumper profile than a sedan, were used for the simulations. Impact positions were chosen to be the center, 300 mm forward or 300 mm backward of the case vehicle's B-pillar. The PDOF and initial velocity were chosen to cover the range of values in previous CIREN cases. Finally, the occupant seating position selected covered the range of fore-aft range of the seat (250 mm) for a 2001 Ford Taurus with

the angle of seat back at 110 degrees. That is, the occupant was positioned mid-track, 125 mm forward of mid-track or 125 mm backward of mid-track.

The response variables were the average maximum principal strain (AMPS) and maximum pressure in the aorta. For AMPS, four adjacent elements in the region with the highest maximum principal strains were selected and averaged; while for pressure, the maximum value in a single aortic element obtained during the entire simulation were tabulated.

7.3 Results and Discussion

Table 7.2 lists the DOCE simulation matrix derived using Latin Square Sampling in modeFRONTIER 4.0 (ESTECO North America), an optimization software, and the response variables. Maximum simulation time for each case run has been tabulated to establish a standardized time scale for comparison of maximum values. Some simulations terminated earlier due to 'negative volume' based on LS-DYNA terminology.

Table 7.2: Latin Square sampling for DOCE and output response variables: AMPS and maximum pressure in the aorta

Run #	Bumper Profile Height	Impact Position (mm)	PDOF (Degrees)	Velocity (km/hr)	Occupant Position (mm)	Maximum Simulation Time (ms)	AMPS*	Time at AMPS (ms)	Maximum Pressure (kPa)	Time at Maximum Pressure (ms)	
1	Low	-300	290	30	+125	56	0.1180	55	105.8	50	
2	Low	-300	270	38.3	0	65	0.2240	44	113.5	46	
3	High	-300	250	46.6	-125	54	0.1650	54	148.0	48	
4	High	-300	310	54.9	0	33	0.0540	33	109.0	33	
5	Low	0	270	54.9	0	52	0.3240	40	135.0	36	
6	Low	0	290	46.6	+125	46	0.1580	44	119.6	36	
7	High	0	310	30	0	78	0.0675	78	104.4	70	
8	High	0	250	38.3	-125	64	0.1650	56	120.0	50	
9	Low	0	310	46.6	-125	80	0.2100	60	127.6	50	
10	Low	0	250	54.9	0	44	0.2580	43	117.7	42	
11	High	0	290	38.3	0	44	0.0330	43	104.3	42	
12	High	0	270	30	+125	70	0.1520	54	110.8	54	
13	Low	+300	250	38.3	0	72	0.2300	44	113.2	48	
14	Low	+300	310	30	-125	80	0.0250	78	90.1	78	
15	High	+300	270	54.9	+125	36	0.2350	34	149.0	34	
16	High	+300	290	46.6	0	76	0.1600	54	123.7	52	
Average								0.16± 0.08		118.23± 15.82	

* Average Maximum Principal Strain (%) = Lower Surface Average Maximum Tensile Principal Strain in the longitudinal axis of the aorta

* AMPS and Maximum pressure curves for each run are presented in Appendix C, Figures C1 and C2

It was observed from the simulation that the maximum principal strain occurred near the isthmus of the aorta, distal to the orifice of the left subclavian artery, in all runs. A maximum strain of 32.4% was recorded in Run #5, which was a sedan impacting the B-pillar (270 degrees) at 55 km/hr with the occupant seated at the B-pillar. The lowest strain of 2.5% was observed in Run #14, which was a sedan impacting 300 mm to the

left of B-pillar at an angle of 310 degrees and a velocity of 30 km/hr with the occupant seated 125 mm in front of the B-pillar.

In order to determine the critical factors, main effects analysis was performed in Minitab 16.1 (Minitab Inc., PA) based on the FE model predicted results listed in Table 7.2. The following figures summarize the relationships between selected design factors and AMPS in the isthmus (Figures 7.2) or peak pressure in the aorta (Figures 7.3) predicted by the WSHBM.

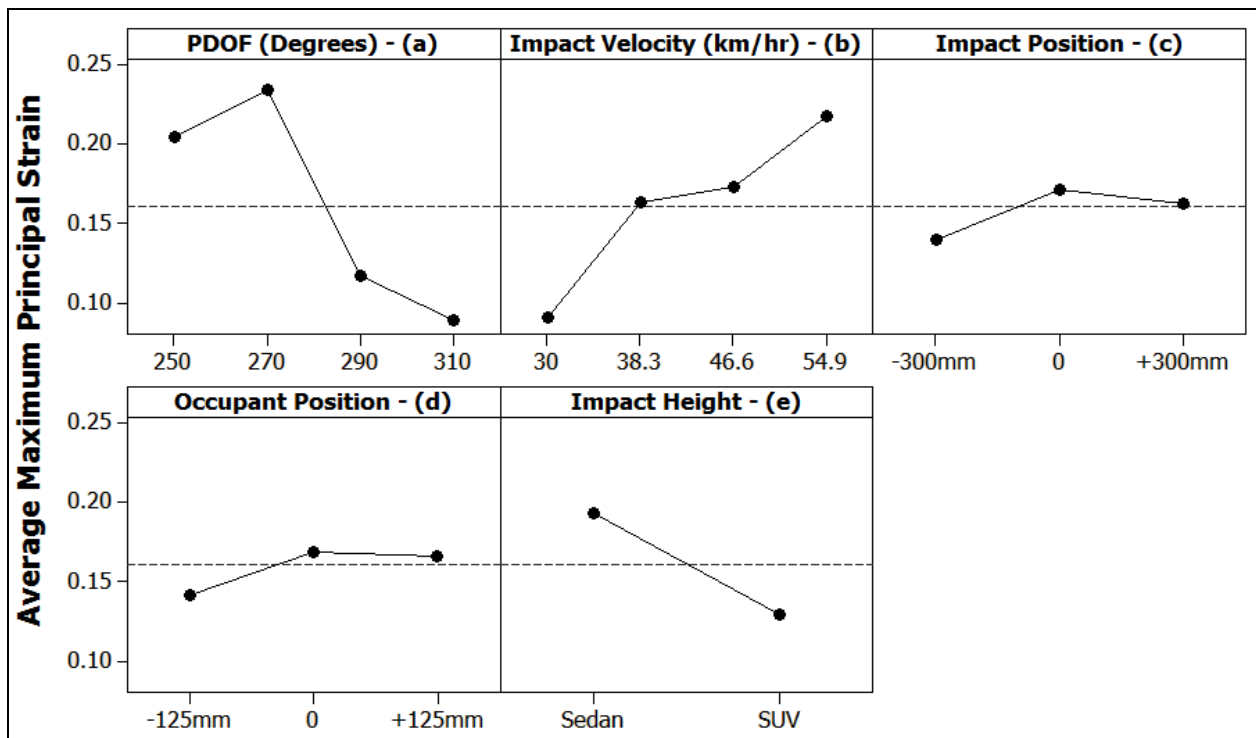


Figure 7.2: Main effects chart for AMPS in the isthmus of aorta

It is noted that a PDOF of 270 degrees resulted in the highest average AMPS (Figure 7.2a) among all factors and levels studied. An increase in impact velocity had a direct correlation with the increase in maximum principal strain (Figure 7.2b), while an

occupant seated at the B-pillar with an impact directed to the B-pillar seemed to generate higher strain in the isthmus region (Figures 7.2c and 7.2d). Bumper height yielded results in contrast to intuitive thinking, impacts from the lower profile Dodge caravan generated a higher isthmus strain compared to a higher profile SUV represented here by a Ford Explorer model (Figure 7.2e).

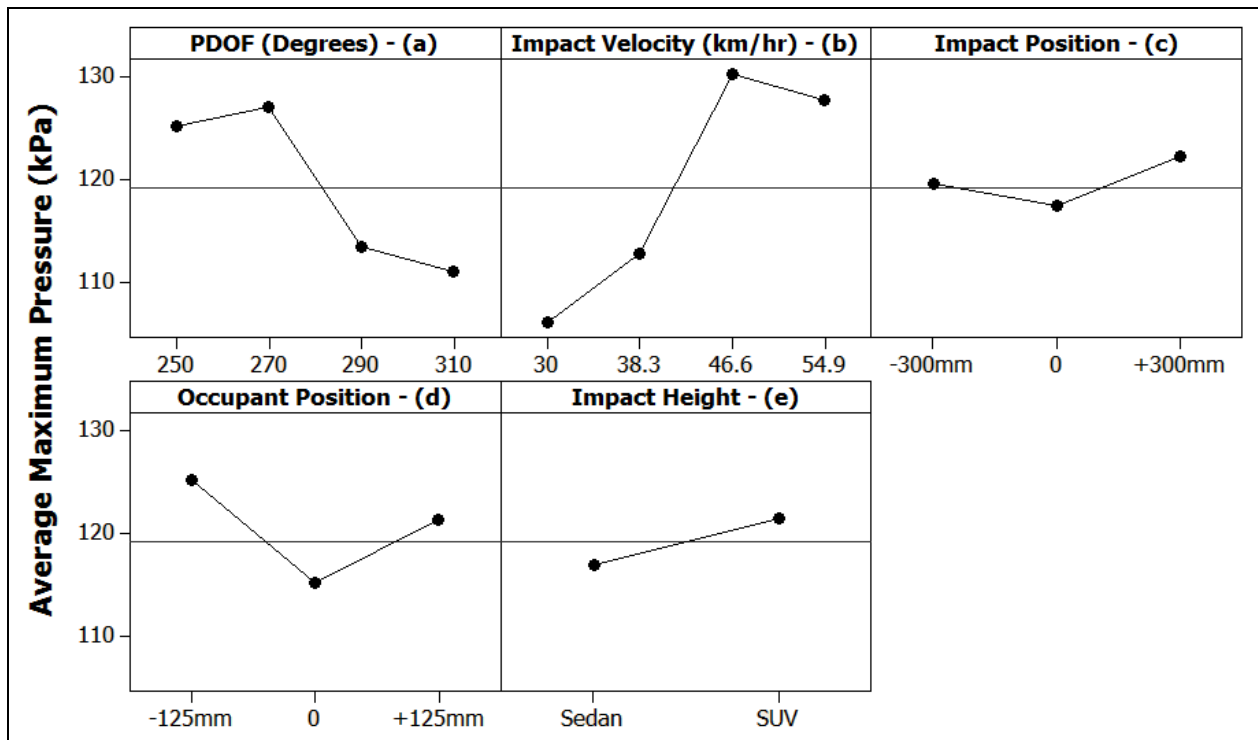


Figure 7.3: Main effects chart for maximum pressure (kPa) in the aorta

From Figure 7.3a, a PDOF of 270 degrees resulted in the highest aortic pressure among all four PDOF's simulated. As the impact velocity increased, the aortic pressure also increased and seemed to vary negligibly after a velocity of 46.6 km/hr (Figure 7.3b). In contrast to the findings for maximum principal strain, an impact position centered on the B-pillar (Figure 7.3c) or an occupant seated at the B-pillar (Figure 7.3d)

generated the lowest aortic pressures, and a higher bumper profile generated a higher aortic pressure (Figure 7.3e).

Table 7.3: Significance of each design factor for an $p=0.05$: AMPS and maximum pressure in the aorta

Significance Order	Design Factor	AMPS	Design Factor	Maximum Pressure
1	PDOF	0.001	Impact Velocity	0.002
2	Impact Velocity	0.055	PDOF	0.028
3	Impact Height	0.068	Occupant Position	0.185
4	Impact Position	0.295	Impact Height	0.283
5	Occupant Position	0.304	Impact Position	0.475

Based on a Student's t-test performed using modeFRONTIER 4.0 (Table 7.3), it was found that PDOF had a significant negative effect on strain, i.e. as PDOF increased the average AMPS in the aorta decreased, while impact velocity had a marginally significant positive effect, impact height had a marginally significant negative effect on FE model predicted average maximum principal strain. In terms of FE model predicted peak aortic pressure, impact velocity had a significant positive effect while PDOF had a significant negative effect.

The effects for coupled variables were analyzed using Pareto charts. In a Pareto chart, the length of the bars indicates absolute value of each individual and coupled variable's effect. The Lenth method based on at-distribution was specially designed to study the effect of computer experiments by assuming that only small shares of variables are significant (Lenth, 1989). From Figure 7.4, we observe that a combination of PDOF (C) and occupant seating position (E) followed by bumper profile height (A) with occupant position (E) have a significant impact on the AMPS while a combination

of PDOF (C) and occupant seating position (E) followed by bumper profile height (A) with occupant seating position (E) had a significant impact on the maximum pressure generated in the aorta in the 16 simulations (Figure 7.5).

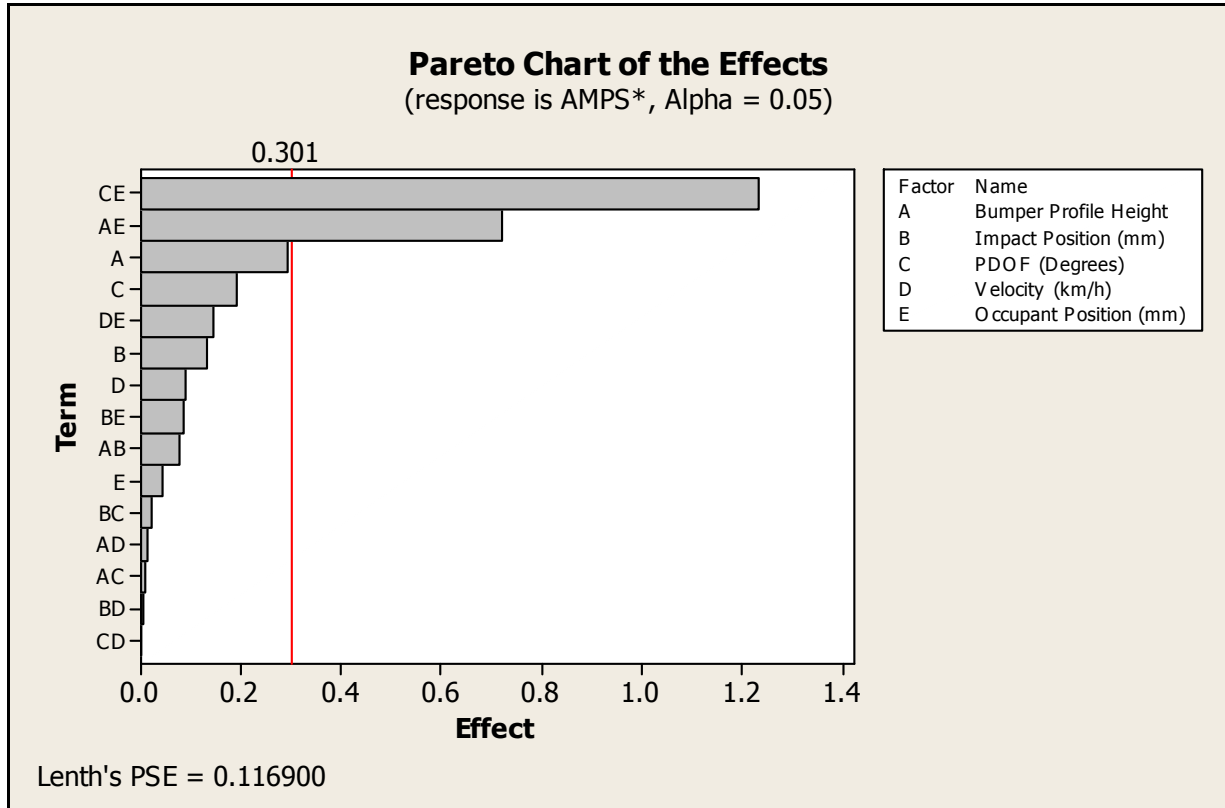


Figure 7.4: Pareto chart of effects for isthmus AMPS

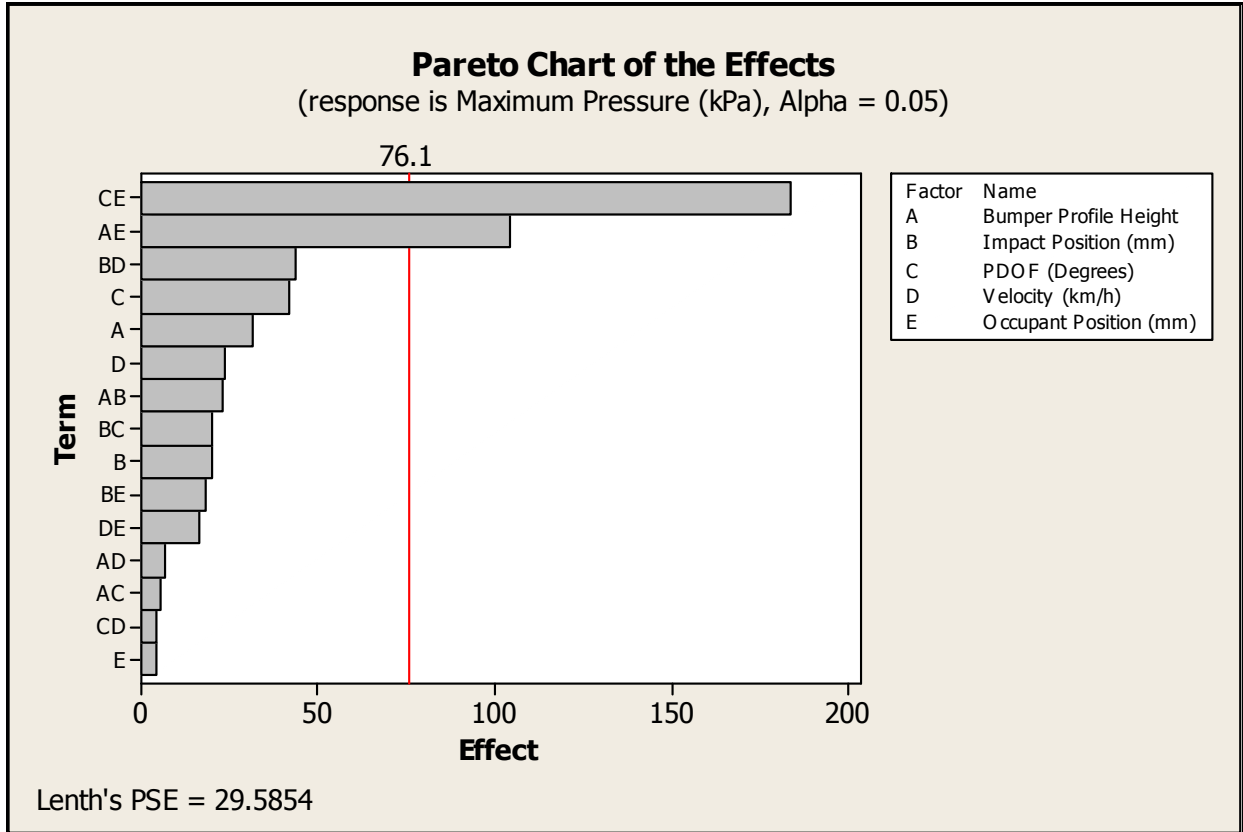


Figure 7.5: Pareto chart of effects for maximum pressure (kPa) in the aorta

From Figures 7.4 and 7.5, we observe that no individual factor is significant enough to affect AMPS and Maximum Pressure in the aorta. Although from Figure 7.4, we observe that Bumper Profile Height (A) is borderline significant for AMPS.

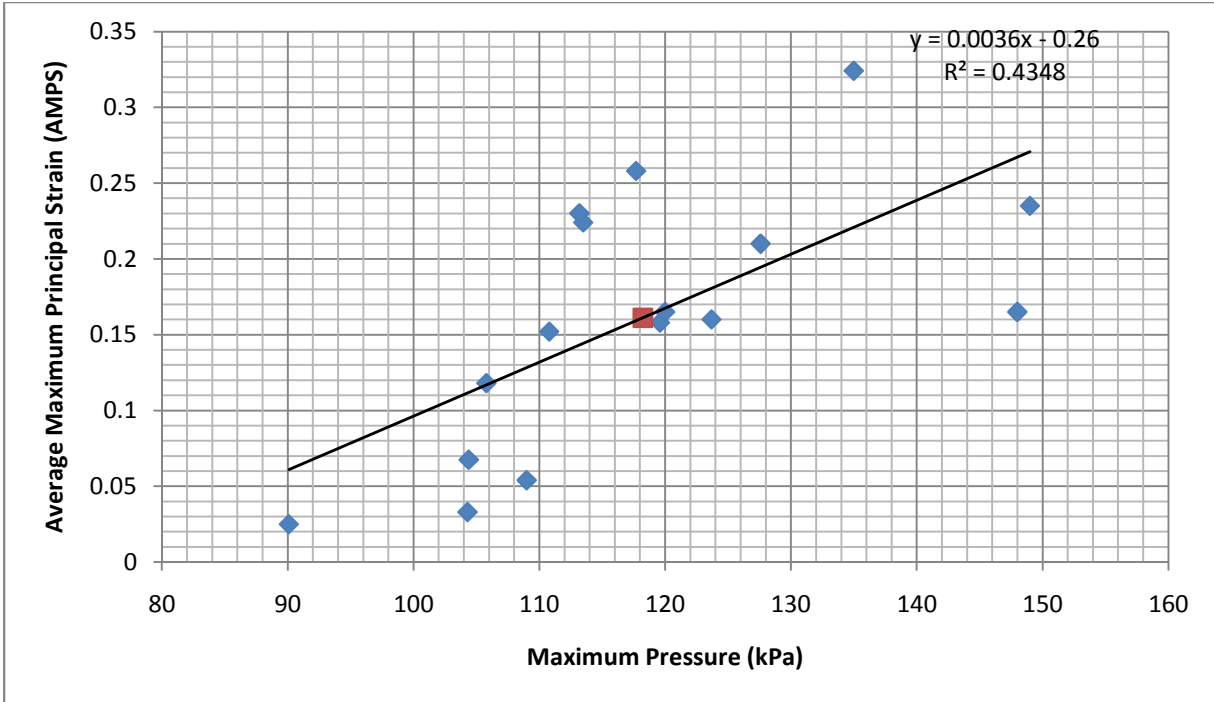


Figure 7.6: Plot of AMPS vs. maximum pressure (kPa)

A plot of AMPS vs. maximum pressure (Figure 7.6) revealed an 'R' square value of 0.4348 with no significant correlation between aortic failure with strain and pressure combined, except in Cases #5, 9 and 15. This was also supported by data from Table 7.2 where no correlation was found between times of occurrence of maximum AMPS and maximum pressure in the aorta for a particular run.

Although there were no significant differences in impact velocity, PDOF, or maximum pressure; it is interesting to note that the runs with high aortic strains had a striking vehicle with a low bumper profile (sedan). It was observed, that in runs with lower bumper profile, the armrest gets pushed into the thorax, which does not occur with a higher bumper profile. Further, because of the mass difference of 488.5 kilograms between the Dodge Caravan (2,028.1 kg) and the Ford Explorer (1,539.6 kg)

FE models, the difference in momentum between the two impacts might have had an effect on the intrusion pattern. A one-way ANOVA performed between the two FE models for average maximum principal strain ($p=0.136$) and maximum pressure in the aorta ($p=0.58$) did not show statistical significance.

Several limitations of the current study are noted. Even though the vehicle models were accurately scaled to match the size and weight of the case vehicles, the stiffness and interior compartment details were not compensated. It is also important to observe that measured external deformation may not correspond to similar occupant compartment intrusion and contact force due to differences in elastic modulus of various interior components. This problem is exacerbated by the fact that deformation profiles are measured at individual points on the external surface leading to variations in actual and simulated profiles.

7.4 AIM B: Conclusions

Sixteen DOCE runs were carried out using FE vehicle models and the second version of the Wayne State Human Body Model. In simulated near side left lateral crashes, the following conclusions can be drawn:

1. Of the four PDOFs simulated, a PDOF of 270 degrees generated the highest average maximum principal strain in the aorta.
2. Peak average maximum principal strain primarily occurred in the isthmus of the aorta, distal to the orifice of the left subclavian artery.

3. PDOF and occupant seating position combined together were significant for both AMPS and maximum pressure in the aorta followed by a combination of bumper profile height and occupant seating position.
4. Although not significant as individual factors, results of design of computer experiments concluded that *occupant-seating position, bumper profile height, and PDOF of impact*, in that order, play crucial roles in the generation of strain and pressure in the aorta, a potential injury mechanism responsible for traumatic rupture of the aorta in automobile crashes.
5. Velocity and impact position were not significant for either AMPS or maximum pressure in the aorta.

CHAPTER 08

AIM C: INJURY MECHANISMS FOR TRA

8.1 Introduction

Aortic injury and related mechanisms have been discussed in the literature for more than a century now. Over the last 40 years, ruptures to the thoracic organs and blood vessels have caused more than 40% of all automotive traumas with 20% of them originating from aortic ruptures (Viano, 2011). From AIM A (Chapter 06), it was observed that in nearside left lateral impacts, CIREN data showed regions of tear in the isthmus of the aorta, which correlated with FE reconstruction data, in which regions of high strain were located in the isthmic / peri-isthmic region of the aorta, distal to the takeoff point of the left subclavian artery. Further, B-pillar intrusion combined with lateral sliding of the occupant into the intruding structures were mainly responsible for thoracic deformation leading to TRA. From AIM B (Chapter 07), it was observed that a PDOF of impact of 270 degrees yielded the highest strain and pressure in the aorta, while a combination of PDOF and occupant-seating position was crucial to the mechanism of TRA. Further, as the PDOF of impact increased from 250 degrees to 310 degrees, the mechanism of strain generated varied.

8.2 Injury Mechanisms for TRA

Chapter 3, Section 3.2 described and listed the various hypotheses published on TRA. For the sake of completeness and in order to aid the reader into continuation on the mechanisms of TRA, Table 8.1 summarizes the mechanisms tabulated in Table 3.1.

There have been numerous hypotheses made on injury mechanisms for TRA as described in Chapter 3. Briefly, these hypothesis were based on: ***inertia*** (Letterer, 1924; Hass, 1944; Roberts et al., 1966; Creasy et al., 1997), ***pressure*** (Oppenheim, 1918; Klotz and Simpson, 1932; Taylor, 1962; Lundevall, 1964; Roberts et al., 1966; Mohan and Melvin, 1982; Carson and Roach, 1990; Siegel et al., 2004), ***strain*** (Rindfleisch, 1893; Hardy et al., 2006; Shah et al., 2006; Hardy et al., 2008), ***atherosclerosis*** (Strassmann, 1947; Lundevall, 1964; Greendyke, 1966; Vande Geest, 2002), and ***other factors*** (Marshall, 1958; Cammack et al., 1959; Zehnder, 1960; Hossack, 1980; Crass et al., 1990; Sevitt, 1977; Voigt and Wilfert, 1969; Melvin et al., 1998; Ben-Menachem, 1993). The advent of finite element human models along with sophisticated testing methodology has significantly helped the understanding of TRA. Unfortunately, most data published in the literature lack the usage of real world crash data and reconstruction methodology.

Table 8.1: List of the various injury mechanisms hypothesized for TRA published in the literature

No.	Author and Year	Mechanism
Inertia based		
1	Letterer, 1924	Downward traction of the heart as a result of falling is responsible for aortic root avulsion
2	Hass, 1944	Differential acceleration (jerk) of the structures within the mediastinum
3	Roberts et al., 1966	Inertia component not primarily required for rupture
4	Creasy et al., 1997	High rate of deceleration along with chest compression might

		cause aortic injuries
5	Forman et al., 2008	Acceleration alone cannot cause TRA. Thoracic deformation is essential for TRA
Pressure based		
6	Oppenheim, 1918	Overpressure – 400 kPa
7	Klotz and Simpson, 1932	Overpressure due to hemodynamic effect of acceleration – explosive
8	Taylor, 1962	Shock waves could initiate a retrograde aortic bulge causing a localized weakness
9	Lundevall, 1964	Water hammer effect due to over pressure
10	Roberts et al., 1966	Transverse tear from pressure to occur if ratio of ultimate transverse stress to ultimate long. Stress > 2
11	Carson and Roach, 1990	Intimal tears at 79 kPa
12	Siegel et al., 2004	Archimedes Lever Hypothesis
Others		
No.	Author and Year	Mechanism
13	Marshall, 1958	Squeezing of the aorta by the parietal pleura
14	Cammack et al., 1959	Torsion of the aorta due to deceleration
15	Zehnder, 1960	Hyper flexion displacement of the aortic arch with the hilum of the lungs acting as a fulcrum
16	Hossack, 1980	Non-circumferential tears as a result of laceration from the ribcage
17	Crass et al., 1990	Osseous pinch mechanism
18	Sevitt, 1977	Discussed multiple mechanisms of injury - ligamentum arteriosum
19	Voigt and Wilfert, 1969	Traction of the superior vasculature - aorta is subjected to tension via the carotid arteries as a result of rapid rearward pitch of the head – involves a dorso-cranial motion of the

		heart in response to frontal impact to the abdomen and thorax – Shoveling mechanism: where compression of the sternum forces the heart upward causing tension in the aorta at the isthmus.
20	Cavanaugh et al. (1990,1993)	Inertial forces exerted by laterally accelerating heart and vessels may pulled on the descending thoracic aorta, which is firmly anchored to the posterior chest wall, causing aortic tears between the aortic arch and the descending thoracic aorta
21	Melvin et al., (1998)	Anterior motion of the sternum away from the spine is limited substantially – Passenger car occupants, the sternum is driven away from the spine anteriorly due to medial motion of the shoulder complex and the deforming ribcage – Sternal popping
22	Cavanaugh et al. (2005)	Suggested the importance of anterior motion of the sternum in side impacts
23	Shah et al., 2007	Sternal popping may not be a mechanism of injury. Hilum of the lung may play a role in TRA

Stretch based

No.	Author and Year	Mechanism
24	Rindfleisch, 1893	Stretch deformation was a significant component of TRA
25	Mohan and Melvin, 1982	Ratio of ultimate transverse stress to ultimate longitudinal axis Stress = 1.2~2.12
26	Hardy et al., 2006	No pulmonary artery injury – motion of aortic arch and heart relative to the fixed descending aorta which straightens the inferior aortic arch
27	Shah et al. 2007	Longitudinal stretch of the aorta
28	Hardy et al., 2008	Tethering of the aorta to the parietal pleura
29	Belwadi et al. 2011	Longitudinal stretch of the thoracic aorta from FE CIREN reconstructions
30	King et al. 2011	Summarized the tests from Hardy et al. (2008) - Longitudinal

		stretch of the thoracic aorta and tethering of the aorta to the parietal pleura
--	--	---

From Table 8.1, it is seen that there are 30 different hypotheses for mechanism of TRA. Strain, pressure, inertia, and other factors (including atherosclerosis); in that order of importance based on real world data (Viano, 1998; Shah et al. 2007; Belwadi et al. 2011a), FE data (Shah et al. 2008; Belwadi et al. 2011b), and cadaveric test data (Hardy et al. 2008, Viano, 2011, King, 2011) play a crucial role in TRA.

Summarizing data from Chapters 6, 7 and 8 along with data from literature, it is evident that one of the factors listed below is essential for TRA to occur:

- Thoracic deformation is essential for TRA
- Acceleration/ inertia alone cannot generate TRA
- In nearside left lateral impacts, B-pillar plays a significant role in TRA
- PDOF and seating position is crucial to TRA
- Longitudinal stretch of the aorta is the primary mechanism for TRA
- Pressure may not be a primary factor, but aids in the generation of TRA
- Although transverse tears are more significant with clinical data, they cannot be used to differentiate between pressure versus strain based failure hypotheses

8.3 Materials and Methods

In order to delineate the mechanism of injury for TRA, the following additional simulations were carried out:

- 1) Three nearside left lateral CIREN cases without a aortic injury was reconstructed using a combination of scaled FE vehicle models and WSHBM in two stages as described in Chapter 5.
- 2) Eight additional cases were simulated in order to perform a paired sensitivity comparison.

Based on literature data and the CIREN reconstructions, the objective of this study was to compare the kinematics of the aorta with published cadaveric data and to look into the hypothesis of “*Sternal Popping*” due to loading via the shoulder in lateral impacts.

8.3.1 CIREN Case Details

Table 8.1 summarizes the details of the three nearside left lateral cases. Letter ‘T’ is denoted for these three cases to signify no aortic injury. Table 8.2 summarizes the vehicle specifications while Table 8.3 details the FE models used in the reconstruction process.

Table 8.1: Summary of left lateral cases used in the crash reconstruction process

Parameter	Case T1	Case T2	Case T3
Accident Details			
Impact Object	Car-SUV	Car-Van	Car-SUV
Delta V (km/hr)	33.6	29.1	22.0
Energy (Joule)	37,835	59,879	24,799
PDOF (Degree)	255	285	300
Collision Deformation Classification (CDC)	08LYAW4	10LZAW4	10LYEW2
Seat Belt Usage	Three-point belt, not in use	Three-point belt, in use	Three-point belt, not in use
Airbag Usage	No airbag deployed	No airbag deployed	No airbag deployed
Occupant / Injury Details			
Parameter	Case T1	Case T2	Case T3
Status	Survived	Survived	Survived
Age (Years) (50±28)	42	26	82
Race	African-American	Caucasian	Caucasian
Gender	Female	Female	Female
Height (cm) (160±5)	160	165	155
Weight (kg) (65.6±18.4)	86	61	50
Aortic injury details	No aortic injury reported	No aortic injury reported	No aortic injury reported
Other Injuries by Body Region			
Head	Loss of consciousness	Loss of consciousness, forehead laceration, left eyelid laceration	Loss of consciousness, left corneal abrasion
Thorax and Upper Extremities	Right hemothorax	Left rib fractures	Left anterior rib fractures with pneumothorax, left forearm contusion
Abdomen	Grade 1 liver contusion and splenic contusion	Right liver laceration Spleen laceration	

Pelvis and Lower Extremities	Pelvic fracture	Left hip contusion	Bilateral inferior and left superior pubic rami fractures
-------------------------------------	-----------------	--------------------	---

Table 8.2: Summary of vehicle models and their initial setup (after scaling) used in the left lateral crash reconstruction process




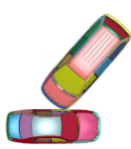
Parameter	Case T1	Case T2	Case T3
Case / Struck Vehicle (Year, Make and Model)	1993 Mercedes Benz 190E	1997 Honda Civic 4-Dr	1996 Chevrolet Cavalier 4-Dr
Case / Struck Vehicle Weight (kg)	1,318	1,098	1,162
FE Vehicle Model Used (Year, Make and Model)	2001 Ford Taurus	2001 Ford Taurus	2001 Ford Taurus
Striking Vehicle (Year, Make and Model)	1993 Mazda Navajo SUV	1991 Ford E-250 Van	1994 Ford Ranger SUV
Striking Vehicle Weight	1,760	2,165	1,350
FE Vehicle Model Used (Year, Make and Model)	1998 Ford Explorer SUV	1998 Ford Explorer SUV	1998 Ford Explorer SUV
Initial Model Setup in the Simulation (km/hr) 			

Table 8.3: Details of the vehicle FE models used in the reconstruction

FE Car Make and Model	Total number of parts	Total number of Elements	Width (mm)	Height (mm)	Wheel Base (mm)	Weight (kg)
2001 Ford Taurus	790	1,057,113	1,856	1,471	2,755	1,665
1998 Ford Explorer	755	619,161	1,841	1,765	2,855	2,240

The response variables were the AMPS and instantaneous peak pressure in the aorta. For maximum principal strain, four adjacent elements in the region with the highest inner surface maximum principal strain were selected and averaged; while for pressure, the maximum value obtained during the entire simulation was reported.

8.3.2 Sensitivity study details

Data from Chapter 7 showed that a PDOF of 270 degrees generated the highest AMPS and pressure in the aorta. Further, AMPS and pressure generated in the aorta decreased as the PDOF increased (from 260 degrees). Further, a combination of PDOF and occupant seating position was a significant factor for both AMPS and maximum pressure in the aorta. It was interesting to note that occupants who survived the crash (from CIREN data) were mostly females and averaged at 160 ± 5 centimeters in height. Schneider et al. (1994) concluded in their review that occupant-seating position might play a role in overall injury thresholds. In order to understand the mechanism of strain generation in the aorta and to compare the kinematics (qualitative) with published data, a paired sensitivity comparison was performed by varying the PDOF and occupant seating position while the other factors remained constant. Highest AMPS was generated in conditions when an occupant was seated in front of the B-pillar (0 mm) or at a delta-v of 54.9 km/hr or when the striking vehicle has a low bumper profile (sedan) or an impact positioned at the B-pillar (0 mm).

Table 8.4: Paired sensitivity table to access the mechanism of injury based on PDOF

Run #	PDOF (Degrees)	Occupant Position (mm)	Impact Position (mm)	Delta-v (km/hr)	Bumper Profile Height
a	260	-125	0	54.9	Low / Sedan
b	270	-125	0	54.9	Low / Sedan
c	250	0	0	54.9	Low / Sedan
d	270	0	0	54.9	Low / Sedan
e	310	125	0	54.9	Low / Sedan
f	270	125	0	54.9	Low / Sedan
g	310	0	0	54.9	Low / Sedan
h	260	0	0	54.9	Low / Sedan

As shown in Table 8.4, runs a and b aimed at depicting the difference between 260 and 270 degrees PDOF when the occupant is seated 125 mm behind the B-pillar; runs c and d aimed at comparing a PDOF of 250 and 270 degrees with the occupant seated in front of the B-pillar; runs e and f aimed at comparing a PDOF of 310 and 270 degrees with the occupant seated 125 mm ahead of the B-pillar and runs g and h aimed at comparing a PDOF of 310 and 260 degrees with the occupant seated in front of the B-pillar. Impact position was centered at the B-pillar (0 mm), delta-v was 54.9 km/hr and a low bumper profile height was selected for all of the runs.

8.4 Results

Three nearside-left lateral CIREN reconstructions and eight sensitivity runs and were carried out using a combination of FE vehicle models and WSHBM. Table 8.5 lists and compares the deformation profiles for C1-C6 points measured in the CIREN case history versus FE simulated results. Table 8.6 lists the human model predicted AMPS

in the isthmus region and the maximum pressure in the aorta for the three new CIREN and the eight CIREN cases (Cases #4, #5, #6, #7, #8, #15, #16, and #17) previously simulated (Chapter 6).

Table 8.5: Comparison of actual deformations obtained from CIREN versus the deformations predicted by the FE reconstruction – Stage I

Deformation in Centimeters	Case T1		Case T2		Case T3	
	Actual	FE	Actual	FE	Actual	FE
C1	0	8	56	60	0	2
C2	10	15	74	80	17	20
C3	33	36	55	57	35	36
C4	46	44	51	48	30	32
C5	39	36	31	28	27	30
C6	0	2	0	5	0	2
Average Variation	6.1%		5.8%		5.3%	

Table 8.6: Output details for the FE reconstructions – Stage II

CIREN Case No.	PDOF (Deg.)	Delta 'V' (km/hr)	Occupant Status	Left Side Door Structure Impact Time with Occupant (ms)	Average Maximum Principal Strain at the Isthmus (AMPS)*	Time at AMPS (ms)	Maximum Pressure (kPa)	Time at Maximum Pressure (ms)
T1	255	33.6	Survived	46	0.0981	62	74.2	60
T2	285	29.1	Survived	38	0.0812	58	67.9	58
T3	300	22.0	Survived	50	0.1233	66	59.8	64
Average					0.100±0.021		67.31±7.21	
4	310	62	Survived	14	0.1452	56	114.8	48
5	310	27.5	Fatal	34	0.1658	54	108.7	60
6	280	55	Fatal	16	0.2767	30	134.0	30
7	280	59	Fatal	22	0.2823	40	132.2	36
8	320	27.6	Fatal	30	0.1851	50	104.6	50
15	270	47	Fatal	26	0.1921	42	102.0	47
16	270	54.4	Fatal	22	0.2955	36	136.0	35
17	260	41	Survived	33	0.1941	42	103.8	52
Average (Case #4 through Case #17)					0.217±0.059		117.01±14.67	
Overall Average					0.1854±0.074		103.45±26.47	

*AMPS: Average maximum principal strain at the level of the isthmus calculated from four elements in the isthmus region

From Table 8.6, for the three new CIREN reconstructions the average AMPS was 0.100 ± 0.021 and the average maximum pressure was 67.31 ± 7.21 kPa. Separating the survival versus fatal cases, for the survival cases (Cases #T1, #T2, #T3, #4, and #17), the average AMPS were 0.1238 ± 0.044 , and the average maximum pressure was 84.10 ± 23.88 kPa. For the CIREN cases with fatality due to aortic rupture (Cases #5, #6, #7, #8, #15, and #16); the average AMPS were 0.2329 ± 0.057 and the average maximum pressure was 119.58 ± 16.05 kPa.

Table 8.7 lists the AMPS and maximum pressure for the eight sensitivity runs along with paired comparisons.

Table 8.7: Paired sensitivity table to access the mechanism of injury based on PDOF

Run #	Maximum Simulation Time (ms)	AMPS	Time at AMPS (ms)	Maximum Pressure (kPa)	Time at Maximum Pressure (ms)
a	42	0.162	42	127.1	40
b	49	0.281	40	126.3	40
c	44	0.258	43	117.7	42
d	52	0.324	40	135.1	36
e	80	0.054	74	108.5	72
f	70	0.152	54	110.8	54
g	78	0.067	78	104.4	70
h	100	0.204	54	115.2	54

8.5 Discussion

For the three CIREN survival cases (T1, T2, and T3) reconstructed, the AMPS ranged from 8.12% to 12.33% and the maximum pressure ranged from 67.9 to 74.2 kPa. For the 11 CIREN cases, the overall average AMPS was 0.1854 ± 0.074 and the overall average maximum pressure was 103.45 ± 26.47 kPa. It is interesting to note that for the two victims who sustained an aortic injury but survived the crashes (Cases 4 and 17), the average AMPS was 17% and the average maximum pressure was 109 kPa. On the other hand, for the three CIREN cases (T1, T2, and T3) where the occupant survived, with no aortic injury reported, the average AMPS was 10% and the average maximum pressure was 67.31 kPa.

It is interesting to note that in Cases T1 through T3, the AMPS and pressure were significantly lower than the first eight CIREN cases reconstructed. Further, the average delta-v for Case #T1, #T2, and #T3 was 28.23 ± 5.84 km/hr while for the original CIREN cases it was 46.68 ± 13.52 km/hr which might have played a crucial role in the

reduced AMPS. It was also seen from FE simulations and crash photographs, than when the PDOF was 255 degrees (Case #T1), **the seat deformed significantly thereby preventing direct thoracic contact from the intruding B-pillar and side-door structures.**

A logistic regression was performed on AMPS (Figure 8.1) and maximum pressure (Figure 8.2) for the eight CIREN cases reconstructed in Chapter 6 along with the three new survival CIREN cases. A 50% risk of aortic failure was 17.1% strain based on AMPS and 102 kPa based on maximum pressure in the aorta. Alternatively, a 90% risk of failure for AMPS was 21.2% strain and 125 kPa for maximum pressure in the aorta. A Chi-Square Goodness-of-Fit Test revealed insignificant Pearson's coefficient (6.066 for AMPS ($p=0.733$) and 7.202 for maximum pressure ($p=0.616$)).

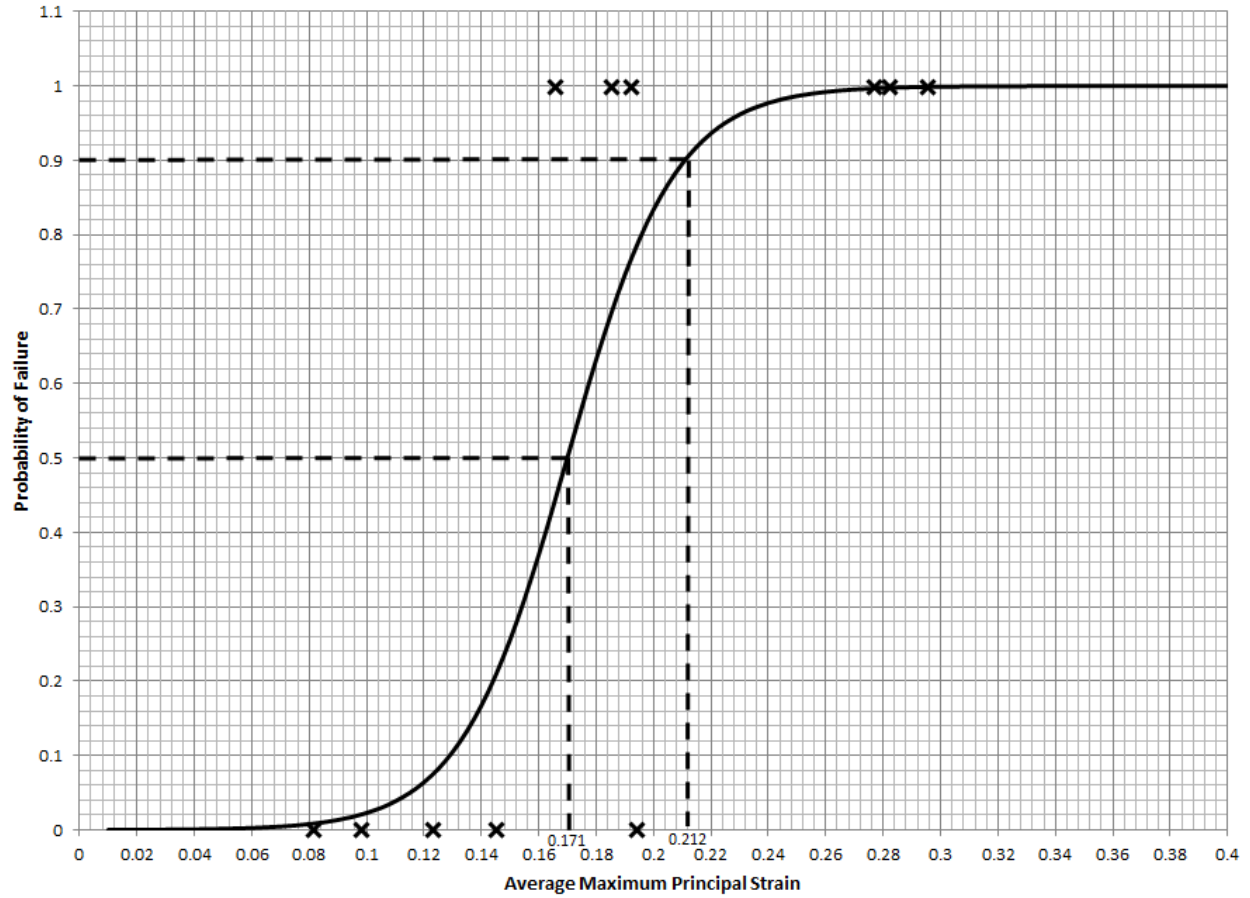


Figure 8.1: Logistic Regression plot with 50th and 90th percent probability of failure for AMPS

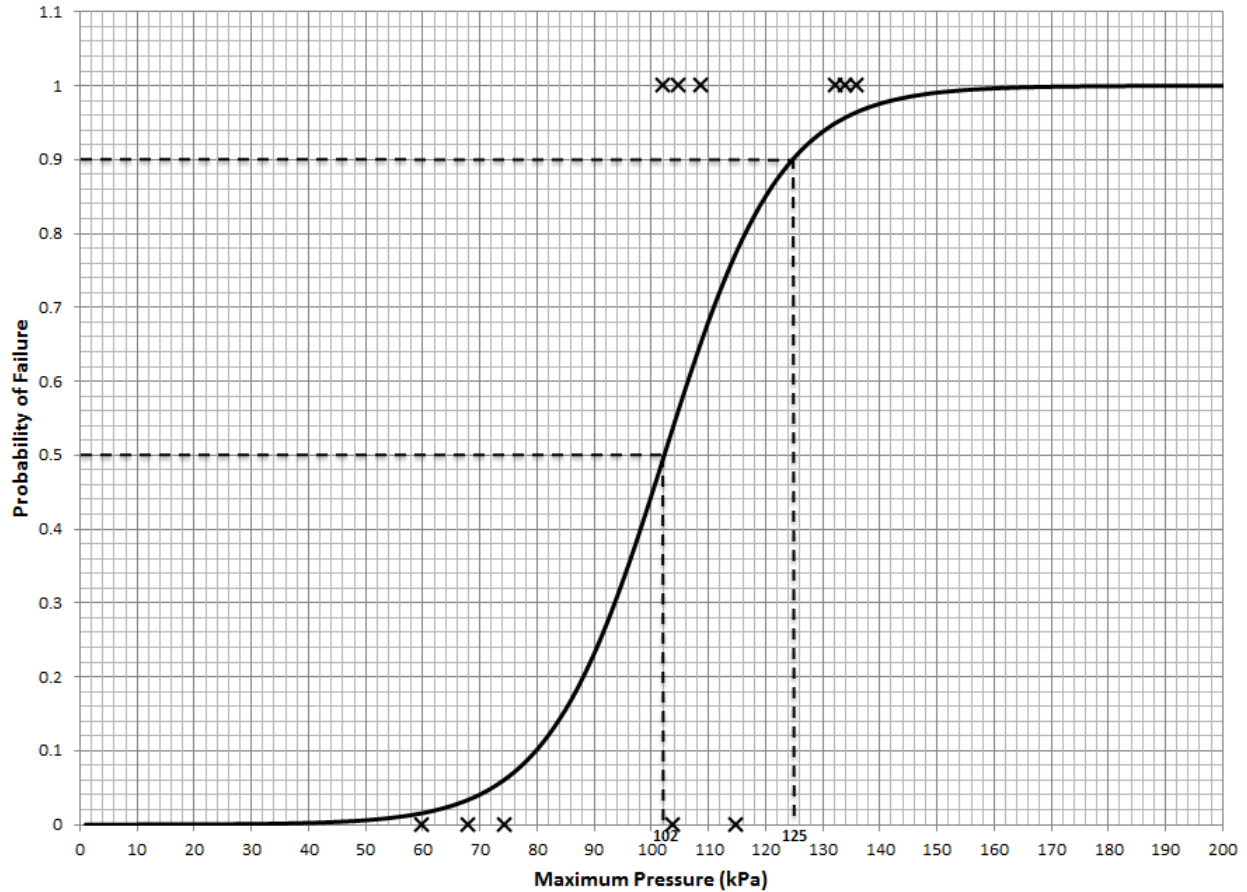


Figure 8.2: Logistic Regression plot with 50th and 90th percent probability of failure for maximum pressure

Bass et al. (2001) reported a 50% risk of tear to the aorta at 120 kPa for occupants 68 years of age based on aortic pressurization tests on 13 cadaveric aortas (10 *in vitro*, 3 *in situ*). Hardy et al. (2008) tested eight unembalmed pressurized cadavers in an inverted configuration and subjected them to a battery of pendulum (32-kg impactor with a 152 mm face) impact tests. The average intraluminal pressure in the aorta ranged from 33.5 to 165.0 kPa with an average of 67.5 kPa. These

experimentally obtained values are of the same order of magnitude with the current study in which a 50% and 90% risk of aortic rupture was 102 and 125 kPa, respectively.

Shah et al. (2006) concluded from *in vitro* biaxial tensile tests at 1 m/s on cruciate shaped specimens that the average longitudinal failure strain to be 23.2% in the ascending region, 27.3% in the descending region and 25.1% in the peri-isthmic region, with an overall average failure strain of 24.4%. In a second series, longitudinal stretch tests conducted by Shah et al. (2007) on whole aortas until failure (1 m/s); an average failure strain of 22.1% was reported. It should be noted that the strain data published in both series of tests were based on isolated aortic specimens and few specimens failed around the region of atherosclerotic plaque deposition. Hardy et al. (2008) in their tests of eight unembalmed cadavers reported an average aortic failure strain of 0.208 ± 0.216 . It is also important to note the large standard deviation reported in the study, owing to biomechanical variability. In the current study, 21.2% AMPS represents a 90% risk of aortic rupture, which falls within the range of values reported. Based on statistical probability, the number of non-failure cases (n=5) might be insufficient for statistical significance. For the three CIREN cases (T1, T2, and T3) without any reported aortic injury, the average AMPS was 0.100 ± 0.021 which was significantly lower than the thresholds for failure defined by Shah et al. (2006) and Hardy et al. (2008). Further, the average maximum pressure of 67.3 ± 7.2 kPa was lower than those reported by Bass et al. (2001) and Hardy et al. (2008) as well. It is interesting to note that the AMPS and maximum pressure recorded for Case #T1 through Case #T3 was lower than those reported for the two victims who sustained an aortic injury but survived the crashes (Cases #4 and #17), the average AMPS and maximum pressure being 17% and 109

kPa respectively. For CIREN cases with no fatality the average AMPS was 0.1238 ± 0.044 and the average maximum pressure was 84.10 ± 23.88 kPa while for the CIREN cases with fatality due to aortic rupture, the average AMPS was 0.2329 ± 0.057 and the average maximum pressure was 119.58 ± 16.05 kPa.

8.5.1 Comparison of kinematics data

Summarizing the hypothesis listed in Table 8.1, it is observed that the premise for TRA generation is based on thoracic deformation (Melvin et al. 1998) combined with longitudinal stretch of the thoracic aorta (Hardy et al. 2008).

In order to compare the kinematics of the aortic arch with the published literature, Figures 8.3 through 8.6 tracks the motion of 18 nodes on the sternum, heart, aortic root, ascending, arch, isthmus and descending aorta along with the thoracic vertebrae for the entire duration of the simulation. To ensure consistency, the exact same nodes were tracked in all the runs. Appendix D, Figures D1 through D4 plots the X, Y, and Z displacement of the sternum (measured mid-sternum) and the spine (measured at the level of the fourth vertebral body).

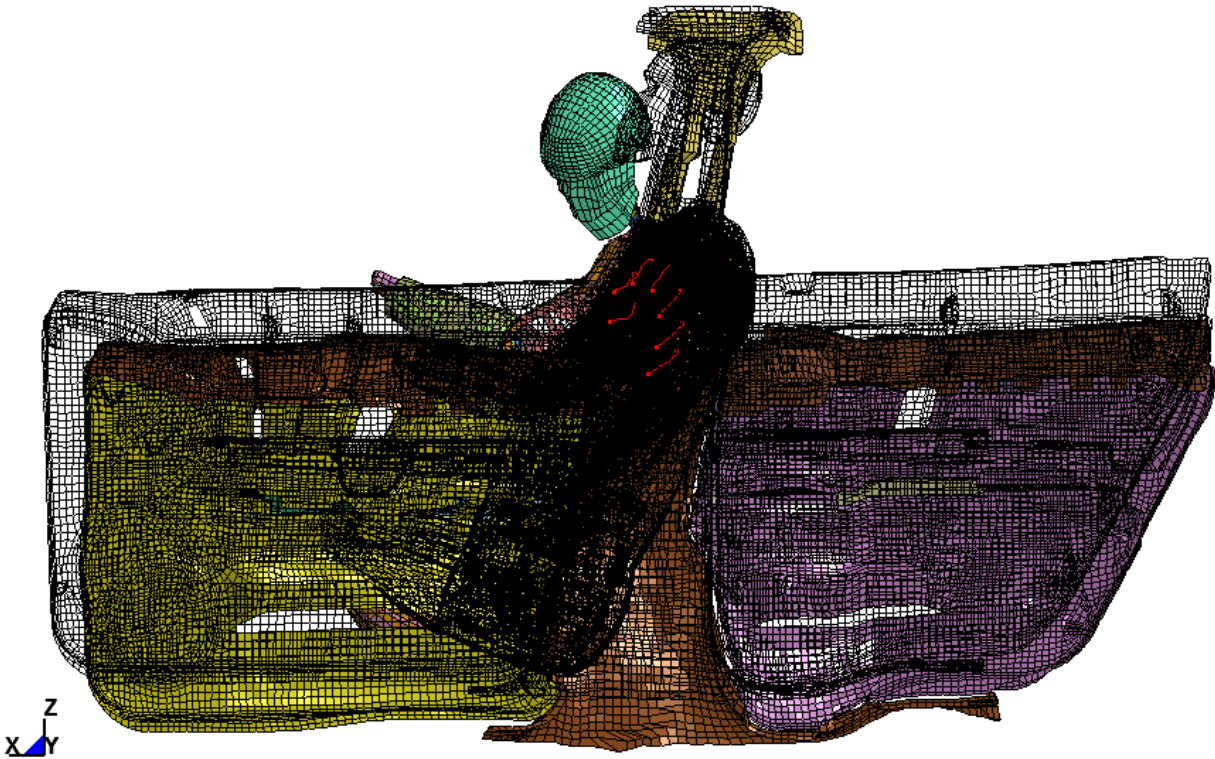
Table 8.8 tabulates the X, Y, and Z displacements of the sternum, tracked for Runs #a through #h. 'X' describes the anterior motion; 'Y' describes the lateral motion and 'Z' describes the superior motion of the sternum and T4 vertebral body.

Table 8.8: X, Y, and Z displacements of the sternum and spine

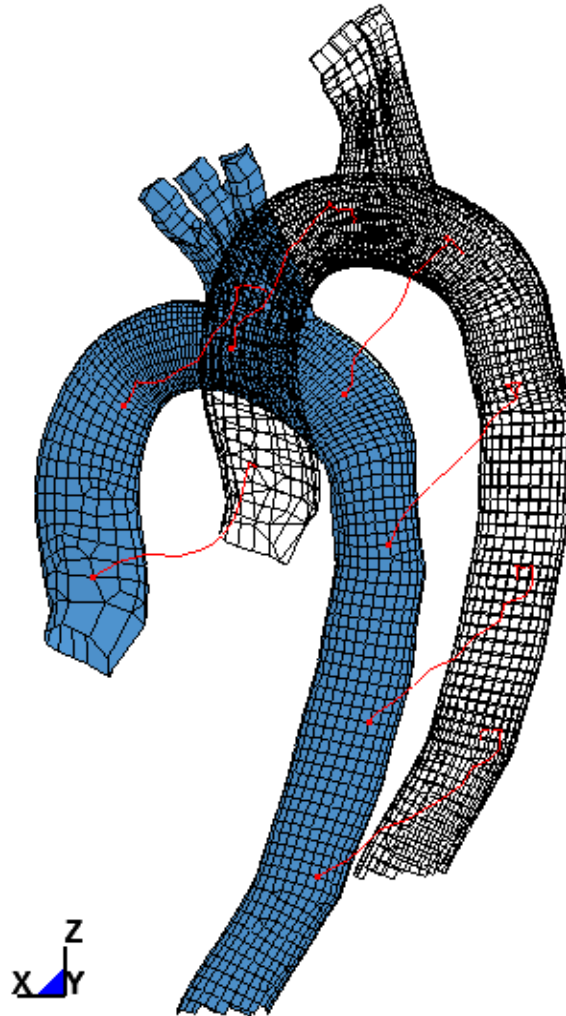
Run #	PDOF	AMPS	Mid-sternum displacement (mm)			T4 vertebral body displacement (mm)		
			X (Anterior)	Y (Lateral) +ve = left side	Z (Superior)	X (Anterior)	Y (Lateral) +ve = left side	Z (Superior)
a	260	0.162	1.5	-9.44	3.4	-3.19	-14.99	-1.30
b	270	0.281	8.2	-90.4	-62.1	-4.28	-126.50	-59.32
c	250	0.258	39.2	-88.2	-5.25	13.10	-90.78	1.37
d	270	0.324	62.4	-254.89	-20.1	37.09	-278.42	-19.41
e	310	0.054	-20.7	-64.1	-13.1	42.10	-155.47	-5.46
f	270	0.152	47.4	-154.2	-11.6	-12.69	-46.42	-15.08
g	310	0.067	-2.9	-21.2	1.9	14.93	-450.73	-16.89
h	260	0.204	21.2	-438.3	-20.3	-1.93	-6.07	1.82
Absolute average (mm)			25.41±22.22	140.13±143.64	17.22±19.57	16.16±15.33	146.17±151.45	15.08±19.36

Melvin et al. (1998) proposed the "Sternal Popping" mechanism as a hypothesis to TRA. From Table 8.8 it is observed that the average sternum displacement in the anterior direction is 25.4±22.2 mm, 140.1±143.6 mm in the medial direction and 17.2±19.5 mm in the superior direction for nearside left lateral impacts. It was seen that as the PDOF increased (from 250 degrees), isthmus strain due to longitudinal stretch of the thoracic aorta transitioned from caudomedial motion of the thoracic spine relative to the sternum (owing to thoracic deformation from the B-pillar) to posterior-anterior motion of the thoracic aorta relative to the ascending aorta (310 degree impact). Kinematics data from the simulations showed that the isthmus of the aorta moved medially and anteriorly during nearside left lateral impacts and transitioned to a dorsocranial motion. From Figures 8.3 through 8.6 it is seen that thoracic deformation pattern may play a significant role than mere sternum motion.

In order to compare the kinematics of simulation with cadaveric motion data published (Hardy et al. 2008); where the motions of the aorta were tracked using high-speed biplanar radiographic method using perfused inverted cadavers, impacts similar to the condition used in Hardy et al. (2008) were chosen for comparison. Figures 8.7 and 8.10 show the initial (Dark mesh) and deformed final position (Shaded colored mesh) for nearside left lateral impacts at a PDOF of 270 degrees, in Sagittal and Coronal sections respectively.



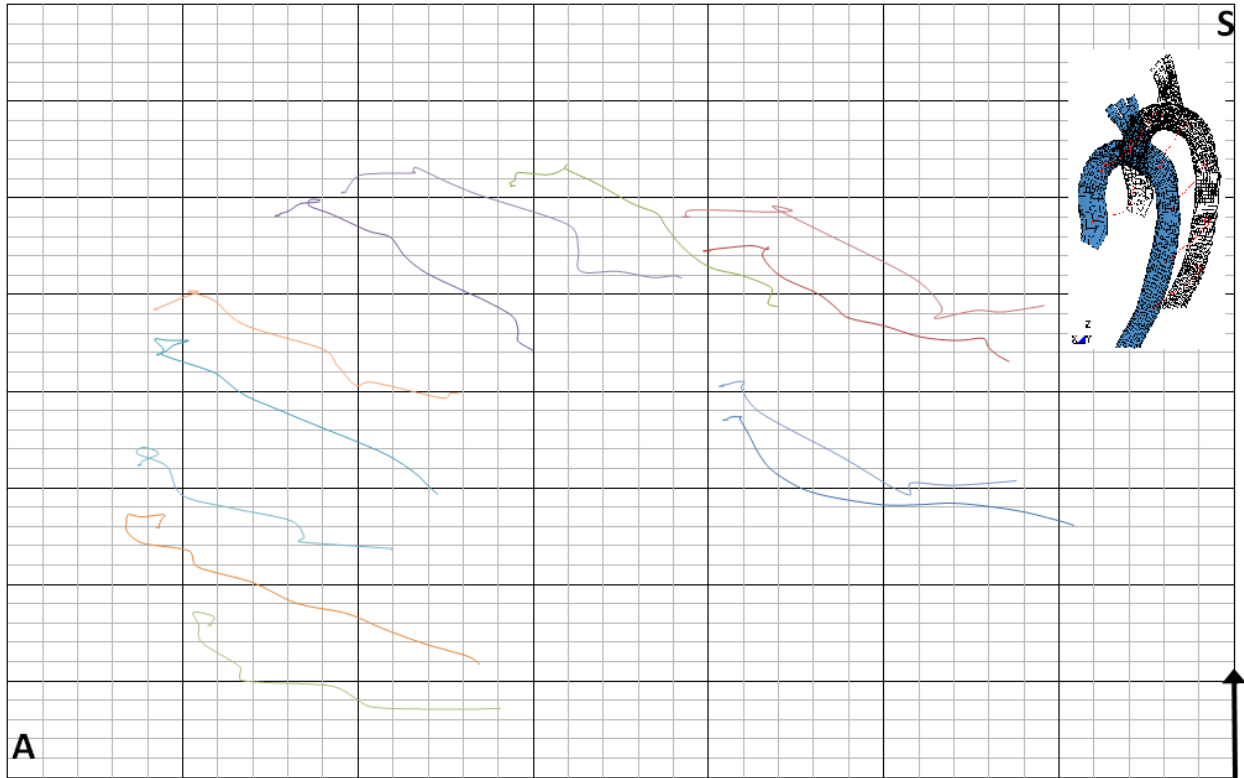
(a)



(b)

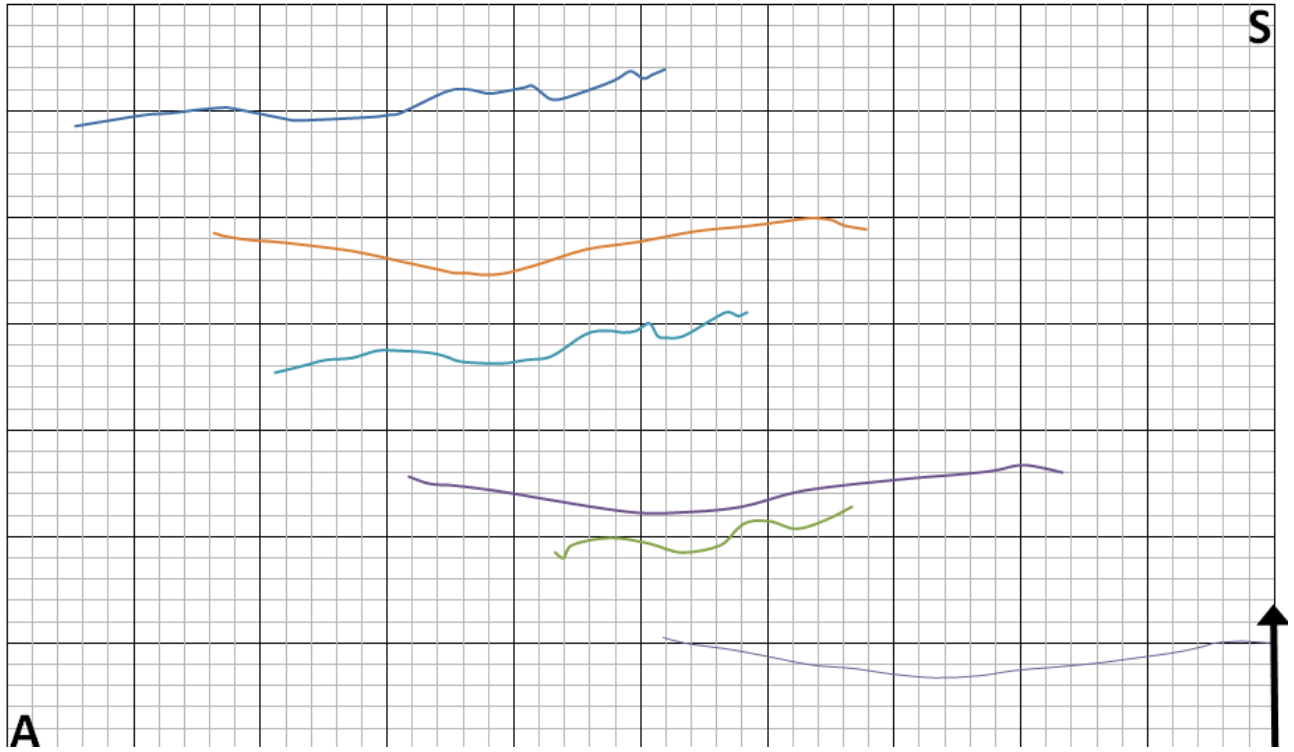
Note: Dark mesh – Initial position: Shaded color mesh – Deformed final position

8.7: Sagittal View (a) WSHBM with the door structures (b) Isolated aorta highlighted with the nodes being tracked (red)



8.8: Motion of the aorta tracked, sagittal view – arrow indicates direction of impact

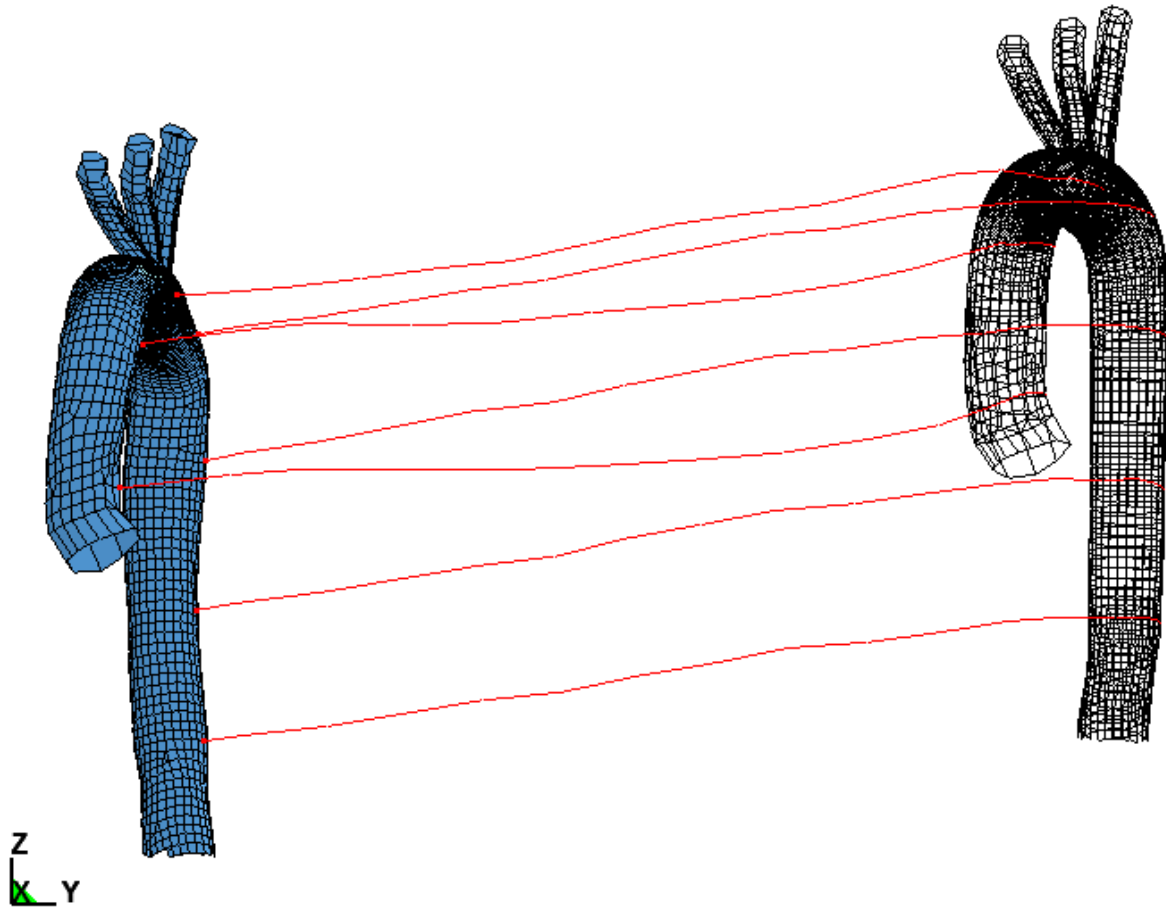
Figures 8.8 and 8.11 plot the motion of the aorta in the sagittal and coronal views respectively while comparing it with data published by Hardy et al. (2008), as in Figures 8.9 and 8.12. The arrow indicates the direction of impact with respect with Anterior (A) and Superior (S) view of WSHBM.



8.9: Hardy et al. (2008) Motion of the aorta tracked, sagittal view – arrow indicates direction of impact



(a)

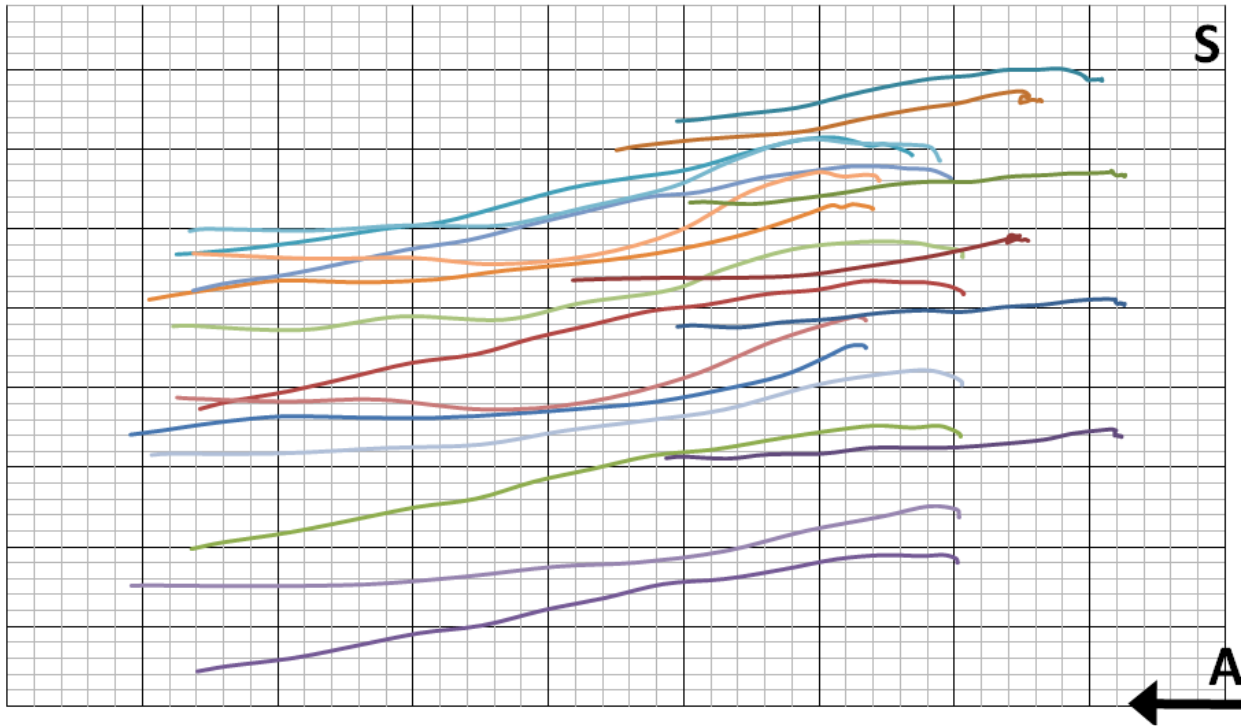


(a)

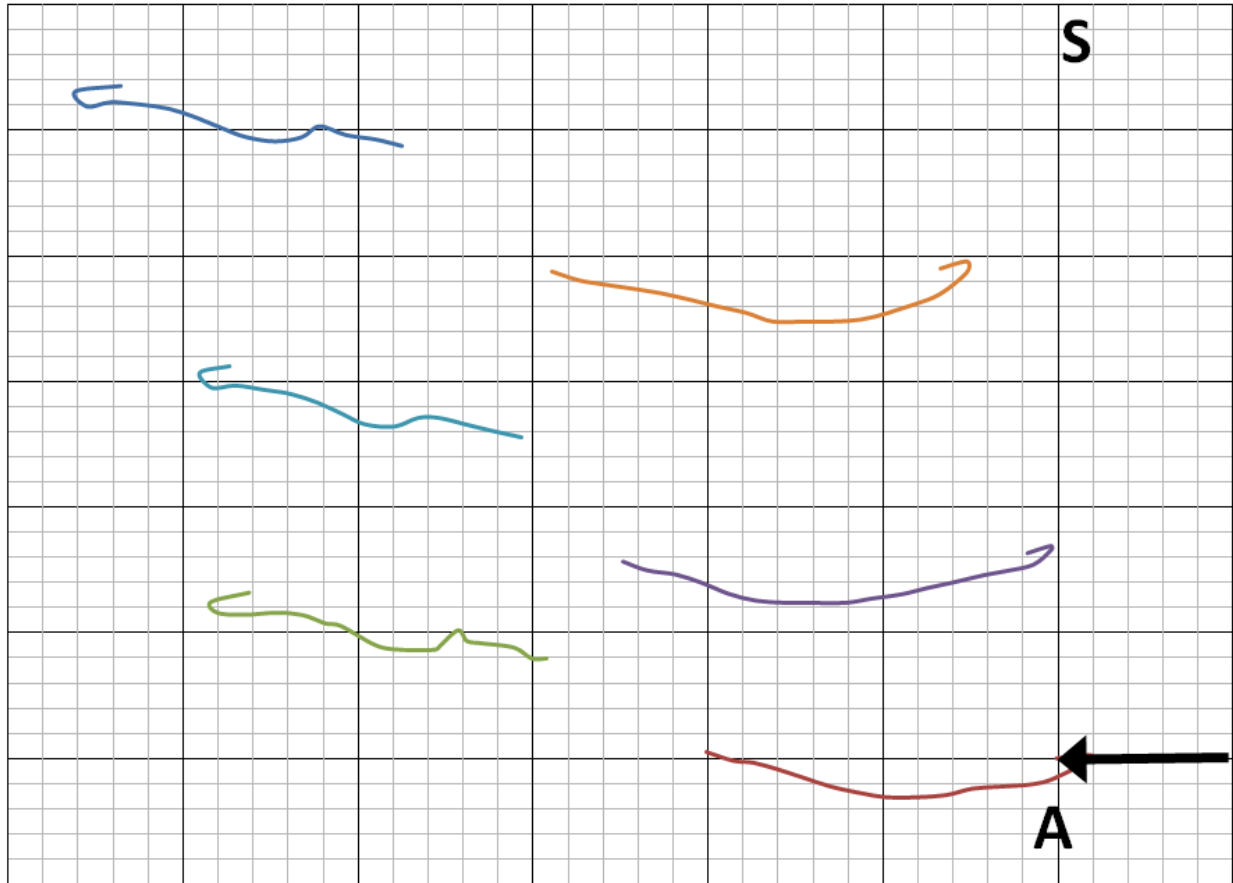
(b)

Note: Dark mesh – Initial position: Color shaded mesh – Deformed position

8.10: Coronal view of (a) WSHBM contacts with the door structures (b) Isolated aorta highlighted with the nodes being tracked (red)



8.11: Motion of the aorta tracked, coronal view – arrow indicates direction of impact



8.12: Hardy et al. (2008) Motion of the aorta tracked, coronal view – arrow indicates direction of impact

Sagittal view (Figures 8.8 and 8.9) demonstrates the anterior motion of the aorta, with slight cranial motion (in comparison with Hardy et al. (2008)) while the coronal section (Figures 8.11 and 8.12) indicates the lateral displacement of the aorta along the line of impact, moving away from the point of impact. The primary motion of the aorta, was lateral (medial deflection of the thoracic structures) and anterior which matched well with the kinematics from Hardy et al. (2008).

Further, four nearside left lateral cases were simulated by varying only the PDOF from 250 degrees to 310 degrees in steps of 20 degrees; to compare the relative motion between the spine (at the level of T4) and sternum(mid). Figures 8.13 through 8.16, each shows the contours of resultant displacement of the thoracic cage during 250, 270, 290, and 310 degrees of impact.

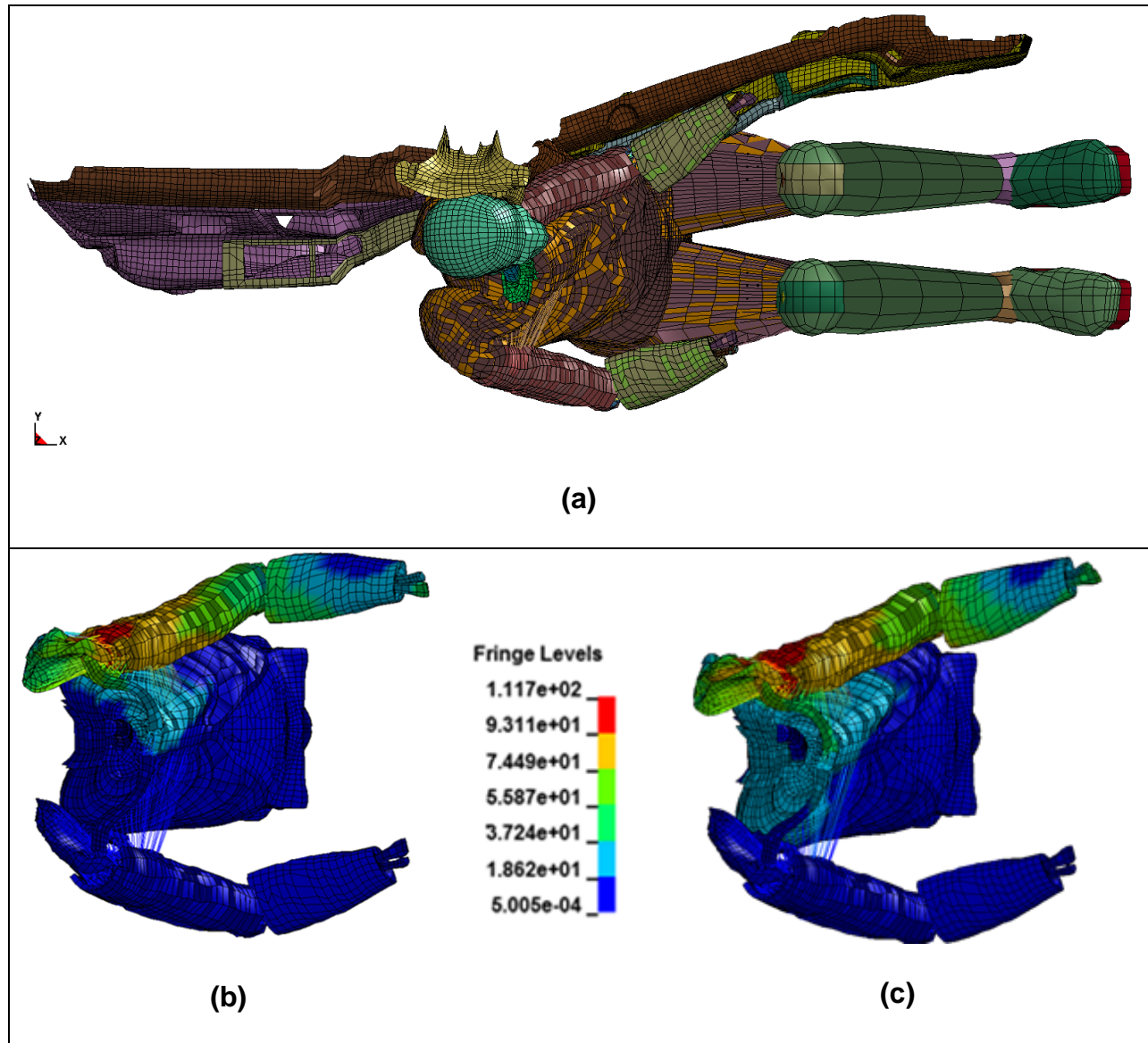


Figure 8.13: Run #10: (a) PDOF = 250 degrees :
Contours of resultant displacement (mm) – (b) 35 ms (c) 38 ms

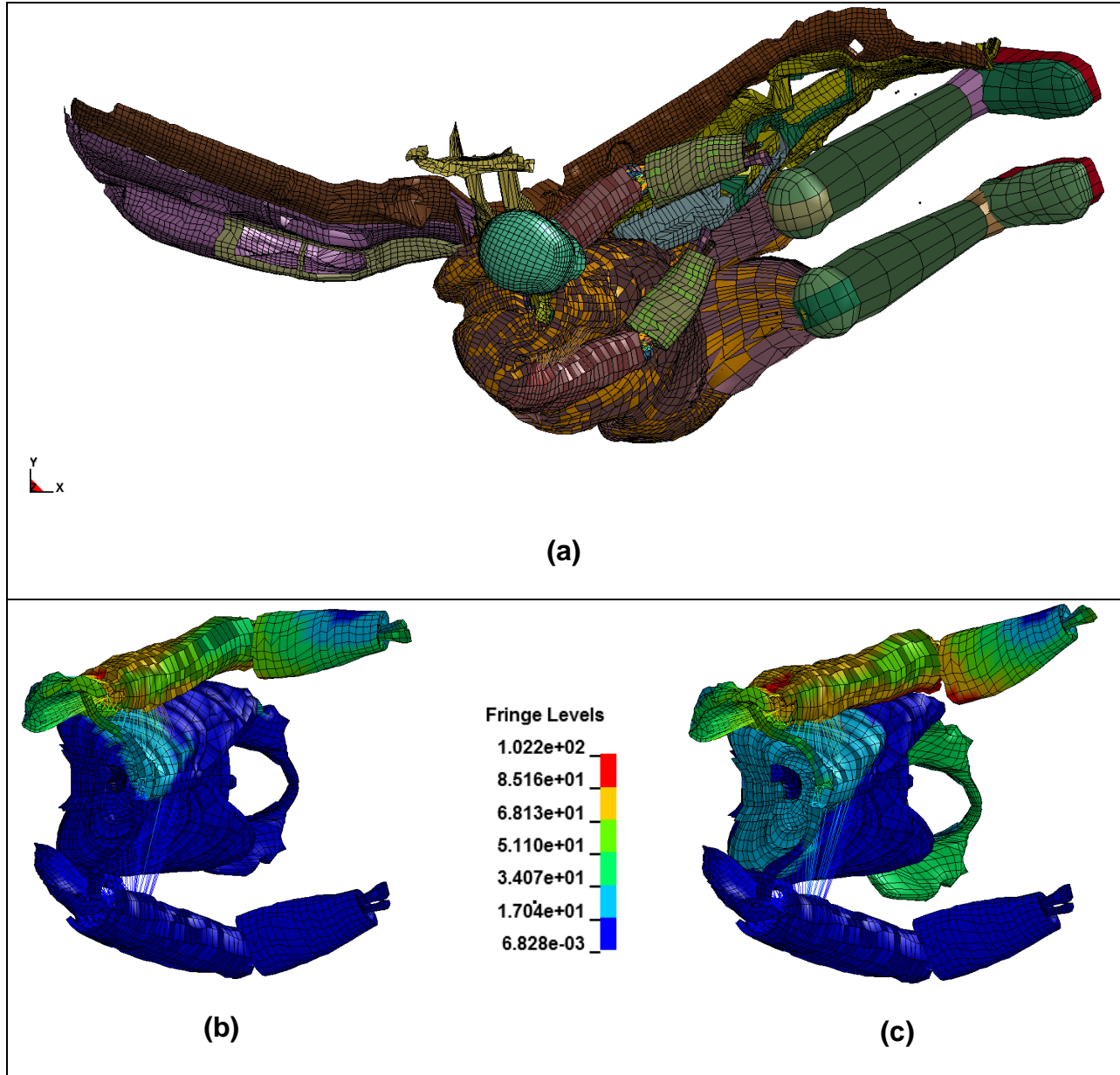


Figure 8.14: Run #5: (a) PDOF = 270 degrees :
Contours of resultant displacement (mm) – (b) 30 ms (c) 34 ms

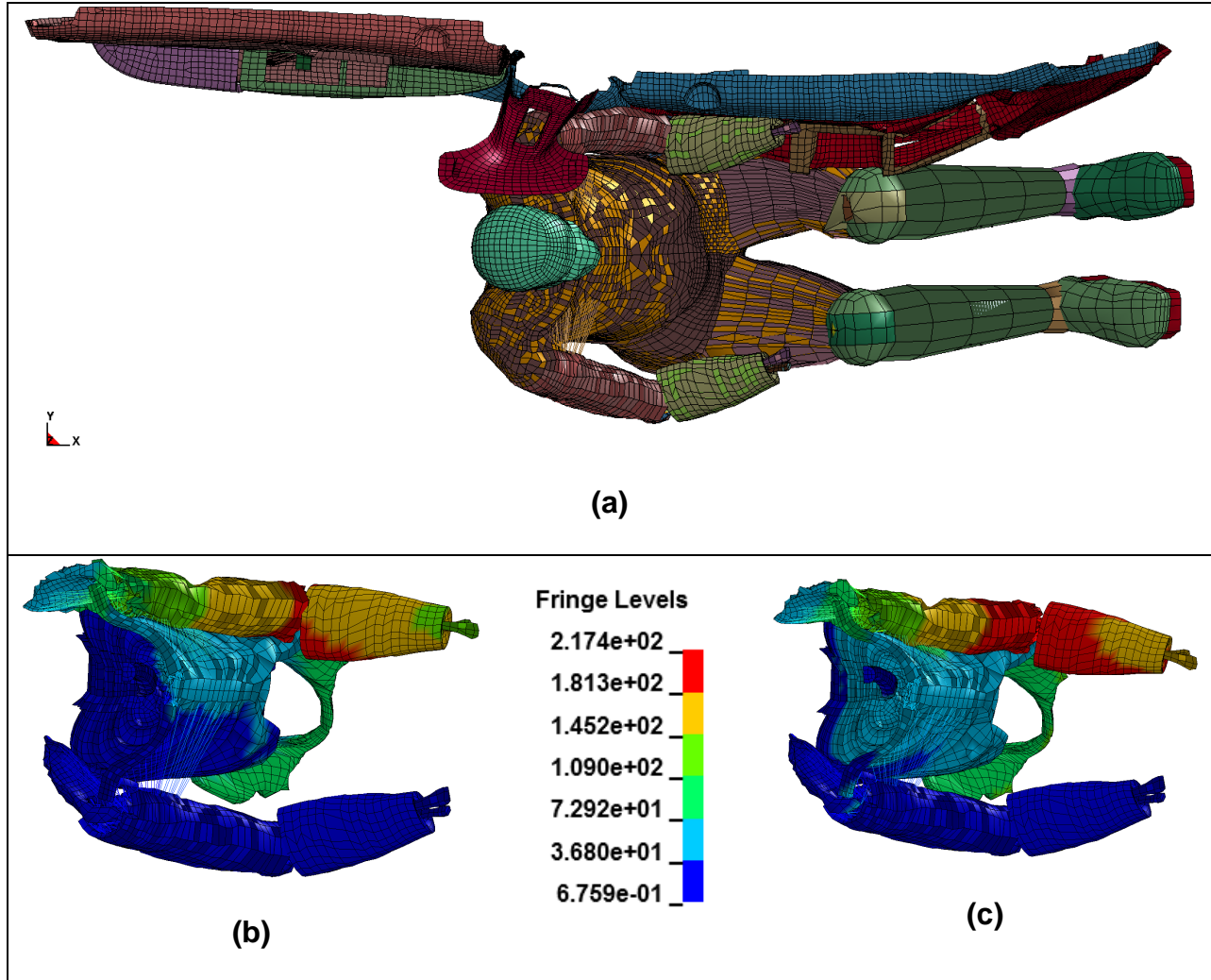
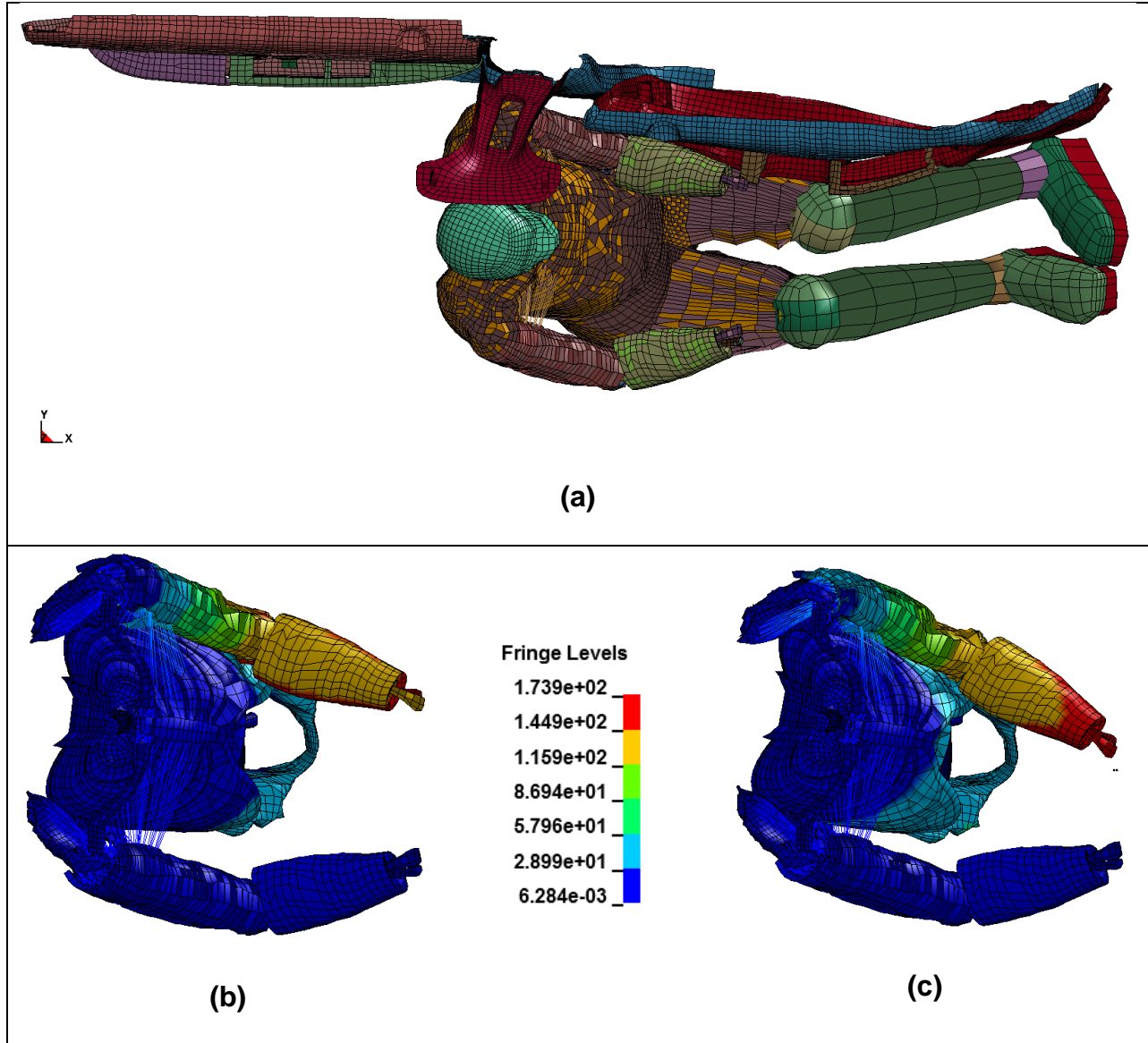


Figure 8.15: Run #11: (a) PDOF = 290 degrees :
Contours of resultant displacement (mm) – (b) 52 ms (c) 58 ms



**Figure 8.16: Run #7: (a) PDOF = 310 degrees :
Contours of resultant displacement (mm) – (b) 70 ms (c) 78 ms**

From Figures 8.13 through 8.16 it is evident that as the PDOF increases from 250 degrees, the relative displacement of the sternum and spine increases. For the purpose of comparison, Figure 8.17 and Figure 8.18 compare the average y-displacement of the two resultant PDOF's (260 and 300 degrees).

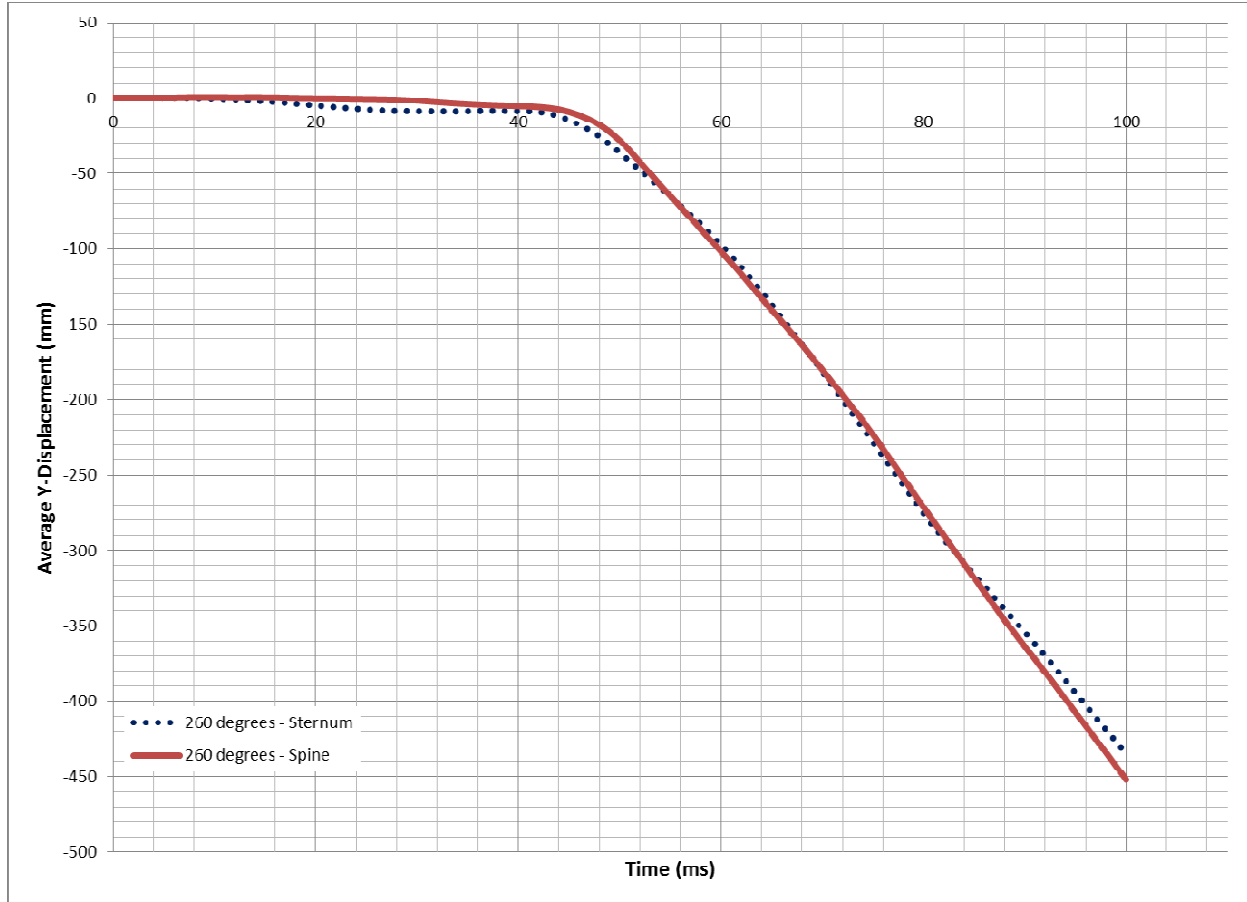


Figure 8.17: Average Y-Displacement (mm) of the sternum and spine for a PDOF of 260 degrees

From Figures 8.17 and 8.18 it is seen that as the average PDOF increases from 260 degrees to 300 degrees, the average relative displacement between the sternum and the spine increases. This is attributed to the fact that in impacts of PDOF from 250 to 270 degrees that B-pillar and the side structures engages the entire thoracic cage while in PDOF greater than 270 degrees (up to 310 degrees, in this study) the side door structures engages the sternum first and then the spine. It is also interesting to note the durations for each case; 450 mm of displacement at 100 ms for a PDOF of 260 degrees while for a PDOF of 310 degrees the displacements are in opposite directions.

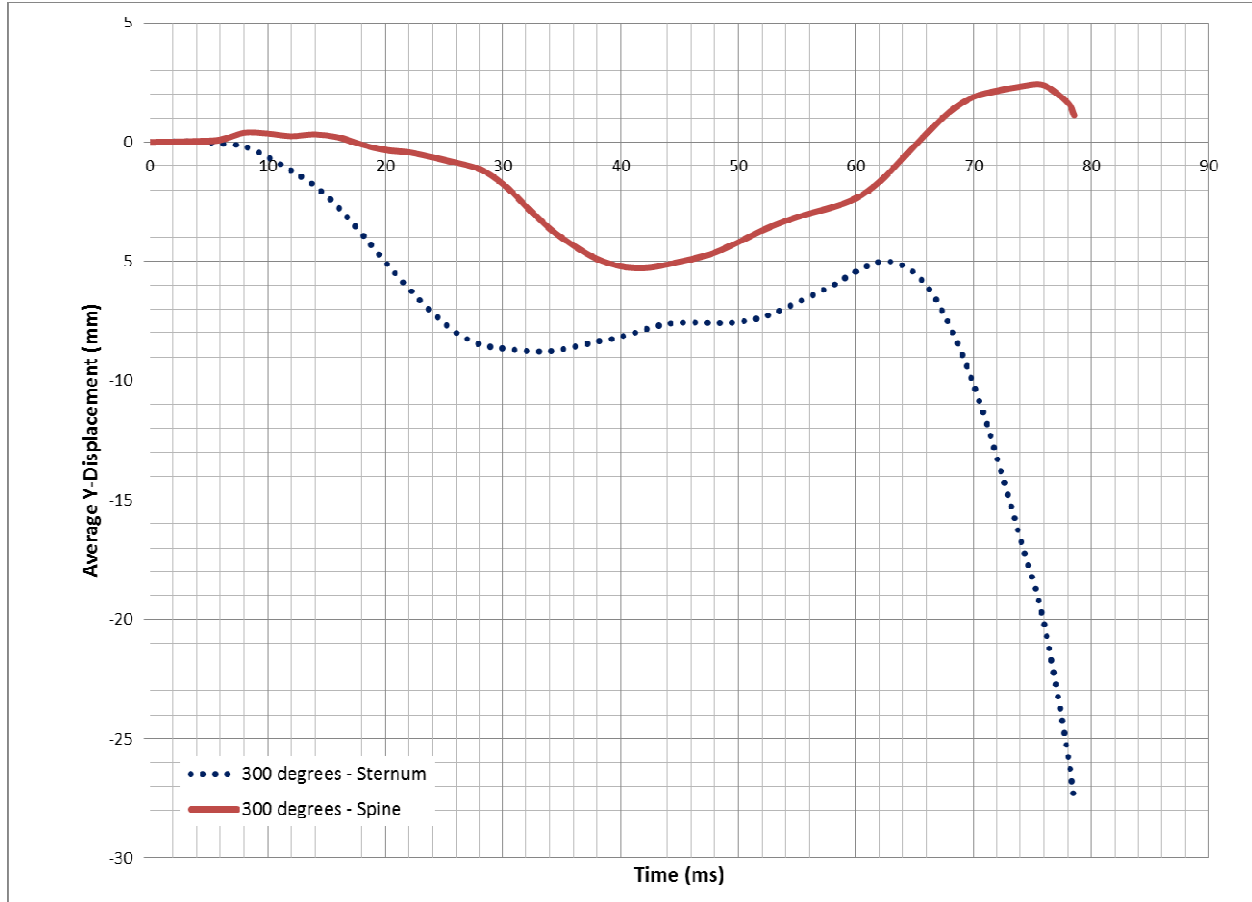


Figure 8.18: Average Y-Displacement (mm) of the sternum and spine for a PDOF of 300 degrees

Figure 8.19 compares the average relative y-displacement between the sternum and spine for an average PDOF of 260 and 300 degrees of impact. A positive shift indicates that the displacement of the spine is greater than that of the sternum.

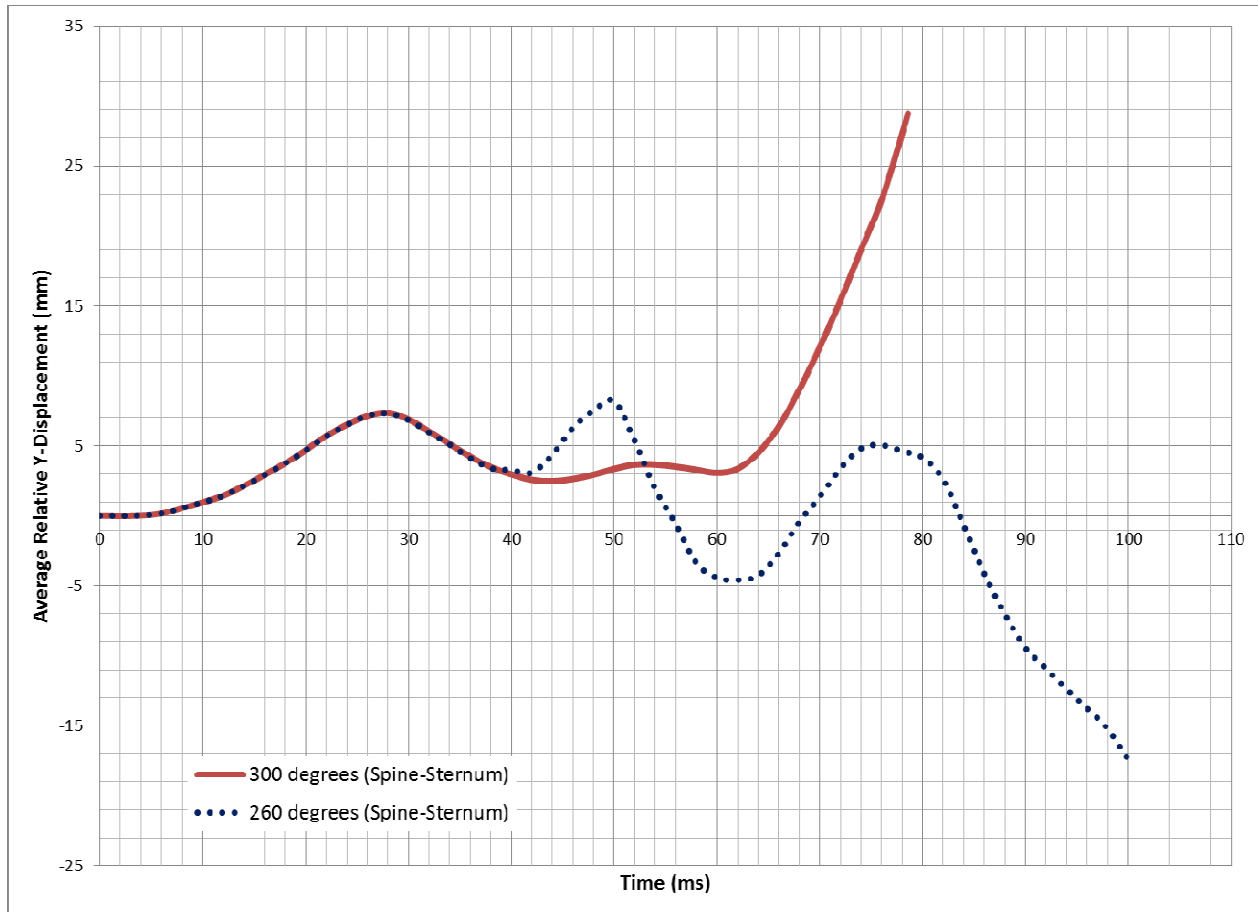


Figure 8.19: Average relative Y-Displacement (mm) of the sternum and spine

Figures 8.20 and 8.21 plots the mid-sternum, superior aspect of the heart, ascending aorta, isthmus of the aorta and T4 vertebral body motion averaged for 260 degrees and 300 degrees of impact respectively. It is seen that in both cases the aortic isthmus rides along with the T4 vertebral body (spinal complex) while the mid-sternum, superior aspect of the heart and ascending aorta pair along (mediastinal complex). However, for a 300-degree impact, the relative displacement between the mediastinal and sternal complex is greater than a 260-degree impact. It is seen that in both cases (260 and 300 degree) that at an average of 62.1 ± 4.5 ms, the mediastinal complex and spinal complex catch up with each other. The highest AMPS were seen to occur at

maximum separation between the two complexes; 55.1 ± 5.6 ms for 260-degree impact and 72.6 ± 6.3 ms for a 300-degree impact.

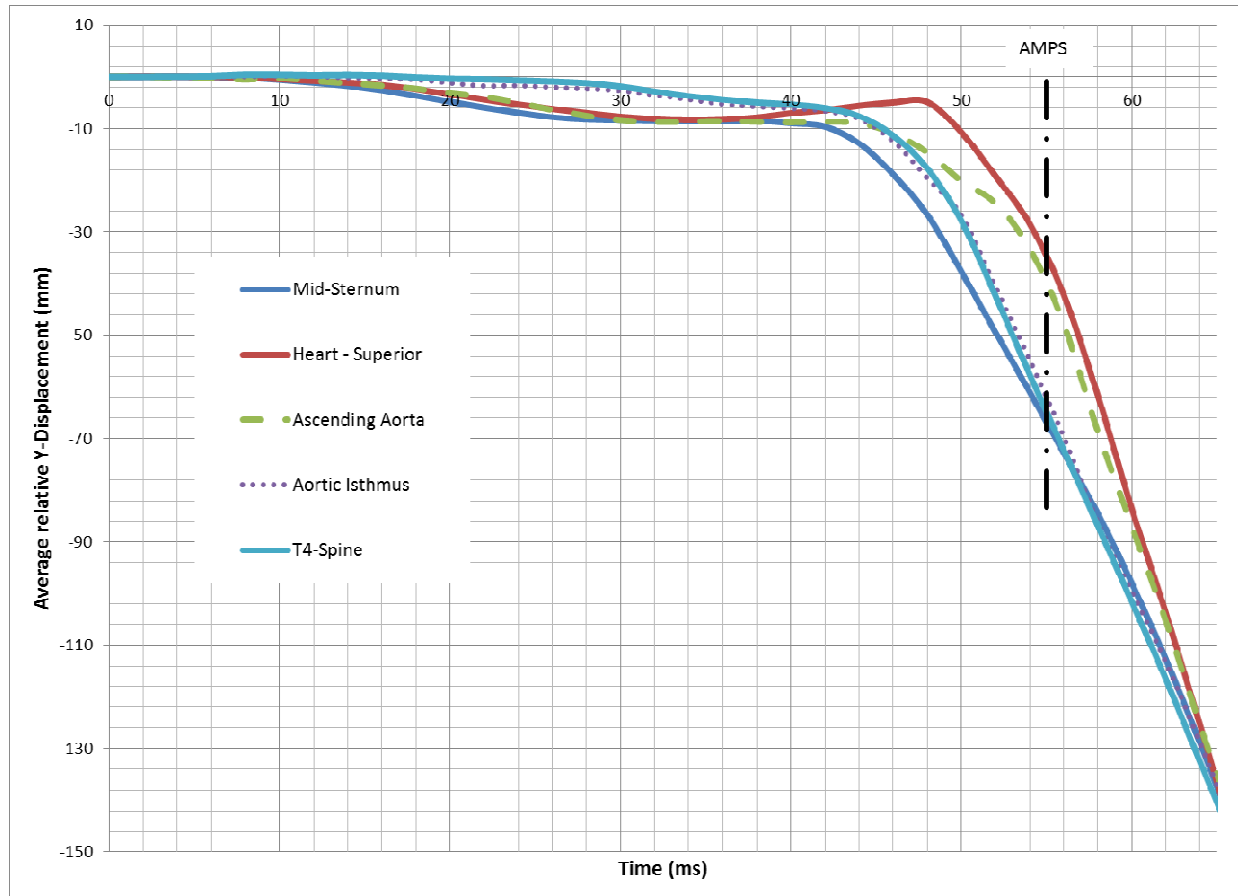


Figure 8.20: Average relative Y-Displacement (mm) - 260 degrees

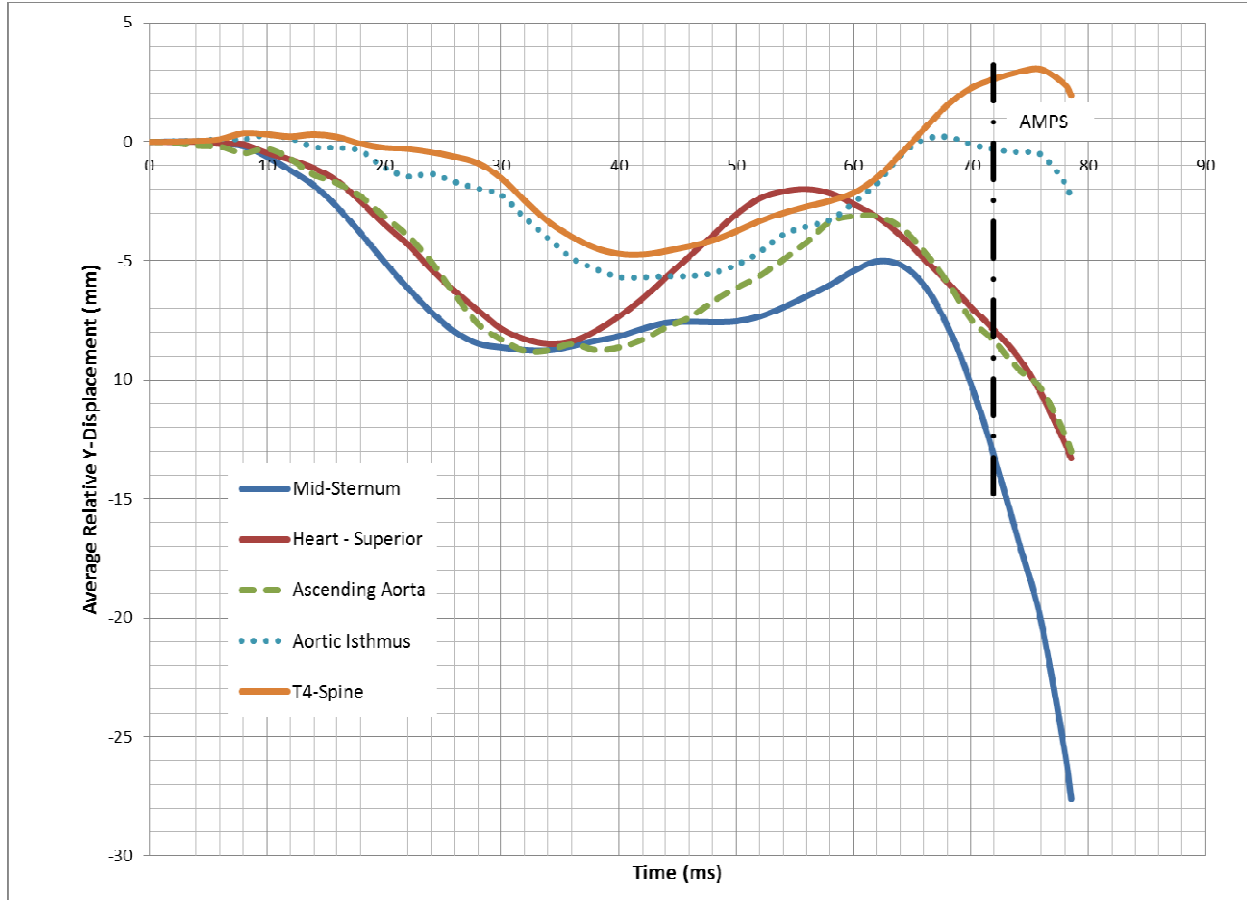


Figure 8.21: Average relative Y-Displacement (mm) - 300 degrees

8.6: AIM C: Conclusions

Three additional CIREN reconstructions (without any reported aortic injury) and eight runs for a sensitivity analysis was carried out using a combination of WSHBM and scaled FE vehicle models. Kinematics of the aorta and sternum displacements were tracked and compared with published data. In conclusion,

- For CIREN cases with no fatality the average AMPS was 0.1238 ± 0.044 and the average maximum pressure was 84.10 ± 23.88 kPa.

- For the CIREN cases with fatality due to aortic rupture, the average AMPS was 0.2329 ± 0.057 and the average maximum pressure was 119.58 ± 16.05 kPa.
- A 50 percent probability of failure for AMPS was 17.1% and a 90 percent probability of failure for AMPS was 21.2%.
- A 50 percent probability of failure for maximum pressure was 102 kPa and a 90 percent probability of failure for pressure was 125 kPa.
- Sternum displacement alone may not be sufficient to quantify the risk of TRA.
- Thoracic deformation pattern might play a role in TRA.
- PDOF of 270 degrees generates the highest AMPS and pressure in the aorta.
- Longitudinal stretch of the thoracic aorta is the primary cause of TRA.
- In nearside left lateral impacts, It was seen that as the PDOF increased (from 270 degrees), isthmic strain due to longitudinal stretch of the thoracic aorta transitioned from caudomedial motion of the thoracic spine relative to the sternum (owing to thoracic deformation from the B-pillar) to posterior-anterior motion of the thoracic aorta relative to the ascending aorta (310 degree impact).
- Kinematics data from the FE simulations matched well with experimental data reported by Hardy et al. (2008) and showed that the isthmus of the aorta moved medially and anteriorly during nearside left lateral impacts and transitioned to a dorsocranial motion.

CHAPTER 9

AIM D: KINEMATICS OF THE AORTA IN HIGH-SPEED RACING CRASHES

9.1 Introduction

Auto racing has been in vogue from the time automobiles were first built. Since the world's first race in 1894 from Paris to Rouen, auto racing has been plagued with injuries and fatalities (Paolozzi, 2003). With the dawn of modern cars came higher engine capacities; the speeds involved in these races and crashes increased as well. However, the advent of passive restraint systems such as the helmet, HANS (Head and Neck Support device), multi-point harness system, roll cage, side and frontal crush zones, racing seats, fire retardant suits, and soft-wall technology, have greatly improved the survivability of the drivers in high-speed crashes. In a majority of these high-speed crashes, the driver walks out with minor or no injuries (Melvin et al. 1998). Melvin et al. (1998) noted that it was like a laboratory setting to study racing crashes as they adhere to strict protocols on the type and shape of car (mandated by the governing body), restraint system usage (5-point or 6-point harness), and driver demographics (mostly males less than 50 years of age in prime fitness). While passenger cars come in all shapes and sizes and a whole lot of variability in terms of restraint system usage and occupant anthropometries, it is interesting to note that a significant number of these racing safety innovations have transitioned into passenger cars with suitable modifications to aid passenger ergonomics and comfort (Melvin et al. 1998).

Figure 9.1 shows a typical Indianapolis type racecar (Indy car), which is usually a single seat, open-cockpit with a carbon fiber/aluminum body. Melvin et al. (1998) noted

that the driver is seated in a “tight fitting tunnel” and the sides of the car are wide structures housing the radiator and cooling systems. They also serve as protective structures in side impacts by forming a crush zone between the driver and the impacting structures. Drivers are usually fitted with double shoulder belts, lap belt along with anti-submarining straps. Although there is very little padding on the side of the driver, a head restraint pad reinforced by the chassis is used to stabilize the head during impacts Melvin et al. (1998).

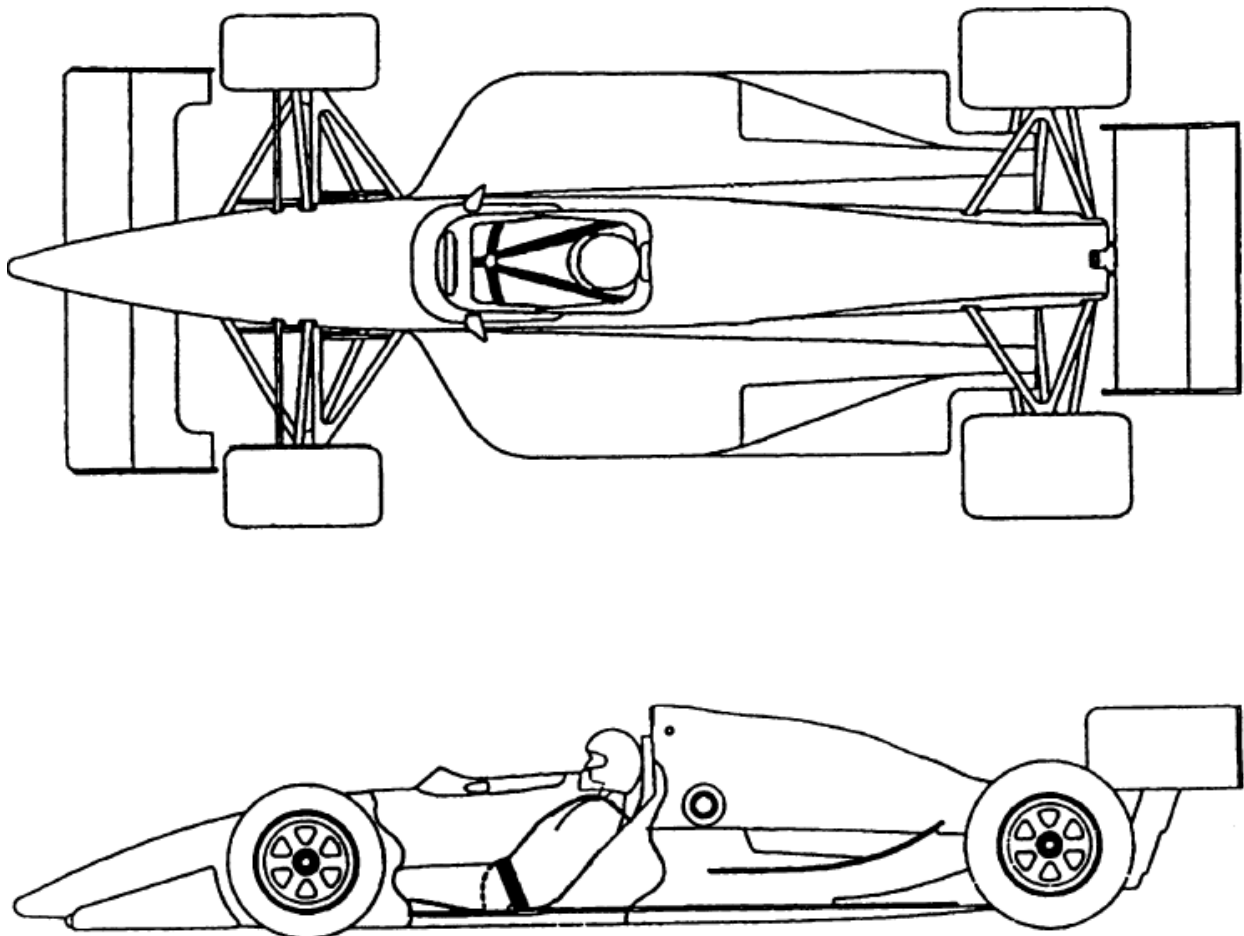


Figure 9.1: Typical Indy car configuration [Adapted from Melvin et al. 1998]

Melvin et al. (1998) in their study showed that Indy racecar drivers could sustain very high accelerations (average of 53.3 g in 143 side impacts) with no aortic laceration. Further, there were no serious thoracic injuries reported. It was hypothesized that the restraint system worn by the drivers limited chest deformation which in turn eliminate the risk of aorta rupture. In 2002, Begeman and Melvin simulated a racing car using nine MADYMO models driven by 3-D accelerations obtained from data recorders on the cars to evaluate Injury Assessment Reference Values (IARVs) for side and frontal impacts. They concluded that the Hybrid-III dummy might have a stiff shoulder, which may affect the simulation results in side impact. Further, Melvin et al. (2006) employed concepts from their earlier study (2002) and extrapolated the data to stock car racing such as National Association for Stock Car Auto Racing, Inc. (NASCAR). More recently, Smith et al. (2011) utilized the Total Human Model for Safety (THUMS) finite element model to simulate high-speed right-lateral impacts of stock car auto racing. They concluded that by using energy absorbing foam padding prevented force concentration on the ribs and reduced the shoulder and clavicle forces.

9.2 Materials and Methods

In order to understand aorta biomechanics in racing car drivers, three left side impact cases reported in Begeman and Melvin (2002), Case #LAS12, #IND14 and #99TX were used as inputs to WSHBM with a simulated racing buck. Melvin and Gideon in 2004 concluded from sled tests that in side impacts, the belt-system was ineffective and the primary means of injury prevention to the thorax was the seat design. The driver in each case had no major injuries reported.

Table 9.1 lists the three lateral impact cases selected from Begeman and Melvin (2002) and the case histories along with the driver injuries.

Table 9.1: Cases selected from Begeman and Melvin (2002)

Case #	Impact location	Peak Vehicle Deceleration (g's)	Delta-v (km/hr)	Occupant Status
LAS12	Left rear/side	127	86.9	Hairline fracture of the left clavicle and pubic symphysis – treated conservatively
99TX	Left rear/side	130	96.6	Slight concussion and minor leg fracture – treated conservatively
IND14	Left rear/side	120	104.6	Concussion for five minutes

The acceleration pulses for the cases are described in Figure 9.2, Figure 9.3, and Figure 9.4 respectively for Case #LAS12, #99TX, and #IND14.

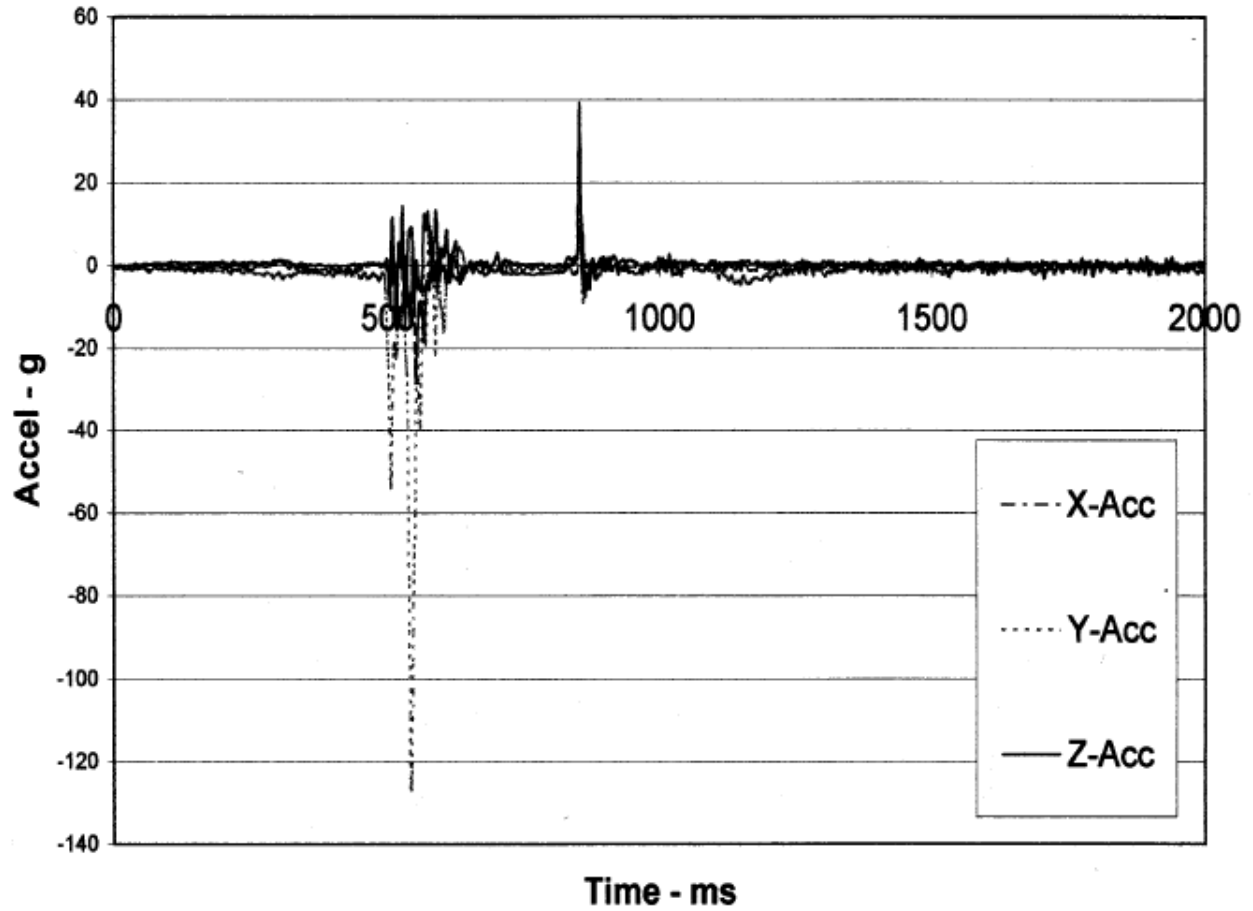


Figure 9.2: Acceleration-time history for Case #LAS12 (Begeman and Melvin (2002))

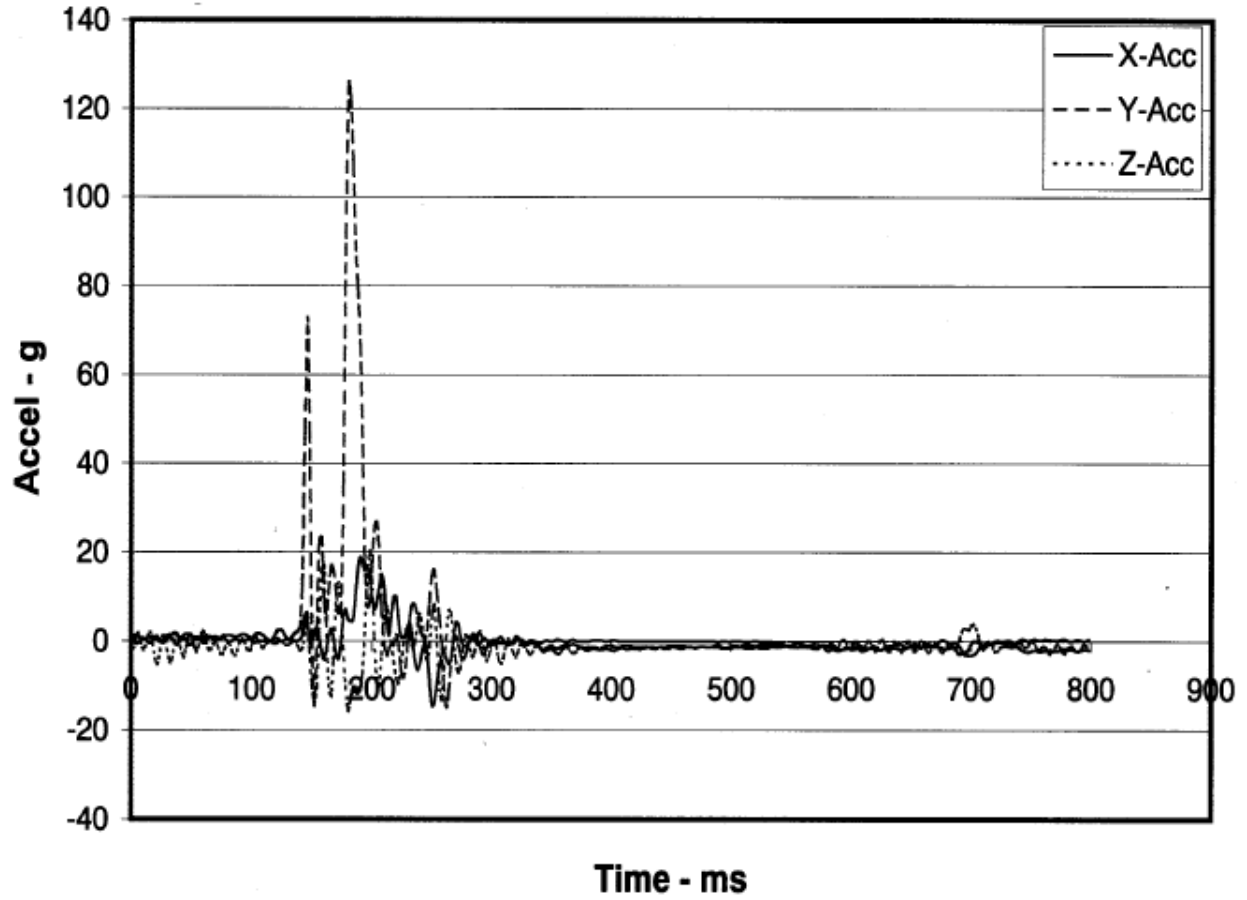


Figure 9.3: Acceleration-time history for Case #99TX (Begeman and Melvin (2002))

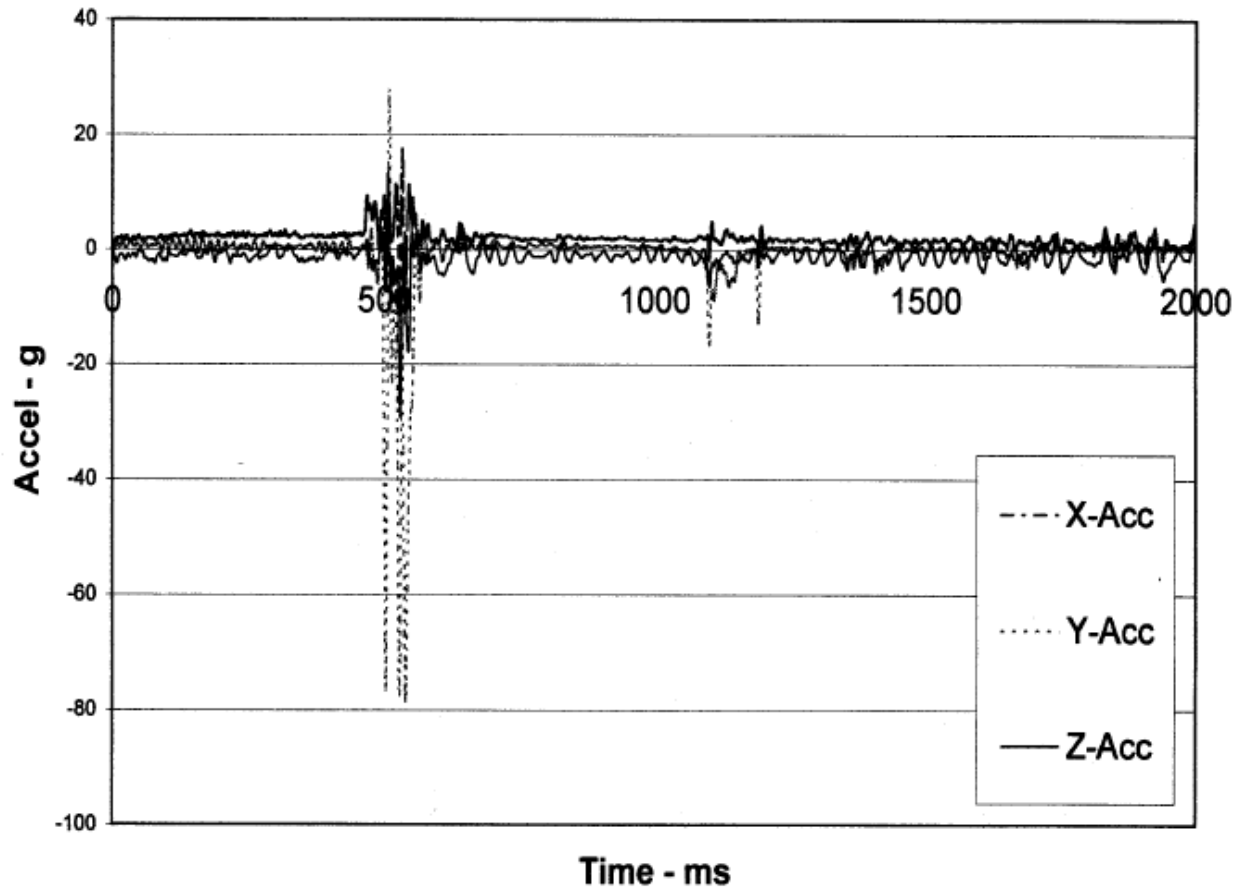


Figure 9.4: Acceleration-time history for Case #IND14 (Begeman and Melvin (2002))

Figure 9.5 shows the FE models developed to represent the seat, six-point harness system, shoulder pads, and head support padding while Figure 9.6 shows the WSHBM seated in the racing buck.



Figure 9.5: Seat, six-point harness system, shoulder support pads, and head support

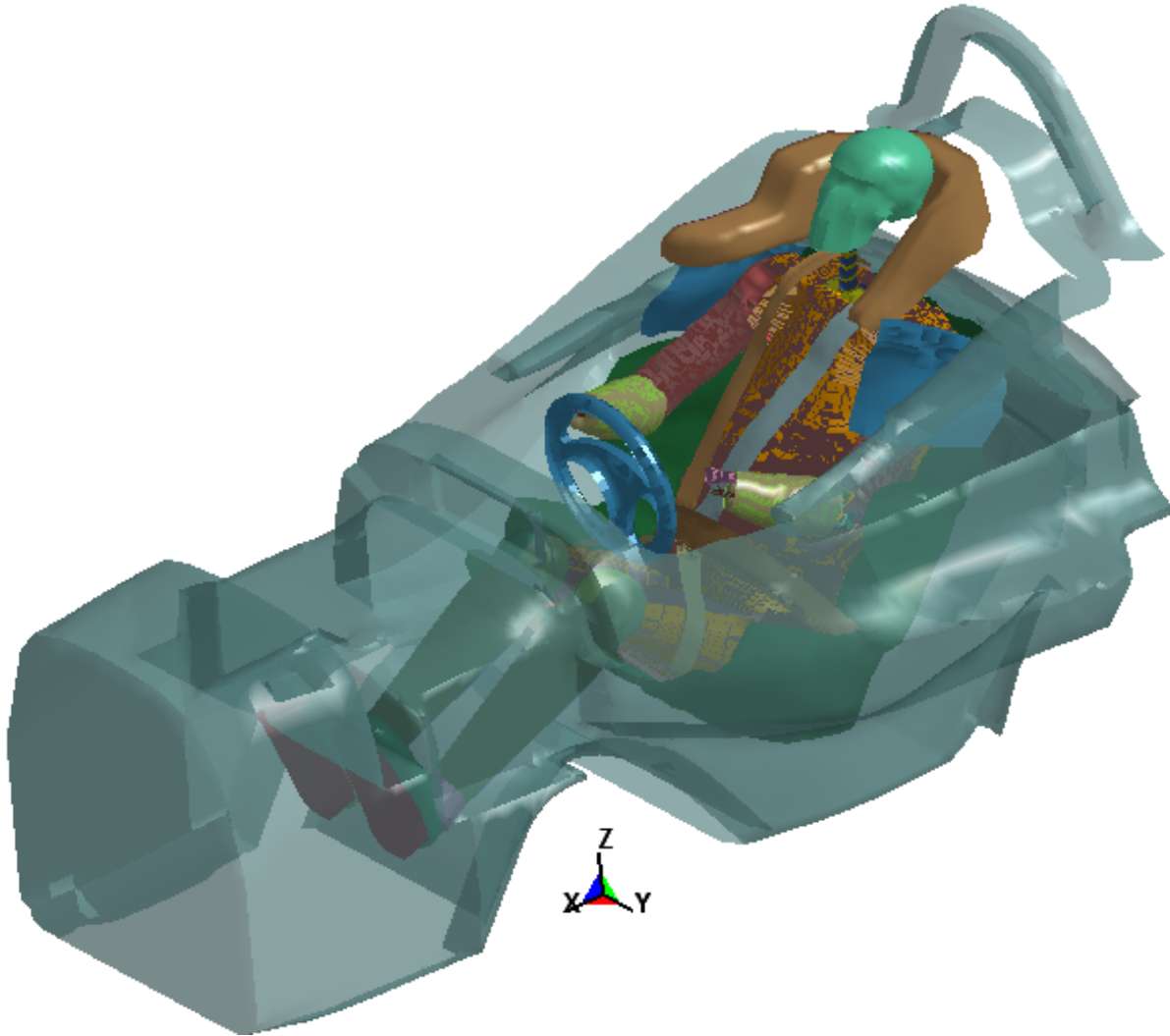


Figure 9.6: Initial position of WSHBM in the racing buck

In order to understand the effectiveness of the belt system and shoulder pad, 12 cases were simulated as part of a design of computer experiments study. Table 9.2 describes the simulation matrix for the runs generated using a Latin Square sampling algorithm in modeFRONTIER 4.1 (ESTECO, North America) with delta-v (km/hr), six-point harness and shoulder pad as input design factors.

Table 9.2: Simulation matrix generated using a Latin Square Algorithm in modeFRONTIER 4.1

Run #	Delta-v (km/hr)	Peak Vehicle Deceleration (g's)	Seatbelt (Six-Point harness)	Shoulder Pad
1 (LAS 12)	86.9	127	Modeled	Modeled
2	86.9	127	Not Modeled	Not Modeled
3	86.9	127	Modeled	Not Modeled
4	86.9	127	Not Modeled	Modeled
5 (99TX)	96.6	130	Modeled	Modeled
6	96.6	130	Not Modeled	Not Modeled
7	96.6	130	Modeled	Not Modeled
8	96.6	130	Not Modeled	Modeled
9 (IND 14)	104.6	120	Modeled	Modeled
10	104.6	120	Not Modeled	Not Modeled
11	104.6	120	Modeled	Not Modeled
12	104.6	120	Not Modeled	Modeled

The simulations were set to run for 15 milliseconds. All simulations were carried out using Hypermesh 10.0 (Altair Corporation, Troy, MI) as the pre-processor, a Massively Parallel Platform (MPP) version of LS-DYNA 970 on a two-node cluster (two processors/node) as the solver, and LS-PREPOST 3.1 (LSTC Corporation, Livermore, CA) as the post-processor. AMPS and maximum pressure along with the motions of the aorta were tracked with deformation of the thoracic cavity.

9.3 Results and Discussion

Table 9.3 lists the AMPS and maximum pressure recorded in these runs.

Table 9.3: AMPS and maximum pressure in the aorta recorded for the cases with the WSHBM in a racing buck

Run # (Case #)*	Delta-v (km/hr)	Seatbelt (Six-Point harness)	Shoulder Pad	Time at AMPS (ms)	AMPS	AMPS (at 6.6 ms)**	Time at maximum pressure(ms)	Maximum Pressure (kPa)	Maximum Pressure (kPa) at 3.0 ms
1 (LAS12)	86.9	Modeled	Modeled	12.0	0.1621	0.0341	12.0	106.2	26.5
2	86.9	Not Modeled	Not Modeled	6.6	0.0626	0.0626	3.4	41.5	36.6
3	86.9	Modeled	Not Modeled	6.6	0.0446	0.0446	3.2	37.4	35.1
4	86.9	Not Modeled	Modeled	10.0	0.1358	0.0322	3.0	28.3	28.3
5 (99TX)	96.6	Modeled	Modeled	8.0	0.1358	0.0459	12.0	110.6	31.2
6	96.6	Not Modeled	Not Modeled	12.0	0.1494	0.0771	11.8	153.1	38.9
7	96.6	Modeled	Not Modeled	6.8	0.1118	0.1101	3.3	42.1	38.2
8	96.6	Not Modeled	Modeled	8.4	0.1419	0.0458	3.0	33.0	33
9 (IND14)	104.6	Modeled	Modeled	9.2	0.1673	0.0869	9.2	114.7	37.4
10	104.6	Not Modeled	Not Modeled	6.8	0.1838	0.1822	3.1	49.8	48.2
11	104.6	Modeled	Not Modeled	8.8	0.1579	0.1001	8.7	135.7	46.8
12	104.6	Not Modeled	Modeled	9.3	0.1855	0.1255	2.7	34.3	38.1
Average of cases from Begeman and Melvin (2002); Run #1, #5, and #9					0.1551±0.0172			110.50±4.25	

* Case numbers in parenthesis depict the input parameters reported in Begeman and Melvin (2002)

** AMPS at 6.6 ms is the average AMPS at that time stamp and at those same four elements and not the scaled data

It was observed from simulations that cases with no shoulder support underwent severe shoulder and upper thoracic deformation leading to early termination due to negative volume (Figure 9.7).

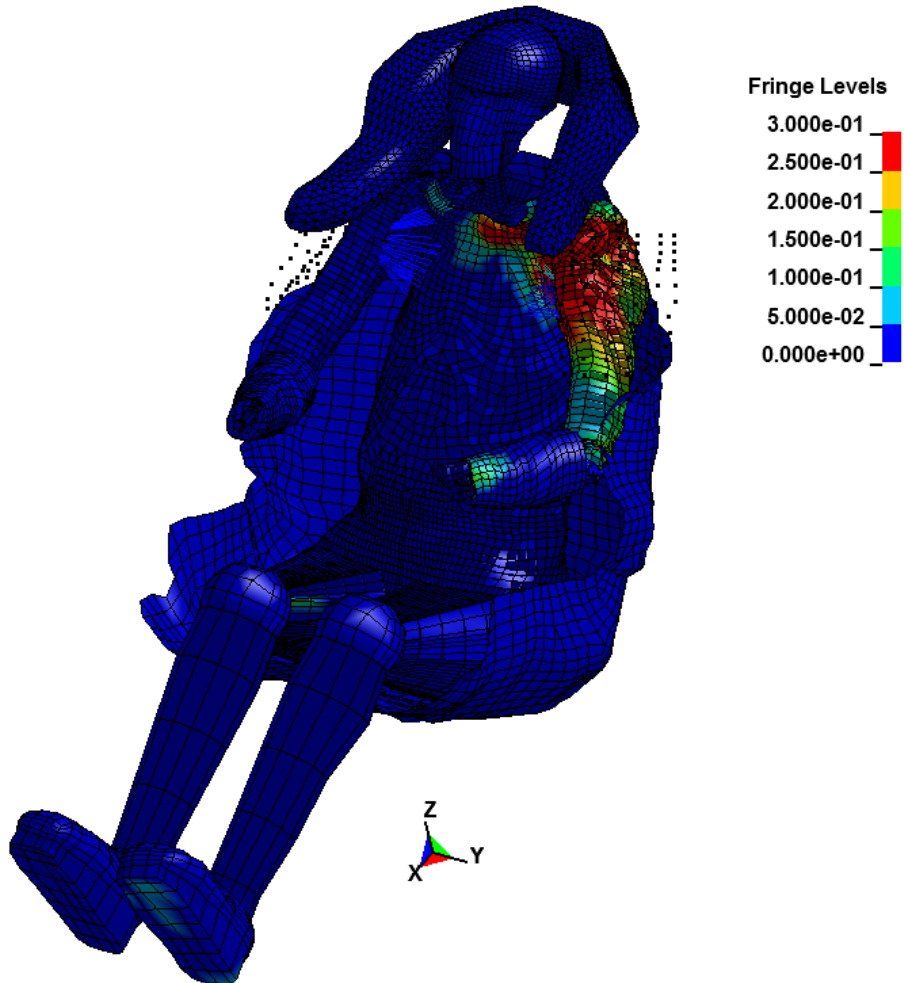


Figure 9.7: Maximum principal strain - Severe shoulder deformation in the absence of shoulder support pads – Dots show the otherwise location of shoulder support pads

From Table 9.3 it is seen that cases without shoulder support (Runs #2, #3, #6, #7, #10, and #11) terminated early and hence any direct comparison of AMPS and maximum pressure with cases having a longer termination time would lead to a bias in the statistics. Hence, AMPS values were tabulated for the lowest termination time,

which was 6.6 ms, and then averaged while maximum pressure was tabulated for 3.0 ms and then averaged. It is important to note that, although the simulations terminated early, the accelerations still represented the prescribed curves from Begeman and Melvin (2002). The curves were trimmed to apply the acceleration-history at the beginning of the simulation using *BOUNDARY_PRESCRIBED_MOTION card in LS-DYNA version 970. However, the AMPS and maximum pressure for cases from Begeman and Melvin (2002) were averaged separately (Runs #1, #5, and #9) since the rest of the matrix was generated to study the effect of the six-point harness system and shoulder support pads in racing crashes.

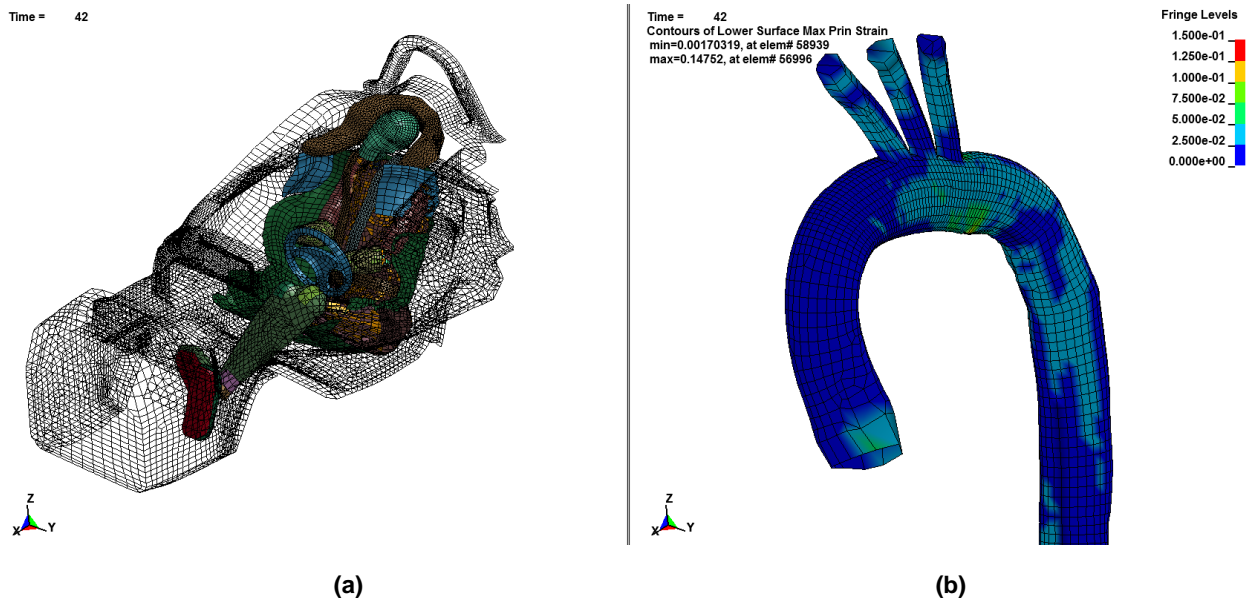


Figure 9.8: Case #99TX: (a) WSHBM kinematics with the racing buck (b) Contours of lower surface maximum principal strain in the aorta

Figure 9.8a shows the kinematics of WSHBM with the racing buck while Figure 9.8b shows the contours of lower surface maximum principal strain in the aorta. It is noted that the average AMPS for the three high-speed racing crashes was 0.1551 ± 0.0172 with a six-point harness system and shoulder support pads while the

overall maximum pressure was 110.50 ± 4.25 kPa. It is interesting to note that the average AMPS and the average maximum pressure recorded were significantly lower than those reported from the CIREN reconstructions in Chapter 8, Table 8.6. For CIREN cases with no fatality, the average AMPS was 0.1238 ± 0.044 and the average maximum pressure was 84.10 ± 23.88 kPa. For the CIREN cases with fatality due to aortic rupture, the average AMPS was 0.2329 ± 0.057 and the average maximum pressure was 119.58 ± 16.05 kPa. Figure 9.9 compares the average AMPS while Figure 9.10 compares the average maximum pressure in the aorta with published data. Similarly, the average maximum pressure for simulated high speed racing crashes was 110.50 ± 4.25 , which was lesser than the values reported for fatality by Bass et al. (2001). However, the pressure was higher than those reported for rupture by Hardy et al. (2008).

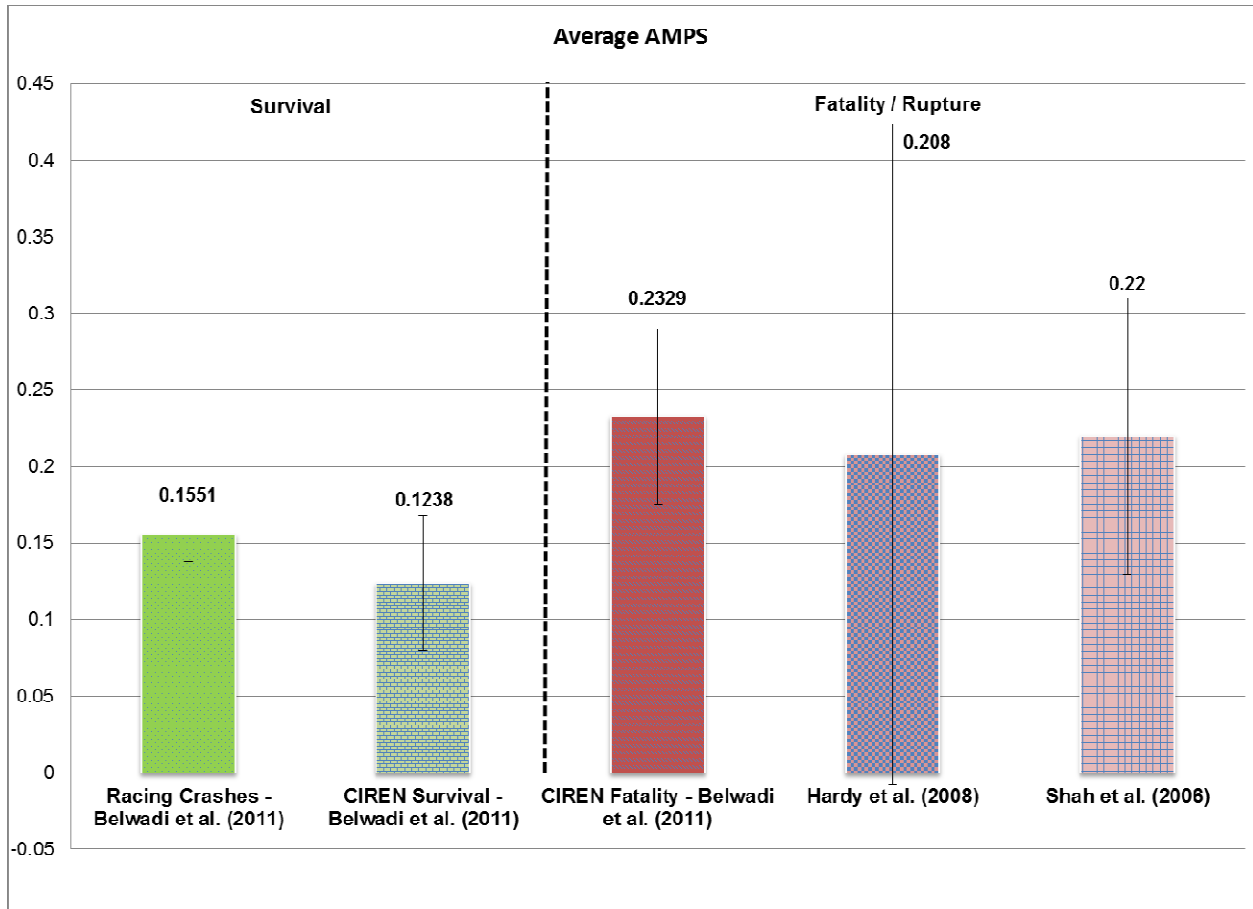


Figure 9.9: Comparison of average AMPS with published data

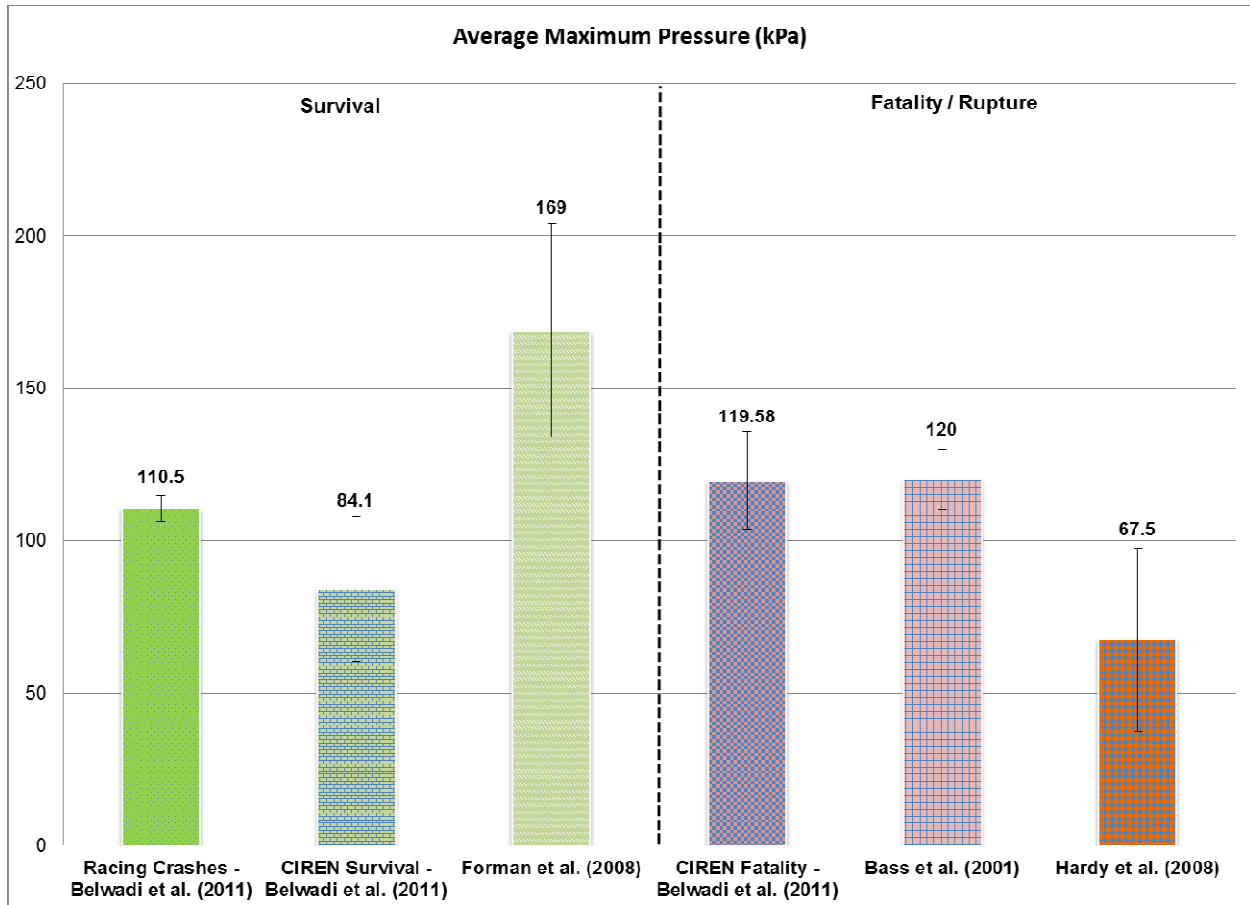


Figure 9.10: Comparison of average maximum pressure with published data

A main effects analysis was performed using Minitab 16.1 (Minitab Inc., State College, PA) to characterize the effect of six-point seat belt and shoulder support pads on AMPS and maximum pressure in the aorta for high-speed racing crashes. Figures 9.11 and 9.12 depict the main effects plot and combined Pareto diagram for AMPS while Figures 9.13 and 9.14 depict the effects plot and combined Pareto diagram for maximum pressure generated in the aorta.

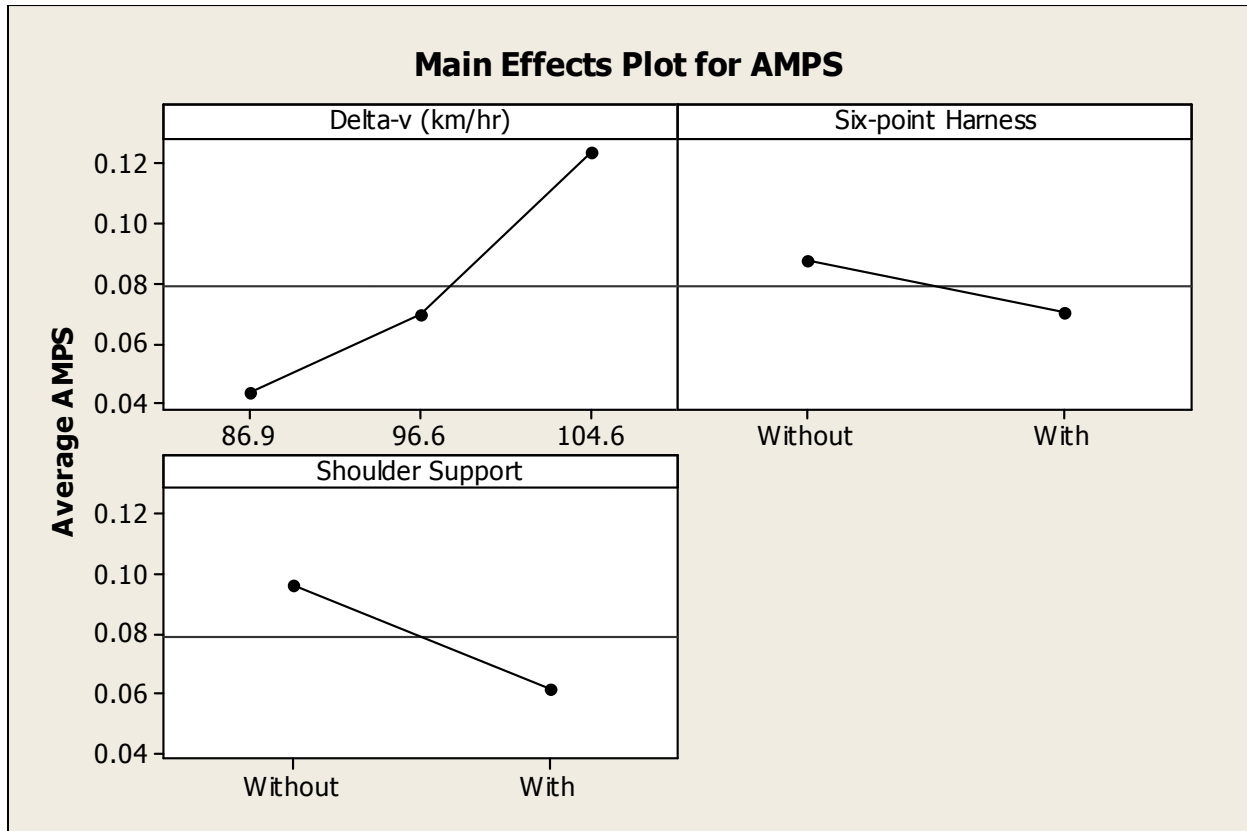


Figure 9.11: Main effects plot for AMPS

From Figure 9.11 it is observed that as the delta-v increased the average AMPS increased as well; which is rather intuitive. However, it was interesting to note that the six-point harness was still effective, just not significant in these high-speed side impacts in reducing the strain generated in the aorta. A Pareto chart of effects (Figure 9.12) revealed that delta-v was the only significant factor for AMPS, followed by shoulder support.

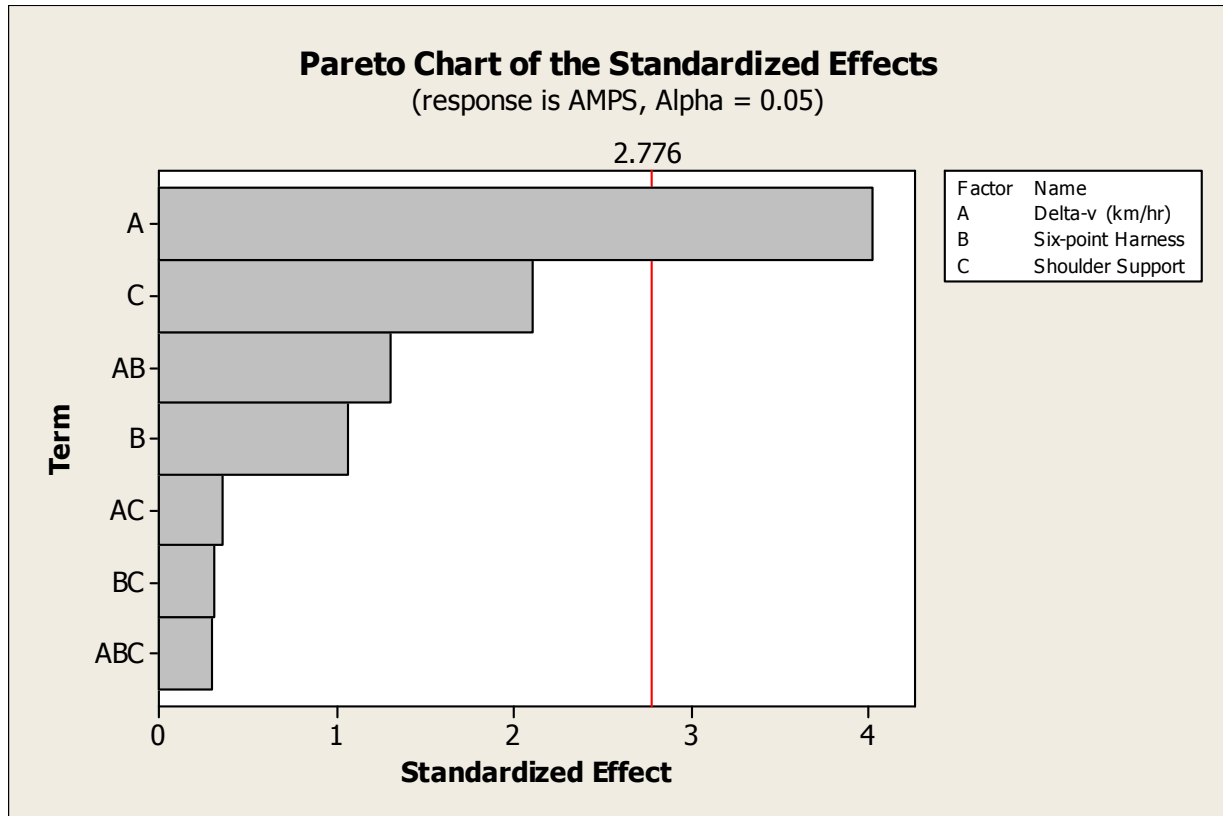


Figure 9.12: Pareto chart of effects for AMPS

A main effects plot for maximum pressure (Figure 9.13) revealed similar findings as that of AMPS. There was no statistical significance indicating the ineffectiveness of the seatbelt in side belt as hypothesized by Melvin and Gideon in 2004. However, the shoulder support pads seemed effective in decreasing the maximum pressure in the aorta.

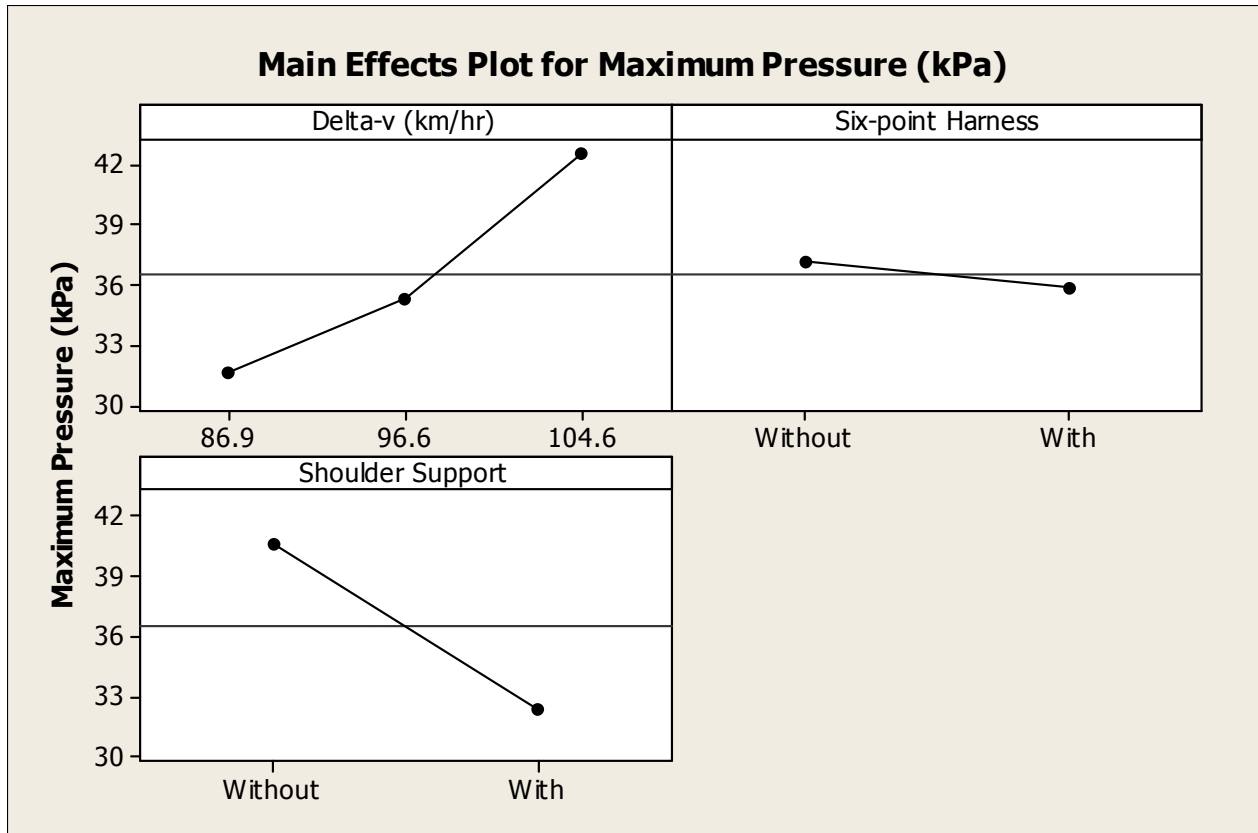


Figure 9.13: Main effects plot for maximum pressure

A Pareto chart of effects for maximum pressure revealed (Figure 9.14) the delta-v and shoulder support pads being significant for reduction of maximum pressure in the aorta.

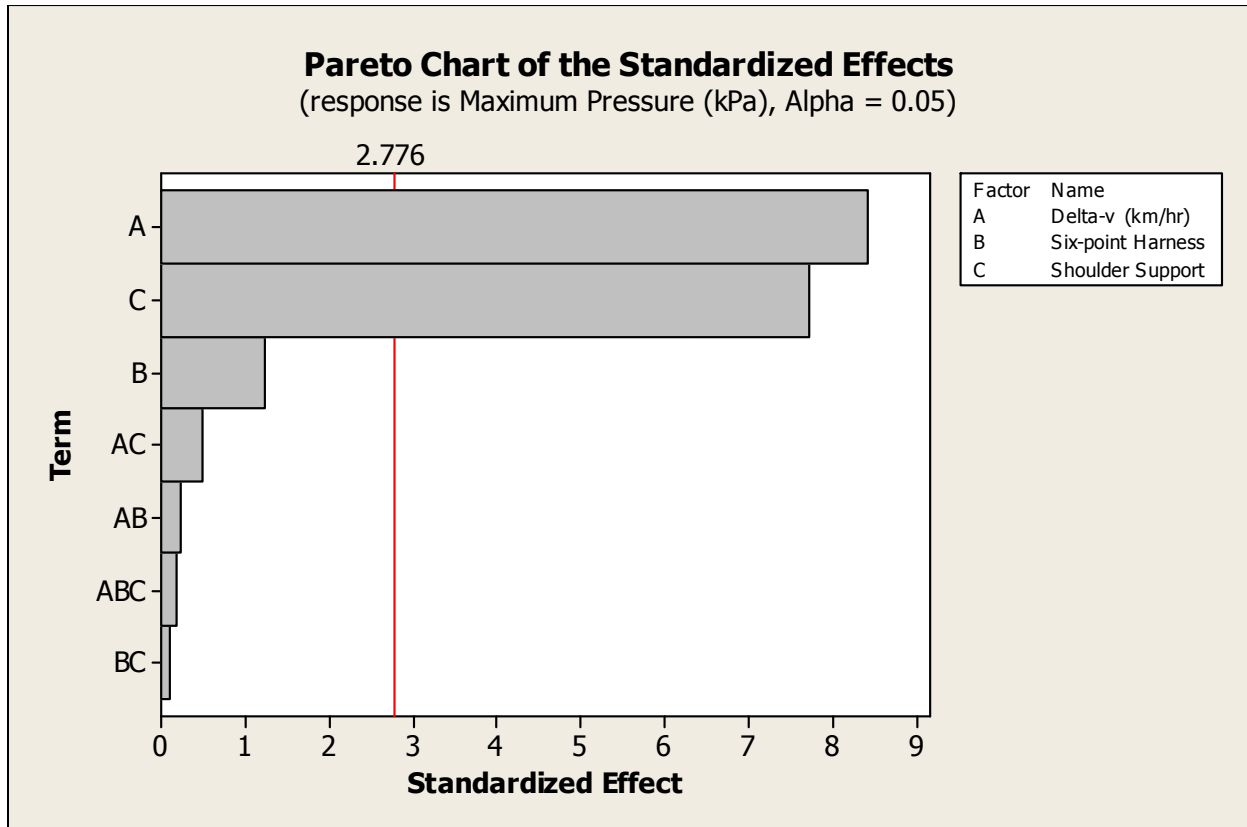


Figure 9.14: Pareto chart of effects for maximum pressure

Figure 9.15 shows the deformation pattern of the thoracic cavity, at 0 ms, 30 ms, and 60 ms into the simulation. The figure shows the lateral (L) and anterior (A) views in the coronal plane. It is interesting to note that in spite of higher delta-v than those for the CIREN reconstruction outlined in Chapter 5, it was seen that there was significantly reduced thoracic deformation owing to the presence of the seat and shoulder support pads.

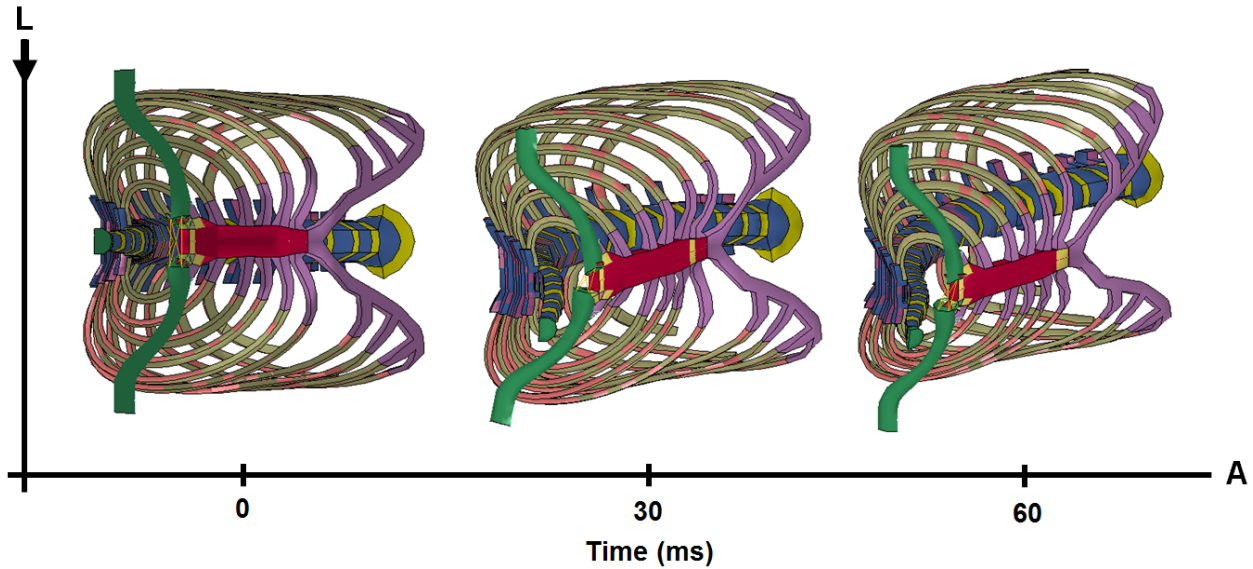


Figure 9.15: Initial (0 ms) and deformed (30 ms and 60 ms) thoracic cavity - Coronal section

9.4 AIM D Conclusions

Twelve simulations were carried out using a combination of WSHBM and a racing buck, with and without a six-point harness. Simulations results indicate the following:

- The average AMPS for the high speed crashes (Begeman and Melvin (2002)) were 0.1551 ± 0.0172 while the average maximum pressure was 110.50 ± 4.25 kPa.
- The average AMPS reported was significantly less than reported for fatality in the CIREN reconstructions in Chapter 6; for rupture by Shah et al. (2006) and Hardy et al. (2008).
- The maximum pressure were significantly less than those reported for fatality as reported by the CIREN reconstructions in Chapter 6; for rupture by Bass et al. (2001) and Hardy et al. (2008).

- Thoracic deformation was significantly less as compared to the CIREN cases in Chapters 6, 7, and 8.
- Thoracic deformation is absolutely necessary for TRA.
- The seat and shoulder support pads plays a crucial role in injury mitigation to the thorax in high speed racing crashes.
- Delta-v had a significant effect on both AMPS and maximum pressure in the aorta while shoulder-harness had a significant effect in reducing maximum pressure in the aorta.

CHAPTER 10

AIM E: CONCEPTUAL COUNTERMEASURES IN NEARSIDE LEFT LATERAL IMPACTS TO REDUCE AORTIC STRAIN

10.1 Introduction

Recent advances involving the use of endovascular stent grafts have resulted in major improvements in the survival of patients with TRA who reach the hospital alive (Demetriades et al. 2008). The fact remains that more than 60% of MVC related AI victims are dead at the scene (Siegel et al. 2004) and between 31% and 57% of the crash survivors have been reported to die either in the emergency room or in the operation room after admission. Hence, it is evident that **effective means of substantially improving the outcome of MVC-induced TRAs is to prevent the injury in the first place.**

From Chapters 8 and 9, the factors essential for TRA are

- Thoracic deformation
- Significant relative motion between the sternum and spine were also seen
- B-pillar and side structure intrusion
- The seat can be play a crucial role in TRA mitigation, as seen in Chapter 9, shoulder supports seems to provide a crucial element in aortic AMPS reduction.

In an effort to provide countermeasures to reduce aortic AMPS, which is precursor to TRA, two strategies were employed:

AIM E1: Providing strategies to reduce B-pillar and side door structure intrusion in nearside left lateral impacts

AIM E2: To improve on existing seat designs; by incorporating structures to **engage the shoulder and reduce thoracic deformation** in nearside left lateral impacts in passenger cars

10.2 AIM E1 - Methods and Materials

As shown in Cases 7 and 25 (from Aim A in Chapter 6), the major injury mechanism producing aortic isthmus disruption appears to be a lateral thoracic impact by the crash-induced B-Pillar intrusion. A PDOF of 270 degrees generated the highest average maximum principal strain in the aorta.

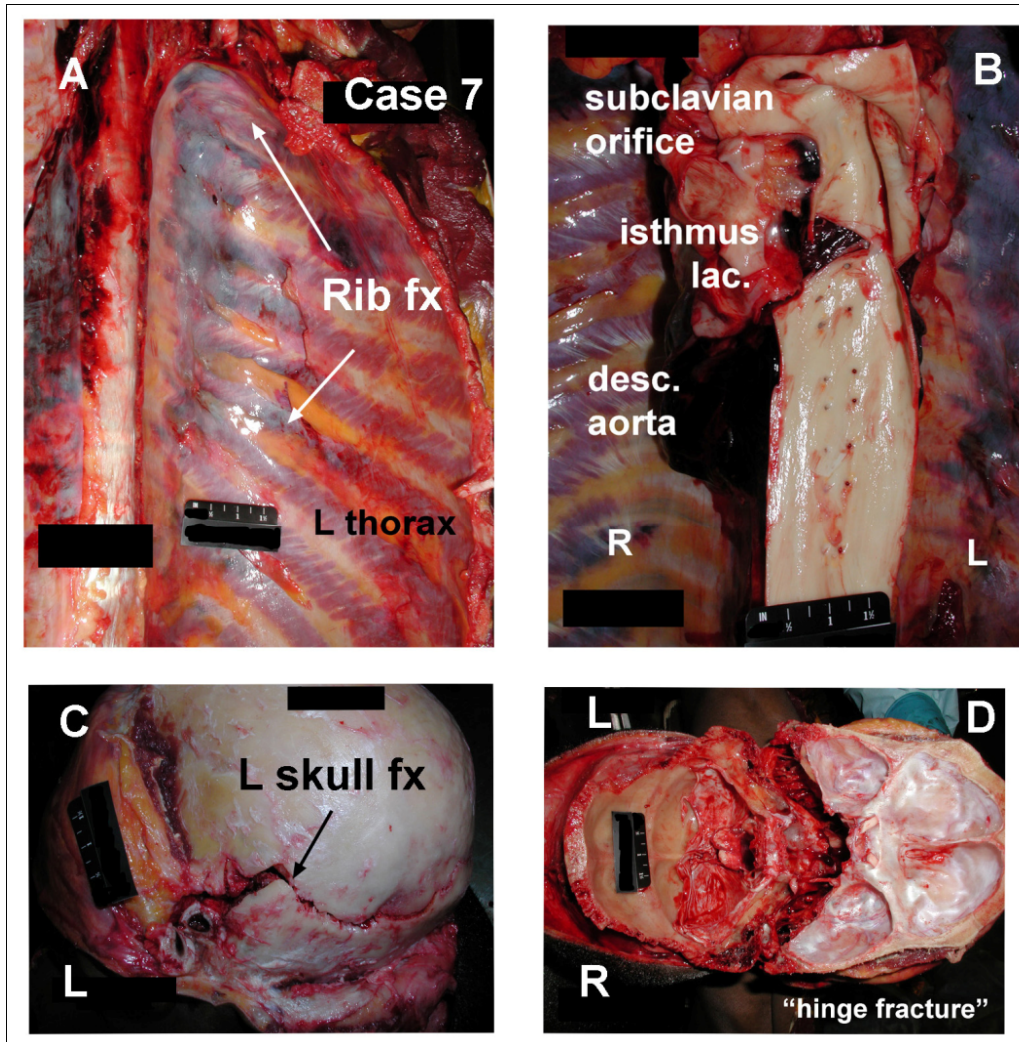


Figure 10.1: Case 7 CIREN data with A) Rib fracture B) aortic rupture C) skull fracture and D) hinge fracture

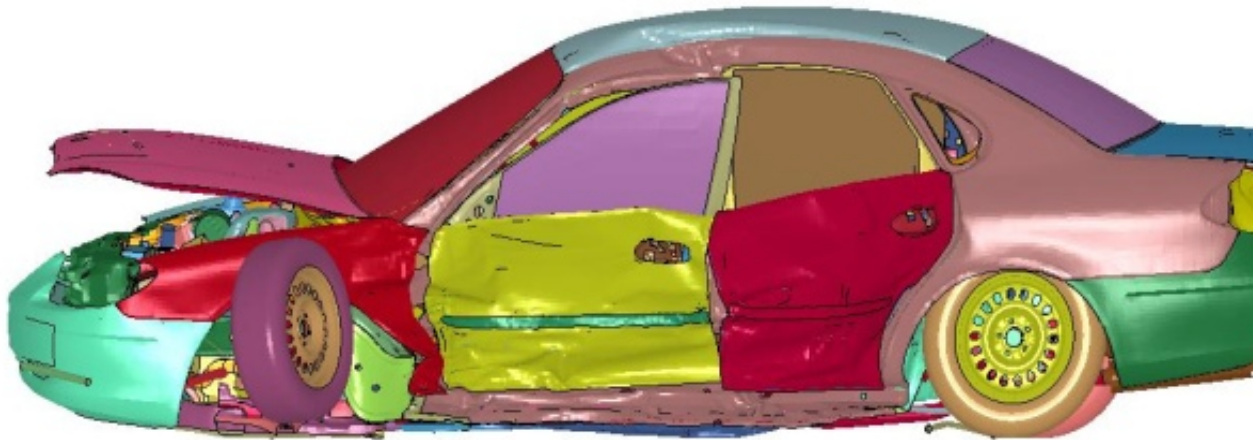
Brain injury was the most common associated major injury found in 80 cases of TRA reported by Siegel et al. 2004. A secondary but often additional serious injury mechanism appears to be an impact with the head, producing a severe brain injury frequently associated with a skull fracture (Figure 10.1(C) and Figure 10.1 (D)). To explore possible strategies for reducing the incidence of TRA as well as the frequently associated lateral head injuries (or vice versa), a series of simulations were carried out

using Case 7 as the baseline case. If a strategy for reducing aortic isthmus strain characteristics could be shown to be effective by using a FE based model in this impact case, then new vehicle safety measures could be devised to reduce the incidence of TRA with its high likelihood of scene death. In a similar fashion, devising a mechanism for preventing head and chest impact with the B-Pillar would be expected to reduce the incidence of brain injury as well.

The baseline case was reconstructed numerically using scaled FE vehicle models and the WSHBM FE model. The reconstructions were carried out in two stages as described in Chapter 5. In Stage I, the “Ford Taurus” FE vehicle model was obtained from vehicle model archives’ at the National Crash Analysis Center (NCAC) and was adjusted for overall dimensions such as the wheelbase, width, and height by scaling the model to match the actual vehicle (1993 Toyota Corolla) dimensions. The principal other vehicle (POV) was modeled using the “Dodge Caravan” FE vehicle model. The FE Caravan model was positioned as reported by crash investigation data and given an initial velocity of 59 km/h. For the case vehicle, the driver side structures including the front and rear doorframe, door armrest, and left B-pillar nodes, were grouped and their motions were recorded in separate binary interface files. These interface files were used in the Stage II simulations. Figure 10.2 shows qualitative comparison of the deformations of FE vehicle model against the actual vehicle. Table 10.1 compares the actual versus simulation deformations.



(a)



(b)

Figure 10.2: (a) Vehicle deformation patterns of the actual case vehicle (b) FE simulation using the scaled FE vehicle model

Table 10.1: Deformation comparison of the simulation with the actual vehicle

Deformation Point (cm)	C1	C2	C3	C4	C5	C6
Actual	0	50	73	62	37	0
FE simulation	2	45	66	59	32	5

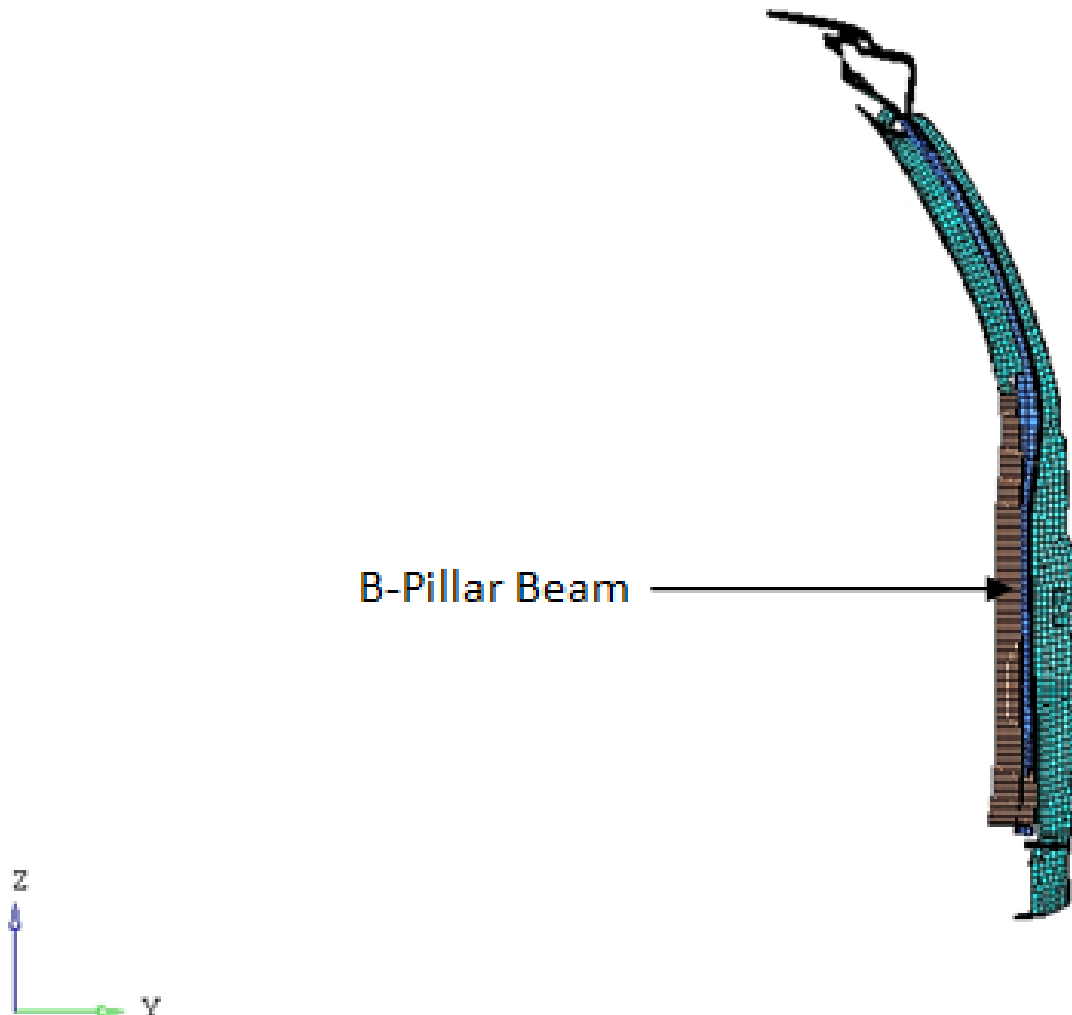
In Stage II, the kinematics time histories of the sub-model, which consisted of structures that might interact with the integrated human model, were used to determine the human responses. The integrated human FE model was imported into the case

vehicle model and was positioned in a seated posture. This posture was estimated based on post-crash photographs of the interior structures and seat. A contact interface was created between the vehicle structures and the occupant. The nodal kinematics of the vehicle structures saved in the interface file was applied to the combined model. The average maximum principal strains (AMPS) were found to be in the range of 18% to 23% in the isthmus region of the aorta.

10.2.2 DOCE Simulations

Six design factors comprising of: (1) introduction of a B-pillar beam; (2) changing the dimensions of the beam; (3) increasing the yield strength of the side door structures; (4) increasing the thickness of the side door-structures; (5) adding a cross-beam across the door and (6) an addition of a large side ‘overall’ airbag spanning the roof to the rocker arm were considered for the DOCE study. 18 DOCE cases (shown in Table 10.1) were generated using a Latin Square Sampling method available in modeFRONTIER 4.1 (ESTECO, Novi). Simulations were carried in two Stages in a manner similar to that described in Chapter 5. For the B-pillar beam, a solid structure, attached to the rocker arm at the top and the bottom of the B-pillar, was created in the B-pillar space to increase the stiffness of the structure, as shown in Figure 10.3(a). Further, a cross-beam was modeled in the door structure to increase the bending strength of the door (Figure 10.3(b)). The cross-beam was modeled as shell elements with an initial thickness of 0.5 mm. A non-production conceptual single inflator overall airbag was modeled and deployed on the left interior door structure in an unfolded state 6 ms after initial door contact (Figure 10.4). This conceptual “blanket” or “overall” airbag was created to represent both a torso and a curtain bag to cover the entire body from

impacting into the lateral structure (B-pillar) in the event of a left lateral impact. It is to be noted in current production vehicles, side impact protection typically includes a side-curtain bag with or without a torso bag. A blanket airbag usually can encounter issues with inflator design and inflation pressure. In the current simulations, it is assume that the inflators can indeed inflate the airbag.



(a)

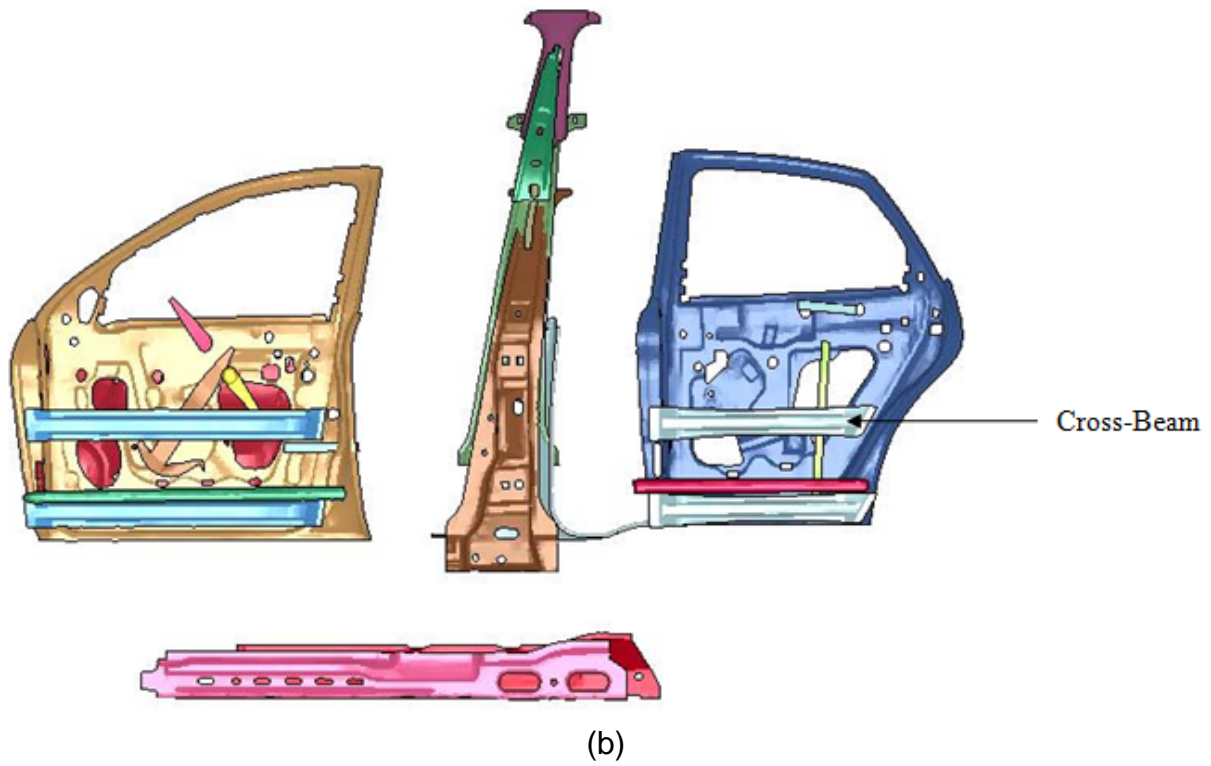


Figure 10.3: Exploded View of structures involved in the DOCE (a) Exterior View and (b) Interior View

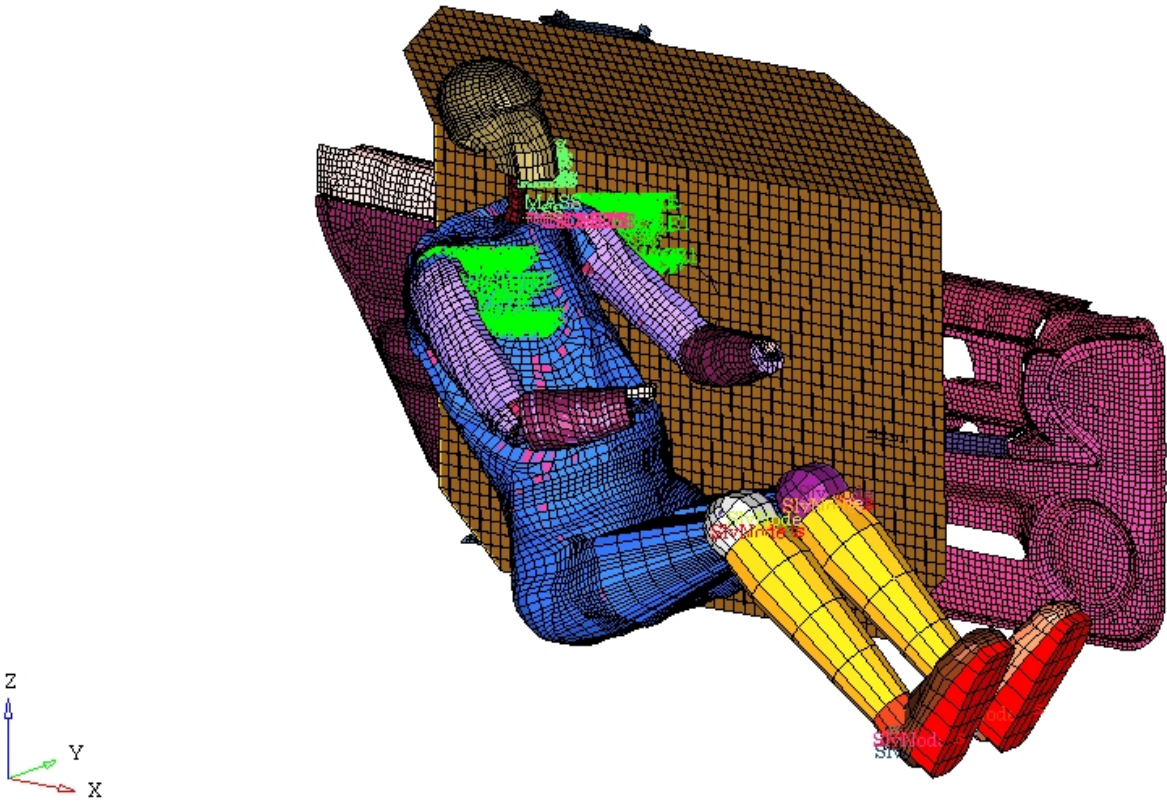


Figure 10.4: Left side door structures, WSHBM along with a conceptual unfolded blanket airbag

Table 10.1: DOCE Matrix generated using modeFRONTIER 4.1 for the simulation runs

Case #	B-pillar Beam	Cross-Beam	Side Airbag	Thickness* factor	Yield Strength (MPa)	B-pillar Beam Dimensions (mm)
I	0	0	1	2	300	10 by 60
II	0	1	1	4		
III	0	1	0	1		
IV	0	0	1	1		
V	1	1	0	2		
VI	1	1	1	4		
VII	1	0	0	4		
VIII	1	1	1	1		
IX	1	1	1	2		
X	1	1	1	4		
XI	0	0	1	1	400	20 by 60
XII	1	1	0	1		
XIII	1	1	1	1		
XIV	1	1	0	1		
XV	1	1	0	1		
XVI	1	1	1	1		
XVII	1	1	1	1		
XVIII	1	1	1	4		

Note:

*Thickness factor as the multiple of the original thickness of the sheet metal components in the door. For example, 2 indicates twice the thickness of the original model. Table E1 in Appendix E lists the actual thickness of the structures simulated)

10.3 Results and Discussion

Table 10.2 lists the AMPS in the isthmus, maximum pressure in the aorta, and B-pillar intrusion obtained for each run. B-pillar intrusion is the maximum recorded intrusion and not the resting deformation.

Table 10.2: AMPS (%), Maximum Pressure (kPa) in the aorta and B-pillar Intrusion (mm)

Parameter Run #	B-pillar Beam	Cross-Beam	Side Airbag	Thickness factor	Yield Strength (MPa)	B-pillar Beam Dimensions (mm)	Isthmus AMPS (%)	Maximum Aortic Pressure (kPa)	Maximum B-Pillar Intrusion (mm)
I	0	0	1	2	300	10 by 60	17.2	126.4	225
II	0	1	1	4			17.6	128.5	165
III	0	1	0	1			25.2	127.2	278
IV	0	0	1	1			20.1	132.7	212
V	1	1	0	2			19.8	120.8	63
VI	1	1	1	4			13.8	113.3	81
VII	1	0	0	4			15.5	113.7	289
VIII	1	1	1	1			20.1	135.1	213
IX	1	1	1	2			19.2	123.2	227
X	1	1	1	4			14.4	117.5	85
XI	0	0	1	1		15.8	128.7	250	
XII	1	1	0	1		17.2	126.7	319	
XIII	1	1	1	1		19.9	124.9	319	
XIV	1	1	0	1		400	20 by 60	19.4	127.8
XV	1	1	0	1	500	18.6		126.8	298
XVI	1	1	1	1	400	18.5		133.4	314
XVII	1	1	1	1	500	17.5		133.7	298
XVIII	1	1	1	4	600	12.5		111.2	78

Note: B-pillar intrusion reported is the maximum intrusion and not the intrusion at the end of the simulation, to accommodate elastic-plastic deformation of the structure (rebound)

Run number XVIII, which simulates the B-pillar beam, cross-beam, blanket side airbag, and a thickness of four times the baseline thickness of the door structure, has the lowest AMPS of 12.5% in the isthmus of the aorta at a B-pillar intrusion of 78 mm. On the other hand, Runs VI and X have a significantly lower maximum principal strain of 13.8% and 14.4% respectively. Both runs simulate all six design-factors with four times the thickness of the baseline door structure. However, in Run X, the B-pillar beam dimensions were 20 by 60 mm instead of 10 by 20 mm simulated in Run VI. Run VI has a maximum intrusion of 81 mm and a maximum aortic pressure of 113.3 kPa while Run X has a maximum intrusion of 85 mm and a maximum pressure of 117.5 kPa. Figure 10.5(a) shows the overall kinematics of Run VI while Figure 10.5(b) shows the regions of the maximum principal strain around the region of the isthmus, distal to the left subclavian artery. A One-way ANOVA performed on runs VI, X, and XVIII versus rest of the simulations revealed statistical significance for AMPS ($p=0.002$); maximum pressure ($p=0.001$), and B-pillar intrusion ($p=0.001$).

WAYNE STATE HUMAN MODEL VERSION 2006-1
Time = 46



(a)

WAYNE STATE HUMAN MODEL VERSION 2006-1
 Time = 62
 Contours of Lower Surface Max Prin Strain
 min=0.00254356, at elem# 62829
 max=0.423292, at elem# 56283

Fringe Levels
 1.000e-01
 8.333e-02
 6.667e-02
 5.000e-02
 3.333e-02
 1.667e-02
 0.000e+00

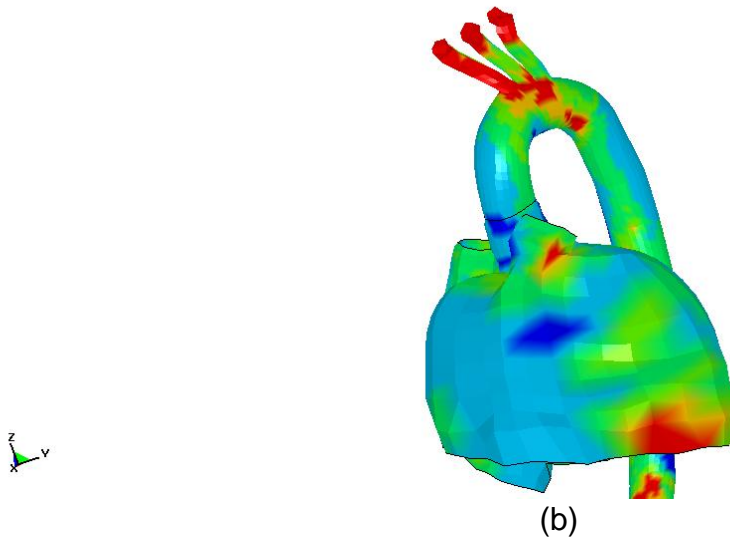


Figure 10.5: (a) Occupant kinematics and (b) Maximum principal strain pattern at the time of maximum vehicle deformation for Run VI

A main effects analysis was carried out on Minitab 15 (Minitab Inc., State College, PA) to estimate the effectiveness of each design factor on aortic strain and the compartmental intrusion. Figure 10.6 shows that adding a crossbeam had a negative effect on the AMPS of the aorta (i.e. increased the aortic strain) while the other three factors had a positive effect (decreased the aortic strain). In addition, B-pillar intrusion decreased with the presence of a B-pillar beam and an increase in thickness while the presence of a side airbag and crossbeam did not significantly change the amount of intrusion. This can be attributed to the fact that neither a side airbag nor a crossbeam can significantly alter the stiffness of the door structure thereby changing the intrusion.

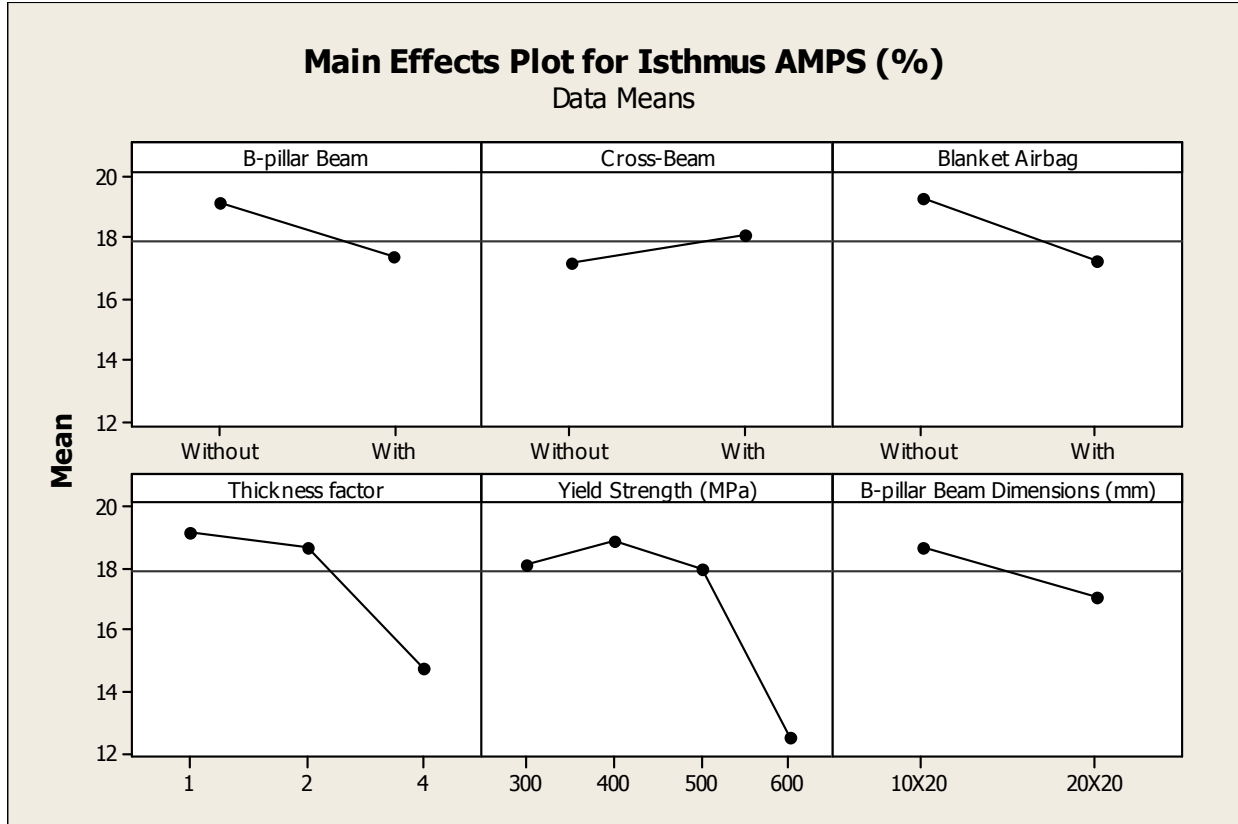


Figure 10.6: Main effects analysis plot – AMPS

From Figure 10.7, it is seen that the maximum pressure in the aorta decreases with the addition of a B-pillar beam and an increase in thickness of the door structures. However, it does not seem to change significantly with the addition of a cross-beam and the blanket side airbag. There is a significant pressure decrease with the change in the yield strength from 500 MPa to 600 MPa, while it increases when changed from 300 MPa to 400 MPa.

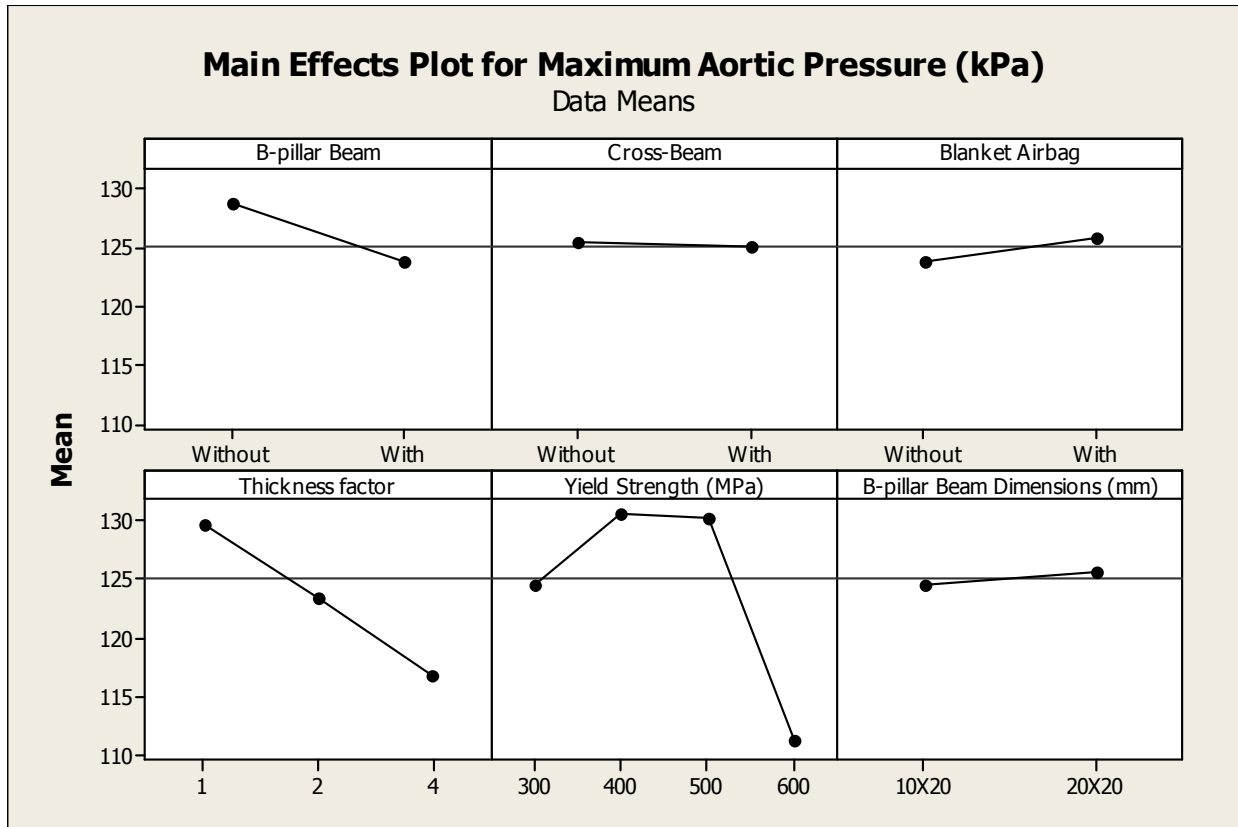


Figure 10.7: Main effects analysis plot - Maximum Aortic Pressure (kPa)

Figure 10.8 shows that addition of a crossbeam, the conceptual blanket side airbag; thickness and change in yield strength have a positive effect (reduced intrusion) on the B-pillar compartmental intrusion. However, changing the dimension of the B-pillar beam from 10 by 60 to 20 by 60 mm has a negative effect on intrusion.

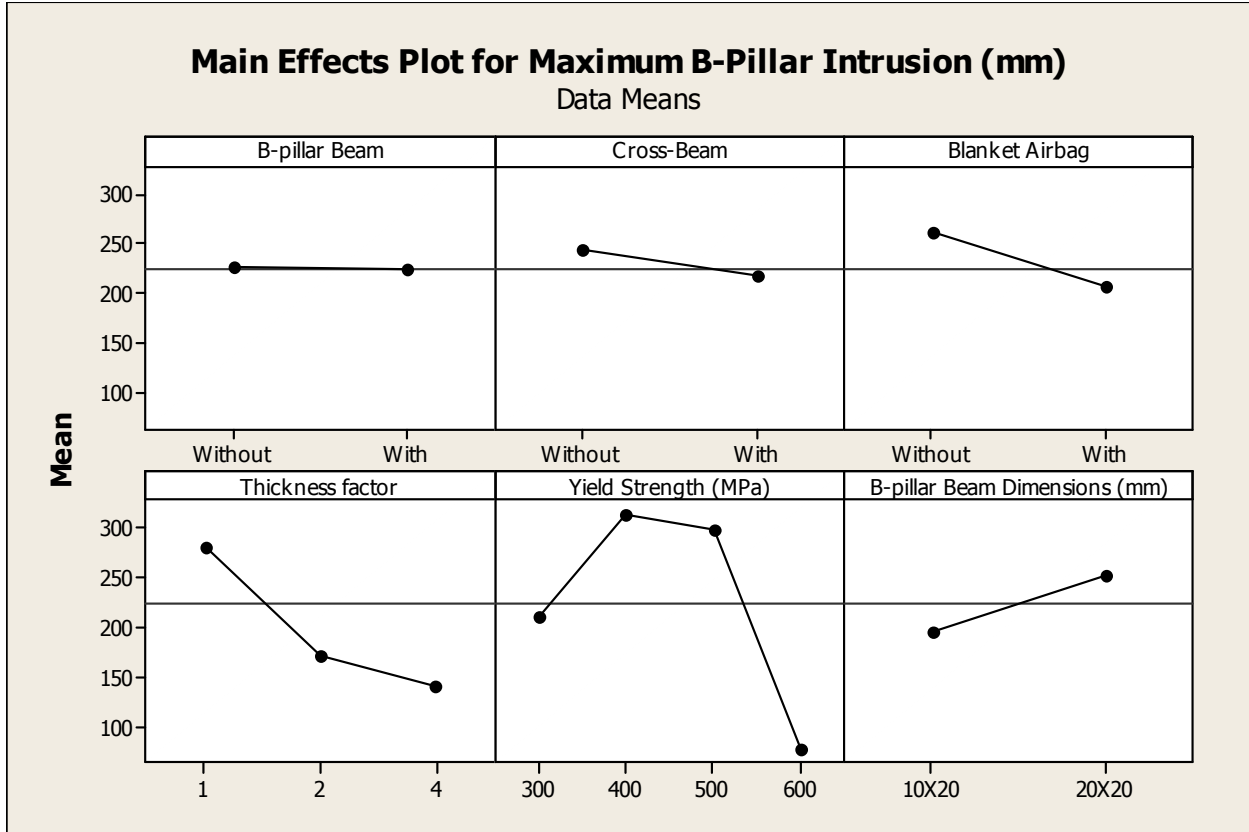


Figure 10.8: Main effects analysis plot – Maximum B-pillar intrusion (mm)

Figure 10.9 through Figure 10.11 plot the Pareto chart of effects for AMPS, maximum pressure, and maximum intrusion respectively. It is seen that none of the combined parameters were significant for AMPS or maximum pressure. However, the additional of a cross beam seemed to make a significant contribution in reducing B-pillar intrusion. Although not significant, a combination of a B-pillar beam and cross beam played a role in reducing intrusion.

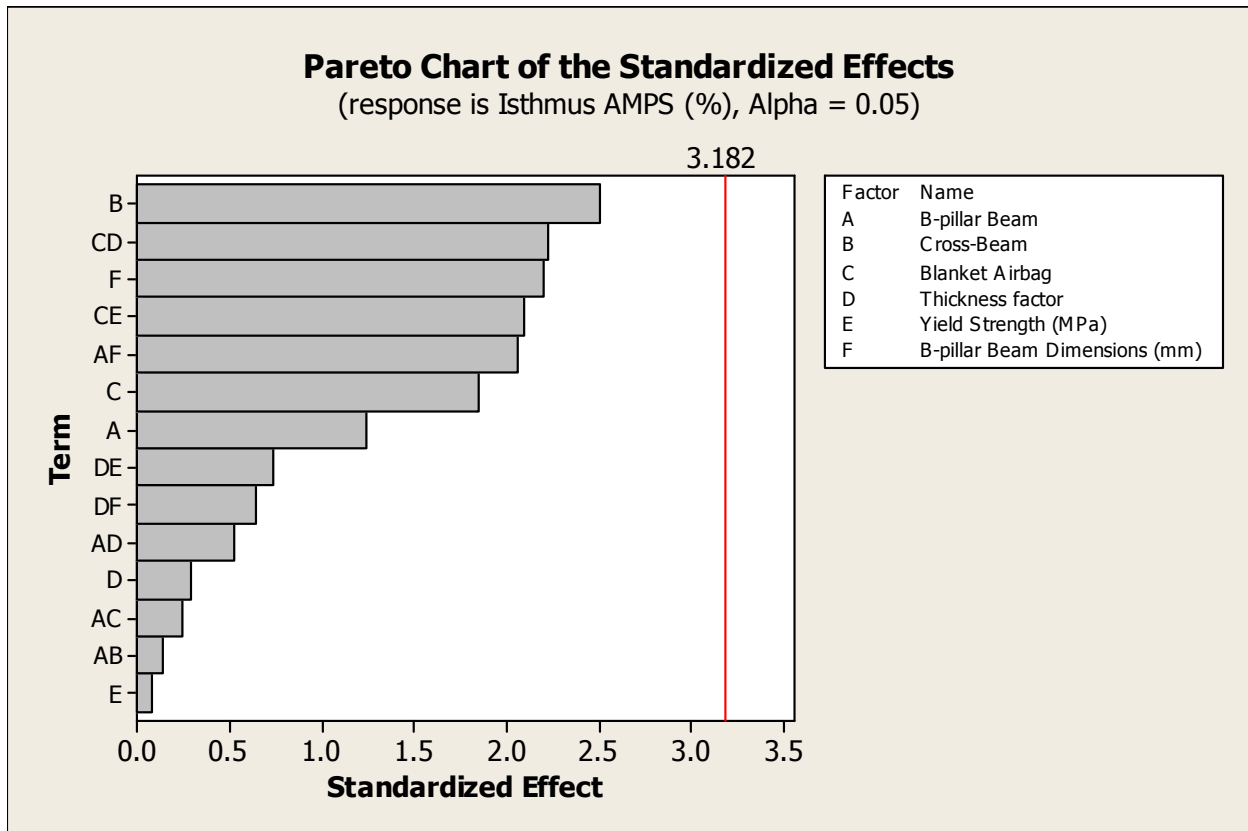


Figure 10.9: Pareto chart of effects for AMPS

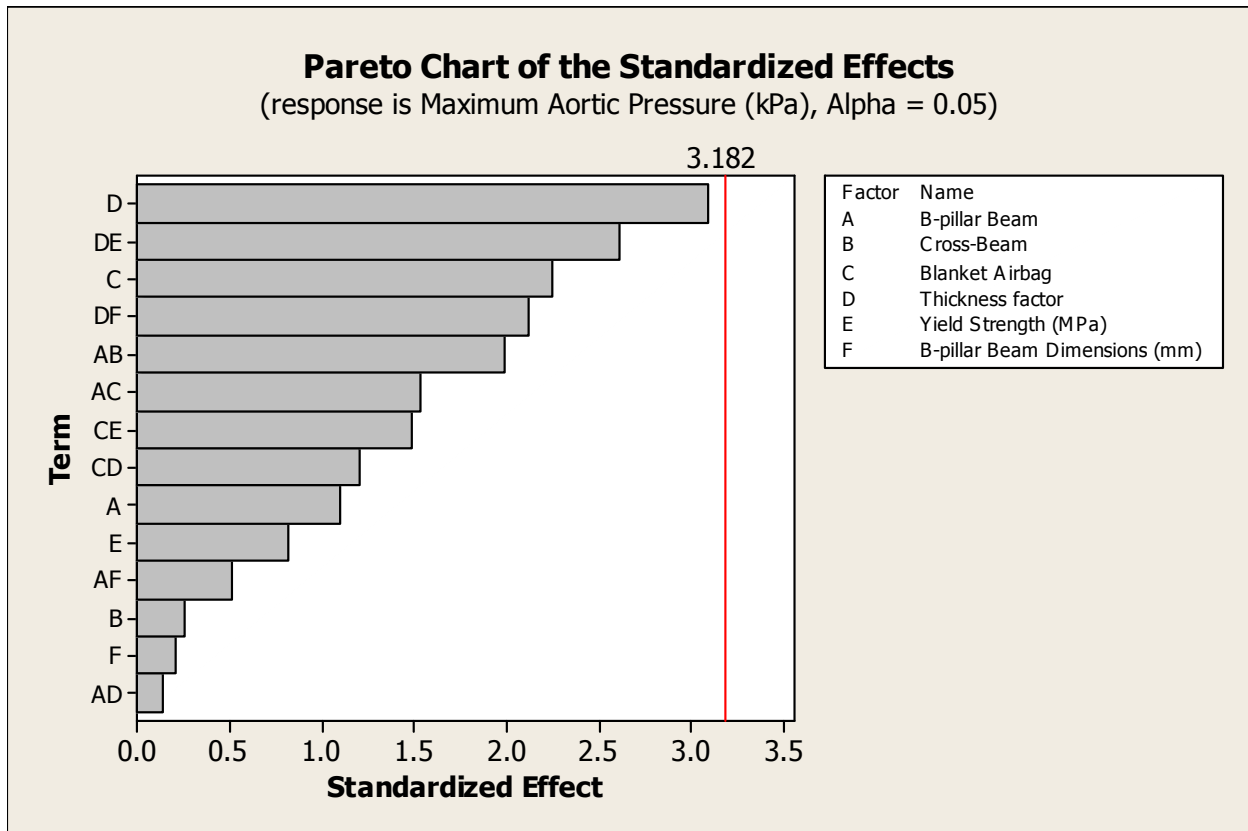


Figure 10.10: Pareto chart of effects for maximum pressure

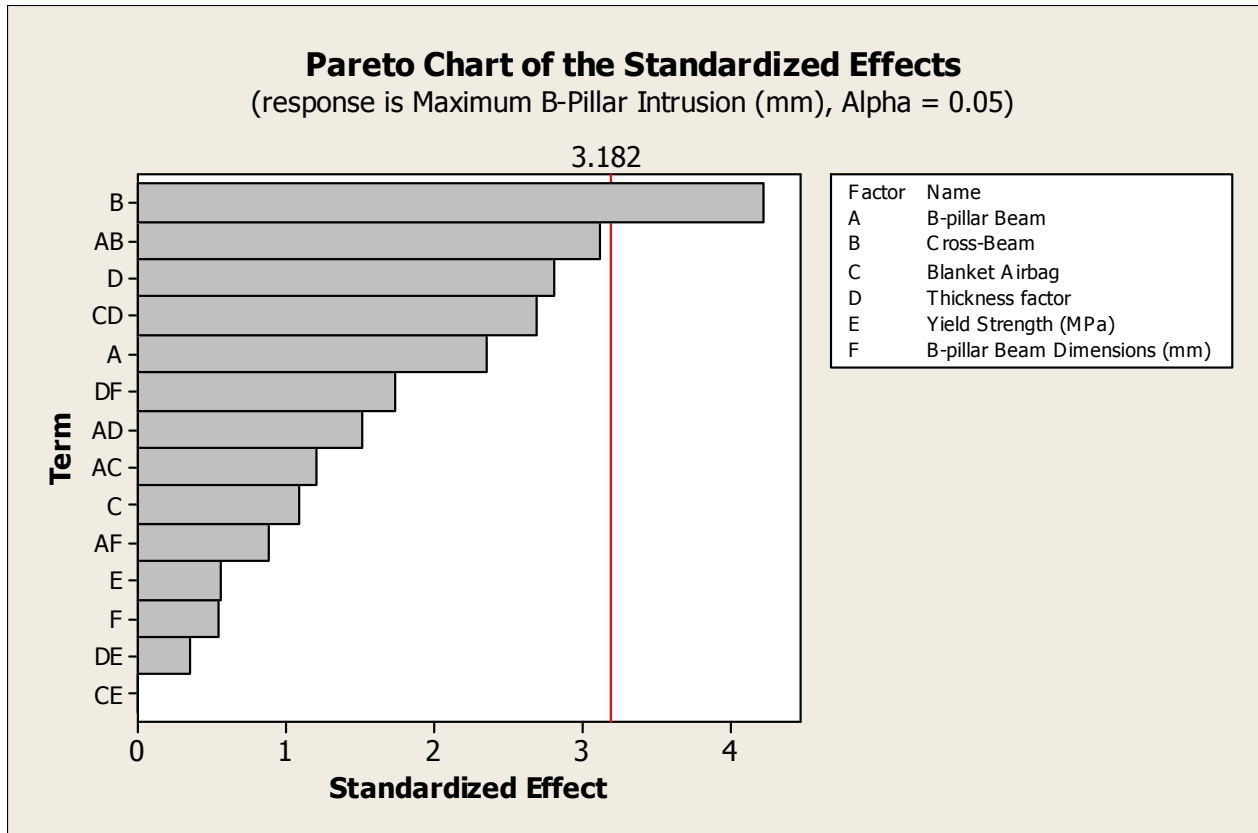


Figure 10.11: Pareto chart of effects for maximum B-pillar intrusion

10.4 AIM E1 - Conclusions

Comparing data from actual scene photographs and FE simulation data, it is strongly evident that the vehicle B-Pillar is the site most likely to be the major causative factor in initiating maximum aortic strain and chest forces. The current study suggest that the protective effects of an improved side-construction standard can be enhanced further by the more rational placement of an airbag-like structure, to buffer head and chest contact with the B-Pillar along its entire length from car seat to roof. It is suggested that the combination of these two safety measures, B-pillar beam and thickness is likely to result in a significant reduction in both head and aortic Isthmus

injury and thus to substantially reduce mortality subsequent to lateral motor vehicle crashes. It is to be noted that the current study did neither consider the effect of increase of weight on the fuel efficiency of the car.

10.5 AIM E2 - Materials and Methods

From Chapter 9, it was seen from high-speed FE simulations of race car accidents that the AMPS and maximum pressure in the aorta were significantly lower than those reported in either of the survival or fatal CIREN reconstructions. The seat played a crucial role in reducing the thoracic deformation leading to reduced AMPS in the aorta.

In the current study, 11 simulations were carried out using the WSHBM and scaled FE vehicle models with a **New redesigned seat** called **Advanced Bilateral Protection Seat[®] (ABPS[®])** with an objective

- a. Prevent / reduce direct thoracic contact with the intruding B-pillar and door structures
- b. Engage the shoulder thereby preventing / reducing a load path to the clavicle and the spine, thus reducing relative motion between the spine and sternum

Figure 10.9 shows the structure of the redesigned seat with shoulder and head padding with the WSHBM. **It is to be noted that a patent filing has been initiated for the Advanced Bilateral Protection Seat[®] (ABPS[®]).** Table 10.3 outlines the material properties and LS-DYNA material models used in the simulations.

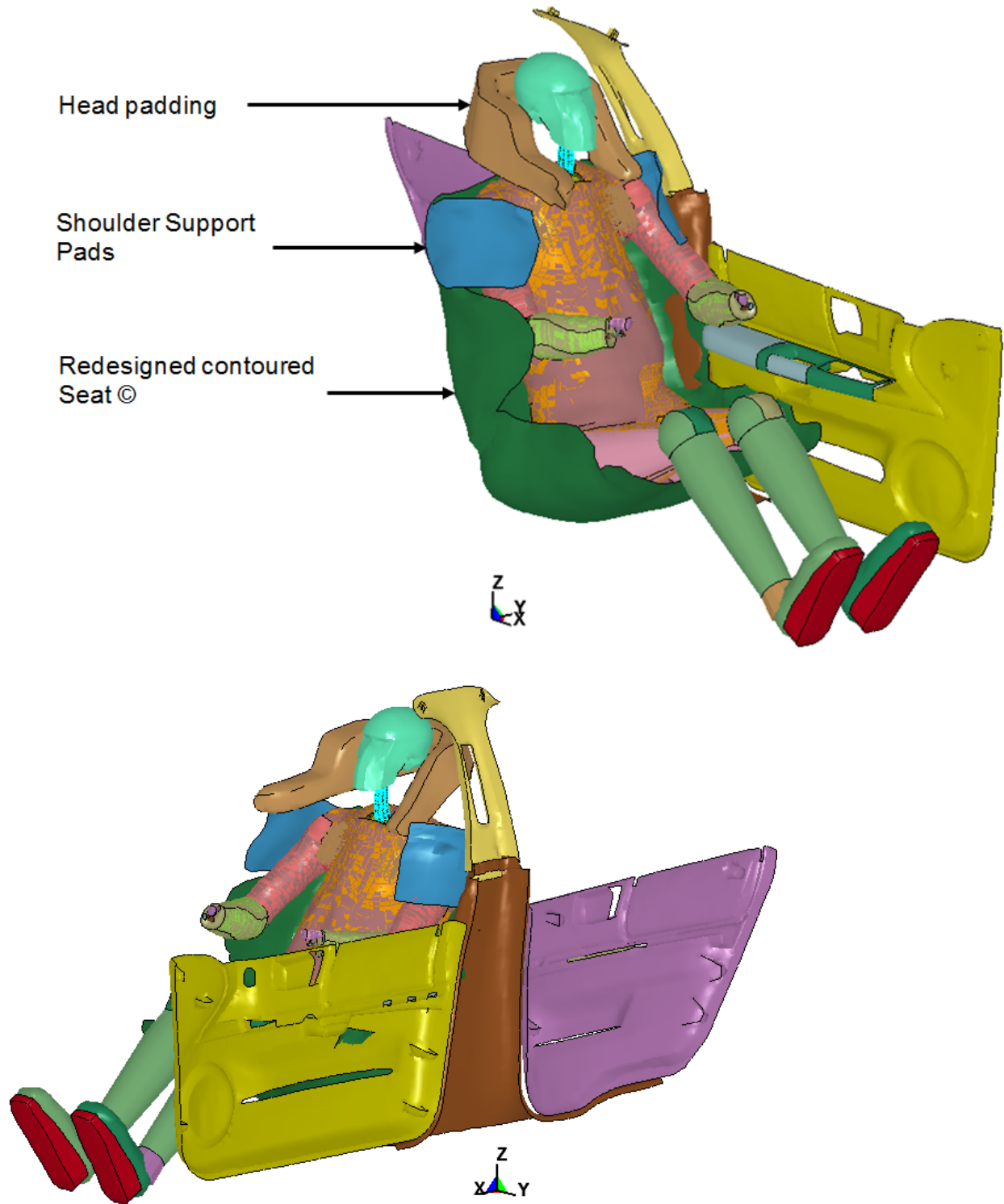


Figure 10.9: Shows the WSHBM with the new redesigned contoured seat, shoulder support pads and head padding – Advanced Bilateral Protection Seat[®] (ABPS[®])

Table 10.3: Material properties and LS-DYNA material models used for the New Redesigned Seat

Component	LS-DYNA Material Model	Material Property		
		Young's Modulus, E (GPa)	Density, ρ (kg/mm ³)	Poisson's Ratio, μ
Seat	*MAT_ELASTIC	210	7.85×10^{-6}	0.3
Shoulder Pad	*MAT_ELASTIC	210	7.85×10^{-6}	0.3
Shoulder and head Pad	*MAT_SOIL_AND_FOAM	7.901×10^{-1}	1.228×10^{-7}	

Table 10.4 outlines the simulation parameters, which were chosen to compare with the initial CIREN reconstructions outlined in Chapters 6 and 8.

Table 10.4: Input design factors for the seat based countermeasure

Run #	PDOF (Degrees)	Delta 'V' (km/hr)	Comparison CIREN Case #	Vehicle / Object History	Occupant Status
1	255	33.6	T1	Car-SUV	Survived
2	285	29.1	T2	Car-Van	Survived
3	300	22.0	T3	Car-SUV	Survived
4	310	62	4	Car-Car	Survived
5	260	41	17	Car-Van	Survived
6	310	27.5	5	Car-Tree	Fatality
7	280	55	6	Car-SUV	Fatality
8	280	59	7	Car-Car	Fatality
9	320	27.6	8	Car-Pole	Fatality
10	270	47	15	Car-SUV	Fatality
11	270	54.4	16	Car-SUV	Fatality

The simulations were carried out in two stages as described in Chapter 5. In Stage I, scaled vehicle FE models were positioned as per the PDOF described in the CIREN case report and velocities applied as resolved vectors. The deformation patterns (C1 through C6) were matched closely to those reported from the actual crash scene. Only those structures, which encountered the occupant, were isolated and their motions recorded in binary interface files. In Stage II, the WSHBM along with the new redesigned contoured seat, shoulder padding and head support pads along with the side isolated structures from Stage I were simulated with the interface files as inputs to the model. The interface files provided the transition between the two stages. AMPS,

maximum pressure, and compartmental intrusion were recorded and compared with those reported from 11 CIREN cases previously reconstructed (Chapters 6 and 8).

10.6 Results

11 simulations were carried out using a combination of WSHBM, new redesigned contoured seat (ABPS[®]) which has an integrated shoulder padding and head padding with scaled FE vehicle models. The objective of the study was to reduce aortic strain and pressure, and compare the data to the original CIREN reconstructions. Table 10.5 lists the AMPS and maximum aortic pressure recorded in the cases with ABPS[®] and compares them to the original CIREN reconstructions. Figures 10.10 and 10.11 plots the AMPS and maximum pressure respectively and compares with cases with and without the ABPS[®]. In order to compare the data with earlier CIREN reconstructions (Chapter 6 and Chapter 8), the left side of the table has been repeated for consistency.

Table 10.5: AMPS and maximum pressure for the cases with and without ABPS®

Original CIREN Reconstructions							CIREN Reconstructions with ABPS®				
PDOF (Deg.)	Delta 'V' (km/hr)	CIREN Case #	Vehicle / Object History	Occupant Status	Isthmus AMPS	Maximum Pressure (kPa)	Run #	Isthmus AMPS	Percentage Reduction of AMPS (%)	Maximum Pressure (kPa)	Percentage Reduction of maximum pressure (%)
255	33.6	T1	Car-SUV	Survived	0.0981	74.2	1	0.0522	46.78	66.9	9.83
285	29.1	T2	Car-Van	Survived	0.0812	67.9	2	0.0430	47.04	57.3	15.611
300	22.0	T3	Car-SUV	Survived	0.1233	59.8	3	0.0387	68.61	45.9	23.24
310	62	4	Car-Car	Survived	0.1452	114.8	4	0.0859	40.84	73.0	36.41
260	41	17	Car-Van	Survived	0.1941	103.8	5	0.1144	41.06	89.2	14.06
Average					0.1284±0.044	84.10±23.88		0.0668±0.032	48.87±11.43	66.46±16.33	19.83±10.45
310	27.5	5	Car-Tree	Fatality	0.1658	108.7	6	0.0461	72.19	90.2	17.01
280	55	6	Car-SUV	Fatality	0.2767	134.0	7	0.2422	12.46	105.7	21.11
280	59	7	Car-Car	Fatality	0.2823	132.2	8	0.0351	87.56	66.9	49.39
320	27.6	8	Car-Pole	Fatality	0.1851	104.6	9	0.0753	59.31	44.3	57.64
270	47	15	Car-SUV	Fatality	0.1921	102.0	10	0.1365	28.94	96.8	5.09
270	54.4	16	Car-SUV	Fatality	0.2955	136.0	11	0.2045	30.79	110.2	18.97
Average					0.2329±0.057	119.58±16.05		0.1233±0.085	48.54±28.97	85.68±25.34	28.21±20.54
Overall Average					0.1854±0.074	103.45±26.47		0.0977±0.071	48.69±21.73	76.95±22.99	24.41±16.55

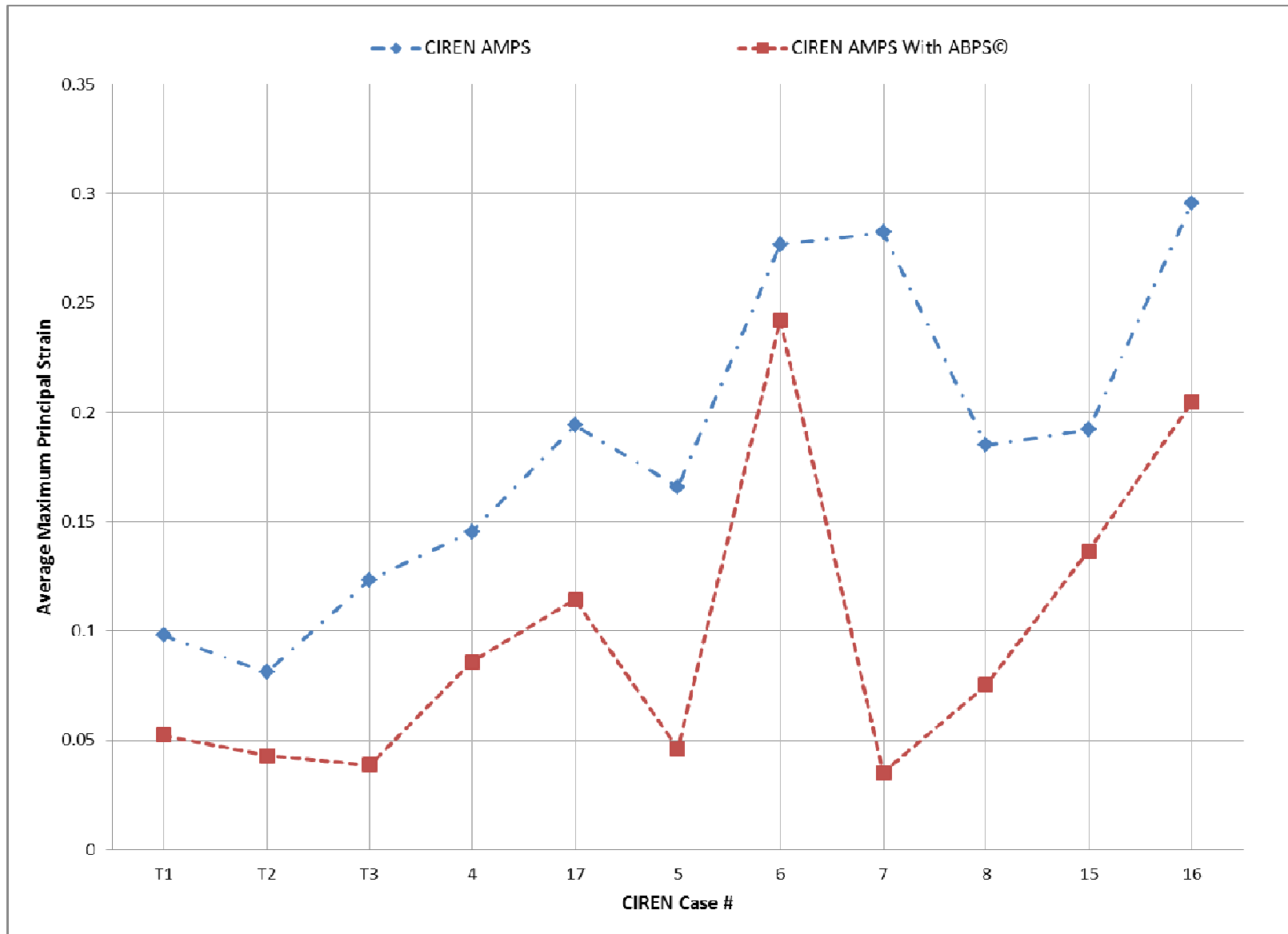


Figure 10.10: AMPS - With and without ABPS[®]

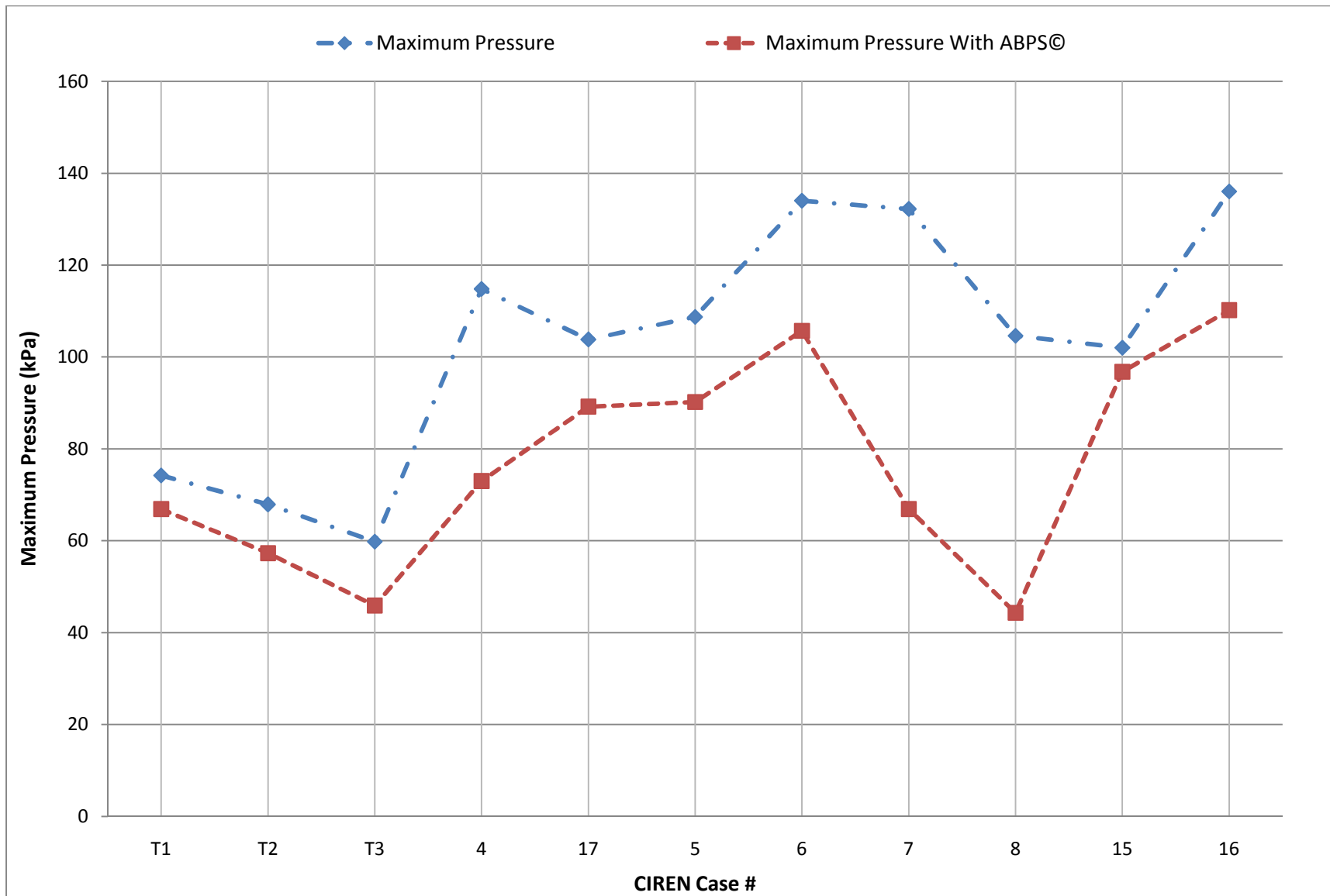


Figure 10.11: Maximum Pressure (kPa) in the aorta - With and without ABPS®

For the CIREN cases reconstructed with ABPS[®], the average AMPS was 0.0977 ± 0.071 and the average maximum pressure was 76.95 ± 22.99 kPa. A One-Way Analysis of Variance (ANOVA) was performed; both AMPS ($p=0.01$) and maximum pressure ($p=0.021$) were found to be significantly lower than the initial CIREN reconstructions.

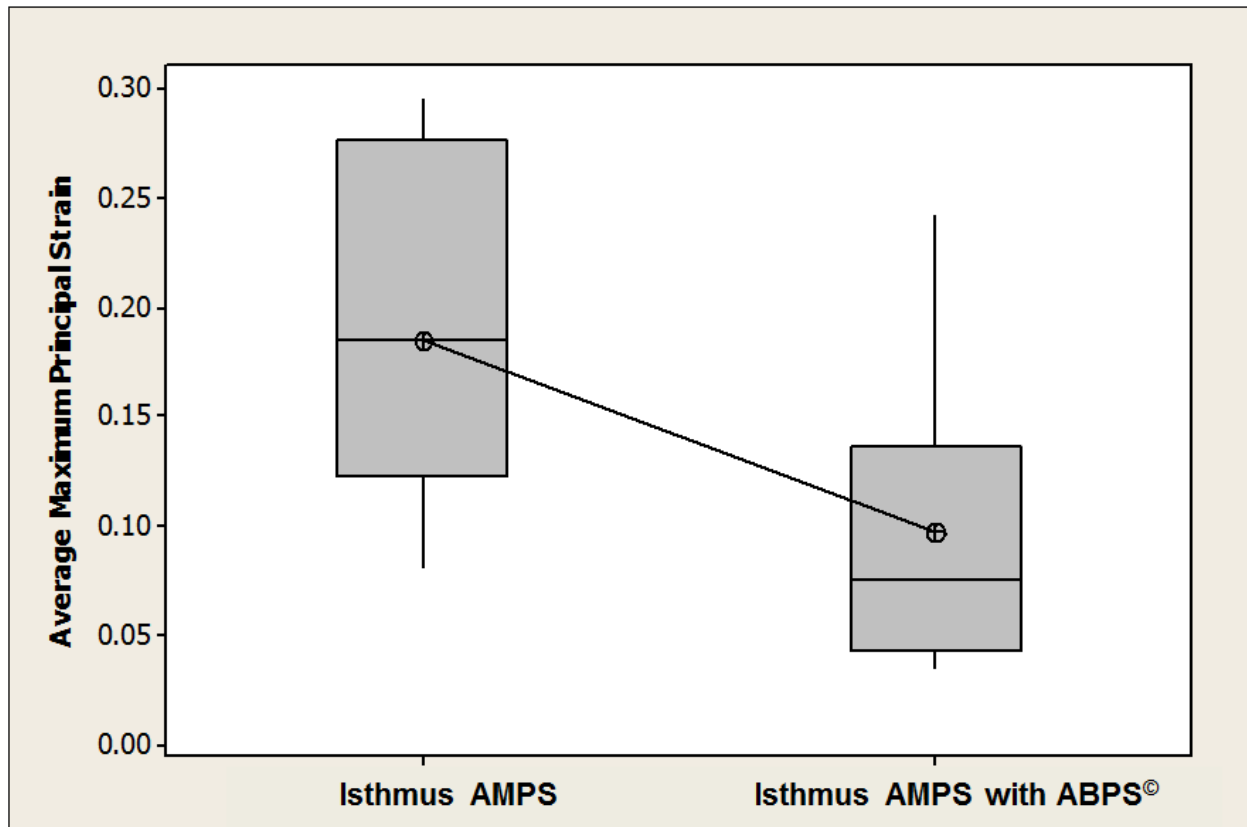


Figure 10.12: Box-plot of AMPS for cases with and without ABPS[®]

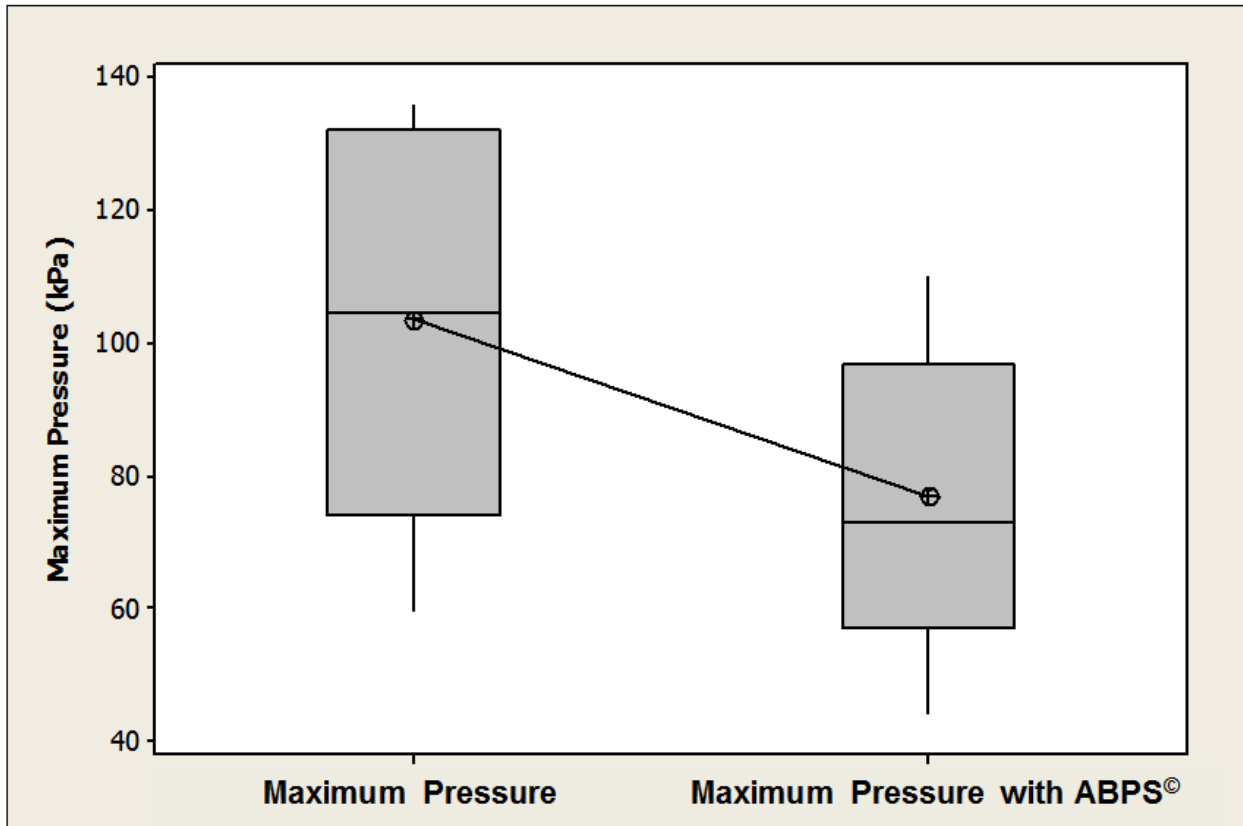


Figure 10.13: Box-plot of maximum pressure for cases with and without ABPS[®]

Figures 10.12 and 10.13 are box-plots of AMPS and maximum pressure respectively. The horizontal line indicates the median of the population. It is seen that there is an average of 47% decrease in AMPS and an average of 28% decrease in maximum pressure in the aorta with the usage of ABPS[®]. It is to be noted that the current study did not account for the increase/change in weight and how it affects the fuel economy and performance of the car.

10.7 AIM E2 - Conclusions

Eleven CIREN cases (from Chapters 6 and 8) were reconstructed with a newly redesigned contoured seat with shoulder and head support pads; called the Lateral Impact Protection Seat System (ABPS[®]). In conclusion,

- Overall average AMPS was 0.0977 ± 0.071 as compared to the 0.1854 ± 0.074 for the original CIREN reconstructions
- There was a **47% reduction in AMPS with ABPS[®]**
- Overall average maximum pressure was 76.95 ± 22.99 kPa as compared to the 103.45 ± 26.47 kPa for the original CIREN reconstructions
- There was a **28% reduction in maximum pressure with ABPS[®]**

CHAPTER 11**CONCLUSIONS, LIMITATIONS, AND SCOPE FOR FUTURE WORK****11.1 Conclusions**

The current study delves further into understanding the mechanism of aortic trauma from real world CIREN data by using a combination of validated FE human body model consists of detailed geometry and organ placement along with validated vehicle models. Figure 11.1 summarizes the conclusions for each objective, aimed at understanding and reducing the trauma associated TRA.

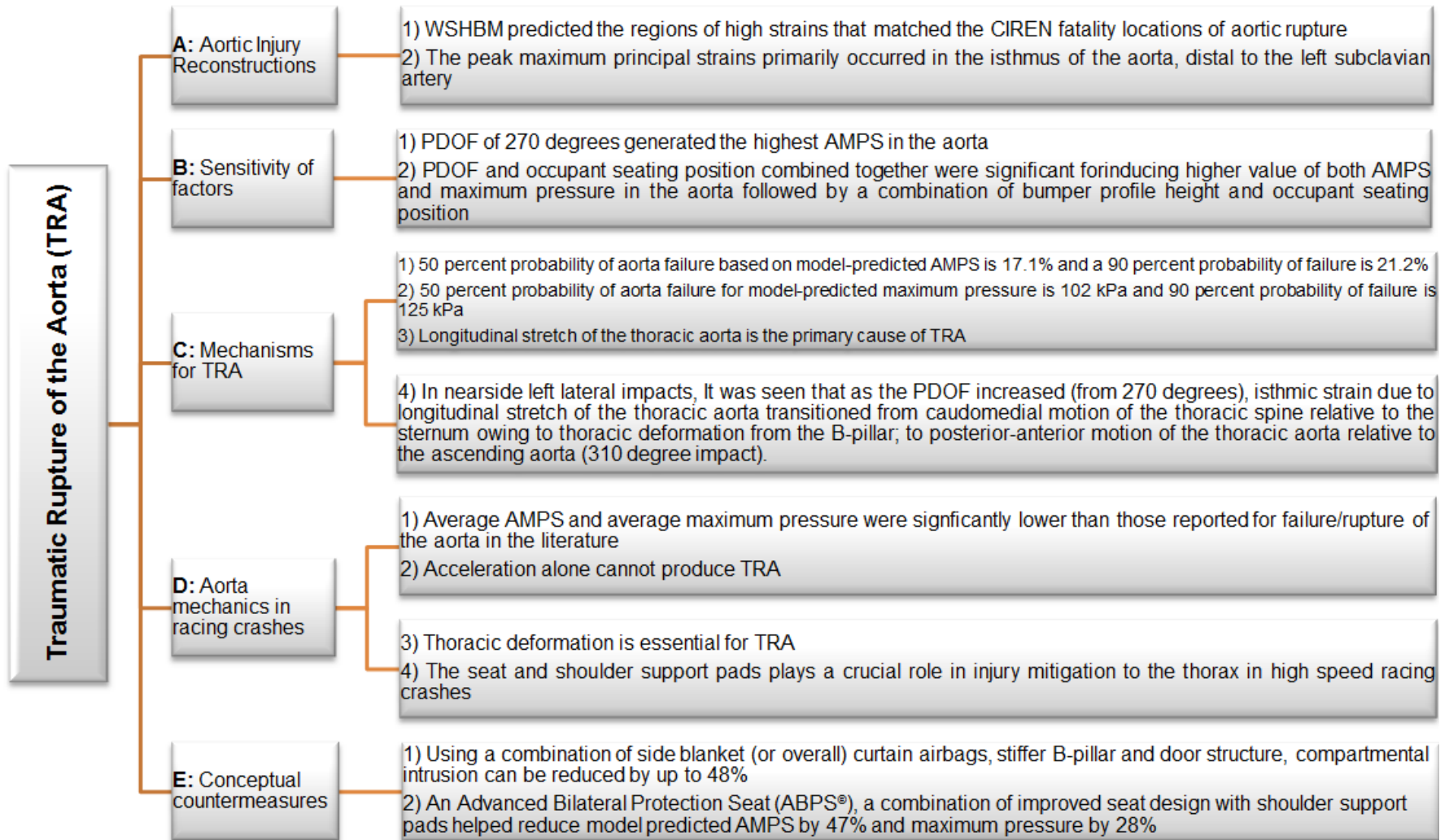


Figure 11.1: Aims and Conclusions - Summary

The aortic injury reconstructions provide a unique insight, using a combination of real world CIREN data and validated FE models in the realm of TRA. From the NASS-CDS review, the CIREN cases, and the FE aortic reconstructions, it was seen that in near side left lateral crashes, the B-pillar followed by the interior door structures were primarily responsible for thoracic deformation leading to high aortic strains (Chapter 6).

11.11 CIREN Reconstructions

- The average AMPS were calculated to be 0.22 ± 0.06 and the average maximum pressure in the aorta was predicted to be 117 ± 15 kPa (fatal and survival cases).
- For CIREN cases with no fatality, the average AMPS was 0.12 ± 0.04 and the average maximum pressure was 84.10 ± 23.88 kPa.
- For the CIREN cases with fatality due to aortic rupture, the average AMPS was 0.23 ± 0.05 and the average maximum pressure was 119.58 ± 16.05 kPa.
- A 50 percent probability of aortic failure based on model-predicted AMPS was 17.1% and a 90 percent probability of failure for AMPS was 21.2%.
- A 50 percent probability of aortic failure based on model-predicted maximum pressure was 102 kPa and a 90 percent probability of failure based on model-predicted maximum pressure was 125 kPa.
- Although there was an increase in aortic pressure in the simulations, it may not be solely responsible for aortic failure.
- The peak maximum principal strains primarily occurred in the isthmus of the aorta, distal to the left subclavian artery.

- A large percentage of the cases (87.5%) reconstructed had multiple left rib fractures, predominantly from the fourth to the ninth rib.
- A great number of the cases (75%) reconstructed showed high strains in the spleen due to rapid caudo-medial motion of the rib cage induced from the intruding B-pillar.
- Sternum displacement alone may not be sufficient to be responsible for TRA.
- Thoracic deformation pattern plays a role in TRA.
- Longitudinal stretch of the thoracic aorta is the primary cause of TRA.
- In nearside left lateral impacts, It was seen that as the PDOF increased (from 270 degrees), isthmic strain due to longitudinal stretch of the thoracic aorta transitioned from caudomedial motion of the thoracic spine relative to the sternum owing to thoracic deformation from the B-pillar; to posterior-anterior motion of the thoracic aorta relative to the ascending aorta (310 degree impact).
- Kinematics data from the FE simulations matched well with data reported by Hardy et al. (2008) and showed that the isthmus of the aorta moved medially and anteriorly during nearside left lateral impacts and transitioned to a dorsocranial motion.

11.12 DOCE Simulations

- Of the four PDOFs simulated, a PDOF of 270 degrees generated the highest average maximum principal strain in the aorta.

- PDOF and occupant seating position combined together were significant for the high magnitude of AMPS and maximum pressure in the aorta followed by a combination of bumper profile height and occupant seating position.
- Although not significant as individual factors, results of DOCE concluded that occupant-seating position, bumper profile height, and PDOF of impact, in that order, play crucial roles in the generation of strain and pressure in the aorta, a potential injury mechanism responsible for traumatic rupture of the aorta in automobile crashes.

11.13 High-speed racings simulations

- The average AMPS for the high-speed crashes (Begeman and Melvin (2002)) were 0.15 ± 0.01 while the average maximum pressure was 110.50 ± 4.25 kPa.
- The average model-predicted AMPS was significantly less than that calculated for fatality in the CIREN reconstructions in Chapter 6; for rupture reported by Shah et al. (2006) and Hardy et al. (2008).
- The maximum pressure were significantly less than those calculated for fatality as reported by the CIREN reconstructions in Chapter 6; for rupture experimentally measured by Bass et al. (2001) and Hardy et al. (2008).
- Six-point restraint system does not have significant effect of what in high-speed lateral racing crashes.
- Thoracic deformation was significantly less as compared to the CIREN cases in Chapters 6, 7, and 8.

- Thoracic deformation is absolutely necessary for TRA
- Acceleration alone cannot produce TRA
- The seat and shoulder support pads plays a crucial role in injury mitigation to the thorax in high speed racing crashes

11.14 Conceptual countermeasures

- Rational placements of an airbag like structure (blanket airbag); to buffer head and chest contact with the B-Pillar along its entire length from car seat to roof is seen to reduce aortic strain.
- A combination of B-pillar beam and increase in beam thickness is likely to result in a significant reduction in both head and aortic isthmus injury and thus to substantially reduce mortality subsequent to lateral motor vehicle crashes.
- A newly redesigned seat and shoulder support called **Advanced Bilateral Protection Seat[®] (ABPS[®])** was utilized to compare AMPS and maximum pressure in the aorta with the original CIREN reconstructions
- With ABPS, the overall average AMPS was 0.09 ± 0.07 as compared to 0.18 ± 0.07 for the original CIREN reconstructions
- There was a **48% reduction in AMPS with ABPS[®]**
- Overall With ABPS, the overall average maximum pressure was 76.95 ± 22.99 kPa as compared to the 103.45 ± 26.47 kPa for the original CIREN reconstructions
- There was a **24% reduction in maximum pressure with ABPS[®]**

11.2 Limitations and commendations for future work

The current version of the WSHBM represents a 50th percentile adult male model with a detailed descriptions within the thoracic cavity and has an anatomically accurate aorta model (Shah et al. 2001). However, it should be noted that in the current study, the WSHBM has been simulated without any scaling or personalized aorta model for the CIREN reconstructions. Further, the superior vasculature from the aorta (Brachiocephalic trunk, left common carotid artery, and left subclavian artery) did not lead all the way up to the head (Figure 11.2); which have been hypothesized to cause stretching of the aortic arch during head/neck excursion (Viano, 1983).

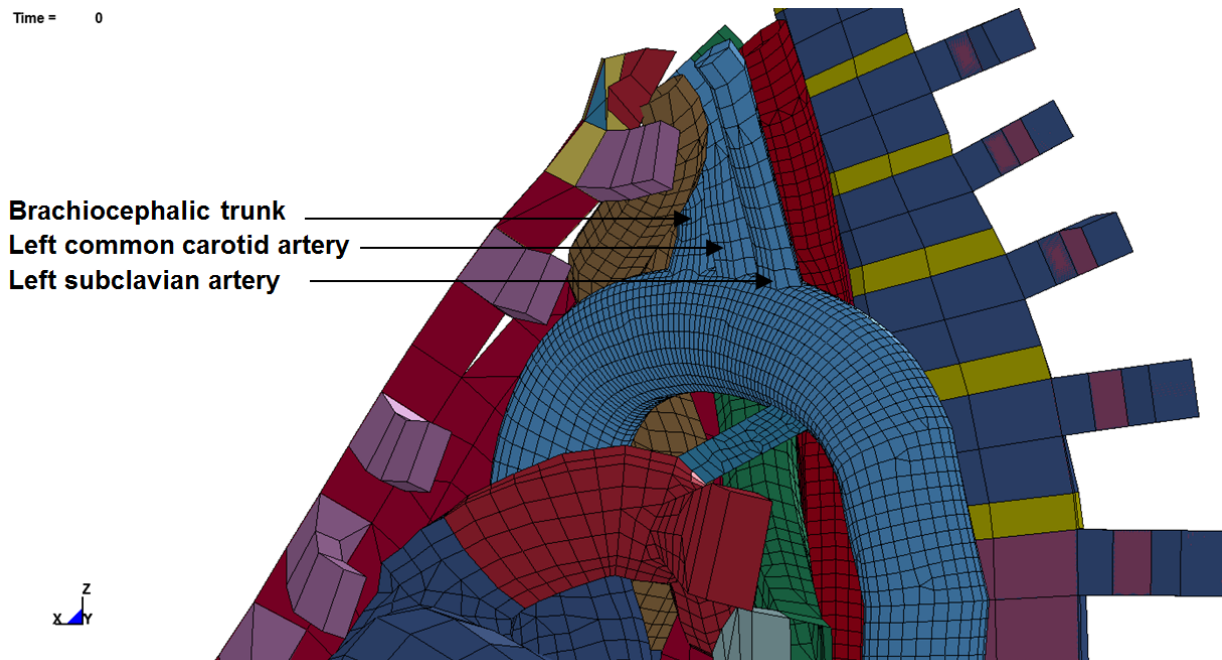


Figure 11.2: Attachment of the superior vasculature in the WSHBM

A detailed neck model with placement of the superior vasculature beyond the level of the clavicle would be useful in validation of the hypothesis of aortic arch motion due to rapid flexion/extension in frontal impacts and medial/lateral rotation in side impacts.

Even though the vehicle models were accurately scaled to match the size and weight of the struck and striking vehicles, the stiffness and interior compartment details did not simulate the actual vehicles involved. The bumper profiles of each striking vehicle and the status of pre-crash braking were different, thus generating varying crush patterns, which may explain the discrepancies in matching the measured physical deformations reported in Chapter 6, Table 6.4.

Further, Niehoff et al. (2006) evaluated 121 NASS-CDS 2000-2003 cases and concluded that the WinSmash program underestimated the delta-v of the striking vehicle by an average of 23%. Additionally, if the striking vehicle is a front wheel drive, the underestimation of delta-v is up to 31%. In this study, only the 2002 Dodge Caravan FE model was a front wheel drive. It is also important to observe that measured external deformations of the vehicle may not correspond to similar occupant compartment intrusions and contact forces due to differences in elastic and plastic moduli of various interior components. This problem is exacerbated by the fact that deformation profiles were measured at only individual points on the external surface leading to localized variations in the actual and simulated profiles.

It is extremely challenging to truly recreate the intricacies of real world crashes due to inaccuracies in field measurement and the accident reconstruction software,

which is typically based on rigid body dynamics. More importantly, variations in general anatomy and health status of the aorta in the human population are largely unknown.

11.2.1 Atherosclerosis

Heart disease, typically atherosclerotic cardiovascular disease remains the primary cause of death and disability in the United States (American Heart Association, 2008). Atherosclerosis is a vascular disease associated with the accumulation of lipids leading to incursion of leucocytes and smooth muscle cells into the intima, which typically leads to the formation of atheroma. Plaque is typically fibrous tissue of varying density and cellularity, primarily consisting of calcium, extracellular lipid, and lipid-laden foam cells (Holzapfel et al. 2006). Data from the literature have shown that during automotive crashes, there is a very high incidence of aortic laceration and embolism leading to death and disability (Holzapfel et al. 2006; Sommer et al. 2008). Hence, it is important to develop a constitutive model by characterizing the material properties of these plaques to be used for FE applications.

It is seen that calcified aortic plaques changes the elastic properties of the aorta making it inextensible in the region of calcification (Holzapfel et al. 2004). Viano (1983) suggested that the presence of atherosclerotic plaque is the weakest link in any traumatic aortic rupture. More recently, Hardy et al. (2008) agreed with Viano's conclusion in their cadaver tests and suggested that diseased aortas may have reduced failure strengths and most failures occur in the region surrounding the diseased tissue. This could play a vital role in determining the failure threshold as well as a possible

reason for occupant-specific aortic failure, which was not considered in the WSHBM model.

The aorta in the current WSHBM is modeled using isotropic linear elastic membrane elements. The Young's modulus was approximated from the uniaxial experiments on the human aortic tissue reported by Mohan and Melvin (1982). Constitutive modeling of the aortic tissue is crucial to any FE modeling efforts aimed at investigating the mechanisms of aortic rupture. Shah et al. (2006) in their previous studies have attempted to model the non-calcified aortic tissue to simulate their high-speed bi-axial tissue testing. As an initial attempt, the aorta was considered transversely orthotropic for simplicity of analysis.

Several published FE modeling efforts by other researchers have used variety of constitutive models for the aortic tissue. Richens et al. (2004) used the Blatz-Ko rubber material model to represent an isotropic finite element aorta model with a Poisson's ratio of 0.463. Their attempt to use the isotropic linear elastic, orthotropic linear elastic, and Ogden material models resulted in numerical instabilities beyond 10% stretch. The basis for selection of Blatz-Ko rubber was that it performed stably up to 80% strain. Darvish et al. (2004) assumed a second order Mooney-Rivlin rubber to model isotropic aortic tissue. The FE aorta model response was compared against quasi-static and dynamic uniaxial tensile tests reported by Mohan and Melvin (1982). Similarly, Delfino et al. (1997) used a hyperelastic material model to study residual stresses in the human carotid artery bifurcation.

For future aorta model developments, it is suggested that the model should include:

- Three-layer aorta model (Holzapfel et al. 2006)
- Non-linear orthotropic material model (*MAT_OPTIONTROPIC_ELASTIC material model in LS-DYNA 971)
- Blood flow modeling (ALE material modeling in LS-DYNA 971)
- Atherosclerotic plaque deposits (Holzapfel et al. (2004))

It should be noted that the response of the aorta is largely dependent on the material properties, element quality, and boundary conditions of all the structures encompassing it. Hence, a detailed validation with improved material models, mesh refinement would be essential to improve the response of the aorta.

APPENDIX A

Table A1: Material Properties of the Wayne State Human Body Model – II: Thoracic Cavity (Shah et al. 2007)

Linear Elastic Model			
Vessel/Organ	Young's Modulus, 'E' (GPa)	Density, ' ρ ', (kg/mm ³)	Poisson's Ratio, ' ν '
Aorta and other blood vessels	10.0	2.0 E-06	0.40
Esophagus	3.0	2.0 E-06	0.40
Trachea	15.0	1.0 E-06	0.40
Diaphragm	65.5	1.0 E-06	0.40
Pleura	5.0	1.0 E-06	0.35
Pericardium	25.0	1.0 E-06	0.30
Intercostal Muscles	10.0	1.0 E-06	0.40
Peritoneum	40.0	1.0 E-06	0.40

Table A2: Material Properties of the left side door structure of a 2001 Ford Taurus FE model

Sl. No.	Component Name	LS-DYNA Material Model	Density, ' ρ ', (kg/mm ³)	Young's Modulus, 'E' (GPa)	Poisson's Ratio, ' ν '	Yield Strength (GPa)	Thickness (mm)
2001 Ford Taurus Left Lateral Door							
1	Door Middle	MAT L-24	7.89 E-06	210	0.3	0.30	1.4
2	Outer Door	MAT L-24	7.89 E-06	210	0.3	0.24	1.1
3	Inner Panel Reinforcement	MAT L-24	1.20 E-06	2.8	0.3	0.045	4.8
4	Detail Door Panel	MAT L-24	1.20 E-06	2.8	0.3	0.045	2.31
5	Lower Left B-Pillar	MAT L-24	1.20 E-06	2.8	0.3	0.045	3.1
6	Upper Left B-Pillar	MAT L-24	1.20 E-06	2.8	0.3	0.045	3.1
7	Door Middle Rear	MAT L-24	7.89 E-06	210	0.3	0.270	1.4
8	Outer Door Rear	MAT L-24	7.89 E-06	210	0.3	0.210	0.9
9	Inner Panel Reinforcement Rear	MAT L-24	1.20 E-06	2.8	0.3	0.045	4.5
10	Detail Door Panel Rear	MAT L-24	1.20 E-06	2.8	0.3	0.045	2.7
11	Door Side Impact Bar	MAT L-24	7.89 E-06	210	0.3	0.800	1.56
12	Rear Door Side Impact Bar	MAT L-24	7.89 E-06	210	0.3	0.800	1.4

Table A3: Material Properties of the front bumper and hood structures of the striking vehicles used in Phase A of the reconstruction

Sl. No.	Name of Component	LS-DYNA Material Model	Density, 'ρ', (kg/mm ³)	Young's Modulus, 'E' (GPa)	Poisson's Ratio, 'ν'	Yield Strength (GPa)	Thickness (mm)
2002 Ford Explorer							
1	Inner Hood	MAT-L24	7.89 E-06	210	0.3	0.24	0.67
2	Outer Hood	MAT-L24	7.89 E-06	210	0.3	0.20	0.94
3	Left Side Fender	MAT-L24	7.89 E-06	210	0.3	0.20	1.10
4	Left Side Upper Front Outer Rail	MAT-L24	7.89 E-06	210	0.3	0.20	1.10
5	Tie-Bar Module	MAT-L24	9.00 E-07	2.8	0.3	0.05	2.80
6	Bumper	MAT-L24	1.20 E-06	2.8	0.3	0.05	2.70
7	Right Side Fender	MAT-L24	7.89 E-06	210	0.3	0.20	1.10
8	Right Side Upper Front Outer Rail	MAT-L24	7.89 E-06	210	0.3	0.20	1.10
9	Front Body Back	MAT-L24	7.89 E-06	210	0.3	0.20	0.92
10	Front Body Top	MAT-L24	7.89 E-06	210	0.3	0.24	1.21
11	Bumper Foam Front Null	MAT-L09	1.20 E-06	X	X	X	0.50
12	Front Bumper Reinforcement	MAT-L24	7.89 E-06	210	0.3	0.30	2.10
13	Bumper Foam Front	MAT-L63	9.13 E-08	0.0306	0.3	X	SOLID SECTION
2002 Dodge Caravan							
1	Inner Hood	MAT-L24	7.89 E-06	210	0.3	0.19	0.62
2	Outer Hood	MAT-L24	1.29 E-05	210	0.3	0.22	0.73
3	Left Side Fender	MAT-L24	7.89 E-06	210	0.3	0.19	0.75
4	Fender Reinforcement	MAT-L24	7.89 E-06	210	0.3	0.37	1.67
5	Bumper	MAT-L24	1.20 E-06	2.8	0.3	0.05	3.55
6	Bumper Beam	MAT-L24	7.89 E-06	210	0.3	0.46	2.04
7	Right Side Fender	MAT-L24	7.89 E-06	210	0.3	0.19	0.75
8	Hood Inner Reinforcement	MAT-L24	7.89 E-06	210	0.3	0.22	0.75
9	Radiator Core	MAT-L26	1.47 E-07	2.07	0.3	0.14	SOLID SECTION
10	Bumper Foam	MAT-L01	7.89 E-08	0.21	0.3	X	SOLID SECTION
11	Radiator Lower Support	MAT-L24	7.89 E-06	210	0.3	0.16	1.87
12	Radiator Core Skin	MAT-L09	7.89 E-06	X	X	X	0.5
13	Bumper Foam Skin	MAT-L09	7.89 E-06	200	X	X	1
2002 Econoline 350							

Sl. No.	Name of Component	LS-DYNA Material Model	Density, 'ρ', (kg/mm ³)	Young's Modulus, 'E' (GPa)	Poisson's Ratio, 'ν'	Yield Strength (GPa)	Thickness (mm)
1	Inner Hood	MAT-L01	8.20 E-07	2.34	0.3	X	2.62
2	Outer Hood	MAT-L01	8.20 E-07	2.34	0.3	X	2.62
3	Left Side Fender	MAT-L24	7.89 E-06	210	0.3	0.27	0.773
4	Left Side Inner Wheel Well	MAT-L24	7.89 E-06	210	0.3	0.21	1.24
5	Left Side Front Engine Bay	MAT-L24	7.89 E-06	210	0.3	0.27	0.96
6	Bumper	MAT-L24	7.89 E-06	210	0.3	0.27	2.37
7	Right Side Fender	MAT-L24	7.89 E-06	210	0.3	0.27	0.77
8	Right Side Inner Wheel Well	MAT-L24	7.89 E-06	210	0.3	0.21	1.24
9	Radiator-Mnt-Uppr	MAT-L24	7.89 E-06	210	0.3	0.27	2.18
10	Radiator-Mnt-Uppr-1	MAT-L24	7.89 E-06	210	0.3	0.27	1.58
11	Right Side Front Engine Bay	MAT-L24	7.89 E-06	210	0.3	0.27	0.96
12	Fender Grill Support	MAT-L24	7.89 E-06	210	0.3	0.27	0.92

APPENDIX B

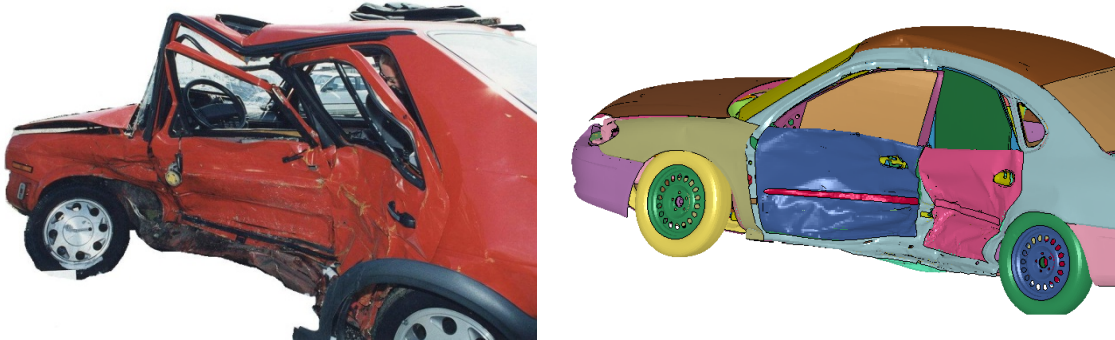


Figure B1: Vehicle deformation comparison of simulated FE vehicle against actual vehicle - CASE 4

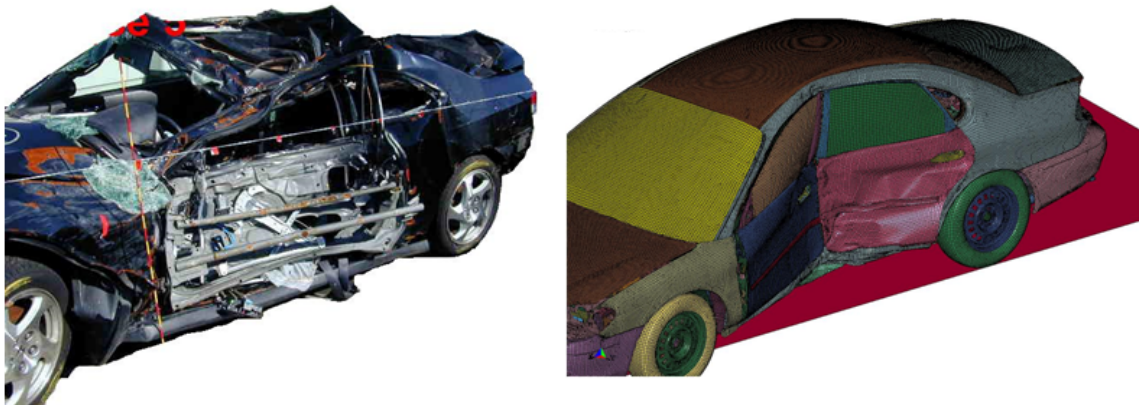


Figure B2: Vehicle deformation comparison of simulated FE vehicle against actual vehicle - CASE 5

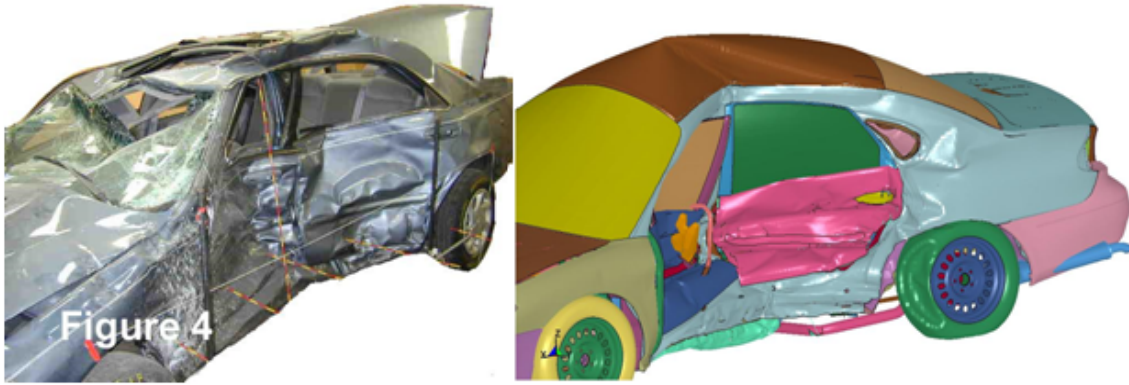


Figure B3: Vehicle deformation comparison of simulated FE vehicle against actual vehicle – CASE 6

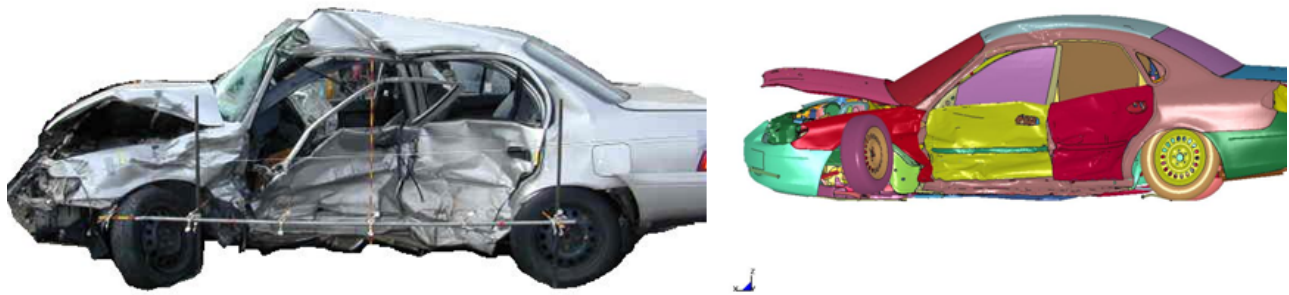


Figure B4: Vehicle deformation comparison of simulated FE vehicle against actual vehicle – CASE 7

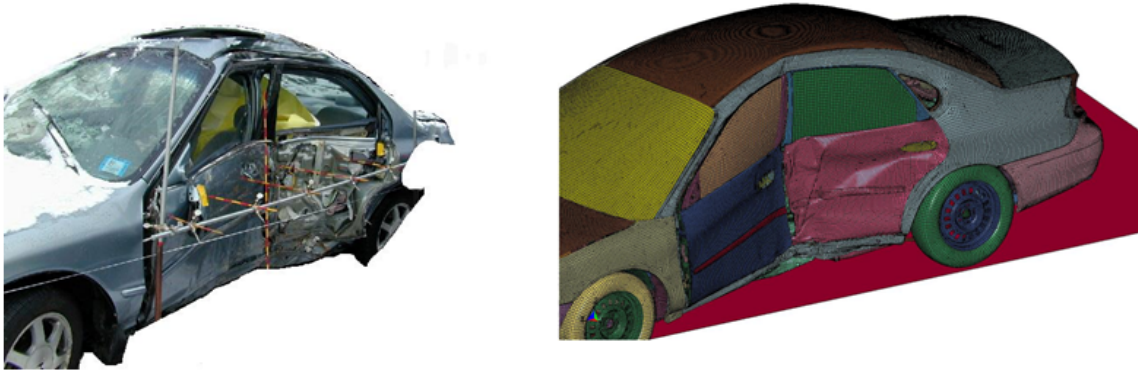


Figure B5: Vehicle deformation comparison of simulated FE vehicle against actual vehicle – CASE 8



Figure B6: Vehicle deformation comparison of simulated FE vehicle against actual vehicle – CASE 15

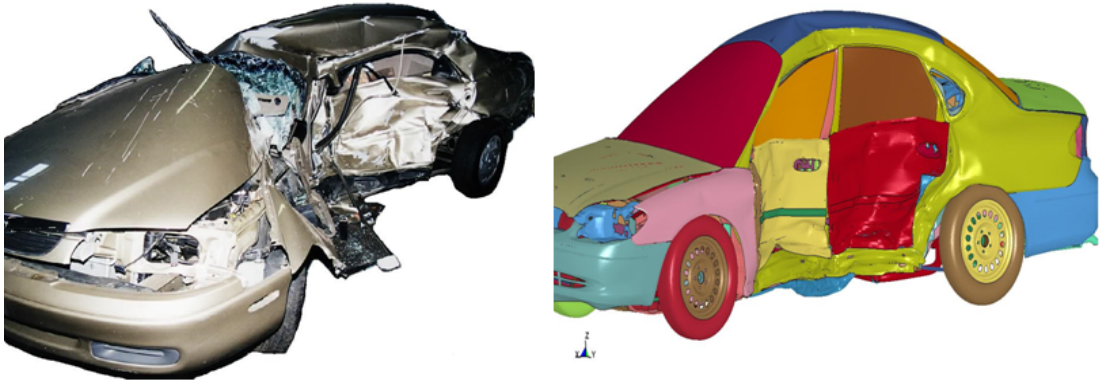


Figure B7: Vehicle deformation comparison of simulated FE vehicle against actual vehicle – CASE 16



Figure B8: Vehicle deformation comparison of simulated FE vehicle against actual vehicle – CASE 17

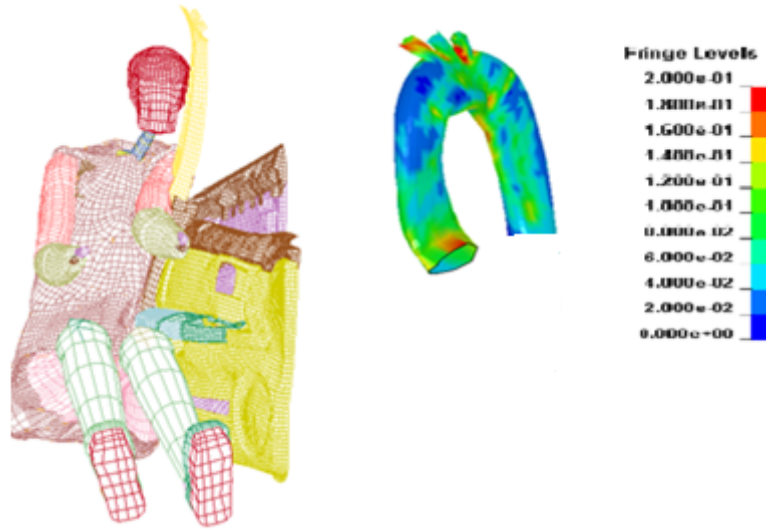


Figure B9: (a) Occupant kinematics and (b) maximum principal strain pattern at the time of maximum vehicle deformation – CASE 4

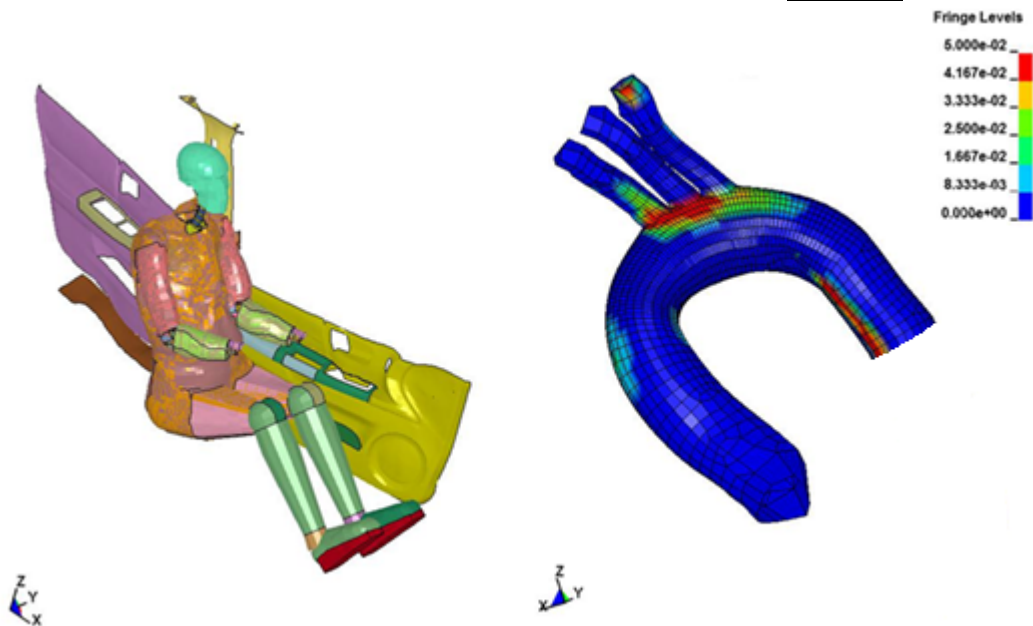


Figure B10: (a) Occupant kinematic and (b) Maximum principal strain pattern at the time of maximum vehicle deformation – CASE 5



Figure B11: (a) Occupant kinematics and (b) Maximum principal strain pattern at the time of maximum vehicle deformation – CASE 6

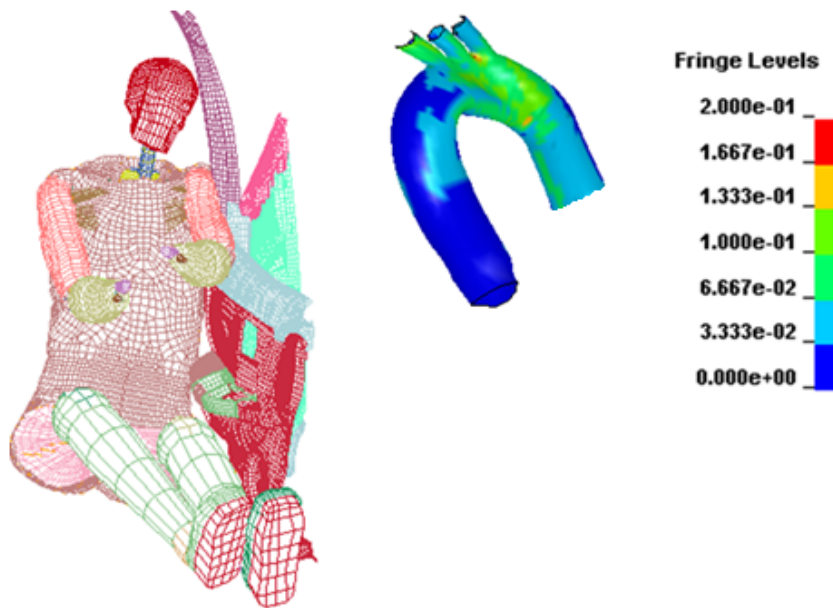


Figure B12: (a) Occupant kinematics and (b) Maximum principal strain pattern at the time of maximum vehicle deformation – CASE 7

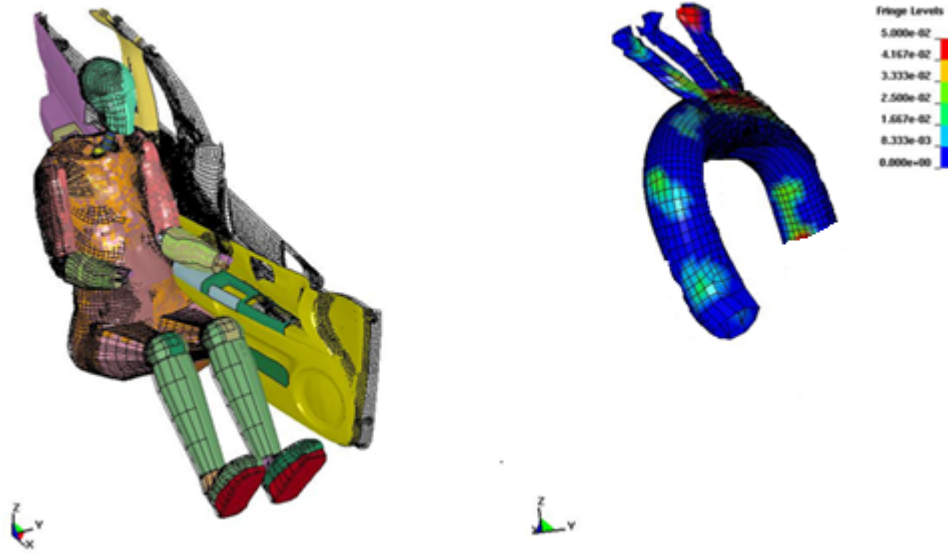


Figure B13: (a) Maximum principal strain pattern and (b) occupant kinematics at the time of maximum vehicle deformation – CASE 8

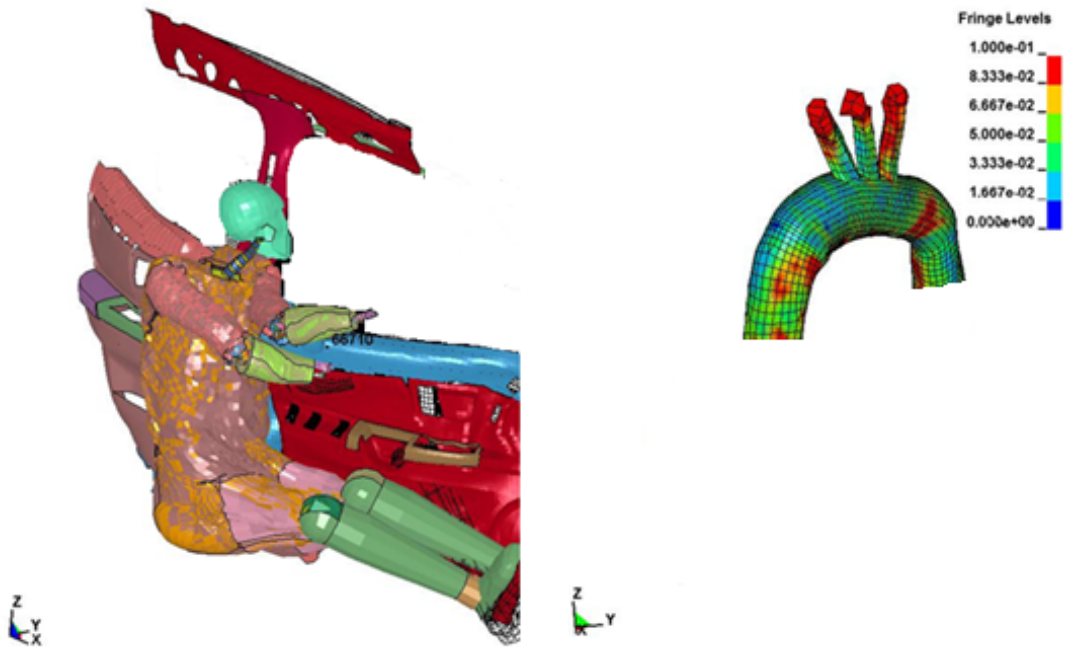


Figure B14: (a) Maximum principal strain pattern (b) Occupant kinematics at the time of maximum vehicle deformation – CASE 15

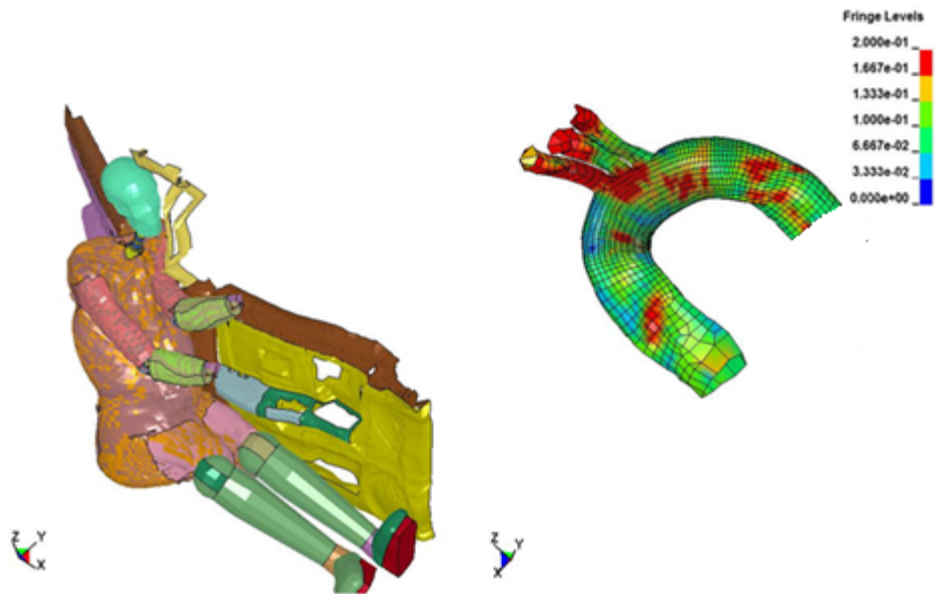


Figure B15: (a) Occupant kinematics and (b) Maximum principal strain pattern at the time of maximum vehicle deformation – CASE 16

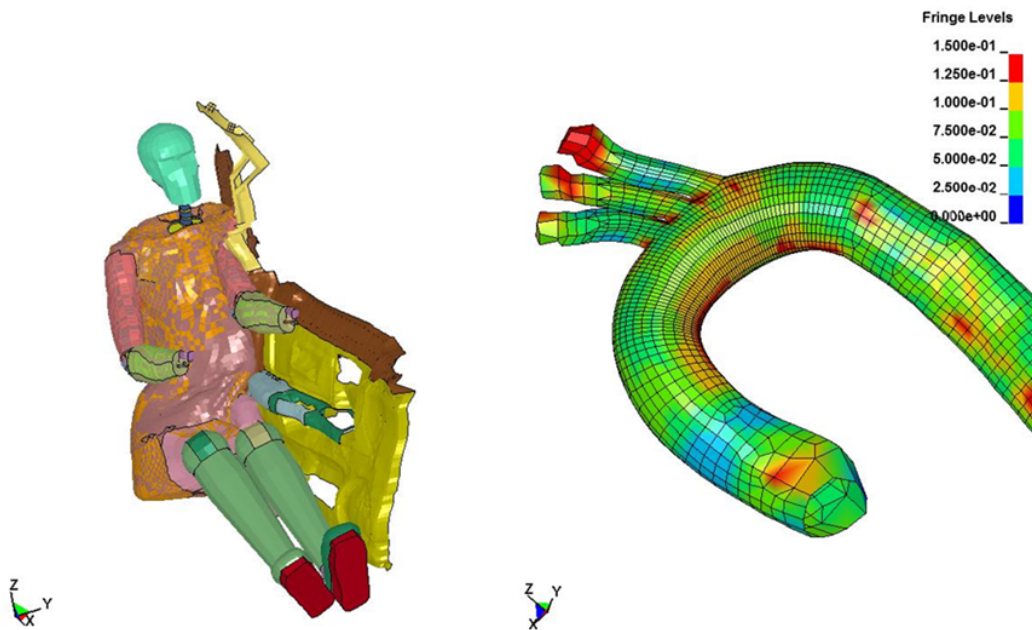


Figure B16: (a) Maximum principal strain pattern (b) Occupant kinematics at the time of maximum vehicle deformation – CASE 17

APPENDIX C

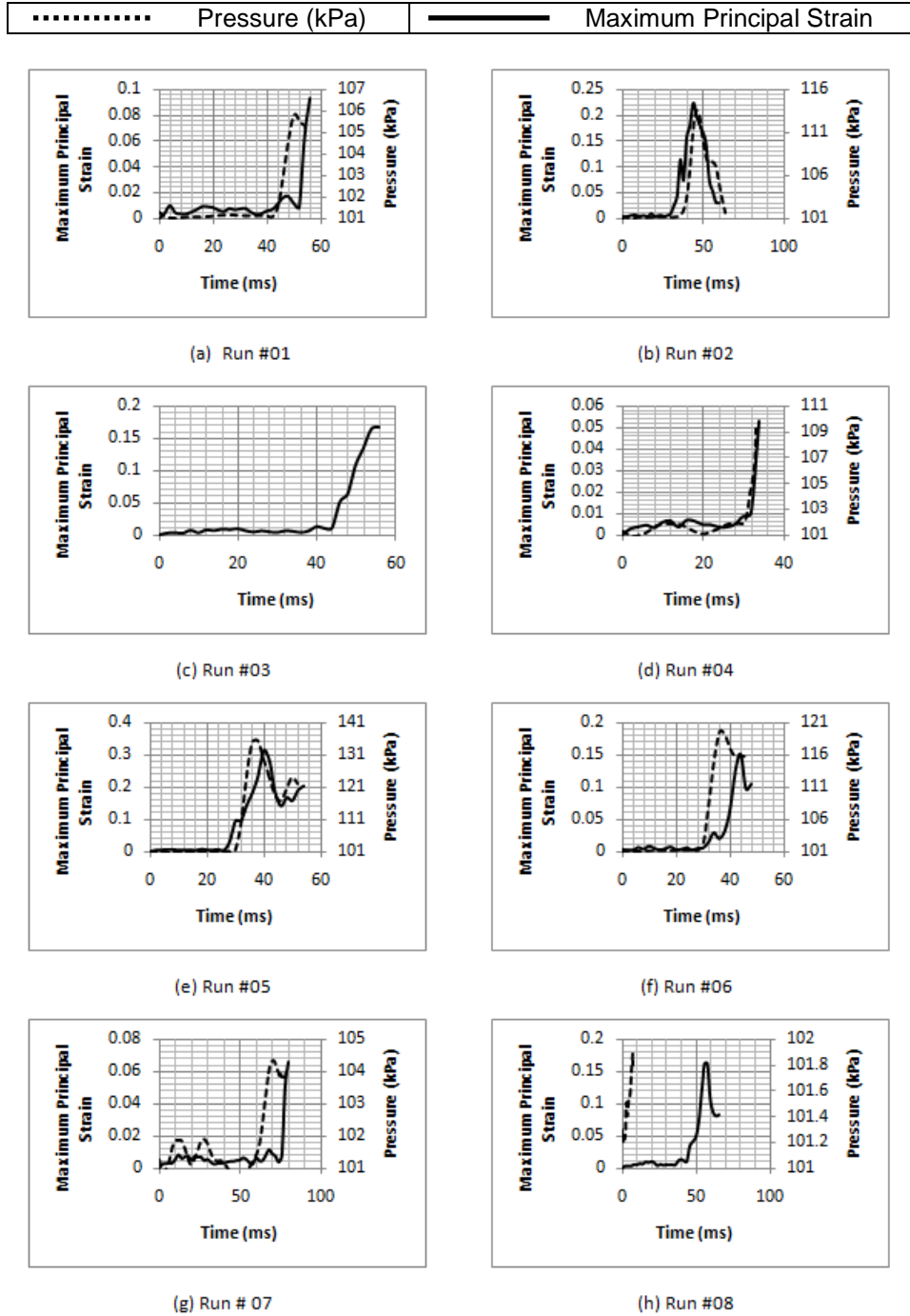


Figure C1: Average Maximum Principal Strain in the Isthmus and maximum pressure in the aorta: Runs #01 through #08

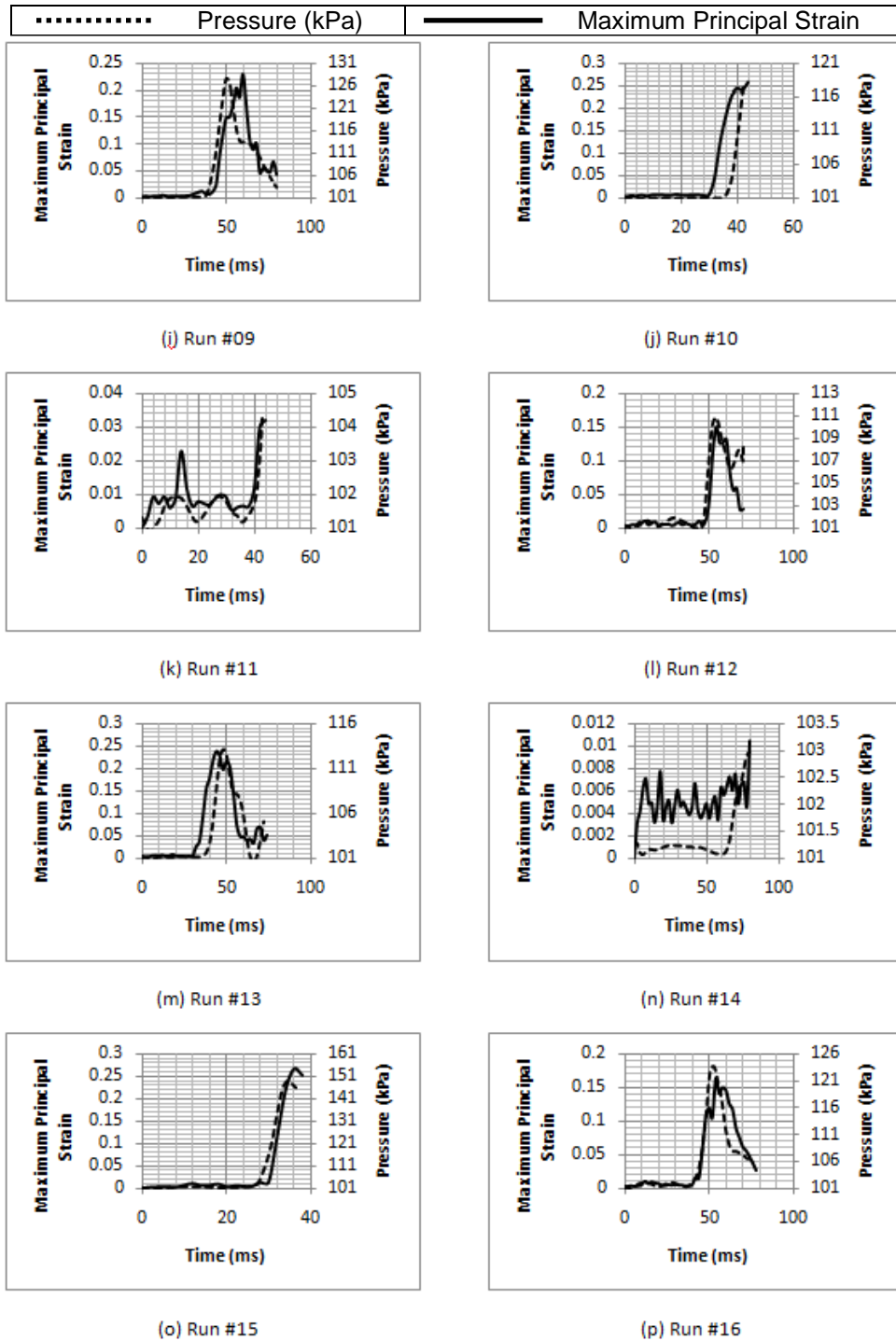


Figure C2: Average Maximum Principal Strain in the Isthmus and maximum pressure in the aorta: Runs #09 through #16

APPENDIX D

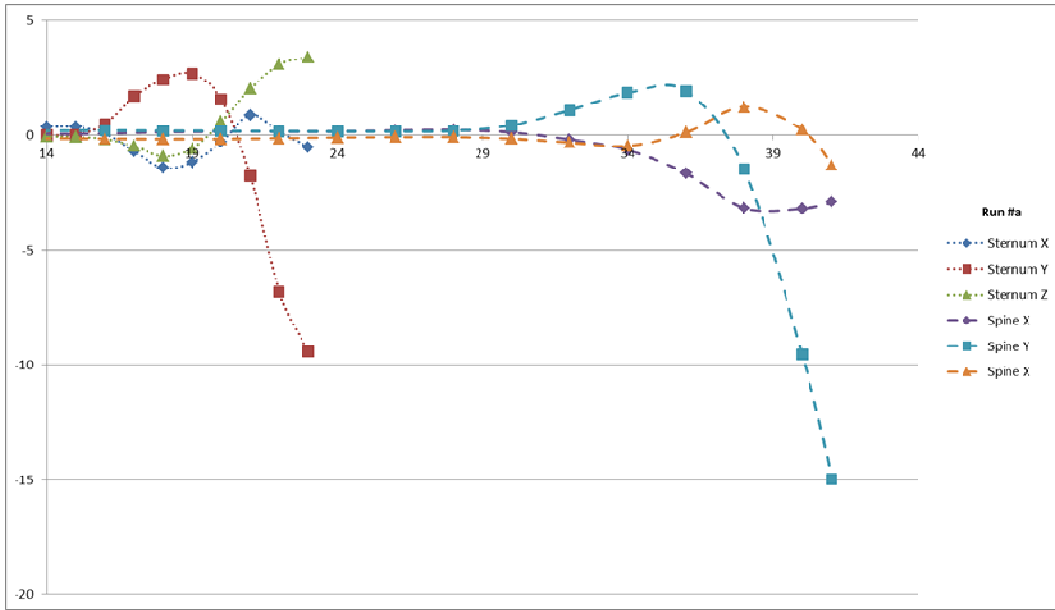


Figure D1: Mid-Sternum vs. T4-spine kinematics for Run #a

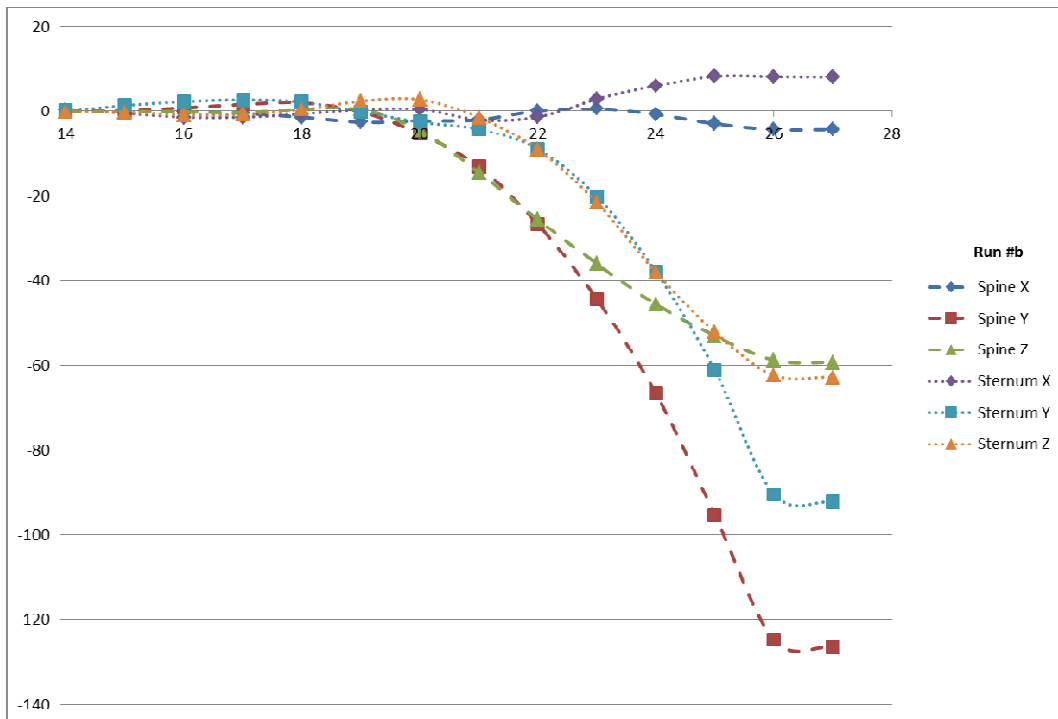


Figure D2: Mid-Sternum vs. T4-spine kinematics for Run #b

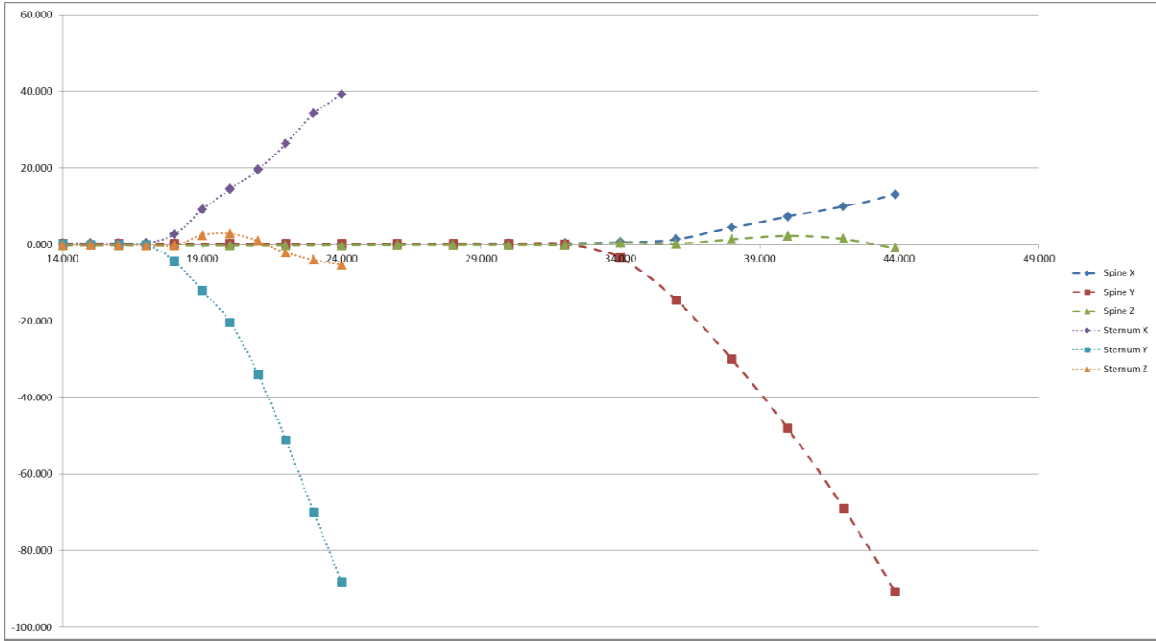


Figure D3: Mid-Sternum vs. T4-spine kinematics for Run #c

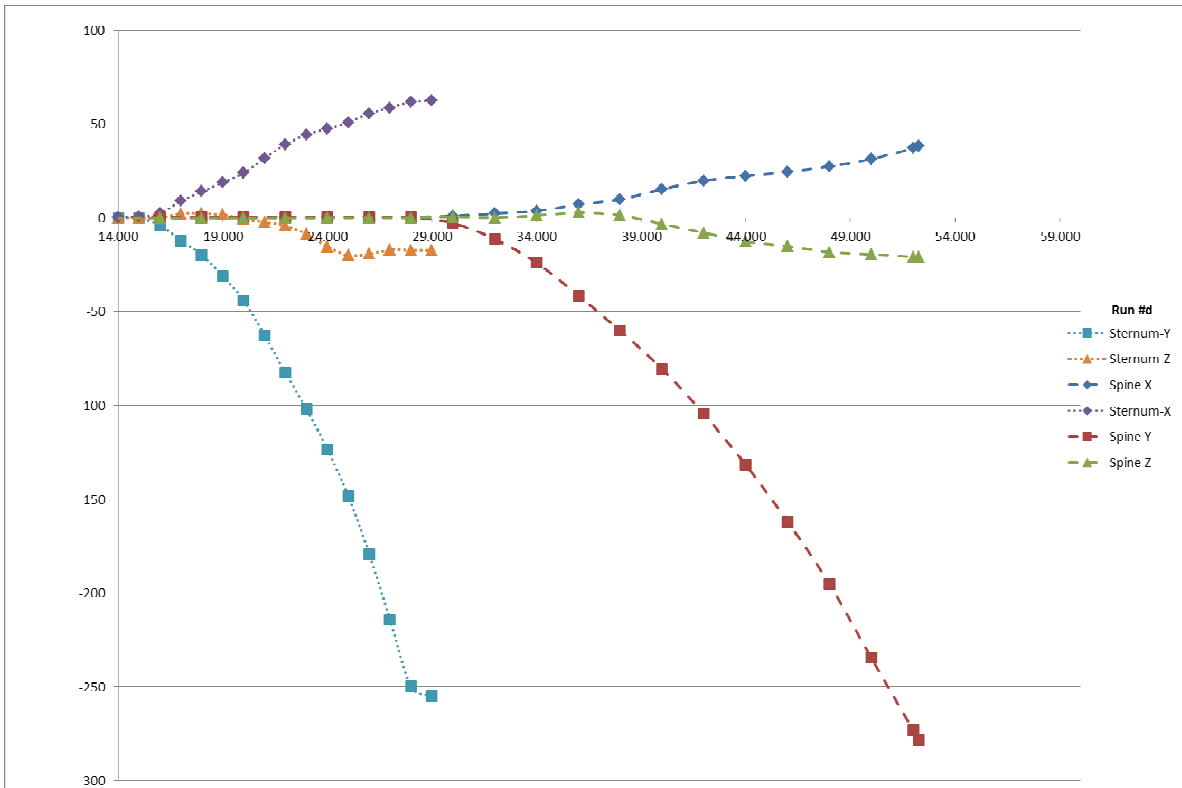


Figure D4: Mid-Sternum vs. T4-spine kinematics for Run #d

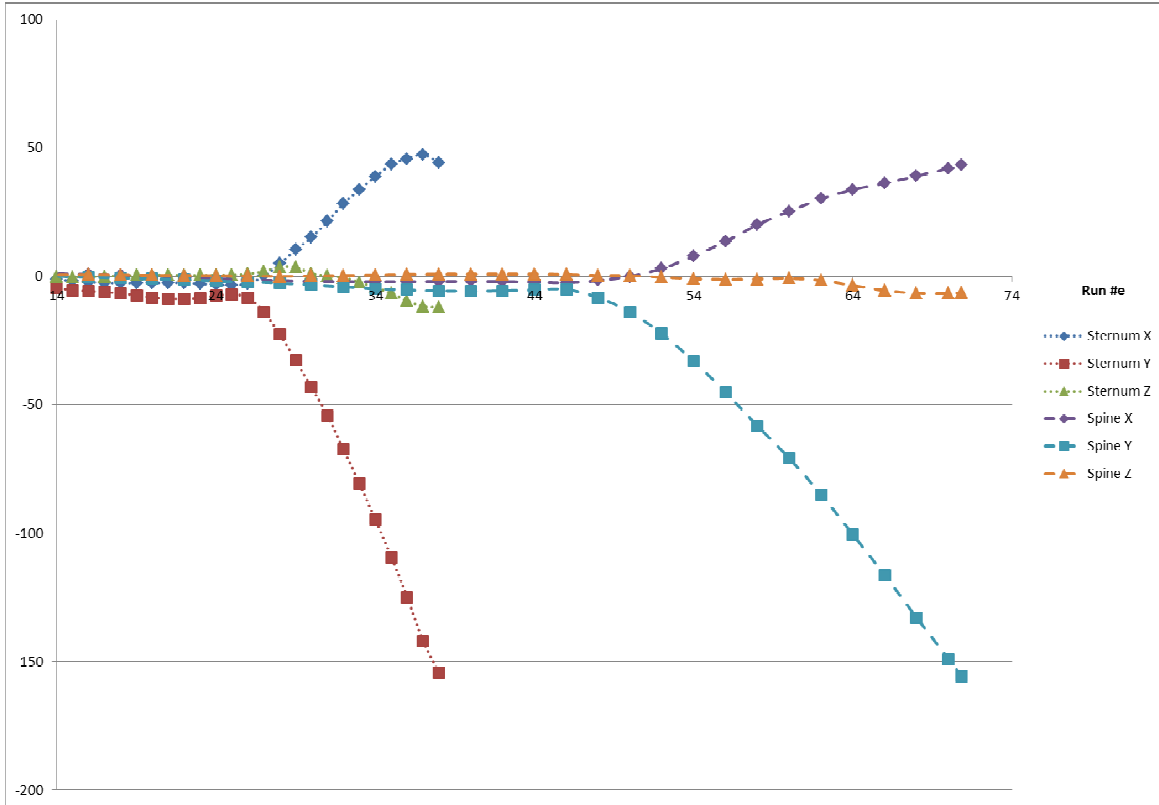


Figure D5: Mid-Sternum vs. T4-spine kinematics for Run #e

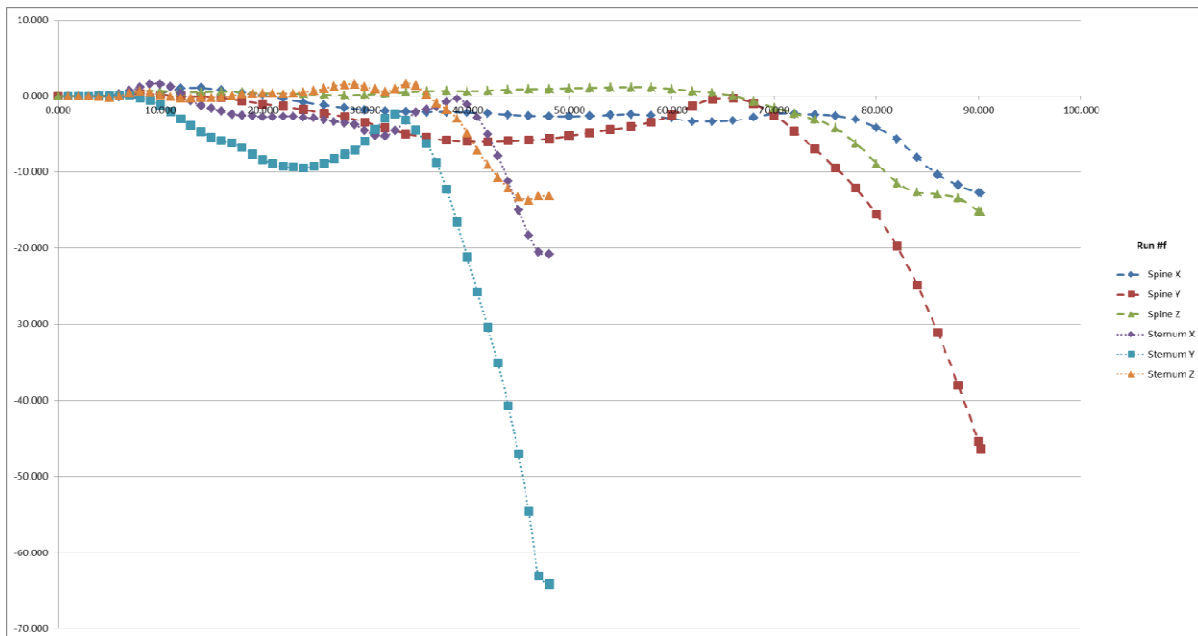


Figure D6: Mid-Sternum vs. T4-spine kinematics for Run #f

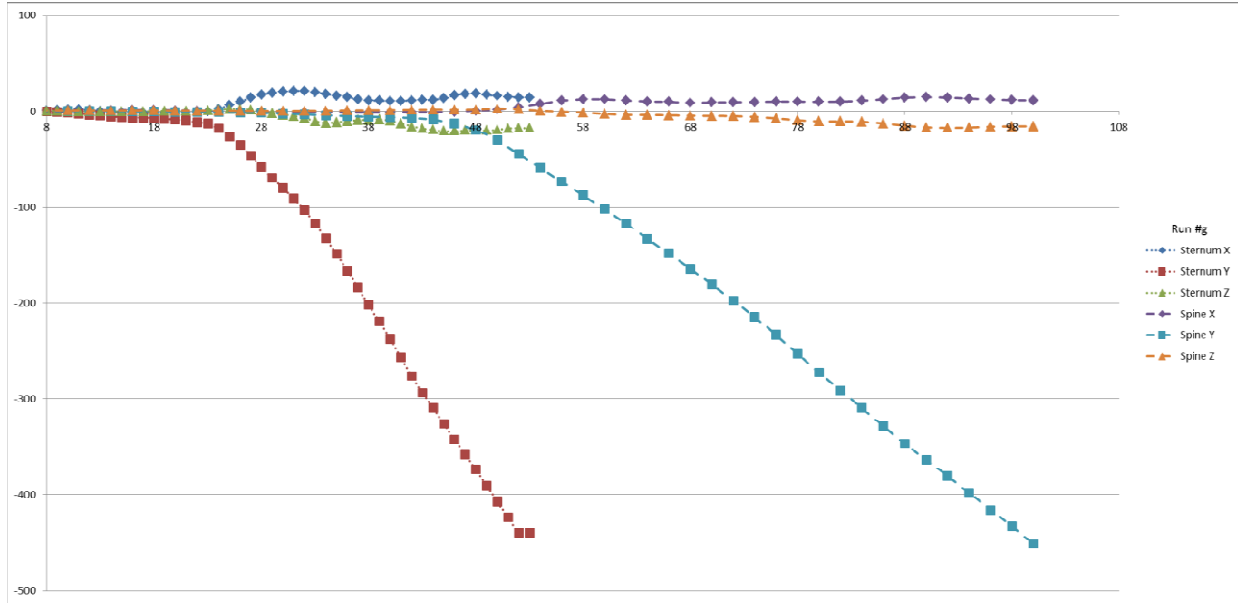


Figure D7: Mid-Sternum vs. T4-spine kinematics for Run #g

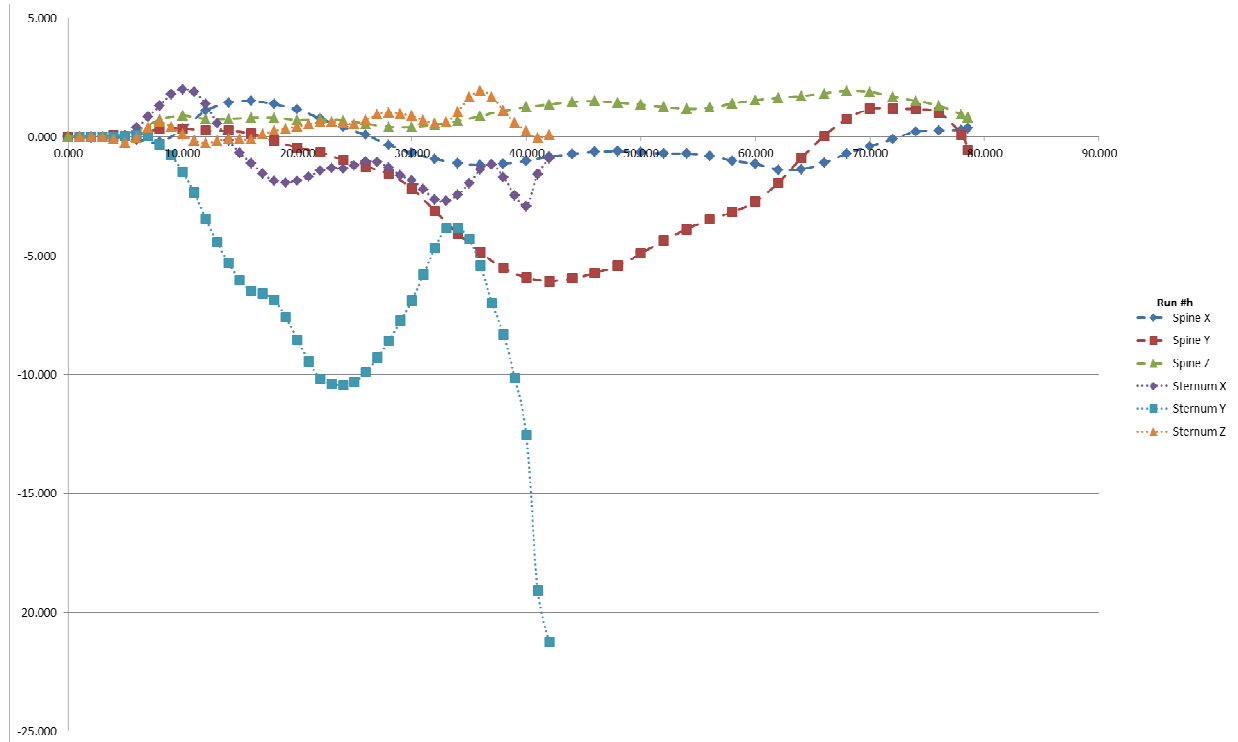


Figure D8: Mid-Sternum vs. T4-spine kinematics for Run #h

APPENDIX E

Table E1: Thickness of side door structures

Part Name	Thickness (mm)
IN - LOWER B PILLAR TRIM - L	3.10
IN - UPPER B PILLAR TRIM - L	3.10
OB - DOR WIN MOTOR 2 - FT - L	1.97
OB - DOR WIN MOTOR 3 - FT - L	1.94
OB-DOR_WIN_SUPPORT_4-RR-L	1.60
OB -DOOR SIDE IMPACT BAR- FT -.1	1.56
BIW - B PILLAR REINFOR 3 - L - I	1.55
BIW - ROCKER PANEL - L - O	1.50
LEFT_REAR_DOOR-SIDE_IMPACT BAR	1.40
BIW - ROCKER PANEL - L - I	1.25
OB-DOR_WIN_SUPPORT_2-RR-L	1.22
OB -DOR WIN REINFORCE-FT-L-I	1.20
BIW - B - PILLAR - L - O	1.13
BIW - B - PILLAR - L - I	1.06
BIW - ROOF REINFORCEMENT - L - I	0.95
BIW - ROOF REINFORCEMENT -L-O	0.90
OB - DOOR - FT - L - O.1	0.71
LEFT_REAR_DOOR	0.70
OB - DOOR - FT - L - I.1	0.68
OB - DOOR - RR - L - I	0.68

REFERENCES

1. Augenstein, J.S., Perdeck, E., Williamson, J., Stratton, J., Murtha, M., Sappas, K., Digges, K., Malliaris, A.C., Lombardo, L. (1997) Heart Injuries Among Restrained Occupants in Frontal Crashes. Society of Automotive Engineers Paper No. 970392.
2. Bass, C. R., Darvish, K., Bush, B., Crandall, J. R., Srinivasan, S. C. M., Tribble, C., Fiser, S., Tournet, L., Evans, J. C., Patrie, J., Wang, C., 2001, "Material properties for modeling traumatic aortic rupture," *Stapp Car Crash Journal* 45, pp. 143-160.
3. Begeman, P. and Melvin, J. (2002), "Mathematical Modeling of Crash-Induced Dynamic Loads on Race Car Drivers", SAE 2002-01-3305.
4. Ben-Menachem, Y. (1993). "Rupture of the thoracic aorta by broadside impacts in road traffic and other collisions: further angiographic observations and preliminary autopsy findings." *Journal of Trauma* 35(3): 363-367.
5. Bertrand, S., Cuny, S., Petit, P., Trosseille, X., Page, Y., Guillemot, H., Drazetic, P. (2008) Traumatic rupture of thoracic aorta in real-world motor vehicle crashes. *Traffic Injury Prevention* 9(2): 153-161.

6. Burkhart, H. M., Gomez, G. A., Jacobson, L. E., Pless, J. E., Broadie, T. A. (2001) Fatal blunt aortic injuries: a review of 242 autopsy cases. *Journal of Trauma* 50(1): 113-115.
7. Crass, J. R., Cohen, A. M., Motta, A. O., Tomashefski, J. F. J., Wiesen, E. J. (1990) A proposed new mechanism of traumatic aortic rupture: the osseous pinch. *Journal of Radiology* 176(3): 645-649.
8. Creasy, J.D., Chiles, C., Routh, W.D., Dyer, R.B. (1997) Overview of Traumatic Injury of the Thoracic Aorta. *Scientific Exhibit*. Vol. 17, No.1, pp. 27-45.
9. Feneis, H. (1994) *Pocket Atlas of Human Anatomy*.
10. FMVSS 214. Department of Transportation NHTSA, Docket No. NHTSA-29134.
11. Franklyn, M., Fitzharris, M., Fildes, B., Yang, K., Frampton, R., Morris, A. (2003) A Preliminary Analysis of Aortic Injuries in Lateral Impacts. *Traffic Injury Prevention* 4(3): 263-269.
12. Guan, F., Belwadi, A., Han, X., Yang, K.H. (2009) Application of Optimization Methodology on vehicular crash reconstruction. *Proceedings of 2009 ASME*

International Mechanical Engineering Congress and Exposition November 13-19,
Lake Buena Vista, Florida, USA. Paper No.: IMECE2009-12810

13. Hardy, W. N., Shah, C. S., Kopacz, J. M., Yang, K. H., Van Ee, C. A., Morgan, R., Digges, K. (2006) Study of Potential Mechanisms of Traumatic Rupture of the Aorta Using *In Situ* Experiments. *Stapp Car Crash Journal* 50: 247-266.
14. Hardy, W. N., Shah, C. S., Mason, M. J., Kopacz, J. M., Yang, K. H., King, A. I., Bishop, J. L., Banglmaier, R. F., Bey, M. J., Morgan, R. M., Digges, K. H. (2008) Mechanisms of traumatic Rupture of the Aorta and Associated Peri-isthmic Motion and Deformation. *Stapp Car Crash Journal* 52: 233-265.
15. Holzapfel, Sommer, G., and Regitnig, P. (2004) Anisotropic Mechanical Properties of Tissue Components in Human Atherosclerotic Plaques. Graz University of Technology, Institute for Structural Analysis, Computational Biomechanics, Austria [Personal Communication]
16. Huang, Y., King, A. I., Cavanaugh, J. M. (1994) Finite element modeling of gross motion of human cadavers in side impact. *Proceedings of the 38th Stapp Car Crash Conference*: 35-53.

17. Iwamoto, M., Miki, K., Mohammad, M., Nayef, A., Yang, K. H., Begeman, P. C., King, A. I. (2000) Development of a Finite Element Model of the Human Shoulder. Proceedings of the 44th Stapp Car Crash Conference: 281-297.
18. Iwamoto, M., Kisanuki, Y., Watanabe, I., Furuu, K., Miki, K., Hasegawa, J. (2002) Development of a Finite Element Model of the Total Human Model for Safety (THUMS) and application to injury construction. Proceedings of the 2002 International Research Council on Biomechanics of Injury Munich, Germany: 31-42.
19. Kassab, G.S. (2006) Biomechanics of the cardiovascular system: the aorta as an illustrative example. Journal of the Royal Society of Interface 3, 719-740
20. Katyal, D., McLellan, B.A., Breneman, F.D., Boulanger, B.R., Sharkey, P.W., Waddell, J.P. (1997) Lateral impact motor vehicle collisions: significant cause of blunt traumatic rupture of the thoracic aorta. The Journal of Trauma 42(5): 769-772.
21. Kroell, C.K., Schneider, D.C., and Nahum, A.M. (1974) Impact tolerance and response of the human thorax II. 18th Stapp Car Crash Conference. Paper No.: 741187.
22. Lee, J. B. and Yang, K. H. (2001) Development of a finite element model of the human abdomen. Proceedings of the 45th Stapp Car Crash Conference: 79-100.

23. Letterer, E. (1924) Beitrage zur entstehung der aortenruptur an typischer stele. Virchows Archiv fur Pathologische Anatomie und Physiologie und fur Klinische Medizin 253: 534-544.
24. Liechty, J. D. (1957) Variations pertaining to the aortic arches and their branches with comments on surgically important types. Q Bull Northwest University Medical School 31(2): 136.
25. Lizee, E., Robin, S., Song, E., Bertholon, N., Lecoz, J., Besnault, B., Lavaste, F. (1998) Development of a 3D finite element model of the human body. Proceedings of the 42nd Stapp Car Crash Conference.
26. Lundevall, J. (1964) The Mechanism of Traumatic Rupture of the Aorta. Acta pathologica et microbiologica Scandinavica 62: 34-46.
27. Mohan, D., and Melvin, J.W. (1983) Failure properties of passive human aortic tissue: Biaxial tension tests. Journal of biomechanics 16(1): 31-44.
28. Niehoff, P. P. (2006) The accuracy of WinSmash delta-V estimates: The influence of vehicle type, stiffness, and impact mode. Annual proceedings / Association for the Advancement of Automotive Medicine. Association for the Advancement of Automotive Medicine (1540-0360), 50, p. 73.

29. Plank, G. R., Eppinger, R. H. (1991) An Improved Finite Element Model of the Human Thorax. 13th ESV: 902-907.
30. Roberts, S. B. and Chen, P. H. (1970). "Elastostatic analysis of the human thoracic skeleton." *Journal of Biomechanics* **3**: 527-545.
31. SAE J224 (1980) Collision Deformation Classification. Society of Automotive Engineers Surface Vehicle Standard, Warrendale, PA.
32. Sauaia, A., Moore, F.A., Moore, E.E., Moser, K.S., Brennan, R., Read, R.A. and Pons, P.T. (1995) Epidemiology of trauma deaths: a reassessment. *J. Trauma*. Vol. 38(2), pp. 185-193.
33. Shah, C.S., Yang, K.H., Hardy, W.N., Wang, H.K. and King, A.I. (2001) Development of a Computer Model to Predict Aortic Rupture Due to Impact Loading. 45th Stapp Car Crash Conference. Paper No.: 2001-22-0007.
34. Shah, C. S., Mason, M. J., Yang, K. H., Hardy, W. N., Van Ee, C. A., Morgan, R., Digges, K. (2005) High-Speed Biaxial Tissue Properties of The Human Cadaver Aorta. Proceedings of IMECE05, 2005 ASME International Mechanical Engineering Congress, IMECE2005-82085.

35. Shah, C.S., Hardy, W.N., Mason, M.J., Yang, K.H., Van Ee, C.A., Morgan, R. and Digges, K. (2006) Dynamic Biaxial Tissue Properties of the Human Cadaver Aorta. 50th Stapp Car Crash Conference. Paper No.: 2006-22-0010.
36. Shah, C. S., Hardy, W. N., Yang, K. H., Van Ee, C. A., Morgan, R. M. and Digges, K. H. (2007) Investigation of the traumatic rupture of the aorta (TRA) by simulating real-world accidents. Proceedings of the 2007 International Research Council on Biomechanics of Injury, Maastricht, The Netherlands: 349-359.
37. Sherebrin, M.H., Kim, H.L. and Roach, M.R. (1994) Calcium mass in human aortas from autopsy. *Physiol. Meas.* Vol. 15, pp. 281-289.
38. Siegel, J. H., Smith, J. A., Siddiqi, S. Q. (2004) Change in velocity and energy dissipation on impact in motor vehicle crashes as a function of the direction of crash: key factors in the production of thoracic aortic injuries, their pattern of associated injuries and patient survival. A Crash Injury Research Engineering Network (CIREN) study. *Journal of Trauma* 57(4): 760-777.
39. Smith, R. S., Chang, F. C. (1986) Traumatic Rupture of the Aorta: Still a lethal injury. *American Journal of Surgery* 152: 660-663.

40. Solomon, E. P., Phillips, G. A. (1987) *Understanding Human Anatomy and Physiology*. Saunders, Philadelphia.
41. Sommer, G., Gasser, T.C., Regitnig, P., Auer, M. and Holzapfel, G.A. (2008) Dissection properties of the human aortic media: an experimental study. *Journal of Biomechanical Engineering*. Vol. 130.
42. Sudaram, S. H., Feng, C. C. (1977) Finite Element Analysis of the Human Thorax. *Journal of Biomechanics* 10(8): 505-516.
43. Swan, K. G., Swan, B. C., Swan, K. G. (2001) Decelerational Thoracic Injury. *Journal of Trauma* 51: 970-974.
44. Viano, D. (1983) Biomechanics of Non-penetrating Aortic Trauma: A Review. *Proceedings of the 27th Stapp Car Crash Conference*: 109-114.
45. Viano, D. C. (1989) Biomechanical Responses and Injuries in Blunt Lateral Impact. *Proceedings of the 33rd Stapp Car Crash Conference*: 113-142.
46. Wang, K. H. (1995) *Development of a Side Impact Finite Element Human Thoracic Model*, Wayne State University.

47. Yang, K.H., Hu, J., White, N.A., King, A.I., Chou, C.C. and Prasad, P. (2006)
Development of Numerical Models for Injury Biomechanics Research: A Review of
50 years of Publications in the Stapp Car Crash Conference. 50th Stapp Car Crash
Conference. Paper No.: 2006-22-0017.

ABSTRACT**FINITE ELEMENT RECONSTRUCTION OF REAL WORLD AORTIC INJURY IN
NEAR-SIDE LATERAL AUTOMOTIVE CRASHES WITH CONCEPTUAL
COUNTERMEASURES****by****ADITYA NEELAKANTA BELWADI****August 2011****Advisor:** Dr. King H. Yang**Major:** Biomedical Engineering**Degree:** Doctor of Philosophy

Traumatic rupture of the aorta (TRA) remains the second most common cause of death associated with motor vehicle crashes after brain injury. On an average, nearly 8,000 people die annually in the United States due to blunt injury to the aorta. It is observed that more than 80% of occupants who suffer an aortic injury die at the scene due to exsanguination into the chest. With the advent of more accurate and established human body finite element (FE) models, FE crash reconstruction methods may become a valuable tool when assessing crash scenarios and occupant injury mechanisms.

The current study is divided into five main aims, near side left lateral real world finite element reconstructions, sensitivity study, thresholds for TRA, aorta mechanics in racing crashes and conceptual countermeasures. In the first study eight nearside left lateral impacts, in which a TRA occurred, were reconstructed using a combination of real world crash data reported in the Crash Injury Research and Engineering

Network (CIREN) database and FE models of vehicles and occupants. The average maximum principal strain (AMPS) in the root, ascending, and the isthmus regions of the aorta were calculated and model predicted high strain areas were compared with real world injury reports. In seven of the eight cases aortic failure occurred in the isthmus region and, the average peak tensile isthmic strain, 20±7 mm distal to the left subclavian artery, was 18±6%.

To identify key parameters for injury causation, 16 Design of Computer Experiments (DOCE) runs, generated using a Latin square sampling technique on modeFRONTIER with FE models of vehicles and the WSHBM as described earlier were performed to evaluate the role of PDOF, impact velocity, impact position, impact height and occupant seating position on aortic strain, aortic pressure and compartmental intrusion. The AMPS decreased significantly with an increase in the PDOF (from 270 degrees). Of the four PDOFs simulated, a PDOF of 270 degrees generated the highest average maximum principal strain in the aorta. Further, strain increased with increase in impact velocity while pressure in the aorta decreased with an increase in PDOF (from 270 degrees).

The data obtained in the CIREN reconstructions were further compared with three CIREN cases without aortic injury to understand and delineate the mechanism for TRA. A paired comparison based sensitivity study was carried out and data compared with literature. It was seen that in nearside left lateral impacts the PDOF of impact played a crucial role in TRA. Further, three Indy car based racing crashes were simulated as part of a comparison study involving nine other simulated cases. It

was seen that for TRA to occur, acceleration along was not enough. Thoracic deformation was essential and the shoulder-clavicle complex played a crucial role in TRA by causing relative motion of the sternum and the thoracic spine.

Utilizing six design factors; B-pillar beam, crossbeam, side conceptual blanket airbag, thickness factor, yield strength and by varying the dimensions of the B-pillar beam, 18 DOCE simulations were carried out. The current study suggest that the protective effects of an improved side-construction standard can be enhanced further by the more rational placement of an airbag-like structure, to buffer head and chest contact with the B-Pillar along its entire length from car seat to roof. It is suggested that the combination of these two safety measures, B-pillar beam and thickness is likely to result in a significant reduction in both head and aortic Isthmus injury and thus to substantially reduce mortality subsequent to lateral motor vehicle crashes.

AUTOBIOGRAPHICAL STATEMENT

ADITYA NEELAKANTA BELWADI

EDUCATION

- 2011** PhD (Biomedical Engineering), Wayne State University, Detroit, MI, USA
- 2007** MS (Biomedical Engineering), Wayne State University, Detroit, MI, USA
- 2006** MS (Mechanical Engineering), Wayne State University, Detroit, MI, USA
- 2002** BS (Mechanical Engineering), R.V. College of Engineering, Bangalore, India

HONORS AND AWARDS

1. Recipient of the prestigious **SAE Ralph H. Isbrandt Automotive Safety Engineering Award** in recognition of outstanding SAE technical paper #2009-01-0249, "A New Device for Multi-Axial Tissue Testing: Application to Combined Bending and Shear Loading of the Spine" presented at the 2009 SAE World Congress held in Detroit, MI
2. Recipient of the prestigious **Dr. Margaret H. Hines Award** for the "Best Poster Presentation" at the 6th Annual Injury Biomechanics Symposium held at Ohio State University, Columbus from May 17-18, 2010

SELECTED PUBLICATIONS

1. **Aditya Belwadi**, John Siegel, Fengjiao Guan, Aadarsh Singh, King Yang and Albert King (2011) "Lateral Aortic Injury Reconstruction – A CIREN data based Finite Element Accident Reconstruction", submitted to ASME's Journal of Biomechanical Engineering.
2. John Siegel, **Aditya Belwadi**, Joyce Smith, Chirag Shah, King Yang (2010) "Analysis Of The Mechanism Of Lateral Impact Aortic Isthmus Disruption In Real-Life Motor Vehicle Crashes Using A Computer Based Finite Element Numeric Model : With Simulation Of Prevention Strategies", Journal of Trauma, 68: 1375-1395
3. **Aditya Belwadi**, King Yang, Joe Mazur and Ed Burley (2009) "A New Device for Multi-Axial Tissue Testing: Application to Combined Bending and Shear Loading of the Spine" SAE International Journal of Passenger Cars – Mech Syst. 2(1):454-461
4. Sriram Balasubramanian, Philippe Beillas, **Aditya Belwadi**, Warren N. Hardy, King H. Yang, Albert I. King and Mitsutoshi Masuda (2004) "Below Knee Impact Responses using Cadaveric Specimens", 48th Stapp Car Crash Journal, Paper No.: 2004-22-0004, pp. 71-88